PHD

High resolution microanalysis of alloy steel

Vatter, Ian A.

Award date:
1993

Awarding institution:
University of Bath

High Resolution Microanalysis of Alloy Steel

Submitted by Ian A Vatter
for the degree of PhD
1993

Ian A Vatter

ProQuest LLC
789 East Eisenhower Parkway
P.O. Box 1346
Ann Arbor, MI 48106-1346

Summary

This thesis describes and compares the techniques of Auger Electron Spectroscopy (AES) and Scanning Transmission Electron Microscopy (STEM) in relation to their use for the detection and quantification of low levels of grain-boundary segregation. The particular system to be studied concerns the equilibrium segregation of phosphorus and chromium to the prior austenite grain boundaries in a 9%chromium steel which has been doped with phosphorus in the range 40 to 560 weight parts per million. The quantification techniques used in association with the AES and STEM techniques have been justified by cross-correlation. It is argued that the results will lead to greater confidence in data obtained by either method in future studies.

The thesis begins with a description of the physical processes involved in the production of characteristic signals in each technique, and how the recorded signal is affected by absorption processes and the method of detection etc. Procedures for quantifying the experimental data are then developed for both techniques in order to determine the extent of grain boundary coverage.

Uncertainties in the quantification procedures are discussed and the statistics of detection used to determine the minimum detectable coverage of the grain boundary and the minimum detectable mass of segregant. The effect of varying the conditions of data collection have been used to evaluate the optimum conditions for detecting grain boundary segregants.

Both techniques have proved to be capable of detecting segregation from a maximum level of approximately 100% down to the detection limit of 6% of a monolayer. This lower limit was the same for both techniques.

The AES technique is best suited to collecting a large amount of data from interfaces in a short time, whereas the STEM is better suited to analysing interfaces in complex alloys when multiple segregation and precipitation is present.

CONTENTS

Chapter 1. Introduction

This chapter discusses the importance of elucidating in detail the microstructure of a material if its properties, mechanical, chemical or physical, are to be fully understood. The development of a number of relevant microstructural techniques is described, which are then compared with particular reference to published work on the analysis of grain boundaries in metals. The chapter concludes with a detailed presentation of the methods of Auger electron spectroscopy and scanning transmission electron microscopy since the use of these techniques forms the basis of the work presented in this thesis.

1.1 Materials Background

It has been known for a long time that metals are polycrystalline and that pure metals usually have low hardness and low tensile properties. It is also recognised that the properties may be sensitive to the presence of additional elements. For example, alloying elements may be chosen to improve mechanical properties, by solid solution or precipitation hardening, although many cases are reported whereby small additions, often adventitious impurities, have extremely deleterious effects. Furthermore the addition required to induce a desired increase depends strongly upon the species added; for example the addition of carbon to iron has a much greater effect on its hardness than corresponding additions of chromium or nickel. Such observations have led to numerous investigations into the nature of the structure of pure metals and the microstructural consequences of the incorporation of alloy additions.

The mechanical properties of a metal can be correlated with microstructure as well as chemical composition. For example grain size has been found to influence hardness such that fine-grained material has a higher hardness than coarse-

grained material due to the increased number of grain boundaries which act as barriers to dislocation movement and decrease the plasticity of the material. Other properties influenced by grain boundaries include creep and fatigue. Fine grained metals exhibit reduced resistance to creep and enhanced tolerance to fatigue damage.

Other microstructural features which influence the properties of a metal include its crystallographic structure, and the dispersion of second phases.

The effect of grain boundaries on the bulk properties of a material is not purely geometrical but includes any abrupt change in chemical composition which occurs in the vicinity. The change in chemical composition may arise because boundaries are regions of disorder where alloying atoms can reside with minimum distortion of the surrounding metal matrix, the reduction in distortion providing the thermodynamic driving force for grain boundary segregation of species (McLean 1957).

Grain boundaries and interfaces, due to their reduced atomic density, provide fast diffusion paths for atoms and this can lead to chemically denuded regions close to grain boundaries. Thus elements may diffuse from a narrow region adjacent to the boundary and along the grain boundary at a rate which is too high for their replenishment by diffusion from the bulk of the grain. This can lead to effects such as the phenomenon of weld decay where chromium depletion occurs in the vicinity of boundaries during the growth of chromium-rich carbides on the boundary. The chromium-depleted region is then more susceptible than the bulk material to corrosion and other forms of chemical attack. Enrichment of impurities and alloying elements can also occur at grain boundaries and the abrupt changes in chemical composition which occur over a distance of a few nanometres can have a marked affect on the bulk properties of the material; for example, impurity segregation to grain boundaries is a major cause of temper embrittlement in steels

(Seah 1977, Guttmann 1980). Elements which are known to segregate to the grain boundaries in steel and produce embrittlement include phosphorus (Okumura 1985, Doig and Flewitt 1978), tin (Doig et al 1982), antimony (Kenik 1986), arsenic and sulphur (Briant 1985, Ellis et al 1985). The grain boundary-segregation of impurities has been studied in systems such as bismuth in copper (Powell 1973, Baumann and Williams 1981), zinc in aluminium (Titchmarsh 1990) and nickel and silicon in irradiated steel (Norris et al 1986, Muroga et al 1987). Enrichment of the grain boundary can occur by either equilibrium or non-equilibrium mechanisms. The former is the more spatially restricted and occurs either at, or within a few atom layers of, the interface. Non-equilibrium segregation is characterised by a compositional change which extends over a wider region, e.g. from a few nm to a few μm.

1.2 Ferritic Steels

Ferritic steels containing additions of 9 to 12% chromium combine high strength and toughness, with good corrosion and oxidation resistance in a range of environments and good elevated temperature creep strength. Such steels are therefore extensively used in high-temperature applications (300°C to ~550°C) and in corrosive environments, for example steam generator tubing in conventional and nuclear power plant, reaction vessels and pipework in the chemical and petroleum industries, and the rotors and blades of gas and steam turbines. (Fujita 1986, Kayano et al 1985). With the trend towards increasingly higher operating temperatures in steam generating plant, in order to reduce fuel costs and improve operating efficiency, there is considerable research to improve the high temperature (up to 600°C) capability of ferritic steels so that they may be used in supercritical steam generation plant. Being economically attractive, such steels are serious

contenders for many other applications where austenitic steels have previously been used.

Ferritic steels offer a number of additional advantages. They are more resistant, than austenitic steels, to environmental cracking processes in aqueous, steam and caustic environments, and they have a lower coefficient of thermal expansion, making them more resistant to thermal shock and thermal fatigue. These properties are important in thick section applications, as for example the structures above the core of nuclear reactors. Ferritic steels also have a lower void swelling coefficient and a greater resistance to embrittlement under irradiation than austenitic steels. (Gettes and Thomas 1983, Bullough et al 1981, Lechtenberg 1985). For these reasons ferritic steels are being considered for the first wall of nuclear fusion reactors (Lechtenberg 1985, Klueh 1982), as cladding materials for fuel in nuclear fission reactors (Dupouy 1983), and for the structures above the core of fast reactors.

For high temperature applications an understanding of the changes which can occur during service is crucial since in ferritic steels, temperatures in the range 400-600°C can induce microstructural changes including the segregation of trace impurities to grain boundaries within the metal. It is well recognised that such changes can influence low-temperature and high-temperature toughness, as well as increasing the susceptibility to environmental cracking. An important example of mechanical property degradation concerns reversible temper embrittlement (Eyre et al 1981, McMahon 1974) which occurs as a result of impurity segregation. The segregation of phosphorus, tin, arsenic and antimony to grain boundaries is known to result in embrittlement of ferritic steel. The embrittlement is most clearly manifested by an increase in the temperature at which the transition between ductile and brittle fracture occurs. In addition the low temperature brittle fracture mode progressively changes from transgranular cleavage to intergranular fracture as the steel becomes more embrittled. The increase in ductile to brittle transition

temperature (DBTT), as measured using blunt-notch Charpy impact specimens, can be large; shifts in transition temperature of 100°C to 200°C have been observed in low alloy steels as a consequence of phosphorus segregation to the grain boundaries during thermal ageing (Kussmaul et al 1978a and 1978b, Tavassoli et al 1983, Druce et al 1985). A linear correlation has also been found between the level of phosphorus segregation and the magnitude of shift in DBTT in low alloy steels doped with phosphorus (Vatter and Hippsley 1991b). Due to the important role which segregation plays in embrittlement processes it is necessary to be able to determine accurately the level of segregation present on grain boundaries of a material. There is a requirement for these measurements to be made both at the start of operational life and during service to enable any increase in segregation levels to be monitored.

The material selected for this study is a 9% chrome ferritic steel doped with phosphorus which has previously been found to suffer from temper embrittlement due to segregation of the phosphorus to the grain boundaries in the metal (Wall 1987).

1.3 The Development of Microscopy Techniques

The observed relationship between microstructure and properties has contributed to the development of a range of microscopy techniques being developed and, since the most pronounced changes in properties are often associated with the finest of microstructural features, the use of high resolution analytical techniques is a prerequisite for a systematic study. However, microstructural studies usually commence with an optical examination of the material. This may be conducted on the fracture surface of a failed component in order to reveal the nature of the fracture process, or on a flat metallographically prepared (i.e. polished and

etched) specimen in order to study the grain size, the morphology of primary and secondary phases and the number density, size and location of large precipitates.

The limit of resolving power of a microscope, as given by the Rayleigh criterion, states that two point objects can just be resolved when placed so close to each other that the intensity maximum of one, in the image plane, is coincident with the first intensity minimum of the other. This gives a diffraction resolution limit for a microscope, $\delta = 0.61\lambda/\text{N.A.}$, where λ is the wavelength of the illuminating radiation and N.A. refers to the numerical aperture of the system. For the best optical microscopes N.A.$\approx$1.5 which means a maximum resolving power of the order of 0.25 μm. To improve resolution and enable a more detailed study of microstructural features to be conducted a microscope using shorter wavelength radiation is, therefore, required.

X-rays satisfy this requirement, but since the focusing and scanning of x-ray beams is difficult, their use for high resolution microscopes has not been pursued to the same extent as with electrons.

The idea that electrons behaved with the properties of both waves and particles was postulated by De Broglie who showed that the electron wavelength, λ, could be related to momentum, p, by $\lambda = {}^{h}/_{p}$, where h=Plank's Constant. Since p=mv, where m and v are mass and velocity of the electron, we may write

$$\lambda = \frac{h}{\sqrt{2mEe}}$$

where e is the charge on the electron and E is the electron accelerating voltage. Thus when accelerated through a potential of 10keV an electron has an associated wavelength of approximately 0.1Å. Using the Rayleigh criteria then gives a potential resolving power using energetic electrons of 0.05Å. In reality chromatic and spherical aberrations introduced by the electron lenses will prevent this potential

limit being achieved. In 1926/7 the mathematics of focusing an electron beam by the use of an electric coil were demonstrated by Busch (Busch 1926, 1927). Knoll and Ruska used the formulations of Busch and produced the forerunners of the transmission electron microscope (TEM) in 1932 (Knoll and Ruska 1932a, 1932b) and the scanning electron microscope (SEM) in 1935 (Knoll 1935). Although the performance of these early machines was poor, even in comparison with optical microscopes, the first machine achieving a magnification of only thirteen times, they laid the foundations for the full range of electron-optical instruments now available. Subsequent years saw refinement of the electron lenses, with particularly notable contributions being made by Boersch (1939), le Poole (1964) and Cooke and Duncumb (1969), all of whose work led to improvements in the focusing ability of the lenses incorporated into electron microscopes.

To turn these early microscopes into machines capable of chemical analysis it was necessary to incorporate methods of detecting the signals which were known to be emitted by a specimen when bombarded with energetic electrons. The earliest observation of such signals was the dependence of the fraction of electrons backscattered by a specimen on sample atomic number (Starke 1898). This was followed by the demonstration that samples emitted x-rays characteristic of their composition when bombarded with electrons of sufficiently high energy (Kaye 1909). These x-rays were detected using ionisation chambers. In 1912 von Laue proposed, and Friedlich and Knipping verified that a crystal could be used as a three-dimensional diffraction grating for x-rays. W H and W L Bragg used this principle to construct the first wavelength-dispersive x-ray spectrometer in 1913. The basic design was refined by de Broglie (1914), Gouy (1916), Johann (1931) and Cauchois (1932) to improve the ability of the diffracting crystal to focus the x-rays onto the detector. A final solution to this problem was found by Johansson (1932, 1933). A spectrometer of this latter design was interfaced to an electrostatic electron microscope which had been modified to operate as a shadow microscope by

Castaing. He used the spectrometer to determine the chemical composition of samples by comparing the count rates of appropriate spectral lines with the electron beam located firstly on a specimen and, secondly, on a standard using the same analysis conditions (Castaing 1951). Later the incorporation of scanning coils by Duncumb and Cosslett (1956) allowed the beam to be more accurately positioned, and the x-ray signal produced was then used to modulate a cathode ray tube scanned in synchronisation with the electron beam, thereby permitting elemental distributions within the sample to be mapped. These advances led to the development of the scanning electron microscope and the electron probe microanalyser.

The addition of chemical analysis capability to a high resolution transmission electron microscope occurred with the commercial production of the electron microscope microanalyser, EMMA 4, (Cooke and Openshaw 1970). This machine was based on the design of Duncumb and incorporated two fully-focusing x-ray crystal spectrometers on the electron column which allowed the chemical composition of particles of approximately 1μm in diameter to be investigated. The use of focusing crystal spectrometers on TEMs was superseded by the development of solid-state lithium-drifted, silicon crystal detectors which were capable of detecting x-rays of all energies simultaneously, a significant improvement over the sequential nature of the wavelength-dispersive detectors. Initially detectors lacked the necessary energy resolution to separate the characteristic x-ray peaks of adjacent elements in the periodic table but in the early 1970's energy resolution and sensitivity improved sufficiently to allow the lithium-drifted silicon detector to become viable for x-ray spectrometry down to energies of approximately 1keV.

In scanning electron microscopy bulk samples are examined using a focused electron beam (diameter a few nm) and signals such as the backscattered electrons (BSE) or secondary electrons (SE) allow the surface morphology to be explored at magnifications in the range x10 to x100,000 with a resolution of a few nm. As well

as its higher resolution, the SEM has a much greater depth of field than the optical microscope which makes it ideal for examining uneven surfaces such as those formed during fracture. In addition x-ray spectrometers fitted to the SEM permit x-rays produced by interaction between the primary electron beam and the sample to be analysed, thus giving an indication of the chemical composition of the material under the electron beam.

The transmission electron microscope differs from the SEM in that a beam of higher energy, typically 100-1000 KeV, electrons is used. The beam is incident on a thin sample of the material under investigation and the electrons recorded are those transmitted through the sample rather than those backscattered. Used to form an image of the sample, they show internal microstructural features such as grain boundaries, second phases, precipitates and, on a finer scale, dislocations and stacking faults. In addition, the transmitted electrons can form a diffraction pattern which contains crystallographic information from the sample. In a similar manner to the SEM, the analysis of x-rays generated in the sample by the beam of electrons permits the chemical composition of the sample to be determined.

An alternative approach to high resolution imaging appeared in 1955 when Müller reported on his structural studies using a field ion microscope (FIM). Whilst the quality of his early micrographs was poor, improvements in technique over the following years enabled the atomic structure of a number of materials to be resolved and matrix defect configurations to be studied (Müller 1958). The FIM employs a completely different approach from electron microscopy in that high resolution imaging is not related to the wavelength of illuminating radiation. The specimen is examined in the form of a fine wire polished to a sharp point of approximately 10 - 100 nm radius. It is introduced into a high-vacuum chamber, cooled, typically to 77°K or below, and held at a high positive potential relative to a viewing screen, which is earthed. A gas, such as helium, is admitted to the sample chamber at low pressure and becomes ionised in the vicinity of the tip. The gas ions are then

accelerated away from the tip in the direction of the viewing screen. Most ionisation events occur in regions of highest field which generally correspond to the protruding atoms on the surface of the tip. Thus bright spots are formed on the viewing screen which correspond to prominent atom sites on the specimen surface. To a first approximation the magnification in a FIM image is the ratio of the sample-screen distance to the tip radius which, in a typical FIM instrument, gives a magnification of $x10^7$. The FIM image can reveal microstructural features such as vacancies, dislocations and grain boundaries. Furthermore chemical analysis of fine details in the sample is possible by placing the entrance aperture of a mass spectrometer over a bright spot in the image and then increasing the voltage applied to the sample to bring about field evaporation of the surface atoms. These atoms follow the same path as the ionised gas atoms used for imaging and consequently, the atom corresponding to the bright spot selected in the image enters the mass spectrometer and can be identified.

Another technique which permits atomic resolution and is not based on the use of short wavelength radiation is the scanning tunnelling microscope (STM) invented by Binnig and Rohrer in 1982. In this method a fine-tipped stylus is brought sufficiently close to the surface of the sample and a bias voltage is applied so as to induce a tunnelling current between the surface and the tip. The magnitude of this current is sensitive to the separation of tip and sample surface and is used to map the surface by one of two approaches. The first scans the fine tip across the sample and monitors the variation in the tunnelling current, whilst the second monitors the vertical displacements required to maintain a constant tunnelling current as the tip is scanned. Both approaches produce a contour map of the sample surface which can be used to identify the atom positions, but there is no direct method of determining the chemical species of the atoms from the STM image.

1.4 Microscopy and Analysis of Microstructure

An overview is now given of the techniques which have been used to detect interfacial segregation. These include chemical sampling, radioactive tracer methods and microscopy techniques such as scanning electron microscopy (SEM), electron probe microanalysis (EPMA), secondary ion mass spectroscopy (SIMS), Auger electron spectroscopy (AES), x-ray photo-electron spectroscopy (XPS), ultra-violet photo-electron spectroscopy (UPS), atom probe/field ion microscopy with time of flight mass spectroscopy (APFIM TOFMS) and scanning transmission electron microscopy with energy dispersive x-ray analysis (STEM/EDX). A more detailed review is given of work carried out using AES and STEM/EDX as they are the principal techniques of interest in this research.

Chemical sampling of the grain boundary region is carried out by producing a polished sample, the surface of which is coated with an impervious mask. The mask is removed by scribing to expose areas of interest, such as the grain boundaries and the exposed area subjected to chemical etching. The composition of the material removed by the etch is then analysed. The etching procedure is repeated with the matrix exposed and the grain boundaries masked off and the results compared in order to detect any enrichment of the grain boundaries or other features investigated. The sensitivity of the chemical etching technique can be improved by increasing the exposed area of grain boundaries either by etching an intergranular fracture surface or grinding the sample into its constituent grains as achieved by Westbrook and Wood (1962) investigating embrittlement of an intermetallic by nitrogen. This approach is only feasible if the sample is very brittle. Additional improvements in sensitivity can be achieved by incorporating a radioactive isotope of the segregating species into the sample (Inman and Tipler 1958). All these variants of the chemical etching technique are, however, limited by the method of sampling. All will include any precipitates present on the grain boundary, possibly leading to an inaccurate value for segregant present at the grain

boundary. For example, thermally aged 9Cr 1Mo ferritic steel contains a molybdenum and phosphorus-rich Laves phase at the grain boundary in addition to any segregation and, consequently, any conclusions about the segregation of chromium, molybdenum or phosphorus must be confirmed by other techniques (Vatter and Titchmarsh 1989).

In the SEM and EPMA the method of interfacial analysis is to position the electron probe so that it is centred on a grain boundary. The composition determined from the x-ray spectrum collected from this volume of material is compared with the composition of the matrix, as determined from an x-ray spectrum collected with the electron probe placed within a grain, remote from grain boundaries and precipitates. Differences in detected composition can be attributed to changes which occur in the vicinity of the grain boundary. However the spatial resolution of the SEM is inadequate to detect low levels of grain boundary segregation. This is due to the large volume of material sampled by the electron beam (several μm^3) compared with the small volume comprising the grain boundary, typically less than 1% of the total, illustrated schematically in figure 1.1. This dilutes any changes in chemical composition to such an extent that they may cease to be detectable with statistical significance.

The FIM, as mentioned earlier, is capable of resolving individual atoms and, when combined with time of flight mass spectroscopy, it is capable of elemental identification and therefore of use in the study of interfacial segregation. Problems which can be encountered with this technique include the production of a specimen which contains an interface of interest within the region of the sharp tip. Also the intense electric fields required to produce field evaporation of atoms from the surface can induce stresses within the sample sufficiently large to cause fracture. This is a particular problem if the material under investigation is embrittled by the segregating species.

A further group of techniques used to study grain-boundary segregation are the surface specific techniques of SIMS, UPS, XPS and AES. Since it is the characteristic signals excited from the outermost layers of a sample surface which are analysed in these techniques, the interface of interest must be exposed by fracture, within the experimental system, before analysis can commence. This requirement is a general drawback when studying grain boundaries because it excludes materials which fracture by transgranular cleavage. Once the grain boundaries have been exposed the techniques vary in the manner in which the characteristic signals are excited and the specie which is detected.

The SIMS technique was developed in 1949 by Herzog and Viehböck and later appeared as a commercial machine built under a NASA contract to investigate samples brought back to earth during the space programme (Liebel and Herzog 1963, Herzog et al 1967). The technique is performed by focusing an energetic beam of ions onto the surface of the sample. Interaction between the beam and the sample causes the removal of atoms from the surface of the sample. Some of the material which is sputtered from the surface is in the form of ions. These secondary ions are deflected into a mass spectrometer which identifies the mass number of each specie removed from the sample. The SIMS technique gives chemical information about the outermost atom layers of the sample. The technique is essentially a destructive one, and if the strength of the primary beam is increased sufficiently, it is possible to conduct dynamic depth profiling experiments in which the chemical composition is monitored as a function of depth. A drawback of the SIMS technique is the different sputter rates of atomic species within a sample which can lead to difficulties with quantification unless well characterised standards are available for comparison. However, the sensitivity of the SIMS technique is good, all elements can be detected and the determination of isotopic ratio is also possible.

The AES, UPS and XPS techniques all detect low energy electrons emitted from the surface of a sample when it is bombarded by electrons, ultra-violet light and x-rays, respectively. The UPS technique, due to the low energy of the exciting source causes only the emission of electrons from the valence bands of the surface atoms. Consequently, the major use of the UPS technique is in the study of the electron band structure of metals, alloys and semi-conductors. It is not suited to the identification of segregating species.

Using x-rays as the exciting radiation (XPS) produces spectra from which element identification can be achieved. In addition, information about the chemical bonding of the atoms may be obtained from analysis of the spectrum. However, the problems associated with focusing of x-ray beams restricts the lateral resolution of this technique. This in turn reduces its usefulness for the study of segregation since it is necessary to relate the level of chemical enrichment to the different features present on a typical fracture surface.

A more detailed description of the techniques of Auger electron spectroscopy and scanning transmission electron microscopy now follows.

1.5 Development and Application of Auger Electron Spectroscopy

When an atom is excited by interaction with energetic electrons, ions, or x-rays and loses an inner shell electron, it can return to the ground state by various processes. Two of these processes are shown in figure 1.2a and 1.2b. In both cases the hole produced in the inner shell is filled by an electron from a higher shell. In figure 1.2a the energy produced by the reduction in energy level of the electron is emitted as an x-ray photon. Figure 1.2b shows a competing process in which the energy released by the relaxation of the atom is transferred to an electron in a higher shell which is itself ejected. The difference between the energy released by the initial relaxation and the energy required to eject the second electron appears as

kinetic energy of the second ejected electron. As both of these processes involve electron transitions between energy levels, the energy distributions of the emitted electrons/photons will be characteristic of the atoms from which they originated. Therefore if the energy distribution of the emitted electrons/photons is measured it can be used to identify the atoms present in the sample.

The ejection of electrons from excited atoms was discovered in 1925 by Pierre Auger (from whom the process took its name) (Auger 1925). The use of Auger electrons to characterise surface chemistry was outlined by Lander (Lander 1953), but it did not become a viable technique until 1968 when differentiation of the Auger signal was proposed (Harris 1968). This differentiation permitted the enhancement of the small characteristic peaks on the large background and set the technique of Auger Electron Spectroscopy (AES) on a firm experimental basis.

The primary beam used in Auger electron microprobes can be x-rays (referred to as XPS), ions or electrons. All of these energetic species penetrate a significant distance into the sample and excite Auger electrons from a large volume of material (several μm^3). The energy of the Auger electrons produced is in the range 0 keV to 2 keV and they undergo intense elastic scattering by the atomic lattice which limits the distance they can travel in the sample. The short path length of Auger electrons results in only those produced in the outermost atom layers being ejected from the sample and subsequently detected, this process is shown schematically in figure 1.3. Therefore the chemical information collected originates from the outermost layers of the sample and gives the AES technique its highly surface specific characteristics.

Most AES systems in use have a primary beam of electrons to excite the Auger signal because of the relative ease with which electron beams may be produced, focused and manipulated compared with the alternatives of x-ray or ion beams. A drawback inherent in the use of an electron beam is the large background

signal generated by reflected secondary electrons, though much of this can be removed by the differentiation of the spectra. In early Auger electron microprobes the differential signal was collected by applying potential modulation to the analyser. On modern systems it is increasingly common for the Auger electron spectrum to be collected in the direct mode, as Auger current versus energy and subsequently to differentiate the spectrum using a microcomputer. The collection of the direct spectrum in conjunction with increased detector efficiency has enabled the use of lower primary beam currents (< 10nA). These lower currents permit the use of smaller electron probes, which gives better spatial resolution. The risk of electron beam induced sample damage is proportional to the current density of the probe rather than the absolute current. The reduction in beam current has also resulted in lower current density probes and a consequent reduction in risk of sample damage. The methods used to produce a fine electron probe and the scanning of the electron beam in the Auger electron microprobe are analogous to those used in the scanning electron microscope. The addition of a secondary electron detector and a CRT to the AES equipment allows an image of the specimen to be acquired and analysis positions to be selected.

AES was initially used to study the phenomenon of surface segregation. In these experiments the surface of a sample was first cleaned under vacuum by ion bombardment or abrasion. The level of segregation present on the surface was then monitored as the sample was heated. The measurement of segregation as a function of time and temperature allowed the thermodynamics and kinetics of segregation to free surfaces to be determined. Surface segregation has been studied in many systems, including phosphorus and sulphur in type 304 stainless steel (Youngbin 1987), and sulphur in an alloy of Cu-5.8%Al (Berning 1986). Surface segregation data can be used to predict qualitatively which elements are likely to segregate to the grain boundaries in these materials.

The advent of ultra-high vacuum AES systems with in-situ fracture facilities allowed the direct measurement of segregation to internal surfaces such as grain boundaries. The method of fracture of the sample to expose grain boundaries facets has to be varied, depending upon the fracture properties of the material. The commonly used methods to induce intergranular fracture are impact, often of cooled or hydrogen-charged samples, and the use of small-scale tensile specimens.

By means of the AES technique many elements have been shown to segregate to grain boundaries. For example, bismuth segregation in copper-bismuth alloys (Powell 1973, Molinari 1984), is reported whereby up to 2 monolayers of bismuth was located at the grain boundary. In embrittled 2¼%chromium-1%molybdenum steel weld metal (Okumura 1985), and aged 2¼%chromium steels containing a range of molybdenum and carbon levels (Nakamura 1979), phosphorus was consistently found by AES at the grain boundaries and was identified as the major embrittling species. Other studies have investigated the segregation of sulphur to the grain boundaries in iron (Briant 1985), and the competition between phosphorus, sulphur and nitrogen to segregate to grain boundaries in steel (Briant and Andresen 1988).

Breummer et al (1985) evaluated several methods available for detecting the presence of grain boundary phosphorus segregation, including secondary ion mass spectroscopy (SIMS), analytical electron microscopy, chemical/electrochemical etching, and AES. The study was conducted on a range of steels, including an iron-phosphorus alloy, chrome-molybdenum-vanadium and nickel-chrome-molybdenum-vanadium rotor type steels. Only the AES and chemical etching tests were able to detect consistently the presence of phosphorus segregation at the level of interest, approximately 30% of a monolayer. The SIMS data was obtained by scanning the ion beam perpendicular to grain boundaries which intercepted the surface of a polished sample rather than examination of a fracture surface. Using this experimental method no evidence was detected for the segregation of phosphorus or

other impurities to the grain boundaries examined. A problem encountered when analysing the rotor steels using the SIMS technique was the amount of peak overlap present, for example the mass to charge ratios of P^+ and $^{62}Ni^{++}$ are 30.974 and 30.964 respectively. The electron microscopy was conducted using both a conventional TEM/STEM system and a dedicated STEM but neither was able to detect more than a very slight enrichment at some of the grain boundaries. The rotor steels were particularly difficult to examine in the STEM due to the almost complete coverage of the grain boundaries with precipitation leaving very little available for analysis, which may in part explain the failure of the STEM technique to detect segregation in these materials. In light of these results Breummer concluded that of the techniques available only AES and chemical etching were capable of consistently detecting the segregation of phosphorus in these alloys. The chemical etching technique has an added advantage as it has the potential for use in the field to indicate phosphorus segregation and, thereby, the materials susceptibility to embrittlement. The techniques of AES and STEM for measuring grain boundary segregation have also been compared by Partridge and Tatlock (1992). The system investigated was the nimonic alloy PE16. Segregation of molybdenum, chromium and phosphorus was detected at the boundaries and analysis of the level of each segregant showed good agreement between the two analytical techniques

1.6 Development and Application of Scanning Transmission Electron Microscopy

A more recent technique in the field of segregation studies is scanning transmission electron microscopy (STEM). The equipment used may be either a combined TEM/STEM system or a dedicated STEM. The former equipment consists of a modified transmission electron microscope which permits a fine electron probe, approximately 10nm in diameter, to be scanned across a conventional TEM specimen. The dedicated STEM is a purpose-built instrument in which operation is only possible in the STEM mode; these instruments are fitted

with field emission sources. The fine probe in both instruments can be stopped at selected positions, and the x-ray signal generated by the interaction of the electron beam and the specimen is collected and analysed. The STEM technique can be used to determine the chemical composition of grain boundaries using the following procedure. The grain boundary is oriented so as to be parallel to the electron beam and x-ray spectra are collected with the electron probe positioned on the boundary and in the matrix away from the boundary. The resultant x-ray emission spectra are analysed and the chemical composition of the two areas compared. This procedure will detect any change in the chemical composition measured at the grain boundary relative to the matrix.

A problem encountered when using a TEM/STEM system with a conventional, heated tungsten hairpin electron source is the low current which can be produced in the fine probes. The low current density in the probe necessitates long counting times in order to obtain reasonable statistics in the collected x-ray spectra. The use of long analysis times is not only time consuming but also increases the problems of specimen contamination (the build up of carbon products under the beam), and specimen drift (which increases the volume of the sample from which x-rays are produced). The problem of specimen contamination can be reduced by storing the sample under alcohol prior to examination, cooling the specimen in a liquid nitrogen stage during analysis and flooding the sample prior to analysis with a high-intensity beam of electrons to fix the contaminants in position. The use of a cooling stage reduces the rate of contamination build up considerably, but has also been found to induce specimen drift as the temperature of the sample varies (Kenik 1986).

Despite the problems encountered using conventional TEM/STEM systems, several workers have detected interfacial segregation using this type of equipment. Examples include a study of gold segregation in iron (Sickafus and Sass 1985), in which an alloy of iron - 1.8%gold, containing a 1.5° twist boundary was examined

with the boundary oriented perpendicular to the electron beam. Using an electron probe with a beam diameter of 20nm an enhanced gold signal was detected from certain areas of the twist boundary. Subsequent Rutherford backscattering experiments confirmed that the enhanced signal in these areas came from gold which was concentrated in the vicinity of the interface. The gold signal was calculated to have come from a segregation level of two monolayers.

The more favourable geometry of sample in which the grain boundary, or other interface of interest, is oriented parallel to the electron beam has been utilised for the majority of segregation studies. This geometry allows more of the segregant to be intercepted by the electron beam and improves the resolution of chemical analysis in a direction perpendicular to the grain boundary, thus allowing a grain boundary chemical composition profile to be obtained. Studies of grain boundary segregation using this specimen configuration have included the detection of bismuth in copper (Baumann and Williams 1981, Michael and Williams 1984). Comparison of the data collected in their study with previously obtained Auger data on copper-bismuth alloys (Joshi and Stein 1971, Powell and Woodruff 1976) indicated that the levels calculated from the STEM data were a factor of 2-3 lower than the coverage determined from the Auger investigation. This discrepancy may be accounted for by the relatively large errors encountered in the quantification of this data due to the low x-ray count rate and carbon contamination problems. The data collected in the TEM/STEM study of copper-bismuth illustrates the difficulties inherent with the low beam current produced by a heated tungsten electron source. The electron probe diameter was 20-30nm and the x-ray spectrum was collected for approximately 60 to 100 seconds. The x-ray spectrum contained characteristic peaks from the copper and bismuth, but the bismuth (L_α) peak contained only 20 to 90 counts compared with the copper K_α peak of between 15,000 and 35,000 counts. Doig and Flewitt (1983) have concluded that to improve the detectability of interfacial segregation it is necessary to increase the x-ray production rate. To

achieve this increase in x-ray count rate with a conventional TEM/STEM system the beam current can be increased by using a larger diameter probe or a thicker foil can be examined. Using this approach the following systems have been investigated; phosphorus segregation in steel (Doig and Flewitt 1978), silicon and manganese segregated to the prior austenite grain boundaries in 2¼%Cr 1%Mo ferritic steel (Doig, Lonsdale and Flewitt 1982a), and tin at the grain boundaries in ½%Cr ¼%Mo ¼%V steel doped with 800 parts per million tin (Doig, Lonsdale and Flewitt 1982b). Other systems investigated by TEM/STEM have included the segregation of calcium in alumina (Kouh et al 1986), phosphorus in electron-irradiated type 304 stainless steel (Fukuya et al 1985), enhanced chromium and depleted nickel at grain boundaries in electron-irradiated steel (Muroga et al 1987) and grain boundary enrichment of magnesium and depletion of aluminium in a magnesium sialon (Clarke 1978).

The required increase in electron probe current can also be achieved by using a higher brightness source, either lanthanum hexaboride or, brighter still, a field emission gun (FEG). The FEG gives an increase in brightness of approximately three orders of magnitude over a tungsten hairpin electron source. This substantial increase in brightness allows smaller electron probes to be utilised whilst maintaining sufficient current to conduct x-ray analysis. A FEG can be fitted to either a conventional TEM or a dedicated STEM. A conventional TEM equipped with a FEG has been used to detect antimony and nickel segregation, and chromium depletion in a 16%Cr 14%Ni stainless steel (Kenik 1986). The FEG allowed a probe size of 1-2nm to be used to produce a compositional profile with a full width at half maximum of approximately 4nm. The dedicated STEM has the advantage over the TEM/STEM system in that it has electron optics optimised for fine probe formation allowing smaller diameter probes to be produced and an ultra high vacuum (UHV) environment which reduces the problem of sample contamination,

which is increased relative to lower brightness systems due to the higher current density of the electron beam.

Examples of the use of dedicated STEM's for segregation studies include the detection of iron at grain boundaries in magnesia (VanderSande et al 1984), and chromium enrichment at the cementite ferrite interface in pearlitic steel (Garrett-Reed et al 1983). The width of the chromium enhancement in this latter example was approximately 2nm. The FEG-STEM has also been used to study the effects of irradiation on stainless steel (Norris et al 1986) in which the width of the chromium depleted region was found to be influenced by the irradiation temperature. At low temperatures ($<350°C$) the depletion profile is only measurable using a FEG-STEM as the averaging effect of the larger diameter beams used in TEMs with conventional electron sources obscures the narrow depletion region. Another advantage of using the STEM technique compared with most other analytical techniques is the spatial resolution at which the structure of the sample can be observed and a detailed relationship between microstructure and chemical composition can be ascertained. The boundaries which are analysed using the STEM technique are not preselected by the process of fracture, as in Auger electron spectroscopy. This permits all types of interfaces to be analysed, including low angle boundaries and particle-matrix interfaces. As well as boundary analysis, STEMs have been used to investigate other microstructural features such as dislocations and second phase particles. In addition to energy dispersive x-ray analysis other analytical facilities are available on the STEM, namely microdiffraction and electron energy loss spectroscopy (EELS).

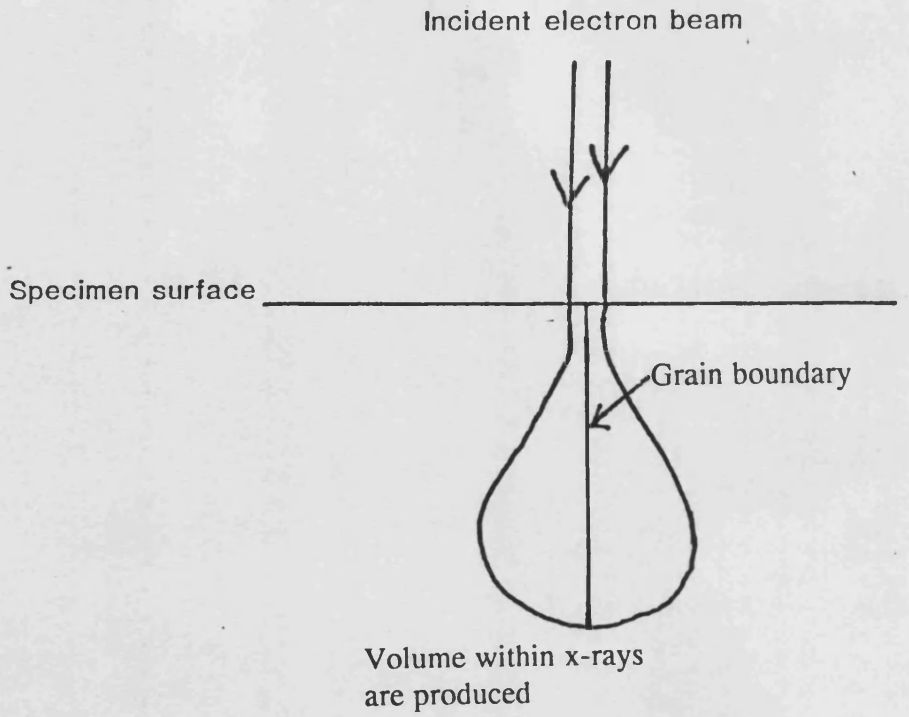

Figure 1.1 Schematic representation of SEM analysis of a grain boundary

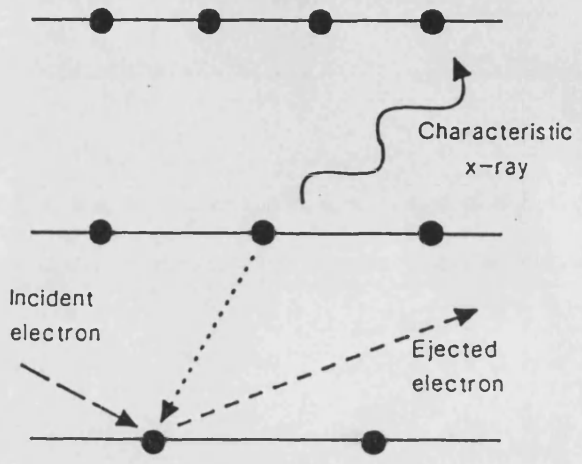

Figure 1.2a Emission of an x-ray from an ionised atom

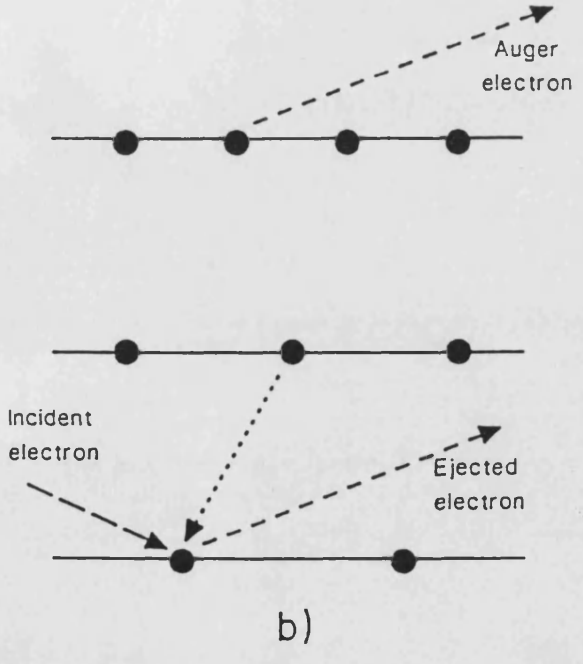

Figure 1.2b Emission of an Auger electron from an ionised atom

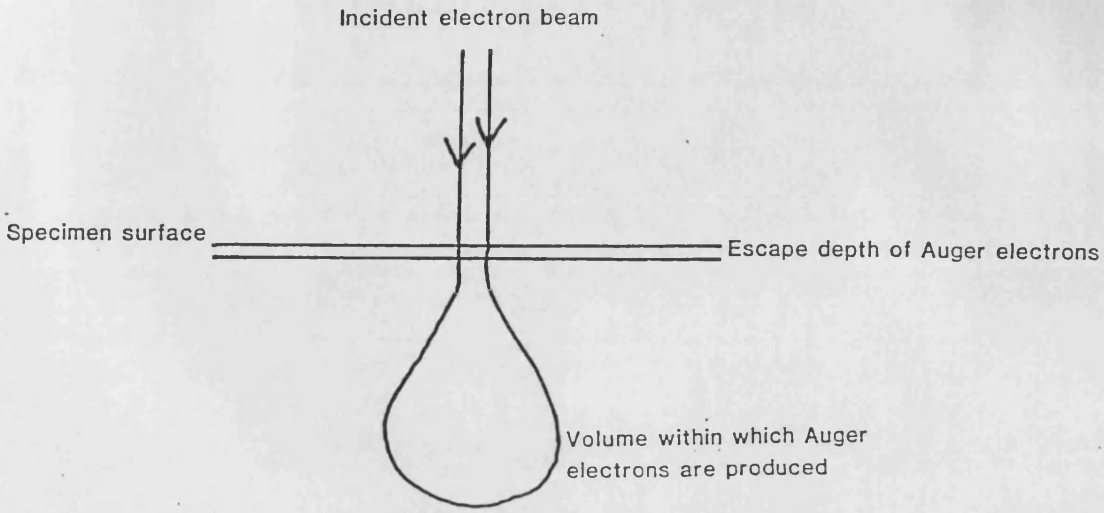

Figure 1.3 Surface sensitivity of the Auger technique

Chapter 2 Scope of the Present Investigation

The thesis describes and compares the application of Auger electron spectroscopy (AES) and analytical electron microscopy (AEM) to the study of fine-scale (sub 10nm) microstructural features, with particular reference to the detection and quantification of elements segregated at grain boundaries in steel.

A description of the physical principles involved in the technique is first given, including the production of the respective characteristic signals and the treatment of the signal generated in the specimen prior to its output by the analysis equipment. Methods for quantifying the experimental data obtained from each technique are developed and applied to determining the extent of grain boundary coverage by elemental species. The uncertainties in quantification procedures are discussed as well as the statistics of detection used to determine the minimum detectable coverage of the grain boundary and the minimum detectable mass of segregant. The effect of varying the conditions of data collection are investigated in order to establish optimum conditions for analysis.

The particular system studied concerns the segregation of phosphorus and chromium to the prior austenite grain boundaries in 9%chromium steels doped with phosphorus in the range 25 to 560 weight parts per million. Experimental AES and AEM data have been collected for phosphorus and chromium segregation on steel samples cut from the same blanks to allow direct comparison of the results determined by each technique. The range of phosphorus segregation, at the grain boundary, investigated is 6% to 100% of a monolayer.

The relative merits and limitations of each technique are discussed and the circumstances identified under which each technique offers distinct advantages.

Chapter 3 Experimental Details

3.1 Materials

The alloy examined in this study was a ferritic steel containing 9% chromium, to which a range of phosphorus additions had been made. The range of phosphorus content was between 25 and 560 parts per million by weight. The chemical composition of the four materials studied are given in table 3.1. They are subsequently referred to as; alloys S560, S300, S120 and S25 containing 560ppm, 300ppm, 120ppm and 25ppm phosphorus respectively.

After casting as bars with dimensions 125mm x 125mm x 900mm the alloys were forged at 1150°C into bars 62mm thick, homogenised at a temperature of 1100°C for 40 hours under vacuum, then reforged to 37mm-thick plate at a temperature of 1150°C. This homogenisation treatment is designed to eliminate any microsegregation that may have occurred during the casting process. The ingots were austenitised at 1100°C and water quenched, finally the samples were tempered at 750°C for 1 hour. The fracture mode of this ferritic steel changes from ductile to brittle as temperature decreases. Interfacial segregation of an impurity such as phosphorus is known to both raise the temperature at which this ductile to brittle transition occurs and induce a change in the brittle fracture mode from transgranular cleavage to intergranular fracture. The specimens for examination in this study were thermally aged at 500°C for 100 hours. A previous study (Wall 1987) had shown that this thermal ageing treatment was sufficient to cause embrittlement of these materials and give intergranular fracture at low temperature.

3.2 Microstructural Analysis

3.2.1 Optical Examination

After ageing, samples of alloys S560 and S300 were mounted in thermosetting resin to allow metallographic preparation. The specimens were ground on successively finer silicon carbide papers and finally polished to a 1μm finish using diamond paste. The polished sample was etched to reveal the microstructure by immersing in a saturated solution of picric acid in ethanol. Photomicrographs were taken of the samples at magnifications of x100 and x500. Five lines 50mm in length were drawn at random on each of the micrographs and the grain size was calculated using the mean linear intercept method.

3.2.2 Scanning Electron Microscopy

The fracture surface of Charpy samples aged for 100 hours at 500°C, which had been tested during a previous study of this material, were examined in an Hitachi S570 SEM. This machine is equipped with a lanthanum hexaboride electron source, and was operated at an accelerating voltage of 25keV.

The samples of particular interest were those which had been fractured at low temperature when the material is brittle. Two modes of brittle fracture exist in this material, namely transgranular cleavage and intergranular fracture. The proportion of intergranular fracture increases in 9%chromium steel as embrittlement progresses. The presence of intergranular fracture is a necessary requirement to allow the AES technique to be used to determine the grain boundary chemistry. An objective assessment was made of the percentage of intergranular fracture present in a each sample after thermal ageing. This was achieved by placing a grid of 100 points over an SEM image of the fracture surface, at a magnification of x200, and recording the number of points which were on intergranular facets. This was

repeated on five fields of view to obtain a representative value for each of the four alloys.

3.3 Principles and Operation of the Analytical Electron Microscope

The analytical electron microscopes utilised for this work were a Philips EM430 transmission electron microscope and a Vacuum Generators HB501 dedicated scanning transmission electron microscope. The basic components of an AEM consist of, an evacuated chamber, a source of electrons, facilities to accelerate and focus the electrons, the sample, imaging and analytical facilities.

The AEM chamber is maintained at reduced pressure for several reasons. First, the production of electrons requires a vacuum in the vicinity of the source, this prevents oxidation of thermionic emitters and helps maintain the clean surface required by field emission systems. Second, the electrons, which are subsequently accelerated, require a flight tube which has been evacuated to a good vacuum in order to reduce scattering by residual gas atoms and the subsequent loss of electrons from the primary beam and, third, the vacuum helps to preserve the sample in a clean state during examination. This requirement to maintain a good vacuum in the AEM places restrictions on the materials which may be used in construction. All of the materials used must have a low vapour pressure and be stable under vacuum. In addition all of the joints between components require vacuum tight seals. This causes particular problems where movement or electrical feed-throughs are required.

The vacuum in the AEMs mentioned above is achieved using a variety of pumping procedures. The initial vacuum is produced using rotary pumps which reduce the pressure in the microscope chamber from atmospheric to approximately 10^{-2} torr. From this point an oil diffusion pump (ODP) is used to reduce the

pressure into the high vacuum regime. An ODP can achieve pressures in the range 10^{-8} to 10^{-10} torr. Additional pumping of the specimen chamber of the EM430 and the gun chamber of the HB501 is provided by ion getter pumps (IGP). The ultimate vacuum achieved in an AEM system depends upon the pumping efficiency of the pumps utilised and the quality of the seals employed on the column. The EM430 operates at a vacuum of 10^{-7}- 10^{-8} torr and the VG HB501 operates in the ultra high vacuum (UHV) regime of 10^{-9}- 10^{-11} torr. The attainment and maintenance of UHV conditions in the STEM is similar to the methods used in AES systems and is described later.

The electron sources used in the AEM fall into two categories, thermionic emitters and field emitters. In each case the objective is to produce conditions under which electrons present in the source are able to overcome the work function of the material, defined as the energy required to remove an electron from the sample to infinity. The work function of most materials is in the region of several electron-volts (Riviere 1969). The two classes of emitters employ different methods to overcome this potential barrier. Thermionic sources are raised to a high temperature, 2600 - 3000°K, at which a proportion of the conduction electrons in the material possess sufficient energy to escape into the surrounding vacuum. Common thermionic emitters are tungsten and lanthanum hexaboride. The latter has a higher brightness and produces a smaller virtual source size, but requires a better operating vacuum due to its high reactivity at elevated temperatures. The EM430 is equipped with a lanthanum hexaboride thermionic emitter.

In the case of field emission the aim is to reduce the magnitude of the energy barrier at the surface of the source. This is achieved by applying an electric field in opposition to the barrier; the intention is not to completely counteract the work function but just to reduce it. The work function barrier extends over a distance of only a few nanometres at the surface of the source and with its reduction in magnitude due to the application of an external field there is a finite probability that

a proportion of the electrons will be able to 'tunnel' through the barrier and escape from the source. Because the work function of a material is increased by the adsorption, onto the surface, of residual gases it is necessary to maintain an ultra-high vacuum (UHV) around the field emission source. The UHV also reduces the risk of flashover between the field emission tip and the electrodes supplying the external field. Such an occurrence could cause overheating and even melting of the source. Even under UHV conditions it is necessary periodically to heat the field emission source to drive off any adsorbed atoms. A field emission source (or gun) may be operated either at room temperature (cold FEG) or at an elevated temperature of approximately 2000K to give thermally assisted field emission. The thermally assisted mode can be more stable than the cold FEG due to the continual removal of any adsorbed gases from the tip. However the energy spread of electrons emitted from the thermally assisted FEG is greater than that from a cold FEG. The VG HB501 dedicated STEM was fitted with a cold field emission gun. It consists of an single crystal of tungsten with a <310> zone axis oriented parallel to the optic axis. The tip of the crystal is etched to a fine point to increase the local field and positioned close to the first anode assembly of the gun. The first anode is maintained at a positive potential of approximately 3.5keV to 4.5keV to provide the high electric field necessary to induce a tunnelling current from the tip. The emitted electron beam is further accelerated to a potential of 100keV. The gun assembly is held at room temperature and under ultra-high vacuum (10^{-11} torr). The field emission process produces a very bright electron beam of low energy spread, typically 0.3eV full width at half maximum.

The brightness of a FEG is approximately 1,000 times greater than that of the thermionic, heated tungsten hairpin electron source; the FEG also produces a much smaller virtual source size. These factors allow considerably smaller electron probes to be formed in a system employing a FEG, in preference to a thermionic source, whilst retaining sufficient current in the probe to conduct chemical analysis.

These advantages are sufficient to warrant the extra cost incurred by having to incorporate UHV technology on an AEM capable of chemical analysis with the highest spatial resolution.

The electron source is held at a high negative potential and the free electrons produced by thermal or field emission are accelerated towards an earthed anode. The EM430 had a maximum operating voltage of 300keV compared to 100keV of the HB501.

The properties of an electron may be described in terms of waves or particles. It is therefore possible to ascribe to an electron a wavelength and a frequency which are dependant upon the energy of the electron. The formula for calculating the frequency of an electron was proposed by De Broglie. As electrons have wavelike properties they can be refracted and diffracted in a manner analogous to light.

When an electron enters a magnetic or electric field it experiences a force acting upon it which causes a deviation from its original trajectory. This characteristic is made use of in electromagnetic and electrostatic lenses respectively.

The electron-optical configuration of the EM430 consists of an electron probe forming system (condenser lenses), which focuses the electron beam onto the specimen, an electron image forming system (objective lens), which focuses the transmitted and diffracted electrons to form an image. This image is magnified and projected onto the viewing screen or recording medium by the electron image projection system (projector lenses). The image and diffraction pattern in an AEM can be viewed on either a fluorescent screen or a TV screen linked to a charge coupled device (CCD) camera system, both of which are placed below the projector lenses. To produce photographic images the fluorescent screen is removed from the electron path and a photographic plate is exposed to the electron beam. Because of

the large depth of focus in an AEM an image which is in focus on the viewing screen will also be in focus on the photographic plate.

Ray diagrams of the two main operational modes of an AEM are shown in figures 3.1 and 3.2. The former shows the imaging mode which produces a magnified image of the specimen on the viewing screen. The latter illustrates the effect of weakening the diffraction lens. This places the diffraction pattern, which is formed at the back focal plane of the objective lens, at the focal point of the projector lenses which then magnify and project an image of the diffraction pattern on to the viewing screen.

The microscope used to collect chemical information with high spatial resolution was the VG HB501, which is a dedicated scanning transmission microscope (STEM) with an ultra high vacuum chamber. The main components of the instrument and ray diagram are shown schematically in figure 3.3. The electron source is a field emission gun as described above. Initial focusing of the electrons is achieved with the 'gun lens', the strength of which is adjusted to produce an image, S1, close to the differential pumping apertures (DPA). The DPA permit the maintenance of the high vacuum in the gun chamber (10^{-11} torr) when it is opened to the lower vacuum in the specimen chamber (10^{-9} torr). A pair of condenser lenses, C1 and C2, are used to transfer images of the source to the plane of the selected area diffraction aperture (SADA) S3. As the excitation of C1 is varied, the position of the intermediate crossover at S2 changes so that the strength of C2 has to be varied to maintain a fixed position for S3. However, such changes in the excitation of C1 and C2 affect the demagnification of the source and the convergence angle, α', at S3. Therefore the size of the probe, S4, at the specimen, together with the convergence angle, α, can be adjusted using a combination of the two condenser lenses. The value of α is determined by the 'field-limiting' aperture, either the objective or the virtual objective aperture (OA and VOA, respectively), which are approximately optically conjugate. It should be noted that the electron optical

configuration using the VOA is essentially different from that using the OA. Using the VOA as the 'field-limiting' aperture, the probe current in S4 is independent of the strengths of the condenser lenses, C1 and C2, so that a reduction in probe size can only be achieved at the expense of increasing the convergence angle up to the limit when spherical aberration dominates. When the OA is used the convergence angle is independent of the excitation of C1 and C2, and the probe size and probe current are reduced by selecting smaller objective apertures. This reduction in probe size can continue until the current becomes too small to produce a useful signal, or until the probe diameter becomes limited by diffraction effects. The fine electron probe produced by the selected combination of lenses is scanned across the sample in a manner similar to that in an SEM. The transmitted electron signal is collected and its intensity used to modulate the brightness of a cathode ray tube (CRT) scanning in synchronisation with the electron beam. The magnification of the image in the STEM is the ratio between the scanned length of the line on the CRT to the length of the line scanned on the sample. As the line length on the CRT is invariant the magnification of the image is increased by reducing the scanned line length on the sample. A recording of a STEM image is made by exposing a photographic plate to the CRT while a single raster is scanned on the sample. For x-ray analysis, the VOA must be used as the beam defining aperture, otherwise electron scattering from the OA would produce an unacceptably high background count of x-rays. During examination ferritic samples are mounted in a holder with a single axis of tilt; the available range of tilt is horizontal to $+60°$. The holder is especially robust in order to withstand the magnetic force acting on the ferritic sample when it is immersed within the field of the objective lens.

3.3.1 Electron-sample interaction in the Analytical Electron Microscope

An energetic electron can interact with the sample in a number of ways. The electron may pass through the sample without interacting with any of the atoms in the sample. It may be elastically scattered by the nucleus of an atom in the sample or inelastically scattered by the electrons present in the sample.

If an electron from the primary beam ionises an atom in the sample by displacing an inner shell electron, the subsequent relaxation of the atom can result in the emission of an x-ray photon or the emission of an Auger electron. The processes of x-ray and Auger electron emission were shown in figures 1.2a and 1.2b. The energy of the emitted specie in each of these processes is a function of the separation of the energy levels in the ionised atom. Consequently measurement of the energy of either of the emitted species will allow identification of the type of atom from which it originated. The number of ionisation events which occur for each element depends upon the ionisation cross-section of the atom. The magnitude of this cross-section has been expressed by Powell (1976):

$$Q = (2\pi b e^4) / (E E_c) \log (4E / B) \qquad 3.5$$

E = incident energy (accelerating voltage)

E_c = critical ionisation energy

B = Constant, best fit value for k-shell ionisation $4xE_c$

b = Constant, best fit value for k-shell ionisation 0.606

The value of the constants, B and b, vary with atomic shell. The values of the constants are also varied by other workers to obtain a good correlation with their data.

equation 3.5 can be rewritten:

$$QE_c^2 = 7.92 \times 10^{-20} \log (U) / U \qquad 3.6$$

U = Overvoltage ratio = E / E_c

The variation of Q with overvoltage ratio, U, is plotted in figure 3.4, for U values from 0 to 14. The overvoltages encountered in the transmission electron microscope are typically ~50 for phosphorus and ~16 for iron for an accelerating voltage of 100KeV. It is therefore necessary to extrapolate from the data shown in figure 3.4. The graph shows that the value of ionisation cross section of phosphorus will be lower than that of iron. The production of x-rays varies as a function of the energy of the ionising radiation, as shown by the presence of the overvoltage term in the equation for ionisation cross section. The energy of an electron beam decreases with its penetration into a sample as the electrons interact with the constituent atoms. This variation in beam energy leads to a variation in the x-ray production rate. In an SEM this variation in x-ray production rate has to be taken into consideration during quantitative analysis of the x-ray spectra. However in AEM samples the primary beam has a higher energy and the samples are much thinner. Consequently the amount of energy lost by the electron beam during its passage through the foil is minimal and the x-ray production rate can be considered to be constant through the thickness of the foil. Examination of an EELS spectrum, where the area under the characteristic edges due to inner-shell ionisations is very small when compared to the number of counts in the zero loss and plasmon peaks, confirms that the majority of electrons pass through the foil with minimal loss of energy (Egerton 1986).

The proportion of ionised atoms which relax with the emission of an x-ray is defined by the fluorescence yield.

For the K shell of an atom the fluorescent yield, ω_K , can be expressed as:

$$\omega_K = X_K / (X_K + A_K) \qquad 3.7$$

X_K = number of x-ray photons emitted.

A_K = Number of Auger electrons emitted

The variation of ω with atomic number (Z) is shown in figure 3.5.

3.3.2 Electron Diffraction Patterns

Because electrons have an associated wavelength they will be diffracted by the regularly spaced atom planes found in crystalline specimens. The principle of electron diffraction is shown in figure 3.6. Constructive interference occurs when the following condition is met:

$$n\lambda = 2d\sin\theta \qquad 3.1$$

where λ is the electron wavelength, d the interplanar spacing and θ the diffraction or Bragg angle. The diffracted beams from all of the atomic planes which satisfy the above condition are brought to a focus at the back focal plane of the objective lens, as shown in figure 3.2. The diffraction pattern consists of regularly spaced spots, the arrangement of which can be used to determine the spacing and angles of the atomic planes in the specimen. In the case of an electron diffraction pattern obtained in the AEM, operating at a known accelerating voltage, the wavelength of the electron can be calculated and the value of interplanar spacing can be obtained. The diffraction angle, θ, is determined by measurement of the separation, R, of the diffraction maxima in the diffraction pattern. The value of θ is determined from the equation

$$\tan 2\theta = R / L \qquad 3.2$$

Where L is the effective distance between the specimen and the recording medium in the AEM. As the angle 2θ is small, in the electron microscope, tan 2θ approximates to 2θ. Substituting in the Bragg equation (eqn 3.1) and rearranging gives

$$d = n\lambda L / R \qquad 3.3$$

λL = Camera constant

The camera constant is obtained by analysing diffraction patterns from a specimen of known interplanar spacing.

In a cubic crystal the interplanar spacing, as determined by eqn 3.3, can be used in conjunction with eqn 3.1 to determine the index of the atomic planes causing diffraction.

$$d = \frac{a}{\sqrt{(h^2 + k^2 + l^2)}} \qquad 3.4$$

a = lattice parameter

h,k,l = Miller indices of diffracting plane

The angles between atomic planes in the sample can similarly be determined by measuring the angle between the relevant maxima in the diffraction pattern.

3.3.3 X-ray Detection

As has been explained in section 3.3.1, the energy of x-rays produced by the interaction of the electron beam and the sample are characteristic of the elements present in the sample. The composition of the sample can therefore be determined by measuring either the energy or the wavelength of the emitted x-rays.

Both the EM430 and the HB501 were fitted with energy-dispersive x-ray spectrometers. In this system the detector is a cooled, lithium drifted, single crystal of silicon to which a bias voltage is applied. When an x-ray photon enters the silicon crystal its energy is dissipated by creating electron-hole pairs, each pair requiring an average of 3.81eV, at a temperature of 80-90 K. Thus the number of electron hole pairs produced by an incoming x-ray is proportional to the energy of the incident x-ray and, consequently, a current is produced in the crystal which is

also proportional to the energy of the incoming x-ray photon. The free electrons and holes drift under the influence of an applied electric field such that they move out of the crystal in a time which is shorter than their recombination time. Provided all of the generated electrons and holes arrive at the electrodes and are not trapped by impurities (the presence of lithium compensates for impurities left after the zone refining of the silicon) or recombine, the charge measured is proportional to the energy of the incident x-ray photon. The charge produced is very small and, therefore, must be amplified by a field effect transistor (FET) which integrates the charge and outputs a proportional voltage. Both the detector crystal and the pre-amplifier FET are cooled to a low temperature using liquid nitrogen in order to reduce the dark current present (i.e. free electrons produced by thermal effects in the absence of x-ray photons). Each voltage pulse is measured and allocated to a position in a multi-channel analyser (MCA) in order to build up the energy-dispersed x-ray spectrum. The amplitude-sorting of the pulses is achieved by the use of an analog-to-digital converter (ADC).

The environment around the cooled silicon crystal must be maintained at a low pressure in order to prevent the deposition of ice and other contaminants which otherwise affect the performance of the detector. Usually, because the vacuum in many AEM instruments is of medium quality, the detector is isolated by a thin, vacuum tight 'window' placed between the microscope chamber and the detector. The material used for this 'window' needs to be of low atomic number so as to minimise attenuation of the x-rays before they reach the detector, and common materials include beryllium and mylar. If the vacuum within the microscope is good enough it is possible to operate in a 'windowless' configuration and allow the unrestricted passage of x-rays between the sample and the detector.

X-ray analysis capability on the Vacuum Generators HB501 STEM is provided by a Link Systems LZ5, windowless energy-dispersive x-ray (EDX) detector. The silicon crystal in this detector has an active area of 30mm^2, set at an

angle of 13.5° to the vertical, the detector subtending a solid angle of 0.07 steradians at the sample. In the windowless configuration, the detection of characteristic x-rays of all elements above and including carbon may be achieved. The resolution of the detector, as defined by the full width at half maximum (FWHM) of the manganese peak (5.9keV), is approximately 150 eV. This system has the facility to warm-up the crystal under vacuum to sublime any deposited ice. The x-ray detector is interfaced to a Link Systems AN10000 microcomputer which controls x-ray acquisition.

3.3.4 Electron energy loss spectroscopy

As electrons pass through a specimen in the AEM some of them lose energy by interactions with valence and core electrons of the sample atoms, the latter process resulting in the ionisation of the atom. The energy losses suffered by the electrons of the primary beam can be measured using a suitable spectrometer. The spectrometer acts in a similar manner to a glass prism dispersing a beam of visible light. Once the electron beam has been dispersed, the electron energy loss spectrum can be collected using the techniques of either serial or parallel acquisition. The EM430 and the HB501 were both equipped with serial acquisition spectrometers in which the dispersed spectrum is projected onto a narrow slit, which defines an energy window, and the number of electrons falling onto a detector placed behind the slit is measured. After each measurement, the dispersed beam is displaced by small increments of energy and the number of electrons passing through the slit remeasured; the spectrum is thus built up by sequential measurements. The spectrum in such a system is commonly divided into 1024 channels, and with collection times in the region of 100ms per channel the overall spectrum acquisition takes approximately 100 seconds. This is comparable to the collection time of typical x-ray emission spectra in the AEM. The second variant of EELS

spectrometer allows parallel detection of the energy spectrum. In this type of spectrometer the electron beam is dispersed in a manner similar to the serial spectrometer. The dispersed beam is incident on a photodiode array consisting, typically, of 1024 channels. The current falling on each of these channels is read simultaneously.

The HB501 was equipped with a VG ELS 501, serial acquisition, electron energy loss spectrometer which was used predominantly to measure sample thickness. The spectrometer has a maximum entrance aperture of 10mrad and an energy resolution of better than 0.75eV FWHM on the zero loss peak. The spectrometer has two counting modes; at low input rates it counts the individual electrons incident on the scintillator which is placed beyond the energy defining slit. When the number of electrons reaching the scintillator increases, the spectrometer switches to an analogue mode. The incident current is detected by generating a voltage across a resistance. A voltage-to-frequency converter then produces pulses at a rate proportional to the current, and the pulses counted and stored in the appropriate channel of the MCA. This latter mode is used to measure the electron distribution in the low loss region of the spectrum (approximately 0 - 300eV). For energy losses greater than this the low count rate mode, pulse counting, is used because the number of electrons experiencing large energy losses is small. The switch-over between the two counting modes is software controlled. The EELS spectrometer was controlled by the Link Analytical AN10000 microcomputer also used to collect x-ray emission spectra.

An advantage of the EELS technique, over EDX, is that the angular spread of the electrons contributing to the spectrum is defined by the entrance aperture of the spectrometer and is of the order of a few milliradians. Electrons which undergo large angle scattering in the sample are excluded from the EELS spectrum. However, x-rays generated by these scattered electrons may be detected and appear

in the EDX spectrum. Consequently the EELS technique has the potential to conduct chemical analysis with higher spatial resolution than EDX.

3.3.5 Probe Size Measurement in the Analytical Electron Microscope

In a conventional TEM it is possible to focus the electron probe onto the viewing screen or the photographic plate and obtain a direct measurement of its diameter. In a dedicated STEM it is not possible to obtain a focused image of the probe and it is, therefore, necessary to employ an indirect method of determining the probe diameter. Measurement of the probe diameter in the HB501 was conducted under standard x-ray analysis conditions, (i.e. using a 25μm virtual objective aperture (VOA), condenser lenses C_1 and C_2 set to give a cross-over in the plane of the selected area diffraction aperture (SADA)) using magnesium oxide crystals supported on a carbon film. These crystals, which form as small cubes, were accurately aligned with a cube face parallel to the electron beam by observation of their electron diffraction pattern. The electron beam was scanned across one of the vertical edges. The 2-dimensional beam size is defined as the distance taken for the signal to rise from 10% to 90% of its ultimate value in the dark field image. The dark field image is used because phase contrast in the bright field image can give rise to apparent resolution below the probe size. Probe size measurements were conducted at various electron beam convergence angles to determine the optimum electron-optical configuration for x-ray analysis.

3.3.6 Sample Preparation for Analytical Electron Microscopy

To enable chemical and crystallographic analysis of the precipitates present in the 9% chromium steel to be conducted in isolation from the matrix, the precipitates were removed using the technique of carbon extraction. Samples were

prepared for replication in a similar manner to those for optical examination except that they were exposed to the etching solution for a shorter time. This lighter etch removed the matrix leaving the precipitates standing proud of the surface. The etched sample was coated with a 50-100nm thick layer of carbon in an evaporator. The carbon film, containing the precipitates embedded within it, was removed from the surface of the sample by scoring it into 2mm square sections and re-immersing the sample in the etching solution to release the precipitates from the matrix. Once the carbon film floated free of the sample it was straightened out by floating it on successive solutions of alcohol and water, containing decreasing proportions of alcohol. The carbon films were finally collected onto fine copper grids, 3mm in diameter, suitable for examination in the analytical electron microscope.

The carbon extraction replicas were examined in a Philips EM430 TEM equipped with a lanthanum hexaboride electron source, at an accelerating voltage of 100 keV. The maximum available accelerating voltage of this microscope, 300 keV, was not used due to the damage that an electron beam of this energy could cause to the fragile carbon film. The electron beam was focused onto a representative selection of the precipitates present on the extraction replica and the x-ray spectra emitted collected using a beryllium windowed EDX detector interfaced to a Link Analytical AN10000 analyser.

The Philips EM430 was also used to obtain an electron diffraction pattern from a representative precipitate. The precipitate was tilted until a low angle zone axis diffraction pattern was obtained. The diffraction pattern was used to determine the interplanar spacing of the atom planes in the precipitate using the technique outlined in section 3.3.2. This permitted positive identification of the precipitate.

Samples for examination by analytical electron microscopy in the form of 3mm diameter discs were trepanned from a ½mm thick slice of each of the alloys using a Eurospark spark machine. These discs were mechanically ground to a

thickness of approximately 0.1mm using silicon carbide grinding papers. The reduced thickness of the 3mm discs used to produce electron transparent samples in this study is important because of the magnetic field the ferritic steel introduces into the electron optical column of the analytical electron microscope. This asymmetric field introduces astigmatism to the electron image. The thinner the 3mm disc the more easily correctable is the astigmatism. After mechanical grinding the 3mm discs were electro-polished in a Struers Tenupol twin jet polisher using a solution of 2% perchloric acid in 2-butoxyethanol. This electro-polishing solution was maintained at a temperature of -5 to -10°C by the periodic addition of liquid nitrogen. A voltage of +45 volts was applied to the sample. Polishing of the sample was terminated when perforation occurred; this was ascertained by the use of a light source placed on one side of the sample and an optical sensor on the other. The voltage applied to the sample was tripped when light passed through the sample and fell upon the sensor. The regions around the hole in the specimen were transparent to 100keV electrons. The polishing solution was removed from the samples by washing in ethanol.

A proportion of the samples were subsequently placed in a Gatan Duomill ion beam thinner. The ion beam thinner was used to expose the sample to two beams of argon ions, at a potential of 7kV and a 10° angle of incidence. The energetic ions removed any surface film which may have been deposited during the electro-polishing phase.

After preparation and before examination the samples were stored in glass capsules filled with absolute alcohol.

3.4 Interfacial Analysis in the Analytical Electron Microscope by EDX

3.4.1 Selection of Interface for Analysis

Each of the electron transparent foils prepared were initially examined in the Philips EM430 TEM, to establish the extent of electron transparent region and confirm the presence of prior austenite grain boundaries and triple points. Prior austenite grain boundaries were easier to detect using the EM430 than the HB501 STEM due to the superior low magnification imaging capability of the former instrument. The location of prior austenite grain boundaries and triple points were noted on sketch diagrams of the foil to aid in their relocation when the sample was later placed in the HB501 for microchemical analysis.

Once a boundary had been located in the HB501 and identified as a prior austenite grain boundary by tracing it to a triple point, a portion of boundary was selected for analysis using the following criteria. Firstly the boundary had to be parallel to the incoming electron beam; this was defined as having a projected width, in the bright field image, of not more than 2nm. The boundary was also required to be free of visible precipitation, and regions of the sample exhibiting strong diffraction were avoided. A micrograph of a grain boundary suitable for analysis is shown in figure 3.7. The amount of tilt available to bring the boundary into suitable orientation was limited due to a single tilt axis holder being used and the increased astigmatism induced by excessive tilting of the magnetic foil. The need for a direct line-of-sight from the foil to the EDX detector further limited the range of tilt.

3.4.2 Acquisition of Chemical Composition Profiles

Determination of grain-boundary chemistry was conducted by positioning a static electron probe on the interface of interest and collecting the emitted x-ray

spectrum. The beam was maintained on the boundary using one of the two following methods. If the contrast of the image of the grain boundary at the analysis magnification of 2 to 5 million times was good (dark boundary against light background) the probe was maintained on the boundary by minimising the detected bright field intensity, monitored on an ammeter, during acquisition of the x-ray spectrum. For images in which there was insufficient boundary contrast the electron beam position was maintained by periodically interrupting the acquisition of the x-ray spectrum and repositioning the probe to compensate for any drift which had occurred. The x-ray spectrum was typically collected for 100 live seconds, the final choice of livetime being influenced by x-ray count rate. In cases where the x-ray count rate was low it was necessary to increase the spectrum acquisition time to maintain adequate statistics in the x-ray spectrum. Once a spectrum had been acquired from the interface the electron beam was displaced perpendicularly to the projected line of the boundary and additional spectra collected to build up a profile of chemical composition. If drift of the specimen between successive interruptions of spectral acquisition exceeded $\pm$½nm for spectra collected within 5nm of the boundary, or $\pm$1nm for spectra collected greater than 5nm from the boundary, x-ray acquisition was terminated and the data rejected.

Once sufficient data points had been collected to characterise the composition of the boundary, (approximately 11 points for a full profile or 3 points for a reduced profile), a thickness measurement of the foil was made. A reduced profile consists of a grain boundary measurement and one spectrum collected from each side of the boundary, >25nm from the boundary to obtain a matrix composition. Reduced profiles do not allow as accurate a determination of the level of segregation present at a grain boundary as do full profiles. The decreased accuracy is a consequence of the assumptions which have to be made about the electron probe size which is required for subsequent deconvolution of the composition data to obtain the concentration of segregant at the boundary. However

the collection of reduced profiles decreases the amount of time required to collect experimental data.

In addition to collecting chemical composition data from prior austenite grain boundaries other interfaces, such as lath boundaries and matrix-precipitate interfaces were examined. The conditions employed during collection of microchemical data were varied in order to investigate their effect on the detectability of segregated elements. The parameters varied were the probe size, achieved by altering the size of the virtual objective aperture, the focus of the probe and the deviation from the ideal case of the grain boundary parallel to the incident electron beam. An alternative to the standard electron optical configuration was also investigated. The strength of the first condenser lens was reduced whilst the strength of the second condenser lens was maintained at an unchanged level and the probe was focused on the sample by reducing the strength of the objective lens. The effect of these changes in lens strengths is to remove the cross-over in the plane of the selected area diffraction aperture (SADA). An advantage of this non-standard electron-optical configuration is that it permits the correction of astigmatism to a greater degree than possible using the conventional configuration, (i.e. with a cross-over in the plane of the SADA), so that increased sample tilt angles can be used. The stability of the segregated phosphorus under the influence of prolonged exposure to the electron beam was investigated by the repeated collection of x-ray spectra from the same section of a well oriented grain boundary.

During examination of samples in the electron microscope, contamination can occur due to the build-up of surface mobile hydro-carbons under the incident beam. The action of the electron beam is to decompose ('crack') the hydro-carbons into a non-mobile form and thus fix them in position. The source of these hydro-carbons is the surface film that is commonly present on samples. This surface film is acquired by the sample surface during all stages of preparation and storage if special precautions are not taken to prevent it. The high current density of the

electron beam in a dedicated STEM increases the rate of contamination build-up. Contamination can increase to a significant thickness when the electron beam is held in one position during acquisition and can consequently obscure image features. The extra thickness of the contamination also increases the scattering of the electron beam, increasing the effective size of the probe and degrading analytical resolution. The contamination build-up also introduces errors in the EELS thickness measurement and reduces sensitivity of EELS compositional analysis due to the increase multiple scattering of electrons.

The rate at which contamination builds-up can be reduced by "flooding" a large area of the specimen around the area of interest with a high intensity electron beam. Flooding has the effect of cracking the hydrocarbons as a thin film over the specimen, thus preventing them from migrating to the static probe during analysis. Additional time is then required before uncracked contamination can migrate to the beam from outside of the flooded area. The ideal solution to the problem of contamination is to examine clean specimens with no film of hydro-carbon products present, hence removing the source of contamination rather than attempting to minimise its build-up. In this study it was found beneficial to store the specimens immersed in dry, absolute alcohol in individual glass bottles. This was found to reduce significantly the amount of contamination on the sample, especially when compared to specimens which had been stored in gelatin capsules which were found to suffer from very high rates of contamination build-up under the static electron beam.

3.4.3 Quantification of X-ray Spectra

X-ray emission spectra collected on an AEM contain information relating to the chemical composition of the material with which the electron beam has interacted. The spectrum comprises a background which increases with decreasing

energy on which are superimposed characteristic peaks from the elements present in the sample.

The background, or Bremsstrahlung radiation, is generated by the slowing down of electrons in the primary beam due to interactions with electrons and nuclei in the specimen. The background extends up to an energy equal to that of the incident beam of electrons. The characteristic peaks, which are superposed upon the Bremsstrahlung radiation, arise from the relaxation of ionised atoms in the sample as described in section 3.3.1. It is the characteristic peaks which are used to determine the chemical composition of the sample.

The initial stage in the analysis of an x-ray spectrum is the identification of the elements giving rise to each of the peaks observed in the spectrum. This identification process involves determining the energy of each peak present in the sample and comparing these with tabulated compilations of x-ray energy values for each element in the periodic table. As the size of characteristic peaks decreases they become increasingly difficult to distinguish from the background particularly at the low energy end of the spectrum where the background increases in magnitude. Unambiguous identification of x-ray peaks is particularly difficult in regions of the spectrum where characteristic peaks from several elements overlap.

When the elements giving rise to the characteristic peaks in the spectrum have been identified it is necessary to measure the number of x-ray counts in each peak of interest by determining the proportion of each peak which is made up of background and characteristic counts respectively. In areas of the spectrum where the intensity of the background is varying slowly and the characteristic peaks are well separated, the most straightforward method of background subtraction is to centre an energy window on the peak of interest and estimate the magnitude of the background by interpolating between the first and last channels in the energy window. To ensure that all of the characteristic counts are included, the width of the

energy window must be several times the FWHM of the peak. In regions of the spectrum where the background is varying more rapidly with energy a linear interpolation is less likely to give an accurate approximation of the background intensity. In such regions the more sophisticated techniques of background modelling, or digital filtering, can be used to obtain a more objective and accurate estimation of the background intensity under the characteristic peak. The net counts thus calculated are converted into chemical concentrations by the operation of sensitivity factors, also referred to as 'k factors' or 'Cliff-Lorimer factors' after the workers who conducted early work in this sphere of analysis (Cliff and Lorimer 1975, Lorimer, Al-Salman and Cliff 1977). These sensitivity factors take account of the differing ionisation cross sections, x-ray fluorescence yields and detector efficiencies for the x-rays of each element. To determine the relevant sensitivity factors it is necessary to collect spectra from samples of well-known composition which are stable under the electron beam. An additional requirement of such a "standard" is that its composition must be homogeneous on the scale of analysis. Fine-scale homogeneity is particularly important when analysis is conducted at high magnification, such as encountered in the AEM. Identifying suitable samples containing all the elements which may be of interest in AEM studies can be difficult. Commonly-used standards are minerals. However, these samples are not always completely homogeneous on a sufficiently fine scale for x-ray microanalysis and, moreover, any alkali metals present have a tendency to be volatile under the electron beam. The restricted set of sensitivity factors required for conducting quantitative analysis of ferrous alloys can be determined from well-characterised solution-treated steels. However, determining the sensitivity factors required to quantify the concentrations of elements commonly present as impurities in steels is more difficult.

An alternative to direct measurement of the sensitivity factors is to calculate them from the theoretical values of ionisation cross-section, absorption,

fluorescence, detector efficiency etc. However this procedure can introduce greater errors due to the uncertainty in each component of the theoretical equation.

A common approach to quantitative analysis is to utilise library values of sensitivity factors. These are experimentally determined, and are tabulated and available in the literature. The library values have the advantage of being experimentally determined. However, accuracy is compromised when the factors are not determined on the same electron beam equipment used to collect the analytical data.

The x-ray data obtained from the STEM were converted into weight and atomic percentages using Link Systems quantification software. The programme used was the filtered least squares, ratio thin section (FLS/RTS2) suite of spectrum processing software. The first operation of this software is to pass a "top-hat" filter through the raw data of the spectrum. The operator inputs a list of those elements present in the sample and the same top-hat filter is applied to a set of elemental profiles stored by the computer. These elemental profiles are extracted from x-ray spectra in which the peaks of interest are well separated from other characteristic peaks. The resolution of the experimental spectrum is determined by measuring the full width at half maximum of the zero strobe peak produced by the computer during acquisition. This experimentally determined resolution is used to match the resolution of the library profiles to that of the experimental data. The software compares the acquired spectrum with its library. The filtered profiles are used to determine the number of counts within each characteristic peak of interest. Deconvolution of peak overlaps is achieved by iterative comparisons of the experimental data with varying combinations of the profiles from the overlapping elements until the best statistical match is obtained. The quality of the match is determined by summing the square of the difference between each channel of the experimental data and the scaled library profiles. The best match is that combination which produces the lowest squared difference. When the areas of all of the peaks

have been measured they are converted to chemical composition by the use of sensitivity factors as outlined above. The sensitivity factors are measured on standards of known composition and take into consideration the ionisation cross-section, x-ray fluorescence yield and detector efficiency. The sensitivity factors used in this study were a combination of experimentally determined values for iron and chromium and literature values for phosphorus and silicon. A solution treated stainless steel sample was used to measure the sensitivity factors, on the HB501, for iron and chromium. X-ray spectra were collected from large area scans, to avoid the problems of small scale inhomogeneities. The values of the sensitivity factors used to convert the spectral data to chemical composition were varied to obtain agreement with the known composition of the steel.

The thickness of the foil, tilt angle of the specimen and take-off angle of the detector are used by the analysis programme in conjunction with the first approximation of the sample composition to determine the degree of attenuation each characteristic x-ray peak will have suffered during its passage through the sample. The concentration of each element is recalculated using the characteristic peak areas corrected for absorption. This process is repeated in an iterative manner until the variation between successive determinations of chemical composition falls to an insignificant level.

In calculating chemical composition from an x-ray spectrum, the assumption is that the material under the electron beam is homogeneous. The composition determined by the analysis routines described above is therefore the average composition of the column of the sample, through which the electron beam has passed. In the measurement of interfacial segregation profiles the chemical composition of the sample is changing on a scale much finer than the probe size. It is therefore necessary to deconvolute the data to obtain the concentration of the segregated elements at the interface. The deconvolution of the data can be achieved using one of two alternate methods. The first method is a simple deconvolution of

an electron beam intensity distribution, which has a full width at half maximum (FWHM) measured from the experimental x-ray profile, with an impurity concentration profile which is assumed to approximate to a delta function. The second method uses Monte Carlo modelling techniques to predict the interaction of the electron beam with a segregant layer and is appropriate in thicker foils where there is significant high-angle elastic scattering of the incident fast electrons (beam broadening). These two deconvolution procedures are explained in detail in chapter 5.

3.4.4 Measurement of Sample Thickness in the Analytical Electron Microscope

Knowledge of the local foil thickness is required firstly to calculate the extent of beam broadening, secondly to derive absorption corrections for use in quantitative analysis of x-ray spectra and thirdly as an input to deconvolution routines used to determine interfacial chemistry. Three of the most commonly used methods for measuring the thickness of an electron transparent foil involve "geometrical features", convergent beam electron diffraction (CBED), and electron energy loss spectroscopy (EELS).

The method of feature separation requires the identification of a feature which intercepts both the top and bottom surfaces of the foil. The projected image width of the feature is measured, the foil tilted through a known angle, and the width of the feature remeasured. The thickness of the foil can then be calculated using trigonometric formulae. Problems which can arise using this method include; a lack of features passing through the foil in the area where the thickness measurement is required, or the amount of tilt available in the microscope limiting the change in separation of the features thus increasing the errors involved in the procedure.

An alternative to locating a feature in the sample which passes through the foil is to create one which sits on the entrance and exit surfaces of the foil. This can be achieved by deliberately allowing contamination to build up under the focused beam, tilting the foil and measuring the separation of the spots. A drawback of this technique is that contamination builds up quickest on the entrance side of the foil and can become large enough to create problems for accurate measurement of the separation. A major drawback of using contamination spots to determine specimen thickness in this study is that their presence is detrimental to high resolution analysis, due to the increased beam broadening they induce. Consequently the procedures of preparation, storage and examination of foils are optimised to reduce or, if possible, to eliminate the production of such contamination spots.

Some of the drawbacks of the previous methods can be overcome using convergent beam electron diffraction (CBED). The production of a CBED pattern is similar in principle to the formation of a selected area diffraction (SAD) pattern except that a highly focused probe is used instead of a parallel beam of electrons. The effect of this change is to produce diffraction discs rather than spots in the back focal plane of the objective lens. The area from which the CBED pattern is produced is defined by the size of the focused probe and can, therefore, be from a much smaller area of the foil than a SAD pattern. In addition to determination of interplanar spacings and angles the CBED pattern also contains information about the crystallographic point and space groups of the specimen and the local thickness. When the specimen is tilted to a two beam condition the diffracted discs exhibit regularly spaced maxima and minima of intensity, the spacing of which can be used to determine the local thickness of the sample (Kelly et al, 1975).

A third method commonly used for determining the local thickness of a sample in the analytical electron microscope is electron energy loss spectroscopy (EELS).(Joy et al 1979, Leapman et al 1984) It is the low energy region of the EELS spectrum which is used for this purpose. The thickness is determined from

the ratio of the area under the zero loss peak to the total area under the energy loss spectrum. This ratio is used in conjunction with a knowledge of the inelastic mean free path of electrons in the sample to determine the thickness.

Upon completion of a chemical composition profile the thickness of the foil in the vicinity of the interface was measured by recording two low-loss EELS spectra (one from each side of the boundary) using the VG ELS 501 electron energy loss spectrometer. The advantages of EELS as a method for measuring foil thickness are that the technique is quick and easy to use and the measurement can be made at the same orientation as x-ray acquisition. The size of the plasmon peaks are affected by the presence of contamination and surface films, consequently the full thickness of the sample is measured. However it must be noted that the mean free path for plasmon excitation will vary in the foil and the surface layer. It is therefore still preferable to have a clean sample to facilitate accurate thickness measurement.

3.5 Principles and Operation of Auger Electron Spectroscopy

In many ways the components of an Auger electron microprobe are similar to those which comprise the analytical electron microscope. Both consist of an evacuated chamber, a source of electrons, a means to accelerate the electrons, a sample upon which the electrons are focused and both include facilities to image the sample and detect the characteristic signals which are emitted. In the following pages only the additional requirements of the AES system are described in detail.

The Auger analysis in this study was conducted using a Vacuum Generators MA500 Auger electron microprobe, the major components of which are shown in figure 3.8. The preparation and analysis chambers are maintained in the ultra high vacuum (UHV) regime of 10^{-10} torr or better. This reduces the rate of adsorption of contaminants, predominantly oxygen and carbon, onto the surface of samples to a

level which does not adversely affect examination and analysis. The initial vacuum in an AES system is achieved using rotary and oil diffusion pumps, as in the AEM. The improvement in ultimate vacuum is achieved by improving the integrity of the seals between components of the system and the use of a bake-out cycle.

In the AEM, elastomeric 'O'-rings are used to provide gas-tight seals between components; in UHV systems, copper gasket seals are used. With this type of seal an annealed copper gasket is placed between two surfaces, which have had knife-edges machined into them. The action of tightening the surfaces together causes the knife-edges to deform the copper gasket and produce a high integrity gas-tight seal. Also metal bellows are used to permit relative movement of two components replacing sliding 'O'-ring seals used in the AEM.

With the improved methods of sealing described above the ultimate vacuum which can be achieved becomes limited by the rate at which adsorbed gases leave the internal surfaces of the instrument at ambient temperatures. This rate of outgassing varies according to material and limits the range of materials which can be used in the UHV environment. However, even with the use of materials with low rates of outgassing properties a very long time would be required to achieve UHV. To reduce the time, the rate of outgassing must be temporarily increased to quickly remove the adsorbed gases, this is achieved by heating the system to a temperature of 150-240°C for several hours. When the temperature of the system returns to ambient the rate of outgassing falls by several orders of magnitude to a level which the oil diffusion pump can cope with. UHV can then be achieved and maintained. This thermal cycling or bake-out cycle further reduces the choice of materials which can be used in the construction of an UHV system. Those selected must not disintegrate, outgas excessively or lose strength during the repeated exposure to elevated temperature they will undergo during the life of the system. The methods of achieving UHV detailed above were used in both the MA500 AES and the HB501 STEM

The MA500 is fitted with thermionic electron emission source consisting of a heated lanthanum hexaboride crystal. The maximum accelerating voltage of the MA500 was 30keV, but during collection of Auger data it was operated at an accelerating voltage of 10keV. The electron-optical configuration of the MA500 Auger electron microprobe is shown in figure 3.9. It consists of two condenser lenses which demagnify the electron source, and an objective lens which forms a fine focused probe of electrons on the surface of the specimen in a manner similar to that employed in the STEM. The current contained in the probe is controlled by varying the strength of the second condenser lens.

The MA500 is equipped with a secondary electron detector which is used to produce an image of the sample and a concentric hemispherical analyser to detect the Auger electrons which are excited by the incident electron beam. The image is formed by collecting the secondary electrons which are produced by the interaction of the sample and the primary electron beam. The focused electron beam is scanned across the specimen surface and the magnitude of the secondary electron signal is used to vary the intensity of the spot on a CRT scanning in synchronisation with the primary beam, as in the STEM. The magnification of the image is varied by altering the length of the line scanned on the specimen. A photographic record of the image is made by exposing the film to a single frame scan of the CRT.

3.5.1 Electron Sample Interactions in the Auger Electron Microprobe

The process of the ionisation and subsequent relaxation of atoms has been described earlier. The process of Auger emission is illustrated in figure 1.2b, where a k-shell electron has been ejected by interaction with the primary beam. The vacancy in the k-shell has been filled by an electron from the L_1 shell and simultaneously an electron from the L_2,L_3 shell has been emitted. This leaves the atom doubly ionised. The nomenclature used to describe the ejected electron is K L_1

L_2L_3. The energy level from which the initial electron is ejected is named first, the level from which the electron falls named next and original level of the ejected Auger electron is named last. The energy of the Auger electron is given by:

$$E_{K\,L_1\,L_2L_3} = E_K - E_{L_1} - E^*_{L_2L_3} \qquad 3.8$$

where E_i are the binding energies of the i^{th} atomic level. The term $E^*_{L_2L_3}$ is starred because it refers to the binding energy of the L_2L_3 level in the presence of a hole in the L_1 level. Thus the energy of the Auger electron is solely a function of the energy levels of the atom, and analysis of the Auger electron energy enables elemental identification.

The proportion of ionised atoms which result in the emission of an x-ray photon was discussed in section 3.3.3 The proportion of ionisation events which result in the emission of an Auger electron is simply one minus the fluorescence yield of x-rays. Consequently, as the probability of x-ray emission falls with decreasing atomic number, so the proportion of Auger electrons produced increases. This increases the sensitivity of the AES technique to the detection of light elements.

Auger electrons are produced in a bulk sample until a depth is reached where the primary beam retains insufficient energy to cause further ionisation of the matrix atoms. The electrons of interest in Auger electron spectroscopy have energies in the range 50-1000 eV. Electrons in this energy range undergo intense inelastic scattering during their passage through a sample, which results in them having very short inelastic mean free paths. A plot of inelastic mean free path (λ) as a function of Auger electron energy is shown in figure 3.10 (Seah and Dench 1979). It can be seen that the inelastic mean free path in the energy range of interest is approximately 2-6 monolayers. However the plot shows considerable experimental scatter about the mean values in this energy range. The escape depth for an Auger electron is related to its inelastic mean free path by the angle of electron emission

between the specimen surface and the detector as shown in figure 3.11. This collection geometry further reduces the distance perpendicular to the sample surface from which Auger electrons are emitted.

3.5.2 Detection of Auger Electrons

The Auger electrons produced within a sample, after interaction with the primary electron beam, can be detected using an energy dispersing spectrometer. The principal analysers used on Auger microprobes are the concentric hemispherical analyser (CHA) and the cylindrical mirror analyser (CMA). The MA500 is fitted with the former type of spectrometer

The main features of the concentric hemispherical analyser are shown schematically in figure 3.12. It consists of two concentric hemispherical surfaces of inner radius R_1 and outer radius R_2. A potential is applied to the hemispheres to make the outer hemisphere negative and the inner hemisphere positive. The plane of zero potential between the two hemispheres has a radius of R_0.

Ideally $R_0 = (R_1+R_2) / 2$. The entrance and exit apertures of the spectrometer are both located on the radius, R_0.

The resolution of the CHA is expressed in terms of the base resolution (width at the base of a characteristic peak),

$$\frac{\Delta E_B}{E} = \frac{w + \alpha^2}{R_0} \qquad 3.9$$

and the full width at half maximum of the peak is

$$\frac{\Delta E}{E} = \frac{w + \frac{\alpha^2}{4}}{2R_0} \qquad 3.10$$

where w = slit width

α = angular range of electrons entering spectrometer

It is common to choose the entrance angle, α, such that

$$\alpha^2 \approx w / 2R_0 \qquad 3.11$$

The above expressions of resolution then reduce to

$$\frac{\Delta E_B}{E} = \frac{1.5\, w}{R_0} \qquad 3.12$$

and

$$\frac{\Delta E}{E} = \frac{0.63\, w}{R_0} \qquad 3.13$$

To obtain the energy distribution of the electrons emitted by the sample a ramped deflecting potential is applied to the hemispherical surfaces, and the current incident on the detector is measured. Thus the Auger spectrum is collected in a sequential manner.

The resolution of the spectrometer can be improved by decelerating, or retarding, the Auger electrons before they enter the spectrometer. The CHA fitted to the MA500 was operated with a constant retard ratio (CRR) of 4.

3.6 Chemical Composition analysis in the Auger Electron Microprobe

To promote intergranular fracture the ferritic steel samples were cooled to a temperature below that of their ductile to brittle transition in a liquid nitrogen cooled fracture stage. When the sample had been cooled sufficiently, (approximately two hours), it was fractured by impact using a hammer. One of the broken halves of the specimen was manipulated into the analysis chamber and oriented towards the Auger electron detector. The secondary electron image of the

fracture surface was observed and intergranular facets were distinguished from areas of cleavage by their appearance, the intergranular facets being smoother than regions of transgranular cleavage which exhibit 'river lines'. These fractographic features are illustrated in figures 3.13a, intergranular fracture, and 3.13b, transgranular cleavage.

Once a suitable facet had been identified, the detected Auger current at an energy of 1000eV was maximised by adjusting the height of the sample to ensure that it was at the focal point of the collecting lens of the concentric hemispherical analyser. Because of the possibility of the specimen's magnetism affecting the trajectory of the low energy Auger electrons, the Auger current at an energy of 10 eV was optimised using magnetic trim pots. When optimum conditions had been obtained spectra were collected in the direct mode giving the number of counts as a function of energy. Initially Auger electrons with energies in the range 50 - 1000 eV were collected to give a full (or wide) spectrum; this was used to identify the elements present on the surface of the facet. Subsequently, wide scan spectra were used to monitor the build up of adsorbents from the vacuum. If the detected signal from carbon and/or oxygen increased significantly, relative to the initial wide scan, data acquisition from the sample was terminated and a new sample was fractured. It was found that the vacuum in the analysis chamber (~10^{-10} Torr) was sufficient to allow several hours examination before contamination increased sufficiently to degrade the validity of the data collected. When the elements present had been identified from the wide scan spectrum, narrow energy regions, centred on these peaks, were selected. The use of narrow energy widows during the acquisition of Auger data improved the statistics of Auger analysis by concentrating acquisition time on the regions of the spectrum which contain relevant data and allowed more facets to be examined before contamination of the sample increased to an unacceptable level. The energy regions and collection parameters for the wide and narrow scans are given below.

Wide Scan	Narrow scans	
50ev - 1000eV	Phosphorus	100eV - 130eV
	Chromium	480eV - 520eV
	Iron	680eV - 720eV
Step size 1eV	Step size 0.5eV	
Dwell time 50ms/channel	Dwell time 100ms/channel	
Retard ratio 4	Retard ratio 4	
No of scans 10	No of scans 10	

Approximately 60 to 80 facets were examined in each alloy.

The effect of varying the angle of sample tilt on the acquired spectra was investigated by collecting several spectra from the same grain boundary facet, altering the orientation of the facet to the detector between each acquisition.

3.6.1 Sample Preparation for the Auger Electron Microprobe

On the MA500 there are three methods which may be used to provide a clean surface for examination these are abrasion, ion bombardment and fracture.

The simplest method of sample preparation is abrasion. This is conducted within the vacuum chamber by dragging a diamond stylus, or similar hard implement, across the sample surface. The freshly exposed material can then be examined. However, it is difficult to clean large areas of a specimen in this manner and the destructive nature of the technique obscures microstructural features.

The second method of cleaning a sample is by ion bombardment. The atoms on the surface of the sample are removed by the transference of sufficient energy from a beam of energetic ions (3-5KV). Although the method is quite slow and different atomic species have different sputtering rates, a larger area of sample can be more uniformly cleaned using this technique. Variability in elemental sputtering

rates can lead to a surface becoming preferentially enriched in one or more of its constituents. The process of surface erosion by ion bombardment can also be used to investigate the variation in chemical composition as a function of distance perpendicular to the sample surface.

An alternative approach to sample preparation is to create, by fracture, a new surface within the vacuum chamber, in preference to cleaning a pre-existing surface. The mechanical method used to initiate fracture is either impact, tensile strain or slow bend, dependant upon the configuration of the fracture stage available within the microprobe preparation chamber. The fracture induced in a sample may be either transgranular or intergranular. The former fracture mode allows determination of matrix composition and the latter interfacial chemistry. Fracture was predominantly used to produce clean surfaces for analysis during this study.

The samples used for Auger analysis were machined from the material remaining after removal of the ½mm thick slice used to make AEM samples. The specification to which Auger samples are normally produced for examination in the MA500 Auger electron microprobe is shown in figure 3.14. The sample has a diameter of 5mm and an overall length of 29.5mm, with a centrally located notch. The size of the available material (20 x 10 x 2.5 mm) prevented the fabrication of standard Auger samples. Therefore 'matchsticks' were cut from the material, of approximate dimensions 2.5 x 2.5 x 20mm, and fitted into (or 'sleeved' with) stainless steel tubes of 3.5mm internal diameter, 5mm external diameter and 13mm in length. The matchsticks did not require mechanically fixing into the sleeves due to the tight friction fit between the two components. The overall length of the composite sample was adjusted to be 29.5mm. A centrally located notch was machined into the sample using a diamond cutting wheel, to provide a stress raiser to aid fracture of the sample within the microprobe. After manufacture the AES samples were ultrasonically cleaned in acetone to remove grease and other contaminants, prior to loading into the fracture stage of the MA500.

The fracture stage of the MA500 can be configured to allow fracture of samples by impact or slow bending, it also has the facility to cool specimens with liquid nitrogen to facilitate intergranular fracture. After fracture one half of the specimen was transferred to the analysis chamber.

3.6.2 Selection of Acquisition Parameters for Auger Electron Spectroscopy

A concern with surface analysis techniques, such as AES, is the possible mobility of a segregant specie once the boundary has been exposed by fracture and subjected to electron beam irradiation. If the segregant is mobile the signal collected from the segregant will reduce during acquisition of the spectrum leading to an artificially low signal being detected. Another consequence of segregant mobility under the electron beam is the possible deposition of material onto areas adjacent to that being studied. To check the stability of phosphorus on the intergranular facets in this study the following experiment was carried out. The initial conditions selected for the collection of Auger spectra were a 10 KeV primary electron beam with a beam current of 10 nA scanned over a facet at a magnification of x5000 (approximate area 20 x 30 μm). Successive spectra were collected from a single facet over a period of an hour and the relative heights of the phosphorus and iron peaks were noted. The detected phosphorus signal decreased as a function of time. To confirm whether the decrease in phosphorus signal was a consequence of the examination with an electron beam of 10nA, the following experiment was conducted on a previously unirradiated area of the sample.

i) a region of transgranular cleavage was examined using a reduced beam current of 5 nA

ii) an adjacent intergranular facet was examined using a beam current of 5 nA

iii) the transgranular cleavage was again examined using a beam current of 5 nA

iv) the adjacent intergranular facet was re-examined using a beam current of 10 nA

v) finally the transgranular cleavage was re-examined using a beam current of 5 nA.

Subsequent analysis of the spectra collected using the above conditions confirmed that the phosphorus was mobile under the influence of the electron beam when it contained a current of 10 nA but not when the current was reduced to 5nA. All subsequent Auger data was collected using a beam current of 5nA.

3.6.3 Acquisition of a Depth Profile

The variation of chemical composition perpendicular to the surface of a grain boundary facet was investigated by conducting an in-situ depth profile. After initial chemical analysis of a facet a 2mm by 2mm area of the sample was exposed to a beam of argon ions at a potential of 10keV, and a beam current of 200nA giving a current density of 5μA cm^{-2}. The approximate erosion rate of a steel surface under these conditions is three atom layers per five minutes exposure (Bishop, private communication). The facet was analysed before erosion and after the removal of approximately ½, 1, 1½, 2 and 4 atom layers.

3.6.4 Analysis of Auger Electron Spectra

The Auger electron spectrum was collected as the number of counts detected as the selected energy range is scanned; this is commonly referred to as the direct or N(E) spectrum. Prior to quantification of the Auger data the direct spectrum was smoothed to reduce the random fluctuations present in the direct spectrum, and so reduce the noise in the differentiated spectrum. Smoothing also reduces the

magnitude of the peaks in the N(E) spectrum. It is therefore necessary to standardise on the number of points used in the smoothing routine so as not to introduce systematic errors into subsequent quantification. After smoothing the spectra were numerically differentiated to give the derivative or dN(E)/dE spectrum. Differentiation has the effect of replacing the sloping background of the direct spectrum with a horizontal one and transforming simple peaks into doublets, improving the visibility of small peaks. A typical example of a direct Auger electron spectrum collected from alloy S300 is shown in figure 3.15. The same spectrum is also shown after smoothing (figure 3.16) and differentiation (figure 3.17). The operation of the spectrometer, smoothing and differentiation of the spectra were all conducted using VG7000 software. Conventionally it is the ratio of the peak-to-peak heights, measured in the dN(E)/dE spectrum which is quoted, in preference to the ratio of peak areas in the direct spectrum. Further processing of the data depends upon the nature of the sample and the use to which the data is to be put. If a comparison is being conducted on the same instrument between various materials, or into the effect of different heat treatments on the same material, the data is commonly quoted as peak to peak height ratios. This allows trends to be identified without the need for further quantification.

The next step to quantification of Auger data is to assume that the material under investigation is homogeneous in a direction perpendicular to the surface. To account for differences in the efficiency of Auger electron production from different constituents of the matrix and convert the peak to peak height ratio to a composition ratio, relative sensitivity factors are required. The accuracy of the quantification is increased if these sensitivity factors are collected on the same machine as used for the acquisition of experimental data. If this direct determination of sensitivity factors is not possible, tabulated collations in the literature can be consulted in a similar manner to sensitivity factors in the AEM.

If I_A, I_B and I_C are the measured peak-to-peak heights of elements A, B and C, and I_A^∞, I_B^∞ and I_C^∞ are the relative sensitivity factors. The concentration of element A (C_A) is given by (Seah 1983):

$$C_A = I_A I_A^\infty / (\Sigma_i I_i I^\infty_i) \qquad 3.14$$

In this study the relative sensitivity factors for iron, chromium and phosphorus were measured in the following manner.

The iron-chromium peak to peak height ratio was measured from several regions of transgranular cleavage in one of the 9% chromium steel samples. The composition of these regions was calculated using equation 3.14 and literature values of sensitivity factors. The average composition was compared to the chemical specification of the steel and the sensitivity factors adjusted so the experimentally determined composition agreed with the specification. Regions of transgranular cleavage were used during this determination because they do not exhibit segregation or large proportions of precipitation, both of which would distort the measured composition. The sensitivity factor for phosphorus was determined using a sample of ferro-phosphorus. The composition of the ferro-phosphorus was determined from the average of twenty measurements obtained in an EPMA. The same sample was placed in the MA500 Auger microprobe; prior to examination it was ion bombarded to produce a clean surface. However, after ion bombardment the spectra indicated the presence of significant levels of carbon and oxygen. To remove the remaining surface layer, and expose a clean surface the sample was abraded under vacuum using a diamond stylus. Analysis of the abraded area revealed that the signal from carbon and oxygen had significantly decreased. Twenty Auger spectra were collected from the abraded region. The differential peak to peak heights of phosphorus and iron were used to calculate the composition of the sample using equation 3.14. The composition was compared to the concentration given by the EPMA and the sensitivity factors for the Auger analysis were

calculated. These sensitivity factors for iron, chromium and phosphorus were used for the subsequent quantification of Auger data. They are listed in Chapter 5.

	Weight Percent				Parts Per Million			
Alloy	Iron	Chromium	Silicon	Carbon	Phosphorus	Sulphur	Tin	Antimony
S560	90.3	9.01	0.6	0.1	560	50	50	50
S300	90.3	9.01	0.6	0.1	300	50	50	50
S120	90.3	9.01	0.6	0.1	120	50	50	50
S25	90.3	9.01	0.6	0.1	25	50	50	50

Table 3.1 Chemical composition of materials examined

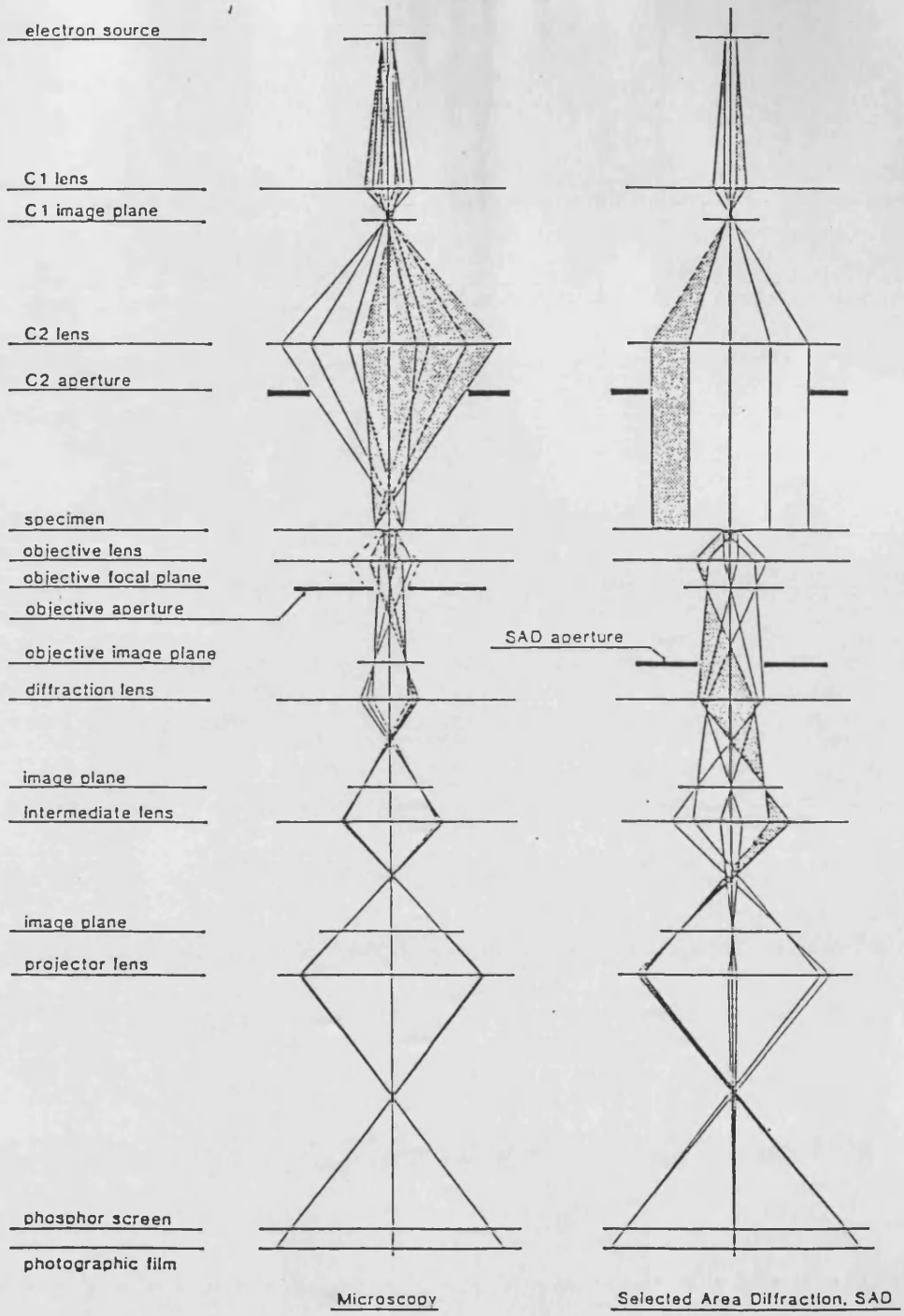

Ray diagrams of transmission electron microscope

Figure 3.1 Imaging

Figure 3.2 Selected area diffraction

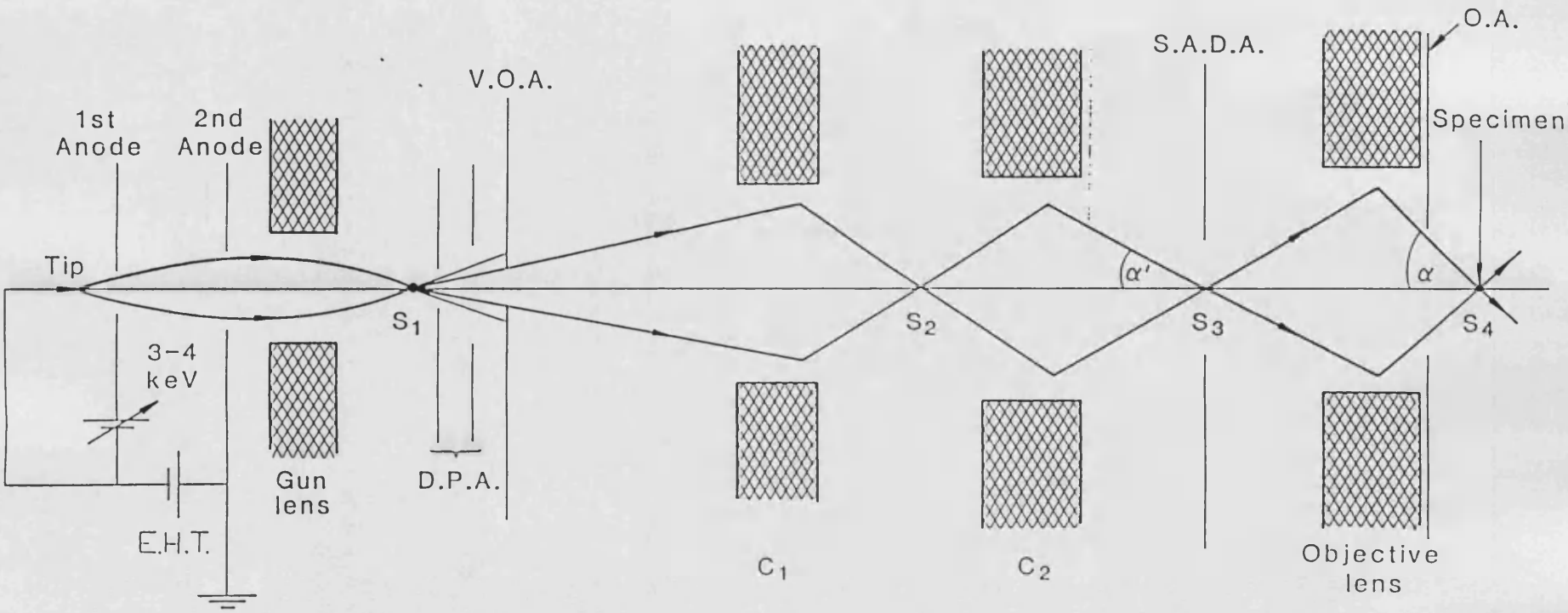

Figure 3.3 Ray diagram of scanning transmission electron microscope, imaging mode

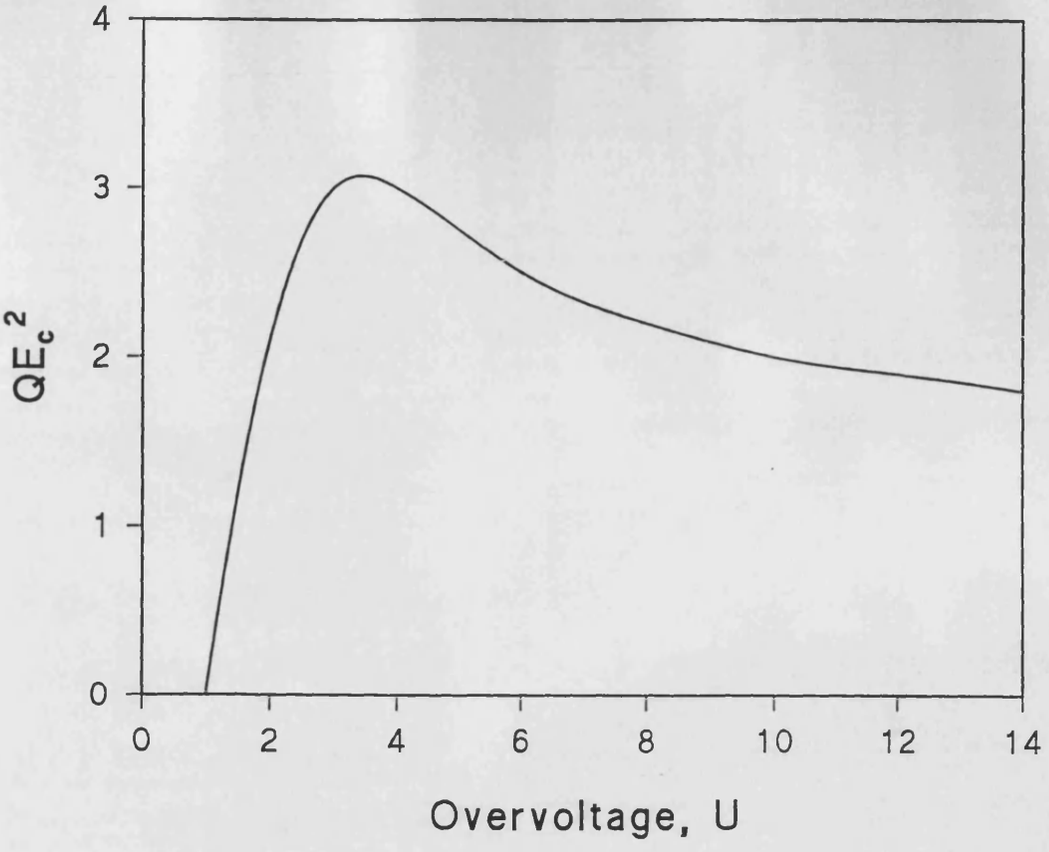

Figure 3.4 Variation of ionisation cross-section as a function of overvoltage

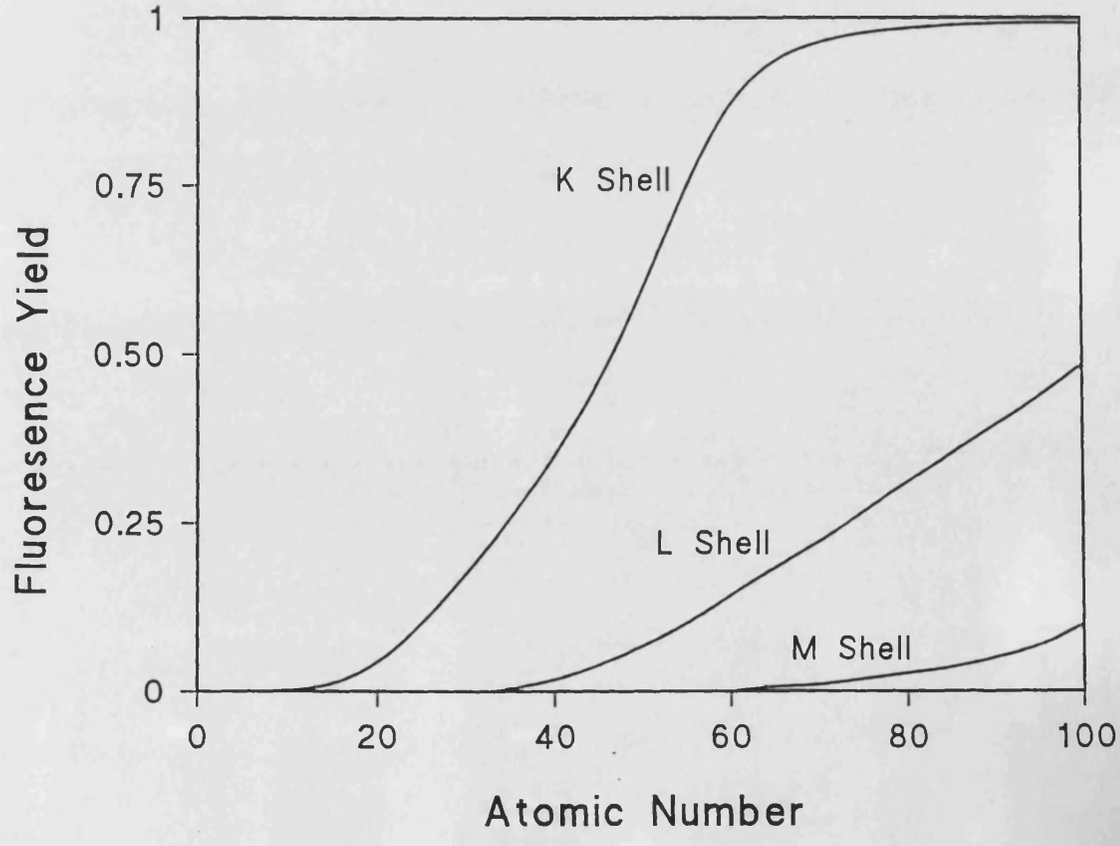

Figure 3.5 Variation in fluorescence yield as a function of atomic number

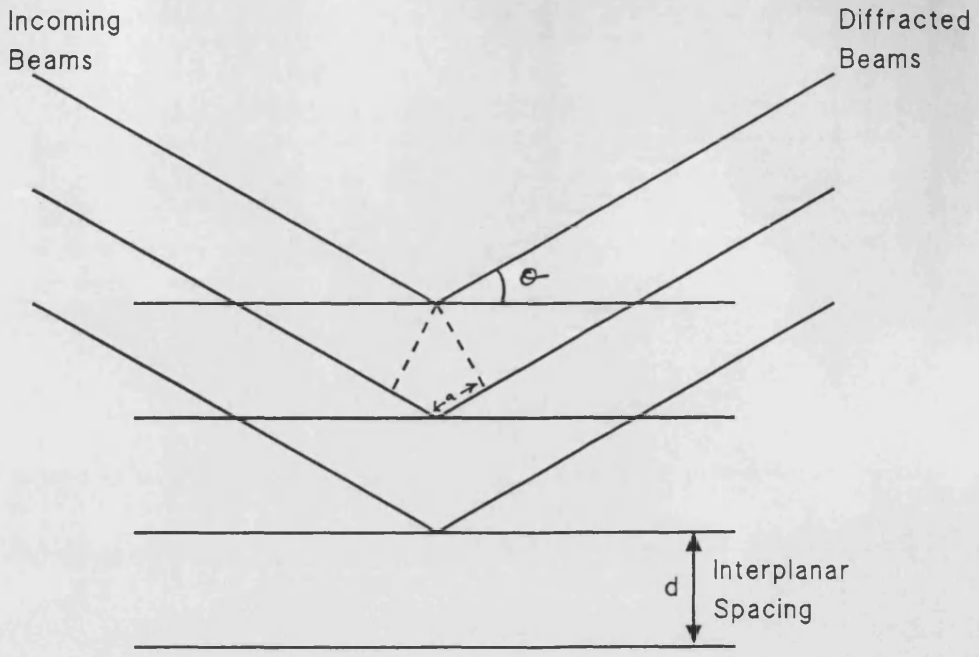

Figure 3.6 Principle of x-ray diffraction

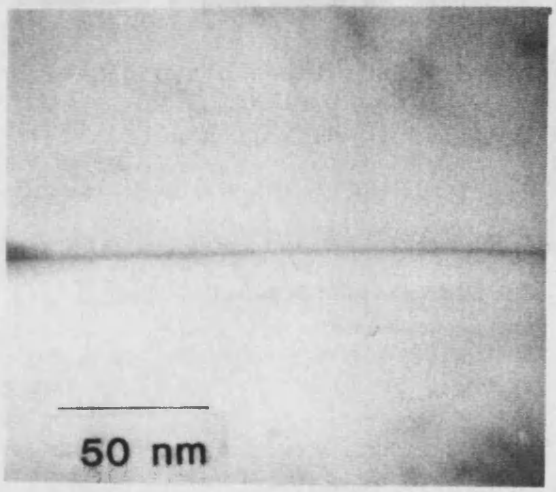

Figure 3.7 Electron micrograph of a grain boundary suitably oriented for analysis in the STEM

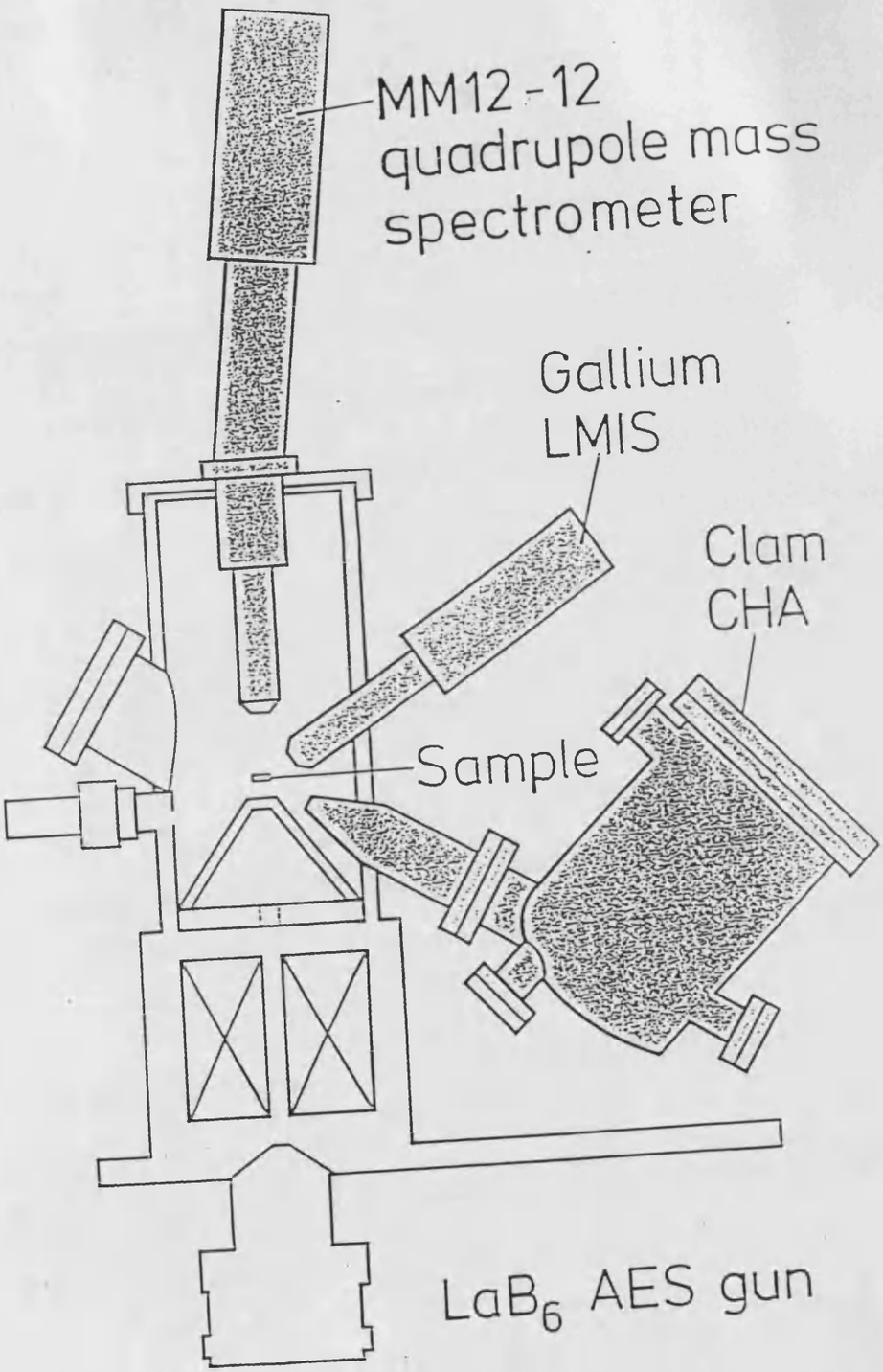

Figure 3.8 Schematic diagram of VG MA500 Auger electron microprobe

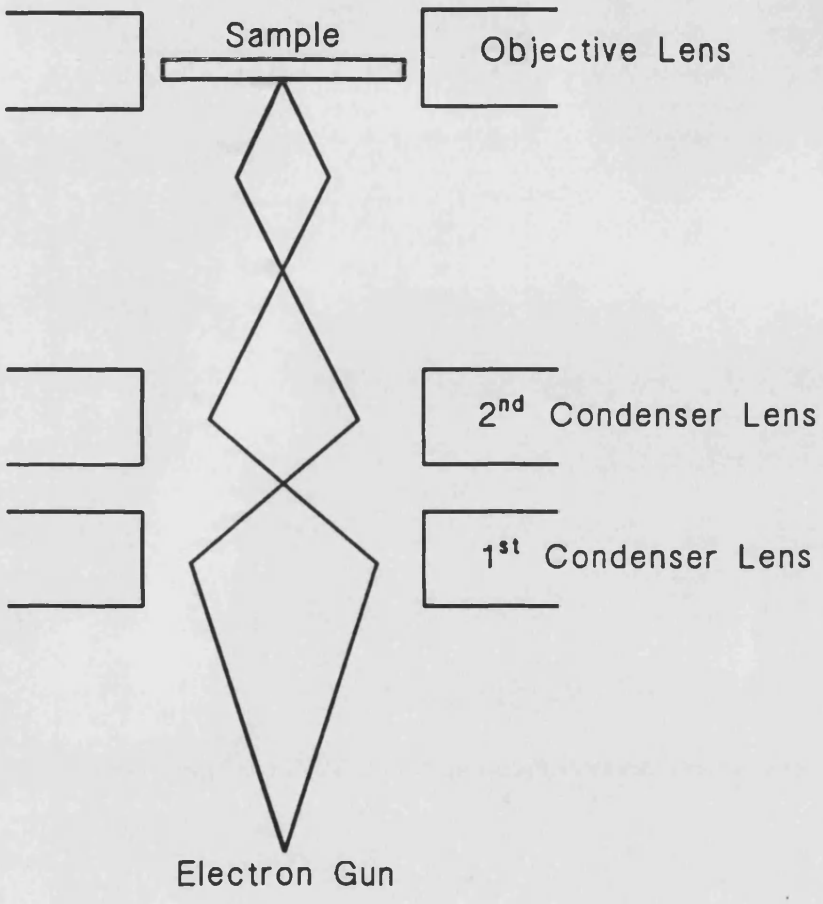

Figure 3.9 Electron-optical configuration of scanning Auger electron microprobe

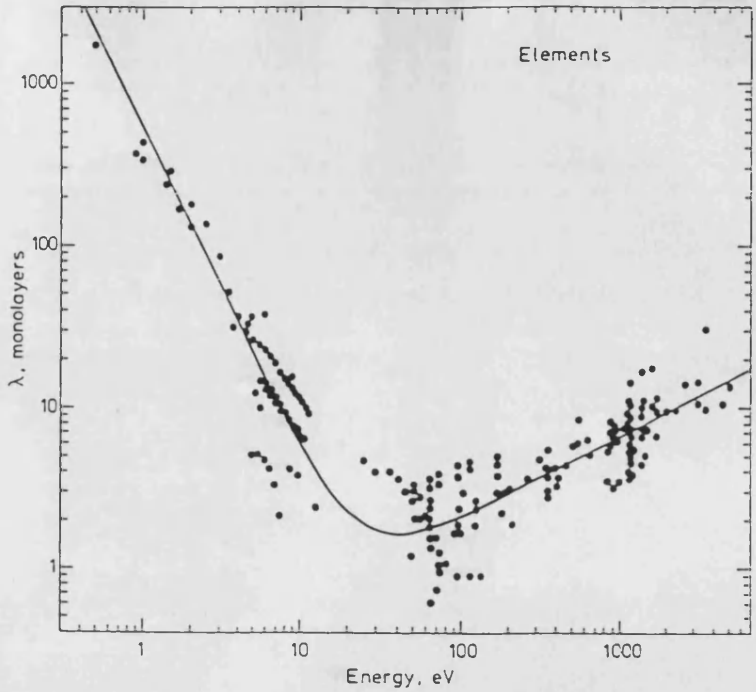

Figure 3.10 Variation of inelastic mean free path as a function of Auger electron energy (Seah and Dench 1979)

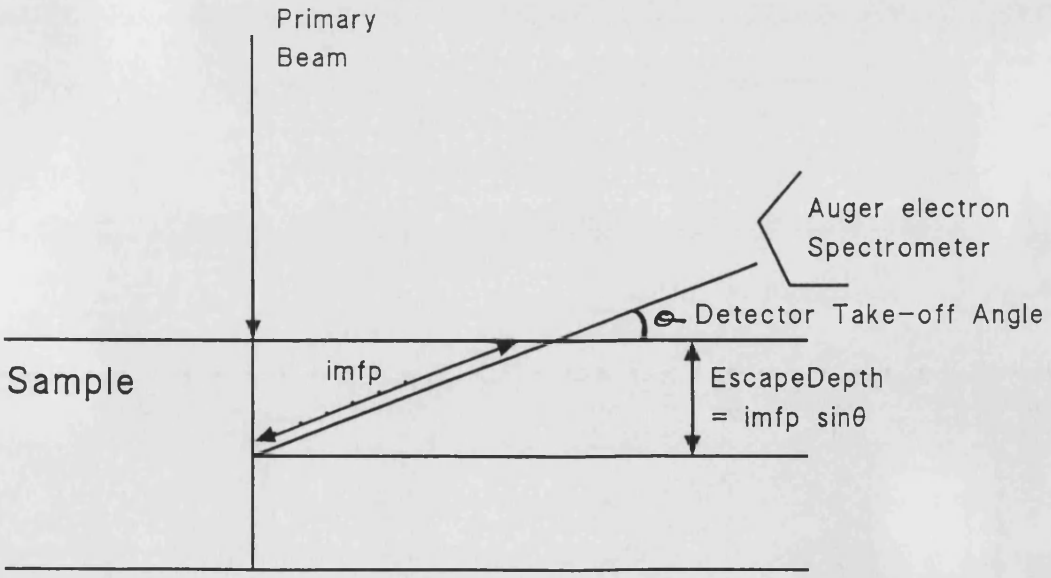

Figure 3.11 Relationship of Auger electron escape depth to the inelastic mean free path and detector take-off angle

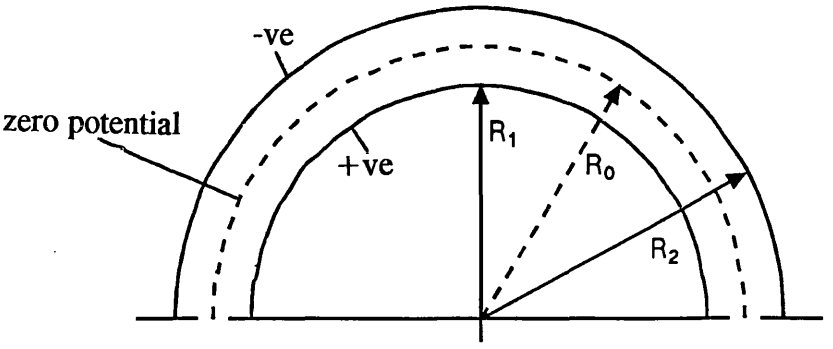

Figure 3.12 Schematic diagram of concentric hemispherical analyser

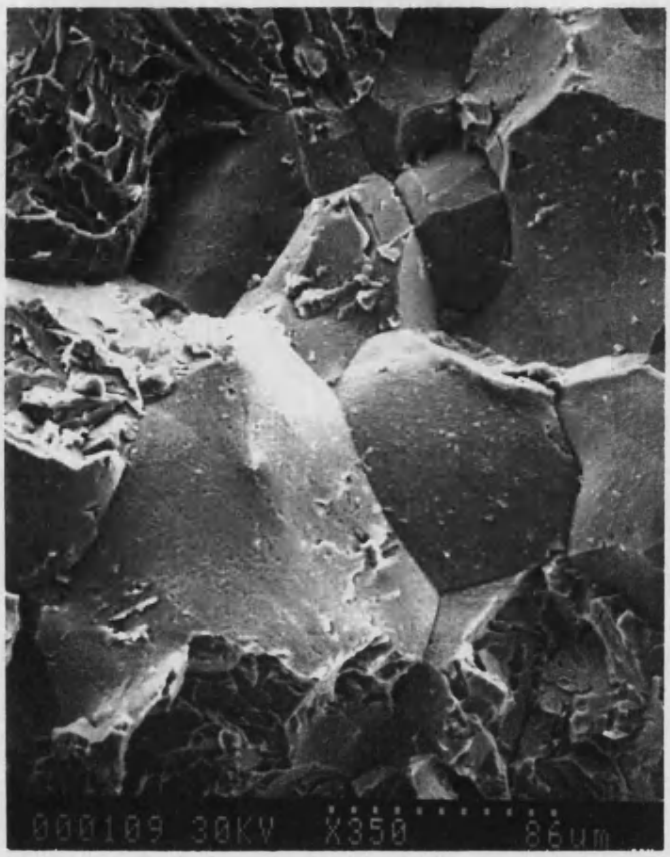

Figure 3.13a SEM micrograph of typical fracture surface showing intergranular fracture

Figure 3.13b SEM micrograph of typical fracture surface showing transgranular cleavage

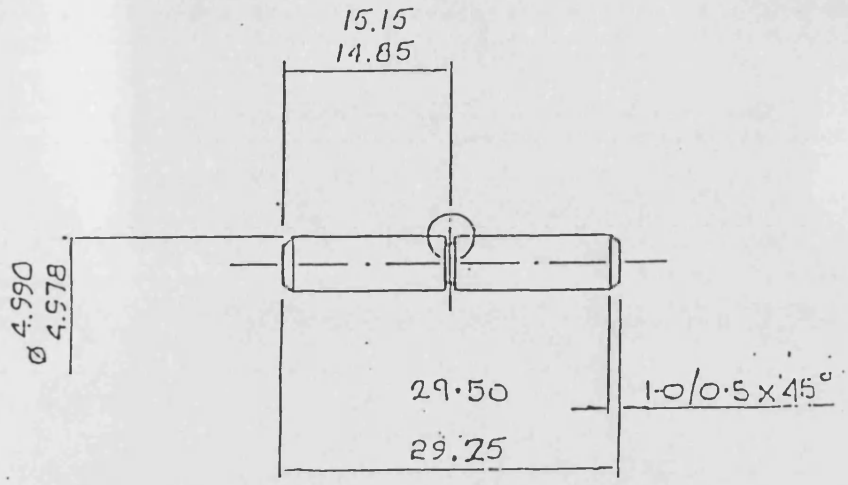

Figure 3.14 Auger sample geometry

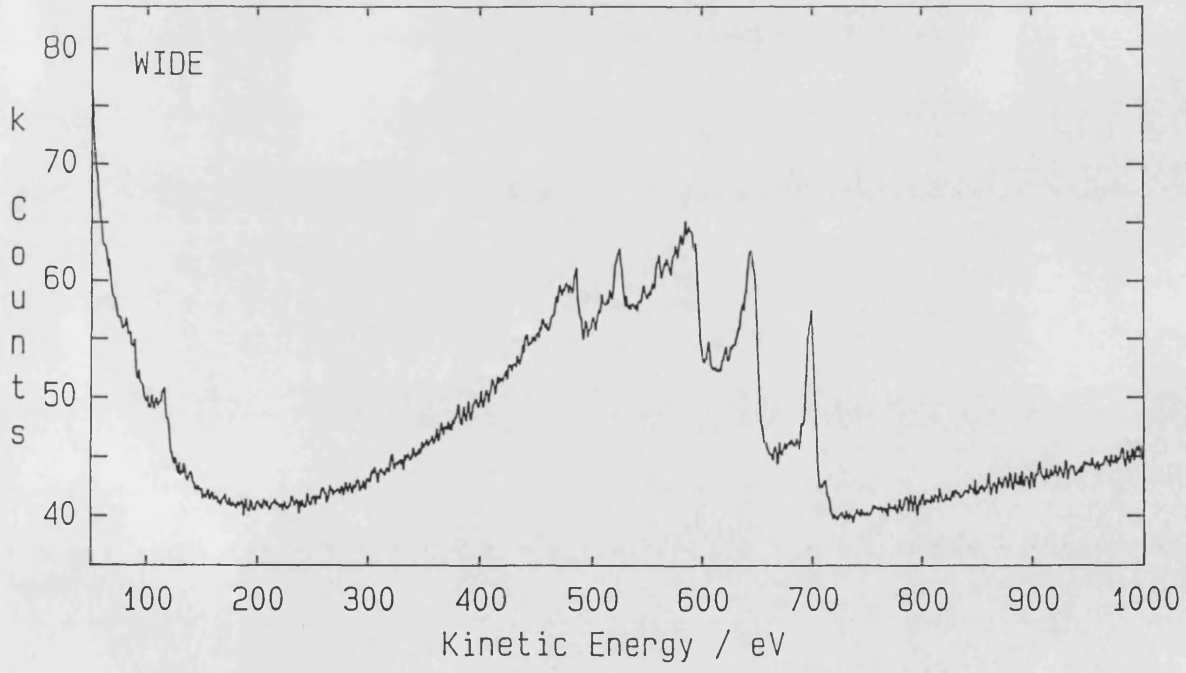

Figure 3.15 Typical direct, N(E), Auger electron spectrum

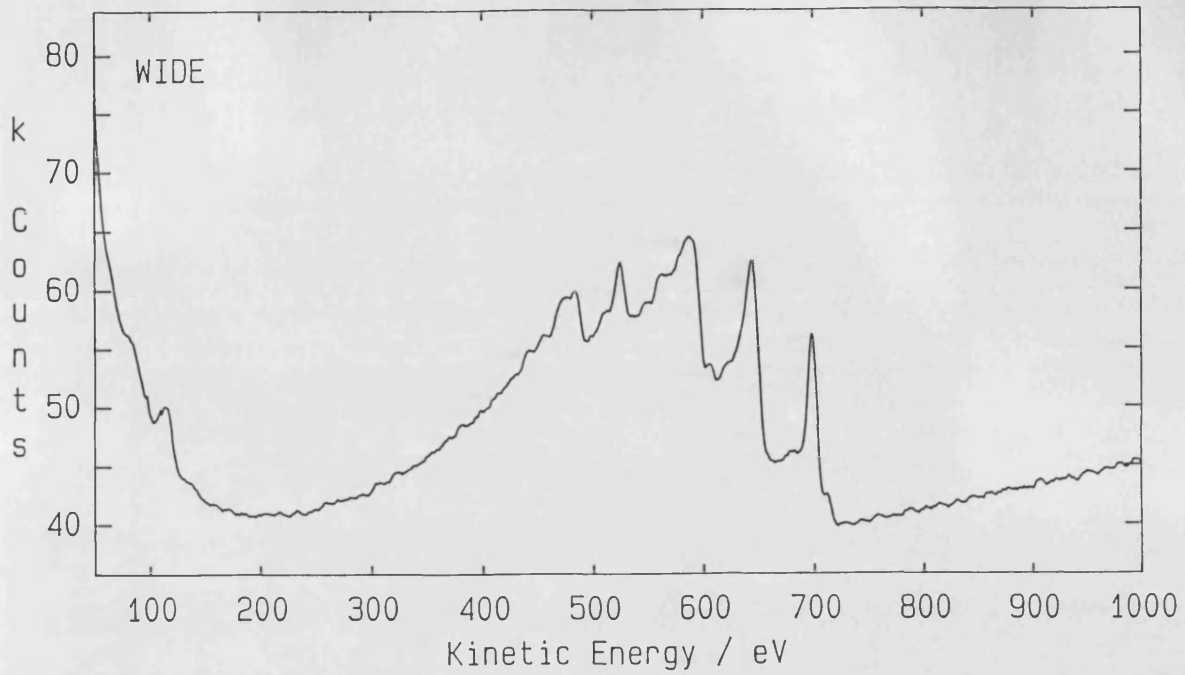

Figure 3.16 Spectrum shown in figure 3.15 after smoothing

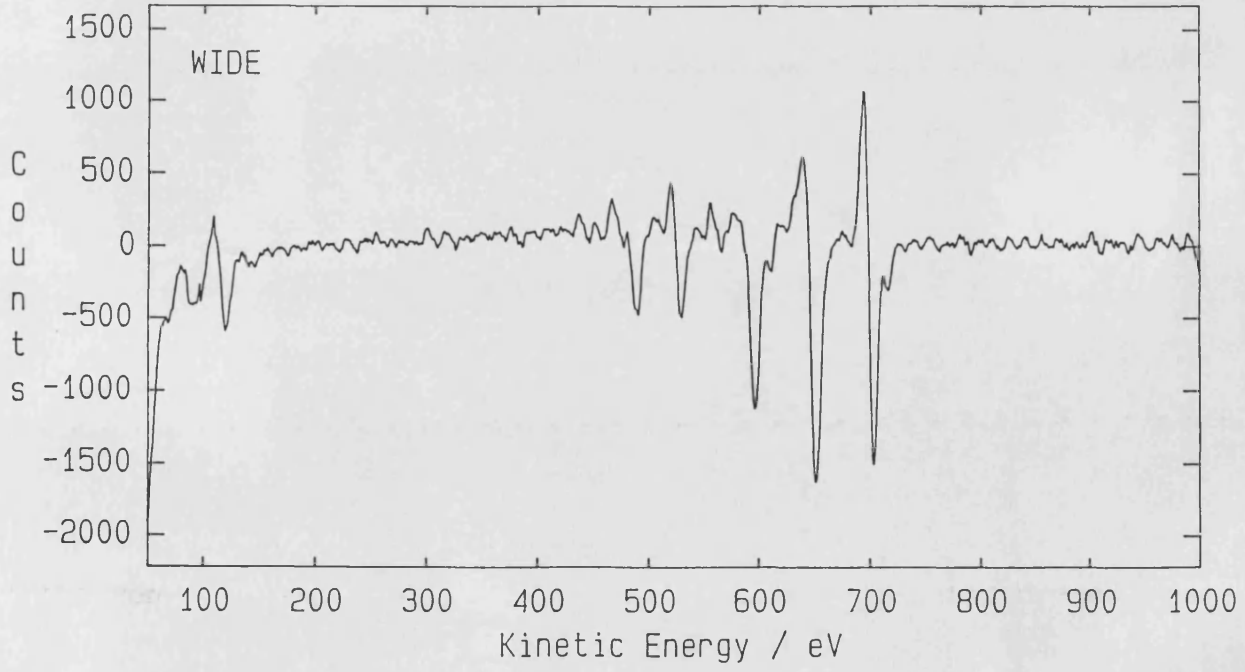

Figure 3.17 Spectrum shown in figure 3.16 after differentiation, dN(E)

Chapter 4 Experimental Results

4.1 Microstructure

4.1.1 Optical Examination

Micrographs taken from polished and etched samples of Alloys S560 to S25 in the quenched and tempered condition are shown in figures 4.1 to 4.4 respectively. The prior austenite grain structure can be clearly delineated in each figure. Within the prior austenite grains is a network of finer structure consisting of ferritic laths. Precipitates can be seen on the prior austenite grain boundaries, the lath boundaries and the ferritic laths.

The grain size of the alloys, as determined by the linear intercept method was found to be between 80μm and 100μm. The addition of phosphorus was found to have no significant effect on the microstructure of the alloys.

4.1.2 Scanning Electron Microscope Examination

A characteristic of the 9% chromium ferritic steel examined in this study is that it undergoes a ductile to brittle transition as the temperature is reduced. This transition can be observed by a change in the morphology of the fracture surface. In the unaged condition the fracture mode, at low temperatures, is transgranular cleavage, an example of which is shown in figure 4.5. As the temperature at which the sample is broken increases, the fracture mode changes to the ductile mechanism of microvoid coalescence, which absorbs a much greater amount of energy. Upon thermal ageing of this alloy the transition temperature between brittle and ductile fracture behaviour increases. Thermal ageing also affects the low temperature fracture mode, bringing about a change from transgranular cleavage to intergranular fracture. An example of the latter fracture mode is shown in figure 4.6. The high-

temperature ductile fracture mode is unaffected by thermal ageing and remains characterised by microvoid coalescence. The proportion of the low temperature fracture surface showing intergranular fracture in each of the aged alloys was measured in the SEM to be 75%, 62%, 76% and 17% for alloys S560-S25, respectively.

4.1.3 Examination of Carbon Extraction Replicas

Carbon extraction replicas from samples of alloy S560 and S300 were examined in the Philips EM430 at an accelerating voltage of 100keV. An electron micrograph of a typical area of the extraction replica of alloy S560 is shown in figure 4.7. The extracted precipitates can be seen to delineate both the prior austenite grain structure and the lath structure of the material; there are also precipitates which had formed intragranularly. The carbon extraction replicas of alloy S560 and S300 showed similar characteristics.

An EDX spectrum collected from a precipitate on a carbon extraction replica is shown in figure 4.8. It contains the following characteristic x-ray peaks in ascending order of energy - silicon, chlorine, chromium, iron and copper. The copper signal arises from the bars of the copper grid upon which the extraction replica is supported and the chlorine signal from residue of the perchloric acid used in the preparation process. Quantitative analysis of the spectrum shown in figure 4.8 using Link systems RTS2 software, after removal of the signals from copper and chlorine, gives a composition for the precipitate of 96% chromium, 3.5% iron and 0.5% silicon (figures in weight percent). This analysis does not take into account the carbon which is present in the precipitate, because the low energy carbon x-rays are absorbed in both the sample and the beryllium window.

A convergent beam electron diffraction pattern from one of the precipitates is shown in figure 4.9, obtained with the beam aligned parallel to the $<11\bar{1}>$ zone axis. Determination of the interplanar spacing indicates that the precipitate is of the $M_{23}C_6$ type and possesses a cubic structure with a_o = 10.6Å.

4.1.4 Examination of Transmission Electron Microscope Samples

Samples from all of the alloys were examined in the Philips EM430 at 100keV accelerating voltage, prior to STEM analysis. Typical electron micrographs of alloy S560 are shown in figures 4.10 and 4.11. The other alloys all showed similar features to those exhibited by alloy S560, but are not illustrated. Figure 4.10 shows a general, low magnification image of a TEM foil containing a central hole surrounded by electron transparent areas. In this electron micrograph it is possible to trace the prior austenite grain network, within which lath boundaries are present. As the magnification of the image is increased, figure 4.11, the lath boundaries and the inter and intragranular precipitates become more readily visible. An EDX spectrum collected with the electron beam focused on an area of matrix which was free of visible precipitation is shown in figure 4.12. Analysis of the spectrum shown in figure 4.12 using Link systems RTS2 quantification routines gives a composition for the matrix of 8.7% ($\pm$0.2) chromium, 1% ($\pm$0.15) silicon, 90.3% ($\pm$0.9) iron (composition in weight percent) and no phosphorus. These figures are comparable with the specified bulk chemistry of the alloys. given in table 3.1. Similar analyses of spectra obtained with the electron beam focused on a selection of precipitates in a foil gave compositions in the range 65-80% chromium, negligible silicon and phosphorus and 20-35% iron. This is in comparison to the measured composition of a precipitate on an extraction replica of 96% chromium, 3.5% iron and 0.5% silicon. The difference in iron and chromium values arise because x-rays are detected from both the precipitate and the matrix surrounding it. The matrix signal

distorts the measured composition of the precipitate and amply illustrates the advantages of using carbon extraction replication techniques for determining the chemical composition of precipitates in isolation from the matrix.

4.2 Probe Size Measurements in the STEM

The probe size in VG HB501 STEM was measured using the method described in section 3.3.6. A typical well-oriented magnesium oxide crystal is shown in figure 4.13 and its diffraction pattern is shown in figure 4.14. The diffraction pattern shows that the crystal is in the symmetric orientation, so that a (100) facet is parallel to the optic axis. The variation in the intensity, measured in the dark field channel, as the electron beam was scanned across the edge of this accurately oriented crystal was recorded as a function of the strength of the first condenser lens. A pair of intensity profiles are shown in figures 4.15 and 4.16; both of these were collected at a magnification of 5 million. The probe size is defined as the distance over which the intensity rises from 10% to 90% of its final value. The strength of the first condenser lens controls the convergence angle of the electron probe in the STEM. The strength of the second condenser lens was varied in conjunction with the first condenser lens to maintain a crossover in the plane of the selected area diffraction aperture. The convergence angle for each combination of condenser lens settings was measured from convergent-beam electron diffractions patterns obtained from the MgO crystals. The probe sizes determined from this method have been plotted as a function of probe convergence angle, α, in figure 4.17. Also drawn on the graph are the theoretical limits on probe size as determined by spherical aberration, beam brightness and diffraction conditions for the HB501. The solid line on the graph has been constructed by adding these parameters in quadrature. As can be seen the experimentally determined probe sizes agree well with the theoretical predictions both in behaviour as a function of convergence angle

and minimum probe size. The HB501 was operated with a convergence angle of ~10mrad in order to achieve a probe size of ~2nm containing 80% of the electron current.

4.3 Electron Energy Loss Spectroscopy and Measurement of Specimen Thickness

A typical EELS spectrum is shown in figure 4.18. It can, for purposes of description, be divided into three regions. First the zero loss peak, which consists of electrons which have not lost little or no energy during their passage through the foil. Included in this peak are electrons which have lost very small amounts of energy due to phonon scattering ($\sim^1/_{40}$ eV). Second, an energy-loss range which contains electrons which have excited plasmons within the sample. This region contains regularly spaced peaks, corresponding to those electrons which have excited one, two or more plasmons on their passage through the foil. Third, an energy-loss range which contains those electrons which have lost energy due to the process of ionising an atom in the sample. These electrons give rise to characteristic edges in the spectrum which can be used to determine the elemental composition of the sample. The amount of energy lost by an electron when it ionises an atom is dependant upon the energy level from which electrons have been removed and is therefore element specific, as described in section 3.3.1.

The method of determining the sample thickness involves the measurement of the number of counts in the low loss region of the spectrum (Joy et al 1979, Leapman et al 1984). The area under the zero-loss peak is given by:

$$I_o = I_t \exp (t/\lambda) \qquad 4.1$$

I_o = the number of electrons in the zero loss peak

I_t = the total number of electrons recorded in the spectrum (Energy ≤250 eV)

t = sample thickness

λ = mean free path for plasmon excitation

This can be rearranged to give:

$$\log_e I_t / I_o = t/\lambda \qquad 4.2$$

The linear relation between t and $\log_e I_t / I_o$ has been shown to be valid to ±10% in the thickness range $0.2 < t/\lambda < 5$ (Hosoi et al 1981, Leapman et al 1984a). Relative thicknesses in the same material can be quoted as the ratio of t/λ. However, for quantitative work the value of λ needs to be determined. This is most easily calculated using an empirical formula suggested by Malis et al (1988), which allows values of λ in a range of materials to be predicted with an accuracy of approximately ±10%.

$$\lambda = \frac{106\, F\, (E_o / E_m)}{\ln (2\beta\, E_o / E_m)} \qquad 4.3$$

where

$$F = \frac{(1 + (E_o/1022))}{(1+(E_o/511))^2} \qquad 4.4$$

and

$$E_m = 7.6\ Z^{0.36} \qquad 4.5$$

λ = inelastic mean free path
E_o = accelerating voltage keV
β = collection angle of spectrometer (mRad)
= 9mRad for 2mm spectrometer entrance aperture on VG HB501

For the 9% chromium used in this study the average atomic number is 25.8.

Therefore $E_m = 24.5$

and $F = 0.77$

giving $\lambda = 77.5nm$

4.4 Interfacial Chemistry

4.4.1 Measurement of Interfacial Chemistry using Scanning Transmission Electron Microscopy

A bright field electron micrograph of a prior austenite grain boundary in alloy S560 which is suitable for chemical analysis at high spatial resolution is shown in figure 4.19. The projected width of the boundary is <2nm, and the thickness of the foil was measured as ~50 nm using the EELS log ratio technique. The chemical composition profile in the vicinity of this boundary was measured by collecting x-ray spectra at points along a line perpendicular to the grain boundary. Spectra were collected on the grain boundary and at distances of 1, 2, 3, 5 and 10nm from the grain boundary into each grain. The chemical composition profiles produced by plotting the data from these spectra is shown in figure 4.20. This shows clearly that there is an increase in the concentration of phosphorus and chromium and a consequent decrease in the concentration of iron at the grain boundary. No change in the level of silicon was detected at this boundary or at any of the other interfaces examined. The full width at half maximum (FWHM) of both the phosphorus and chromium profiles are ~3-3.5 nm. This is comparable to the size of the electron beam, ~2.5nm, as measured using magnesium oxide crystals, allowing for some beam broadening as the probe travels through the sample. X-ray spectra taken with the probe centred on the grain boundary and with the probe placed in the matrix a few nanometres from the boundary are shown in figure 4.21a and b. The phosphorus peak, at an energy of 2.02 KeV, is visible in the grain boundary

spectrum and absent from the matrix spectrum. The increase in the chromium signal from the grain boundary can be seen when the two spectra are compared. The observation that the full width at half maximum of the electron beam and the measured chemical composition profile are comparable is consistent with the segregant being present as a monolayer at the grain boundary or in a thin region very close to the boundary. If the segregant were to be significantly more widely dispersed, the FWHM of the experimental profiles would be expected to exceed the FWHM of the electron probe.

The results using non-standard conditions to collect spectra and obtain profiles, as detailed in section 3.4.2, are shown in figures 4.23 to 4.26. The experiments included varying the focus, varying the size of the virtual objective aperture (VOA) which defines the beam diameter, tilting the grain boundary away from the vertical condition and altering the strength of the first condenser lens so as to remove the cross-over in the plane of the (SADA). The effect of collecting grain boundary spectra with varying amounts of over and under focus is shown in figure 4.22. The magnitude of the x-ray signal detected from the segregated phosphorus decreases as the probe becomes less focused. The magnitude of the change in segregant detection with varying focus is important in assessing the consequences of instabilities in the objective lens current during spectrum acquisition which affect the focus of the probe.

Altering the size of the beam defining aperture, the VOA for x-ray analysis, affects the beam diameter (probe size) and also the current which the probe contains. Decreasing the size of the VOA reduces the probe diameter and current, similarly increasing the size of the VOA enlarges the probe diameter and the current it contains. As can be seen in figure 4.23, reducing the size of the probe increases the magnitude of the signal detected from the segregated phosphorus layer, due to the smaller probe sampling less of the surrounding matrix. However the reduced current contained within the probe results in the statistical accuracy of the segregant

peak being degraded, as evidenced by an increase in the magnitude of the error bars which indicate ± one standard deviation for the phosphorus signal as calculated by the quantitative software routines. This increased uncertainty is a consequence of the statistical variation in a characteristic x-ray peak being proportional to the square root of number of counts it contains. As the probe size is increased the reverse occurs and the magnitude of the signal detected from the segregant decreases as more matrix is sampled by the larger probe and the statistics of quantification improve.

The ferritic samples were mounted within the HB501 using a specially strengthened specimen holder to withstand the forces acting on such samples due to immersion within the field of the objective lens. This holder has a single axis of tilt. The method employed to obtain chemical composition profiles from a boundary at different tilt angles was to select a boundary the orientation of which, with respect to the incoming electron beam, varied along its length. This method was chosen in preference to tilting a well-oriented boundary away from the ideal condition due to the restraints imposed by the single tilt axis and the extra astigmatism introduced into the image by tilting the foil. This allowed profiles to be acquired at varying boundary tilts relative to the incoming electron beam. The experimental chemical composition profiles were obtained from a grain boundary in a 77nm thick foil of alloy 1 at three different tilts. These were nominally parallel to the electron beam and at angles of 2.5° and 4° to the vertical position. The tilt of the boundary was determined trigonometrically from the projected width of the boundary, measured in the bright field image, and the thickness of the foil, as measured using EELS. The profiles obtained using these acquisition parameters are shown in figure 4.24a, b and c. These profiles show that the maximum detected segregant signal decreases and the profiles become increasingly asymmetric as the degree of boundary mis-alignment increases.

It was found that the images obtained in the STEM from some of the samples examined in this study were too astigmatic to allow correction, even with the foil horizontal in the microscope. The excessive astigmatism was caused either because the trepanned disc from which the sample was prepared was too thick or because the hole produced during thinning was off centre. In such cases it was found that decreasing the strength of the first condenser lens and focusing the image by reducing the strength of the objective lens allowed the correction of greater amounts of astigmatism. The effect of this change in lens configuration, on the electron paths is shown in figure 4.25. The cross-over in the plane of the selected area diffraction aperture (SADA) is no longer present under these conditions. A chemical composition profile collected from a well oriented grain boundary under these electron optical conditions is shown in figure 4.26. As can be seen the width of the profile, as defined by the FWHM, has not been significantly degraded compared to the composition profiles collected using the standard conditions. This indicates that the electron probe is of a similar size in both electron optical conditions.

Shown in figures 4.27-4.29 are chemical composition profiles taken traversing lath boundaries in alloys S560, S300 and S120 respectively. As can be seen only alloy S560, doped to the highest level of 560 ppm phosphorus, exhibited detectable segregation to lath boundaries. The magnitude of the detected phosphorus and chromium enrichment with the electron probe centred on the lath boundary is comparable to that detected on grain boundaries in this alloy. Alloys S300, S120 and S25 showed no significant enrichment of phosphorus or chromium at lath boundaries.

The variation of chemical composition across matrix/precipitate interfaces in alloys S560, S300 and S120 is shown in figure 4.30 to 4.32. In each case the level of phosphorus segregation detected at the interface is similar to that found on boundaries free of precipitation. It is more difficult to determine whether chromium

enrichment occurs at the precipitate/matrix interface due to the high levels of chromium present in the precipitate. In certain types of stainless steel the presence of chromium rich precipitates, such as those found in this study, has been shown to be associated with depletion of chromium from the grain boundary and a narrow region of the adjacent matrix (Pande et al 1977). This chromium depletion increases the material's susceptibility to intergranular corrosion. To investigate whether the level of chromium segregation decreased close to precipitates in this material, the chemical composition profile of a grain boundary in alloy S560 was measured 15 nm from a precipitate. The profile obtained is shown in figure 4.33 and shows that there is no apparent decrease in the level of either chromium or phosphorus segregation at this proximity to a precipitate in comparison with portions of grain boundaries remote from precipitation.

In certain instances, especially when examining alloy S25, the lowest phosphorus containing cast, where long x-ray spectrum acquisition times had to be used to collect x-ray spectra containing statistically significant phosphorus peaks, full profiles of chemical composition were not acquired. In such cases an x-ray spectrum was acquired from the well aligned grain boundary and one spectrum from the matrix on either side of the boundary. This procedure reduces the overall time required to characterise an interface. The data from these reduced profiles are subsequently quantified assuming a probe diameter similar to that determined from direct probe size measurements using MgO, and previous grain boundary composition profiles. As with the collection of full profiles the thickness of the foil adjacent to the grain boundary was measured by analysing EELS spectra collected from the grains on each side of the boundary. The matrix composition was measured on both sides of the boundary to confirm the absence of coherent Bremsstrahlung peaks (Spence et al 1983) which might otherwise contribute to, or be confused with the phosphorus characteristic peak.

The stability of the segregated phosphorus under electron irradiation was investigated by collecting 13 x-ray spectra, each of 50 live-seconds duration, from the same portion of a well oriented grain boundary in alloy S300. The variation in phosphorus signal as a function of boundary exposure time is plotted in figure 4.34. As can be seen there is no systematic variation in the phosphorus signal with exposure time, confirming that the phosphorus was not affected by exposure to the focused electron beam in the STEM.

The number of x-ray counts contained within the characteristic peaks of iron, chromium, silicon and phosphorus for all of the x-ray spectra collected for each alloy are summarised in table 4.1. Also tabulated is the local thickness of the foil and the composition as determined by the quantitative software routines, given as both atomic and weight percentages, with associated uncertainties.

4.4.2 Measurement of Interfacial Chemistry by Auger Electron Spectroscopy

Following fracture at low temperature in the Auger electron microprobe to expose the grain boundaries of interest, Auger spectra were collected from intergranular facets in each of the alloys. Spectra were also periodically collected from the regions of transgranular cleavage which were present in each of the samples. The purpose of analysing the transgranular areas was to monitor any increase in surface contamination by carbon and oxygen, and to confirm that movement of phosphorus from intergranular facets during examination was not occurring.

Using the initial acquisition parameters listed in section 3.6.2 (10nA beam current) successive Auger spectra were collected from the same facet over a period of an hour. The phosphorus to iron peak height ratios for these spectra are given in table 4.2 and are plotted as a function of time in figure 4.35. In the absence of

contamination build-up, which would have a tendency to mask the signal emitted by the segregant, the phosphorus to iron ratio should remain constant. In this experiment the ratio of phosphorus to iron in the derivative spectrum decreased from an initial level of 0.65 down to 0.5. To confirm that the phosphorus was being moved due to the action of the electron beam the experiment described in section 3.6.1 was conducted on a previously unexamined region of the sample. The phosphorus to iron peak height ratios for these spectra are also given in table 4.3. The initial level of phosphorus detected on the area of transgranular cleavage was negligible and it remained so after examination of the adjacent intergranular facet using a beam current of 5 nA. However, after the examination of the same intergranular facet using a reduced beam current of 10nA a significant level of phosphorus was detected on the region of transgranular cleavage. This confirms that the phosphorus is moved by the higher beam current of 10 nA and is redeposited on to adjacent areas. For this reason all subsequent spectra were collected using a beam current of 5 nA and the data previously collected using a primary beam current of 10nA were not included in subsequent quantification.

After collection of the Auger electron spectra in the direct mode they were smoothed and numerically differentiated. The peak-to-peak height ratio (PPHR) of phosphorus to iron in the differentiated spectrum varies depending on the number of points over which the smoothing routine extends. This is shown graphically in figure 4.36. As the number of smoothing points is increased above three (the minimum value permitted by the software routine) the PPHR increases due to a decrease in the amount of noise present in the smoothed spectrum. As the number of points is increased further the ratio of phosphorus to iron falls as the phosphorus peak is smoothed out until a point is reached when the peak is no longer detectable. The number of smoothing points standardised on for all spectra in this study was 11.

A comparison of Auger electron spectra taken from an intergranular facet and a region of transgranular cleavage is shown in figure 4.37a and b for the direct spectrum and figure 4.38a and b for the differential spectrum. These spectra were collected from a sample of alloy S560. The Auger peaks present in the direct spectrum are identified as follows; phosphorus (115eV), carbon (263eV), chromium (486, 525 and 568eV) and iron (589, 645 and 700eV). The carbon peak arises partially from grain boundary carbides and partially from a small amount of carbon contamination present on the surface of the sample. It is the contribution from this latter source that requires monitoring during the examination of samples. If the level of carbon contamination increases, due to the adsorption of residual gases from the vacuum, it will tend to mask the Auger signals received from the matrix and the segregant. In the derivative spectra the differentiation process has replaced the sloping background present in the direct spectrum with a horizontal one on which sharp doublet peaks now sit. Conventionally the energy of a differentiated peak is quoted as the energy of the negative lobe. The peaks present can thus be identified as phosphorus (120eV), carbon (272eV), chromium (489, 529 and 571eV) and iron (598, 651 and 703eV). The presence of the phosphorus peak and enhanced chromium signal on the intergranular facet is clearly discernible in both the direct and derivative spectra. The changes are most obvious in the derivative spectra.

The ratios quoted in this study are from peak-to-peak height ratios measured in the derivative spectrum. The peaks used were the phosphorus 120eV and chromium 529eV both of which are ratiod to the iron 703eV peak. To obtain the peak height ratios the magnitude of the peak of interest is divided by the magnitude of the iron peak. In this case the magnitude of the differentiated peak is defined as the height between the bottom of the negative portion to the top of the positive portion.

The peak height ratios of the spectra recorded during the depth profile experiment conducted on alloy S560 are given in table 4.4, and plotted against

monolayers removed in figure 4.39. It can be seen that the phosphorus signal detected falls sharply as the outer layers of the sample are removed. This confirms the supposition that the phosphorus is concentrated very close to the grain boundary rather than dispersed over a significant number of atom layers. The concentration of chromium falls in a similar manner to the phosphorus. However it does not fall to the matrix value as determined from analysis of the transgranular facets. This indicates that chromium is present as a segregant with a similar spatial distribution as the phosphorus segregant. The value of chromium signal decreases as the segregated layer is removed and the remaining enhanced level of chromium is due to the presence on the grain boundary of chromium-rich precipitates. The presence of these chromium-rich precipitates complicates the quantification of the amount of segregated chromium present. The knowledge that chromium rich precipitates are present on the intergranular facets can lead to the assumption, in the absence of depth profile data, that the enhanced chromium signal is due solely to precipitation and not to segregation of chromium.

It has been noted in previous work (Vatter and Hippsley 1991a) that the low energy portion of Auger electron spectra collected on the MA500 can be adversely affected by the magnetic field produced by ferritic samples. This is largely counteracted by the incorporation of a lens at the entrance aperture of the spectrometer. The strength of this lens is varied in order to optimise the Auger current collected at a low energy, typically 10eV. To further correct for any variation in the Auger collection efficiency at low energy, the signal intensity of the background at an energy just above the phosphorus and iron peaks was measured. The ratio of the phosphorus background to the iron background are reported in the same tables as the peak height ratios for each alloy. These background ratios are centred on unity. However some samples show a greater variation than others. Correction for these variations has been performed by normalising each phosphorus to iron peak height ratio with its respective background ratio.

The influence on measured peak-height-ratios of the angle of inclination of a facet to the spectrometer was investigated by altering the tilt of the specimen during the collection of a series of spectra from a single facet. The variation of the phosphorus to iron peak to peak height ratio with specimen orientation is shown in figure 4.40. As can be seen the phosphorus to iron ratio falls as the angle between the sample normal and the spectrometer is decreased. This variation in peak-height-ratio is subsequently used to estimate the contribution of tilt angle to the spread of the experimental data.

The differential peak heights of phosphorus, chromium and iron and background intensities measured above the phosphorus and iron peaks for all of the facets investigated are given in table 4.5. All of these results were derived from data recorded using a beam current of 5nA; those taken with higher beam currents (10nA) were discarded due to the problems encountered with the mobility of phosphorus reported earlier.

Alloy S560 Data																
		Fe		Cr		Si		P		Wt%						
Thick	Pos	Cnts	Error	Cnts	Error	Cnts	Error	Cnts	Error	Fe	Error	Cr	Error	Si	Error	P	Error
48	0	47977	409	8709	180	627	77	1271	94	82.8	0.7	14.1	0.3	1.0	0.1	2.1	0.2
48	-2.5	46646	402	5845	151	464	69	348	73	88.2	0.8	10.3	0.3	0.8	0.1	0.6	0.1
48	-5	43983	390	4745	137	573	69	3	64	89.8	0.8	9.1	0.3	1.1	0.1	0.0	0.2
48	-10	44584	394	4682	138	539	69	-10	63	90.1	0.8	8.9	0.3	1.0	0.1	0.0	0.1
48	-20	40729	375	4306	132	459	65	-56	59	90.2	0.8	8.9	0.3	1.0	0.1	-0.1	0.1
48	-50	38650	366	4409	132	544	64	15	60	89.3	0.8	9.5	0.3	1.2	0.1	0.0	0.1
48	2.5	40129	374	8012	170	495	70	466	75	82.7	0.8	15.4	0.3	1.0	0.1	0.9	0.1
48	5	34935	349	12020	203	375	66	258	68	74.7	0.7	24.0	0.4	0.8	0.1	0.5	0.1
48	10	32148	337	12341	206	385	64	149	66	72.8	0.8	26.1	0.4	0.8	0.1	0.3	0.1
48	15	29364	322	13075	210	275	61	116	66	70.0	0.8	29.1	0.5	0.6	0.1	0.3	0.1
48	20	32465	335	8716	174	351	62	62	61	79.2	0.8	19.9	0.4	0.8	0.1	0.1	0.1
48	25	32891	337	8476	172	295	61	170	61	79.7	0.8	19.2	0.4	0.7	0.1	0.4	0.1
48	30	34529	344	6143	150	369	62	84	60	84.8	0.8	14.1	0.3	0.9	0.1	0.2	0.1
48	40	35829	352	4424	129	398	62	85	60	88.6	0.9	10.2	0.3	0.9	0.1	0.2	0.1
48	50	35291	348	3956	125	355	61	-43	58	89.8	0.9	9.4	0.3	0.9	0.1	-0.1	0.1
48	60	35924	350	3877	123	396	60	-79	57	90.1	0.9	9.1	0.3	1.0	0.1	-0.2	0.1
48	100	33449	337	3605	118	332	59	-6	57	90.1	0.9	9.1	0.3	0.9	0.2	0.0	0.2
48	PPT	6854	163	29867	304	56	49	127	54	19.8	0.5	79.7	0.8	0.2	0.1	0.3	0.1
48	0	29553	317	5130	139	315	56	639	68	83.8	0.9	13.6	0.4	0.9	0.2	1.7	0.2
48	10	17405	243	1782	84	177	41	-25	38	90.6	1.3	8.7	0.4	0.9	0.2	-0.1	0.2
48	15	15910	232	1689	82	188	40	-21	37	90.1	1.3	9.0	0.4	1.0	0.2	-0.1	0.2
48	20	14641	224	1647	80	150	39	-17	37	89.8	1.4	9.5	0.5	0.9	0.2	-0.1	0.2
48	0	14506	225	2481	96	130	41	314	51	84.1	1.3	13.5	0.5	0.7	0.2	1.7	0.3
48	5	16226	235	1897	86	151	42	51	41	89.2	1.3	9.8	0.4	0.8	0.2	0.3	0.2
48	10	14556	226	1543	80	98	38	-15	37	90.5	1.4	9.0	0.5	0.6	0.2	-0.1	0.2
48	15	13411	216	1295	75	137	39	5	36	90.9	1.5	8.2	0.5	0.9	0.3	0.0	0.2
48	20	13940	218	1495	77	158	39	14	37	89.9	1.4	9.0	0.5	1.0	0.2	0.1	0.2

Table 4.1 X-Ray Data

		Fe		Cr		Si		P		Wt %							
Thick	Pos	Cnts	Error	Cnts	Error	Cnts	Error	Cnts	Error	Fe	Error	Cr	Error	Si	Error	P	Error
41	0	24961	295	4949	135	398	55	923	73	80.8	1.0	15.0	0.4	1.3	0.2	2.9	0.2
41	-2.5	32417	331	3949	122	348	58	139	60	88.6	0.9	10.1	0.3	1.0	0.2	0.4	0.2
41	-5	30911	326	3449	118	513	59	64	56	89.0	0.9	9.3	0.3	1.5	0.2	0.2	0.2
41	-10	19235	257	2084	91	385	47	-6	42	89.2	1.2	9.0	0.4	1.8	0.2	0.0	0.2
41	-20	37616	361	4022	128	606	64	-31	59	89.6	0.9	9.0	0.3	1.5	0.2	-0.1	0.1
41	-50	37900	359	4146	128	543	63	-44	56	89.6	0.8	9.2	0.3	1.3	0.2	-0.1	0.1
41	2.5	35680	351	5348	140	406	63	490	73	85.8	0.8	12.0	0.3	1.0	0.2	1.2	0.2
41	5	33909	342	4063	127	512	60	135	61	88.4	0.9	9.9	0.3	1.4	0.2	0.4	0.2
41	10	33395	337	3643	122	355	57	-27	57	89.9	0.9	9.2	0.3	1.0	0.2	-0.1	0.1
41	20	30605	325	3258	117	362	55	-3	54	90.0	1.0	9.0	0.3	1.1	0.2	0.0	0.2
41	50	28084	310	3168	111	388	52	30	51	89.2	1.0	9.4	0.3	1.3	0.2	0.1	0.2
41	0	16475	243	17674	238	211	51	509	65	49.2	0.7	48.8	0.7	0.6	0.1	1.5	0.2
41	-2.5	25000	296	12345	203	354	56	280	61	67.4	0.8	30.9	0.5	1.0	0.2	0.7	0.2
41	-5	28132	311	6607	152	432	53	167	55	80.6	0.9	17.7	0.4	1.3	0.2	0.5	0.2
41	-10	29001	315	4386	130	398	53	39	52	86.5	0.9	12.2	0.4	1.2	0.2	0.1	0.1
41	-20	27761	306	3181	112	357	49	-5	48	89.3	1.0	9.6	0.3	1.2	0.2	0.0	0.2
41	-50	27180	303	3002	107	323	49	-14	49	89.7	1.0	9.3	0.3	1.1	0.2	0.0	0.1
41	2.5	9297	186	20671	255	98	45	193	55	32.5	0.7	66.5	0.8	0.3	0.2	0.7	0.2
41	5	7300	167	23459	272	100	43	213	53	25.1	0.6	73.9	0.9	0.3	0.1	0.7	0.2
41	10	7831	173	28338	296	42	45	8	54	23.1	0.5	76.7	0.8	0.1	0.1	0.0	0.1
41	20	8767	186	30577	307	49	47	86	52	23.7	0.5	75.9	0.8	0.1	0.1	0.2	0.1
41	50	7090	167	32529	316	54	46	12	50	19.2	0.5	80.6	0.8	0.1	0.1	0.0	0.1
85	0	45284	393	6514	156	476	61	585	72	86.1	0.7	11.6	0.3	1.1	0.1	1.2	0.2
101	0	72693	499	9547	189	566	75	618	84	87.6	0.6	10.8	0.2	0.9	0.1	0.9	0.1
148	0	113532	623	17281	252	897	89	1624	111	85.4	0.5	12.1	0.2	1.0	0.1	1.5	0.1
171	0	124010	652	15743	245	924	89	900	101	87.7	0.5	10.4	0.2	1.0	0.1	0.9	0.1

Table 4.1 X-Ray Data

		Fe		Cr		Si		P		Wt %							
Thick	Pos	Cnts	Error	Cnts	Error	Cnts	Error	Cnts	Error	Fe	Error	Cr	Error	Si	Error	P	Error
49	0	23519	282	3530	115	244	50	501	59	85.3	1.0	12.0	0.4	0.9	0.2	1.8	0.2
49	-2.5	24904	292	3073	108	249	49	191	51	88.2	1.0	10.2	0.4	0.9	0.2	0.7	0.2
49	-5	26627	299	2776	104	343	50	109	48	89.7	1.0	8.8	0.3	1.2	0.2	0.4	0.2
49	-10	26278	298	2726	103	348	50	2	44	90.0	1.0	8.7	0.3	1.3	0.2	0.0	0.2
49	2.5	25465	293	3754	118	312	52	442	60	85.6	1.0	11.8	0.4	1.1	0.2	1.5	0.2
49	5	25221	293	2944	108	289	49	169	51	88.7	1.0	9.7	0.4	1.1	0.2	0.6	0.2
49	10	25038	291	2619	102	286	48	156	48	89.6	1.0	8.8	0.3	1.1	0.2	0.6	0.2
49	0	28038	309	3447	114	305	53	402	61	87.7	1.0	10.1	0.3	1.0	0.2	1.3	0.2
49	RIGHT	14401	221	1320	74	151	36	58	36	90.8	1.4	7.8	0.4	1.0	0.2	0.4	0.2
49	LEFT	10913	192	1063	66	102	32	35	29	90.6	1.6	8.3	0.5	0.9	0.3	0.3	0.2
50	0	19386	257	3526	112	257	45	464	55	82.8	1.1	14.1	0.4	1.1	0.2	2.0	0.2
50	LEFT	11247	194	1108	67	108	30	-6	30	90.8	1.6	8.4	0.5	0.9	0.3	-0.1	0.3
50	RIGHT	8024	165	906	61	104	28	-2	23	89.4	1.8	9.5	0.6	1.2	0.3	0.0	0.3
60	0	21709	272	4082	121	175	46	699	64	82.2	1.0	14.4	0.4	0.7	0.2	2.7	0.2
60	-10	23753	285	2492	98	256	47	2	45	90.1	1.1	8.9	0.3	1.1	0.2	0.0	0.2
60	10	20459	264	2080	93	243	42	9	42	90.2	1.2	8.6	0.4	1.2	0.2	0.0	0.2
66	0	20602	268	4246	127	329	56	662	69	80.7	1.0	15.5	0.5	1.3	0.2	2.5	0.3
66	-2.5	35212	356	4585	140	551	70	412	74	87.0	0.9	10.6	0.3	1.4	0.2	1.0	0.2
66	-5	33243	345	3659	129	445	68	171	66	89.2	0.9	9.2	0.3	1.2	0.2	0.5	0.2
66	-7.5	35514	356	3917	130	477	70	-34	67	89.6	0.9	9.3	0.3	1.2	0.2	-0.1	0.2
66	-10	33865	347	3747	129	433	68	5	66	89.6	0.9	9.3	0.3	1.2	0.2	0.0	0.1
66	-20	33035	344	3480	125	461	68	111	63	89.6	0.9	8.8	0.3	1.3	0.2	0.3	0.2
66	2.5	26022	304	3809	126	417	64	375	69	85.7	1.0	11.7	0.4	1.4	0.2	1.2	0.2
66	5	26042	304	3034	114	383	61	51	59	88.8	1.0	9.7	0.4	1.3	0.2	0.2	0.2
66	7.5	26102	306	2760	112	436	60	43	56	89.5	1.0	8.9	0.4	1.5	0.2	0.2	0.2
66	10	24985	300	2709	109	357	58	-9	54	89.7	1.1	9.1	0.4	1.3	0.2	0.0	0.2

Table 4.1 X-Ray Data

		Fe		Cr		Si		P		Wt %							
Thick	Pos	Cnts	Error	Cnts	Error	Cnts	Error	Cnts	Error	Fe	Error	Cr	Error	Si	Error	P	Error
66	20	23643	288	2443	105	362	56	-70	52	90.2	1.1	8.7	0.4	1.4	0.2	-0.3	0.2
45	0	23756	287	3694	118	389	58	357	65	85.1	1.0	12.4	0.4	1.3	0.2	1.2	0.2
45	-2.5	24232	290	3670	120	413	257	460	67	85.0	1.0	12.0	0.4	1.4	0.9	1.5	0.2
45	-5	23905	287	3692	120	458	58	449	67	84.7	1.0	12.2	0.4	1.6	0.2	1.5	0.2
45	-7.5	23286	286	3530	116	300	57	359	65	85.6	1.1	12.1	0.4	1.1	0.2	1.3	0.2
45	-10	22694	284	3039	110	395	57	217	63	86.9	1.1	10.9	0.4	1.5	0.2	0.8	0.2
45	-15	23398	287	2564	104	452	59	152	60	88.7	1.1	9.1	0.4	1.7	0.2	0.6	0.2
45	-20	22979	286	2485	102	323	57	13	57	89.7	1.1	9.1	0.4	1.2	0.2	0.1	0.2
45	-50	21349	272	2350	100	349	55	46	55	89.2	1.1	9.2	0.4	1.4	0.2	0.2	0.2
45	-100	19801	263	2203	96	319	52	28	51	89.2	1.2	9.3	0.4	1.4	0.2	0.1	0.2
45	2.5	28312	316	3421	118	469	61	298	66	87.8	1.0	9.9	0.3	1.4	0.2	0.9	0.2
45	5	28109	317	3111	115	429	62	171	65	89.0	1.0	9.2	0.3	1.3	0.2	0.5	0.2
45	7.5	27496	312	2887	111	537	62	58	63	89.4	1.0	8.8	0.3	1.7	0.2	0.2	0.2
45	10	26790	308	2802	109	428	60	108	61	89.5	1.0	8.8	0.3	1.4	0.2	0.3	0.2
45	15	26658	308	2923	111	379	61	-31	60	89.7	1.0	9.2	0.3	1.2	0.2	-0.1	0.2
45	20	26581	304	2763	108	438	60	128	61	89.5	1.0	8.7	0.3	1.4	0.2	0.4	0.2
45	50	27298	310	3002	111	397	59	64	58	89.4	1.0	9.2	0.3	1.3	0.2	0.2	0.2
45	100	26863	308	2914	110	321	57	42	56	89.7	1.0	9.1	0.3	1.0	0.2	0.1	0.2
40	0	22764	280	4274	127	424	57	592	69	82.1	1.0	14.4	0.4	1.5	0.2	2.0	0.2
40	-2.5	23063	282	4383	127	362	57	623	69	82.1	1.0	14.6	0.4	1.2	0.2	2.1	0.2
40	-5	25821	298	3650	121	393	57	411	65	86.1	1.0	11.4	0.4	1.2	0.2	1.3	0.2
40	-7.5	26806	304	2967	110	454	58	181	58	88.8	1.0	9.2	0.3	1.4	0.2	0.6	0.2
40	-10	25283	297	2865	108	408	56	101	55	88.9	1.0	9.4	0.4	1.4	0.2	0.3	0.2
40	-15	25468	296	2715	105	364	56	9	55	89.8	1.0	9.0	0.3	1.2	0.2	0.0	0.2
40	-20	25901	300	2746	104	414	56	5	55	89.7	1.0	8.9	0.3	1.4	0.2	0.0	0.2
40	-50	24491	291	2777	104	441	58	88	55	88.7	1.1	9.4	0.4	1.5	0.2	0.3	0.2
40	2.5	31420	330	3386	116	362	60	75	63	89.8	0.9	9.1	0.3	1.0	0.2	0.2	0.2

Table 4.1 X-Ray Data

		Fe		Cr		Si		P		Wt %							
Thick	Pos	Cnts	Error	Cnts	Error	Cnts	Error	Cnts	Error	Fe	Error	Cr	Error	Si	Error	P	Error
40	5	31703	332	3397	117	479	61	60	60	89.6	0.9	9.0	0.3	1.3	0.2	0.2	0.2
40	7.5	30077	325	3231	116	469	59	112	60	89.4	1.0	9.0	0.3	1.3	0.2	0.3	0.2
40	10	30639	325	3166	113	416	58	29	60	90.1	1.0	8.7	0.3	1.2	0.2	0.1	0.2
40	15	29987	324	3345	116	455	59	101	59	89.1	1.0	9.3	0.3	1.3	0.2	0.3	0.2
40	20	28539	315	3042	110	356	58	47	59	89.8	1.0	9.0	0.3	1.1	0.2	0.1	0.2
40	50	25372	297	2789	108	387	55	-39	54	89.6	1.0	9.2	0.4	1.3	0.2	-0.1	0.2
37	0	17076	245	3406	113	259	49	718	66	80.6	1.2	15.0	0.5	1.2	0.2	3.2	0.3
37	-2.5	17046	243	2453	97	328	48	272	54	85.6	1.2	11.5	0.5	1.6	0.2	1.3	0.3
37	-5	16988	240	2006	88	308	47	44	46	88.5	1.3	9.8	0.4	1.5	0.2	0.2	0.2
37	-10	16416	238	1703	84	265	45	-27	44	90.0	1.3	8.7	0.4	1.4	0.2	-0.1	0.2
37	-20	15827	234	1720	83	232	45	-10	42	89.7	1.3	9.1	0.4	1.2	0.2	-0.1	0.2
37	2.5	20236	264	2424	99	290	48	109	52	88.5	1.2	9.9	0.4	1.2	0.2	0.5	0.2
37	5	19409	261	2161	91	242	45	34	46	89.5	1.2	9.3	0.4	1.1	0.2	0.2	0.2
37	10	17985	248	1992	89	373	46	63	45	88.8	1.2	9.2	0.4	1.7	0.2	0.3	0.2
37	20	17683	245	1823	87	252	43	7	45	90.1	1.2	8.7	0.4	1.2	0.2	0.0	0.2
37	0	10979	194	2688	97	140	39	624	58	77.3	1.4	17.7	0.6	0.9	0.3	4.1	0.4
37	0	14376	223	1914	86	267	42	165	47	86.7	1.3	10.8	0.5	1.5	0.2	0.9	0.3
37	-1	13147	214	2251	93	217	43	335	52	83.4	1.4	13.4	0.6	1.3	0.3	2.0	0.3
37	-2	13542	216	2795	102	243	46	474	58	80.5	1.3	15.5	0.6	1.4	0.3	2.6	0.3
37	-3	12712	211	2534	98	183	45	551	58	80.6	1.3	15.0	0.6	1.1	0.3	3.3	0.3
37	-4	12893	211	2172	91	228	43	382	53	83.2	1.4	13.1	0.5	1.4	0.3	2.3	0.3
37	-5	12923	210	1867	85	274	43	220	48	85.4	1.4	11.5	0.5	1.7	0.3	1.4	0.3
37	-6	12647	209	1606	80	172	42	93	42	87.8	1.5	10.4	0.5	1.1	0.3	0.6	0.3
37	-7	12939	211	1398	77	220	42	46	41	89.2	1.5	9.0	0.5	1.4	0.3	0.3	0.3
37	-8	12742	210	1489	76	212	42	13	41	88.8	1.5	9.7	0.5	1.4	0.3	0.1	0.3
37	1	16748	240	2013	89	216	43	90	47	89.5	1.3	10.0	0.4	1.1	0.2	0.5	0.2
37	2	17579	245	2007	91	229	44	67	46	89.1	1.2	9.5	0.4	1.1	0.2	0.3	0.2

Table 4.1 X-Ray Data

Alloy S300 Data																
		Fe		Cr		Si		P		Wt %						
Thick	Pos	Cnts	Error	Cnts	Error	Cnts	Error	Cnts	Error	Fe	Error	Cr	Error	Si	Error	P	Error
20	0	16187	247	4128	133	245	47	716	61	78.0	1.2	17.9	0.6	1.1	0.2	3.1	0.3
20	-1	19800	267	3316	125	277	48	369	53	84.2	1.1	13.2	0.5	1.1	0.2	1.5	0.2
20	-2	18481	256	2432	111	237	45	203	48	87.3	1.2	10.8	0.5	1.1	0.2	0.9	0.2
20	-3	19393	263	2120	107	258	44	65	41	89.5	1.2	9.2	0.5	1.1	0.2	0.3	0.2
20	-5	17443	251	1783	100	196	40	36	38	90.2	1.3	8.6	0.5	1.0	0.2	0.2	0.2
20	-10	16024	238	1663	95	201	39	0	38	90.2	1.3	8.8	0.5	1.1	0.2	0.0	0.0
20	1	19764	266	2701	115	175	45	302	49	86.9	1.2	11.1	0.5	0.7	0.2	1.2	0.2
20	2	19469	263	2247	109	150	41	112	43	89.2	1.2	9.6	0.5	0.7	0.2	0.5	0.2
20	3	19472	262	2001	103	177	41	17	40	90.5	1.2	8.7	0.4	0.8	0.2	0.1	0.2
20	5	17819	251	1706	98	109	39	23	38	91.2	1.3	8.2	0.5	0.5	0.2	0.1	0.2
20	10	16806	242	1717	96	160	38	22	37	90.4	1.3	8.7	0.5	0.8	0.2	0.1	0.2
32	0	22204	278	4926	146	269	52	804	66	79.8	1.0	16.5	0.5	0.9	0.2	2.8	0.2
32	-1	23305	286	4493	143	247	49	628	63	82.2	1.0	14.8	0.5	0.9	0.2	2.1	0.2
32	-2	24237	292	3070	126	257	46	273	50	87.7	1.1	10.4	0.4	0.9	0.2	1.0	0.2
32	-5	21463	276	2167	109	198	42	33	39	90.5	1.2	8.6	0.4	0.8	0.2	0.1	0.2
32	-10	20091	266	1992	107	174	40	3	38	90.8	1.2	8.4	0.5	0.8	0.2	0.0	0.1
32	0	24876	298	5166	153	308	54	789	68	80.9	1.0	15.7	0.5	1.0	0.2	2.5	0.2
32	1	27951	314	3553	136	255	50	141	52	88.3	1.0	10.5	0.4	0.8	0.2	0.4	0.2
32	2	28813	321	3142	130	243	50	102	50	89.8	1.0	9.2	0.4	0.7	0.2	0.3	0.2
32	3	25215	301	2579	120	274	47	50	46	90.2	1.1	8.6	0.4	1.0	0.2	0.2	0.2
32	5	26239	305	2557	121	214	48	21	46	90.9	1.1	8.3	0.4	0.7	0.2	0.1	0.2
32	10	23800	291	2325	116	242	45	5	44	90.8	1.1	8.3	0.4	0.9	0.2	0.0	0.2
133	0	76089	520	10900	230	699	82	950	91	86.1	0.6	11.5	0.2	1.1	0.1	1.3	0.1
133	-1	83088	550	12089	231	746	86	1202	97	85.8	0.6	11.7	0.2	1.1	0.1	1.5	0.1
133	-2	83881	553	10015	214	790	85	719	90	88.1	0.6	9.8	0.2	1.1	0.1	0.9	0.1
133	-3	82647	549	9099	204	793	83	448	83	89.1	0.6	9.2	0.2	1.2	0.1	0.6	0.1

Table 4.1 X-Ray Data

		Fe		Cr		Si		P		Wt %							
Thick	Pos	Cnts	Error	Cnts	Error	Cnts	Error	Cnts	Error	Fe	Error	Cr	Error	Si	Error	P	Error
133	-5	83505	553	8758	199	839	83	224	79	89.7	0.6	8.8	0.2	1.3	0.1	0.3	0.1
133	-10	83610	553	7946	192	684	82	53	76	90.8	0.6	8.1	0.2	1.0	0.1	0.1	0.1
133	1	90158	575	11217	221	706	88	668	93	88.0	0.6	10.2	0.2	1.0	0.1	0.8	0.1
133	2	82787	550	9586	205	577	83	351	83	89.0	0.6	9.7	0.2	0.9	0.1	0.5	0.1
133	3	76619	530	8741	197	628	79	257	80	89.1	0.6	9.5	0.2	1.0	0.1	0.4	0.1
133	5	74765	523	7893	186	562	78	138	75	90.0	0.6	8.9	0.2	0.9	0.1	0.2	0.1
133	10	81770	548	8102	191	559	80	-61	75	90.8	0.6	8.4	0.2	0.9	0.1	-0.1	0.1
90	0	23613	292	3264	119	201	53	336	57	86.6	1.1	11.2	0.4	0.9	0.2	1.4	0.2
90	-2.5	25885	304	3422	124	201	54	295	59	87.3	1.0	10.8	0.4	0.8	0.2	1.1	0.2
90	-5	23638	290	3107	116	169	51	198	53	87.7	1.1	10.8	0.4	0.8	0.2	0.8	0.2
90	-7.5	25281	300	2573	112	237	51	65	46	90.1	1.1	8.6	0.4	1.0	0.2	0.3	0.2
90	-10	25877	304	2570	110	264	51	-12	44	90.5	1.1	8.4	0.4	1.1	0.2	-0.1	0.2
90	0	25488	302	3212	122	276	55	254	58	87.6	1.0	10.3	0.4	1.1	0.2	1.0	0.2
90	2.5	22875	287	2624	111	225	53	105	53	89.0	1.1	9.6	0.4	1.1	0.2	0.5	0.2
90	5	23193	289	2300	109	196	51	24	50	90.6	1.1	8.4	0.4	0.9	0.2	0.1	0.2
90	7.5	23435	289	2316	108	228	53	-35	48	90.7	1.1	8.4	0.4	1.1	0.2	-0.2	0.2
90	10	22735	285	2134	106	221	51	-11	49	91.0	1.1	8.0	0.4	1.1	0.2	-0.1	0.2
90	25	22238	283	2272	104	172	51	-12	49	90.5	1.2	8.7	0.4	0.9	0.3	-0.1	0.2
90	-25	23380	289	2344	107	184	46	55	42	90.4	1.1	8.5	0.4	0.9	0.2	0.2	0.2
254	0	109066	628	14689	253	813	90	1202	110	86.4	0.5	10.9	0.2	1.2	0.1	1.5	0.1
254	-2.5	152038	738	16501	276	957	102	488	111	89.4	0.4	9.1	0.2	1.1	0.1	0.5	0.1
254	-5	148898	733	15456	267	870	100	73	105	90.1	0.4	8.8	0.2	1.0	0.1	0.1	0.1
254	-7.5	147019	724	14964	263	973	99	268	105	90.0	0.4	8.6	0.2	1.2	0.1	0.3	0.1
254	-10	147066	725	15012	261	775	98	-21	102	90.4	0.4	8.7	0.2	0.9	0.1	0.0	0.1
254	0	136597	696	17601	275	1038	100	1256	119	87.0	0.4	10.5	0.2	1.3	0.1	1.3	0.1
254	2.5	140510	705	16702	267	1133	99	906	115	88.0	0.4	9.8	0.2	1.4	0.1	0.9	0.1
254	5	135258	692	14422	253	932	95	290	107	89.5	0.5	9.0	0.2	1.2	0.1	0.3	0.1

Table 4.1 X-Ray Data

		Fe		Cr		Si		P		Wt %							
Thick	Pos	Cnts	Error	Cnts	Error	Cnts	Error	Cnts	Error	Fe	Error	Cr	Error	Si	Error	P	Error
254	7.5	130397	679	13621	246	967	92	179	102	89.7	0.5	8.8	0.2	1.3	0.1	0.2	0.1
254	10	130279	680	13197	241	917	92	101	103	90.1	0.5	8.6	0.2	1.2	0.1	0.1	0.1
254	2.5	122176	658	14933	250	938	93	755	108	87.8	0.5	10.0	0.2	1.3	0.1	0.9	0.1
254	25	123849	662	12799	237	851	89	120	98	89.9	0.5	8.7	0.2	1.2	0.1	0.1	0.1
254	-25	117501	645	12076	230	759	89	55	91	90.1	0.5	8.7	0.2	1.1	0.1	0.1	0.1
50	0	27391	309	4350	133	355	56	633	68	84.5	1.0	12.6	0.4	1.1	0.2	1.9	0.2
50	-2.5	33291	337	3652	126	355	55	55	55	89.7	0.9	9.2	0.3	0.9	0.1	0.1	0.1
50	-5	31746	331	3382	121	303	56	15	53	90.1	0.9	9.0	0.3	0.8	0.2	0.0	0.1
50	-7.5	31162	330	3085	118	332	55	88	55	90.4	1.0	8.4	0.3	0.9	0.2	0.2	0.2
50	-10	30253	326	3016	118	310	57	67	55	90.5	1.0	8.4	0.3	0.9	0.2	0.2	0.2
50	-25	28017	311	3042	116	373	55	-19	53	89.8	1.0	9.1	0.3	1.2	0.2	-0.1	0.2
50	0	31616	333	4278	135	328	57	382	65	87.1	0.9	11.0	0.3	0.9	0.2	1.0	0.2
50	2.5	31536	331	5561	148	424	61	881	76	83.0	0.9	13.7	0.4	1.1	0.2	2.2	0.2
50	5	32335	337	4264	134	351	61	301	66	87.5	0.9	10.8	0.3	0.9	0.2	0.8	0.2
50	7.5	32505	335	3472	123	398	59	-14	57	90.0	0.9	9.0	0.3	1.1	0.2	0.0	0.2
50	10	32285	334	3393	122	440	59	31	58	89.9	0.9	8.8	0.3	1.2	0.2	0.1	0.1
50	25	30516	325	3225	121	404	56	16	56	89.9	1.0	8.9	0.3	1.2	0.2	0.1	0.2
163	0	174256	790	24403	327	1484	120	2239	141	86.2	0.4	11.3	0.2	1.1	0.1	1.4	0.1
163	-2.5	151698	738	19017	289	1364	109	1059	120	87.7	0.4	10.3	0.2	1.2	0.1	0.8	0.1
163	-5	153886	738	17148	276	1234	106	488	110	89.2	0.4	9.3	0.1	1.1	0.1	0.4	0.1
163	-7.5	155763	744	16119	267	1248	106	210	103	90.0	0.4	8.7	0.1	1.1	0.1	0.2	0.1
163	-10	152062	733	15586	262	1128	105	223	104	90.2	0.4	8.7	0.1	1.0	0.1	0.2	0.1
163	-25	154518	740	15806	262	1141	104	58	103	90.3	0.4	8.7	0.1	1.0	0.1	0.0	0.1
163	0	149373	727	19995	288	1253	109	1514	126	86.9	0.4	10.9	0.2	1.1	0.1	1.2	0.1
163	2.5	156906	745	19430	283	1248	109	1173	124	87.9	0.4	10.2	0.1	1.1	0.1	0.9	0.1
163	5	153417	737	16143	262	1014	106	620	115	89.8	0.4	8.9	0.1	0.9	0.1	0.5	0.1
163	7.5	150721	728	15301	258	1072	104	420	110	90.1	0.4	8.6	0.1	1.0	0.1	0.3	0.1

Table 4.1 X-Ray Data

		Fe		Cr		Si		P		Wt %							
Thick	Pos	Cnts	Error	Cnts	Error	Cnts	Error	Cnts	Error	Fe	Error	Cr	Error	Si	Error	P	Error
163	10	146166	718	14799	250	983	101	310	106	90.3	0.4	8.6	0.1	0.9	0.1	0.3	0.1
163	25	146349	716	14905	252	970	101	206	106	90.3	0.4	8.6	0.1	0.9	0.1	0.2	0.1
163	0	171788	779	23311	308	1524	113	1251	134	87.0	0.4	11.0	0.1	1.2	0.1	0.8	0.1
163	-2.5	179625	797	24529	314	1549	116	1311	137	87.0	0.4	11.1	0.1	1.1	0.1	0.8	0.1
163	-5	168167	768	22644	302	1335	112	1163	132	87.2	0.4	11.0	0.1	1.0	0.1	0.8	0.1
163	-7.5	175499	783	20857	292	1406	110	578	125	88.7	0.4	9.9	0.1	1.1	0.1	0.4	0.1
163	-10	173648	782	18367	278	1448	109	153	117	89.9	0.4	8.9	0.1	1.1	0.1	0.1	0.1
163	-25	180797	795	18150	278	1408	111	-33	116	90.4	0.4	8.5	0.1	1.1	0.1	0.0	0.1
163	0	169461	770	23011	301	1420	112	1325	131	87.0	0.4	11.0	0.1	1.1	0.1	0.9	0.1
163	2.5	180738	795	19559	283	1471	113	153	118	89.7	0.4	9.1	0.1	1.1	0.1	0.1	0.1
163	5	178595	789	18576	278	1544	112	-66	116	90.1	0.4	8.8	0.1	1.2	0.1	0.0	0.1
163	7.5	178789	789	18426	275	1573	111	11	115	90.1	0.4	8.7	0.1	1.2	0.1	0.0	0.1
163	10	178140	788	18049	274	1483	111	-49	115	90.3	0.4	8.6	0.1	1.1	0.1	0.0	0.1
163	25	180117	792	18572	275	1300	109	-174	115	90.4	0.4	8.7	0.1	1.0	0.1	-0.1	0.1
47	0	45114	392	7215	163	516	69	944	84	84.6	0.7	12.7	0.3	1.0	0.1	1.8	0.2
47	-1	50961	419	6727	160	772	72	679	81	86.8	0.7	10.7	0.3	1.4	0.1	1.2	0.1
47	-25	53450	428	5260	145	524	70	-43	67	90.8	0.7	8.4	0.2	0.9	0.1	-0.1	0.1
47	25	45034	393	4247	131	384	66	-14	66	91.2	0.8	8.1	0.2	0.8	0.1	0.0	0.1
47	5	47073	402	4368	132	393	66	62	70	91.2	0.8	7.9	0.2	0.8	0.1	0.1	0.1
47	3	45500	396	4292	132	449	66	124	69	90.8	0.8	8.0	0.2	0.9	0.1	0.3	0.1
47	2	44113	391	4230	130	433	65	110	66	90.7	0.8	8.1	0.3	0.9	0.1	0.2	0.1
47	1	41267	377	5261	141	458	66	389	75	87.7	0.8	10.5	0.3	1.0	0.1	0.8	0.2
47	-2	49367	412	5076	141	457	68	218	70	90.1	0.8	8.7	0.2	0.9	0.1	0.4	0.1
47	-3	50176	414	4678	136	384	65	81	68	91.2	0.8	8.0	0.2	0.7	0.1	0.2	0.1
47	-5	51963	423	4973	140	459	67	40	67	91.0	0.7	8.2	0.2	0.8	0.1	0.1	0.1
47	0	47814	406	7800	171	598	72	1057	89	84.2	0.7	12.8	0.3	1.1	0.1	1.9	0.2

Table 4.1 X-Ray Data

		Fe		Cr		Si		P		Wt %							
Thick	Pos	Cnts	Error	Cnts	Error	Cnts	Error	Cnts	Error	Fe	Error	Cr	Error	Si	Error	P	Error
122	0	81151	539	15400	253	984	98	2458	129	81.6	0.5	14.4	0.2	1.2	0.1	2.8	0.1
122	0	75999	524	17787	267	1131	100	3417	139	77.7	0.5	16.9	0.3	1.4	0.1	3.9	0.2
122	-25	106755	620	10595	226	1251	100	152	99	90.1	0.5	8.4	0.2	1.3	0.1	0.2	0.1
122	25	102946	609	10356	222	957	96	48	100	90.4	0.5	8.5	0.2	1.1	0.1	0.1	0.1
122	-1	92457	591	13363	244	1039	99	1447	118	85.7	0.5	11.6	0.2	1.2	0.1	1.5	0.1
122	-2	94180	594	10609	225	978	98	551	106	88.9	0.6	9.4	0.2	1.2	0.1	0.6	0.1
122	-3	92147	585	10088	217	986	97	497	103	89.1	0.6	9.1	0.2	1.2	0.1	0.6	0.1
122	-5	94320	593	9244	213	916	95	116	96	90.5	0.6	8.3	0.2	1.1	0.1	0.1	0.1
122	-10	85971	564	8284	205	847	91	191	92	90.5	0.6	8.2	0.2	1.1	0.1	0.2	0.1
122	1	80948	549	12678	236	1084	98	1585	120	84.4	0.6	12.3	0.2	1.4	0.1	1.9	0.1
122	2	84271	557	9519	213	840	91	557	103	88.8	0.6	9.4	0.2	1.1	0.1	0.7	0.1
122	3	82854	554	9014	209	890	90	373	98	89.2	0.6	9.1	0.2	1.2	0.1	0.5	0.1
122	5	80498	546	8319	198	775	87	60	91	90.1	0.6	8.7	0.2	1.1	0.1	0.1	0.1
122	10	81519	547	7937	197	782	87	-39	91	90.7	0.6	8.3	0.2	1.1	0.1	-0.1	0.1
	0	47730	420	9080	194	537	79	1673	103	81.2	0.7	14.4	0.3	1.1	0.2	3.2	0.2
176	0	169933	779	23731	316	1360	127	1962	140	86.5	0.4	11.3	0.2	1.0	0.1	1.3	0.1
176	-1	203541	853	24270	330	1680	136	1120	139	88.5	0.4	9.9	0.1	1.1	0.1	0.6	0.1
176	-2	201408	849	22593	317	1618	133	811	131	89.1	0.4	9.4	0.1	1.0	0.1	0.5	0.1
176	-3	200800	846	21777	309	1481	132	479	126	89.7	0.4	9.1	0.1	1.0	0.1	0.3	0.1
176	-5	198129	838	20897	303	1614	131	306	123	89.9	0.4	8.9	0.1	1.1	0.1	0.2	0.1
176	-10	199816	843	21065	301	1536	130	245	122	90.0	0.4	8.9	0.1	1.0	0.1	0.1	0.1
176	0	190317	824	25097	322	1504	134	1705	142	87.3	0.4	10.8	0.1	1.0	0.1	1.0	0.1
176	1	192330	825	27191	332	1635	135	2292	154	86.3	0.4	11.4	0.1	1.1	0.1	1.3	0.1
176	2	176892	793	22992	309	1710	128	1457	141	87.3	0.4	10.6	0.1	1.2	0.1	0.9	0.1
176	3	183727	807	20146	296	1839	128	460	133	89.2	0.4	9.3	0.1	1.3	0.1	0.3	0.1
176	5	180080	799	19111	288	1991	126	238	129	89.5	0.4	8.9	0.1	1.4	0.1	0.2	0.1
57	0	38864	365	8104	170	600	71	1513	95	80.0	0.8	15.6	0.3	1.3	0.2	3.2	0.2

Table 4.1 X-Ray Data

		Fe		Cr		Si		P		Wt %							
Thick	Pos	Cnts	Error	Cnts	Error	Cnts	Error	Cnts	Error	Fe	Error	Cr	Error	Si	Error	P	Error
57	-1	51812	425	7491	167	690	76	808	87	85.8	0.7	11.6	0.3	1.2	0.1	1.4	0.1
57	-2	43116	385	4965	139	606	67	262	70	88.6	0.8	9.5	0.3	1.3	0.1	0.6	0.1
57	-3	43590	386	4098	129	599	66	79	65	90.5	0.8	8.0	0.3	1.3	0.1	0.2	0.1
57	-5	41278	377	3876	124	487	63	55	62	90.8	0.8	8.0	0.3	1.2	0.1	0.1	0.1
57	1	36560	354	6268	151	555	67	982	82	83.1	0.8	13.3	0.3	1.3	0.2	2.3	0.2
57	2	41763	379	4478	131	491	66	268	70	89.3	0.8	9.0	0.3	1.1	0.2	0.6	0.2
57	3	41144	376	4441	133	589	68	267	70	89.0	0.8	9.0	0.3	1.4	0.2	0.6	0.2
57	5	40746	375	4108	127	402	65	64	66	90.4	0.8	8.5	0.3	1.0	0.2	0.2	0.2
57	10	39594	370	3786	123	487	64	152	66	90.4	0.8	8.1	0.3	1.2	0.2	0.4	0.2
57	-10	47212	402	4523	133	595	68	-82	65	90.8	0.8	8.1	0.2	1.2	0.1	-0.2	0.1
57	-25	52880	426	5157	143	710	74	30	71	90.4	0.7	8.3	0.2	1.3	0.1	0.1	0.1
57	25	38552	361	3796	122	493	64	99	64	90.2	0.8	8.3	0.3	1.2	0.2	0.2	0.2
Alloy S120 Data																	
113	0	27779	324	39140	364	213	71	560	85	43.1	0.5	55.7	0.5	0.3	0.1	0.9	0.1
113	-2.5	35272	361	17353	249	604	72	839	87	66.7	0.7	30.5	0.4	1.2	0.1	1.6	0.2
113	0	26862	317	24358	290	465	71	1169	91	52.7	0.6	44.1	0.5	0.9	0.1	2.3	0.2
113	-2.5	39783	380	6309	159	654	70	93	66	85.6	0.8	12.7	0.3	1.5	0.2	0.2	0.1
113	-5	38999	376	4741	140	461	67	-62	66	88.9	0.9	10.1	0.3	1.1	0.2	-0.1	0.1
113	-10	34501	356	3554	124	485	64	-49	59	90.1	0.9	8.7	0.3	1.4	0.2	-0.1	0.2
113	-25	37702	373	3605	127	557	67	41	63	90.4	0.9	8.1	0.3	1.4	0.2	0.1	0.2
113	2.5	18848	270	37509	354	132	66	375	77	35.1	0.5	64.0	0.6	0.3	0.1	0.7	0.1
113	5	18182	265	36645	348	26	63	72	71	35.1	0.5	64.7	0.6	0.1	0.1	0.1	0.1
113	10	16966	259	35165	343	59	61	-44	66	34.6	0.5	65.4	0.6	0.1	0.1	-0.1	0.1
113	25	15941	249	32718	332	46	61	25	66	34.7	0.5	65.2	0.7	0.1	0.1	0.1	0.1
113	Matrix	71104	504	7262	173	918	85	-130	80	90.3	0.6	8.6	0.2	1.3	0.1	-0.2	0.1
115	0	107435	624	13743	235	1620	111	1227	121	87.1	0.5	10.4	0.2	1.5	0.1	1.0	0.1
115	-25	98763	597	9939	201	1436	101	11	94	90.1	0.5	8.5	0.2	1.5	0.1	0.0	0.1

Table 4.1 X-Ray Data

		Fe		Cr		Si		P		Wt %							
Thick	Pos	Cnts	Error	Cnts	Error	Cnts	Error	Cnts	Error	Fe	Error	Cr	Error	Si	Error	P	Error
115	25	125439	668	12478	223	1469	110	-52	111	90.4	0.5	8.4	0.2	1.2	0.1	0.0	0.1
115	-2.5	106656	616	11665	217	1443	106	99	105	89.4	0.5	9.2	0.2	1.3	0.1	0.1	0.1
115	-5	108801	620	10903	210	1393	104	173	104	90.1	0.5	8.5	0.2	1.3	0.1	0.2	0.1
115	-10	108420	617	10536	207	1429	102	-77	99	90.5	0.5	8.2	0.2	1.3	0.1	-0.1	0.1
115	2.5	116582	640	12210	219	1395	108	508	113	89.6	0.5	8.8	0.2	1.2	0.1	0.4	0.1
115	5	118895	643	11564	215	1478	109	330	109	90.3	0.5	8.2	0.2	1.3	0.1	0.3	0.1
115	10	120176	645	11761	216	1379	109	54	107	90.5	0.5	8.3	0.2	1.2	0.1	0.0	0.1
173	0	187594	808	22608	295	1829	126	679	132	88.6	0.4	10.0	0.1	1.1	0.1	0.4	0.1
173	-5	185585	801	20066	280	1997	124	205	121	89.6	0.4	9.1	0.1	1.2	0.1	0.1	0.1
173	5	192152	814	20923	285	1733	123	22	127	89.7	0.4	0.2	0.0	1.0	0.1	0.1	0.7
148	0	143689	703	18181	263	1611	113	415	116	88.1	0.4	10.4	0.2	1.2	0.1	0.3	0.1
148	-5	154251	729	16115	251	1703	117	46	111	90.0	0.4	8.8	0.1	1.2	0.1	0.0	0.1
148	5	139770	691	15050	241	1610	107	-25	107	89.8	0.4	9.1	0.1	1.2	0.1	0.0	0.1
102	0	98670	588	13906	229	1494	104	618	111	88.6	0.5	11.4	0.2	1.4	0.1	0.6	0.1
102	0	99609	589	14455	232	1536	105	520	113	86.4	0.5	11.7	0.2	1.4	0.1	0.5	0.1
102	-2.5	85500	545	9755	197	1106	94	325	96	88.9	0.6	9.5	0.2	1.2	0.1	0.4	0.1
102	-5	87837	554	10348	199	1005	95	234	98	88.9	0.6	9.8	0.2	1.1	0.1	0.2	0.1
102	-10	84638	541	9479	194	1116	94	265	95	89.1	0.6	9.3	0.2	1.3	0.1	0.3	0.1
102	-25	86221	549	9934	195	1075	95	236	96	89.0	0.6	9.6	0.2	1.2	0.1	0.3	0.1
102	25	74111	506	8881	183	936	87	9	93	88.8	0.6	10.0	0.2	1.2	0.1	0.0	0.1
102	0	15004	234	14005	219	198	53	409	62	52.6	0.8	45.2	0.7	0.7	0.2	1.4	0.2
102	-2.5	3619	121	13218	207	22	38	59	42	23.0	0.8	76.5	1.2	0.1	0.2	0.4	0.3
102	-5	3886	127	14918	222	60	38	47	41	22.1	0.7	77.3	1.1	0.4	0.2	0.3	0.2
102	-10	4320	131	16349	233	-13	37	7	42	22.5	0.7	77.5	1.1	-0.1	0.2	0.0	0.2
102	-25	4392	134	13414	211	23	37	-3	40	26.4	0.8	77.4	1.2	0.1	0.2	0.0	0.3
102	2.5	19350	264	2649	102	256	49	-9	43	87.6	1.2	11.2	0.4	1.3	0.2	0.0	0.2

Table 4.1 X-Ray Data

		Fe		Cr		Si		P		Wt %							
Thick	Pos	Cnts	Error	Cnts	Error	Cnts	Error	Cnts	Error	Fe	Error	Cr	Error	Si	Error	P	Error
102	5	19795	268	2205	96	305	50	11	42	89.2	1.2	9.3	0.4	1.5	0.2	0.1	0.2
102	10	21210	278	1990	96	267	50	3	45	90.8	1.2	8.0	0.4	1.2	0.2	0.0	0.2
102	25	26847	311	2826	110	342	54	4	47	89.9	1.0	8.9	0.3	1.2	0.2	0.0	0.1
102	0	27957	317	2912	111	324	55	63	54	89.9	1.0	8.8	0.3	1.1	0.2	0.2	0.2
102	-10	29286	325	3009	113	290	54	176	55	89.8	1.0	8.6	0.3	1.0	0.2	0.6	0.2
102	10	25673	305	2563	105	278	52	72	52	90.3	1.1	8.4	0.3	1.1	0.2	0.3	0.2
102	50	69184	495	7504	176	887	83	-32	81	89.7	0.6	9.1	0.2	1.2	0.1	0.0	0.1
102	-50	75275	514	7917	177	791	89	398	91	89.7	0.6	8.8	0.2	1.0	0.1	0.5	0.1
102	0	59147	459	8487	181	887	85	812	93	85.9	0.7	11.5	0.2	1.4	0.1	1.2	0.1
102	-2.5	66424	485	8147	180	931	89	700	94	87.7	0.6	10.1	0.2	1.3	0.1	1.0	0.1
102	-5	69899	497	7281	172	846	88	591	93	89.3	0.6	8.7	0.2	1.2	0.1	0.8	0.1
102	-7.5	95492	583	9511	199	979	102	439	106	90.2	0.6	8.4	0.2	1.0	0.1	0.4	0.1
102	-10	88808	562	8912	191	980	100	217	102	90.2	0.6	8.5	0.2	1.1	0.1	0.2	0.1
102	-25	89753	561	9458	195	985	99	357	101	89.7	0.6	8.9	0.2	1.1	0.1	0.4	0.1
102	-100	97125	587	10630	207	1309	105	259	105	89.3	0.5	9.1	0.2	1.3	0.1	0.3	0.1
102	2.5	80053	531	8731	187	1008	93	353	92	89.3	0.6	9.1	0.2	1.2	0.1	0.4	0.1
102	5	80448	534	8208	183	877	91	-39	88	90.4	0.6	8.6	0.2	1.1	0.1	0.0	0.1
102	7.5	86876	556	8995	189	1173	95	256	93	89.7	0.6	8.7	0.2	1.3	0.1	0.3	0.1
102	10	90447	568	9161	195	1113	97	18	95	90.2	0.6	8.6	0.2	1.2	0.1	0.0	0.1
102	25	91672	569	9097	194	1094	96	35	92	90.4	0.6	8.4	0.2	1.2	0.1	0.0	0.1
102	100	90035	562	9313	193	1092	94	40	91	90.1	0.6	8.7	0.2	1.2	0.1	0.0	0.1
44	0	65211	480	11685	206	1044	92	839	95	83.7	0.6	14.0	0.2	1.3	0.1	1.0	0.1
44	-10	67623	484	7902	176	741	87	212	82	89.1	0.6	9.7	0.2	0.9	0.1	0.3	0.1
44	10	64714	470	8442	178	992	88	155	80	87.8	0.6	10.7	0.2	1.3	0.1	0.2	0.1
152	0	219807	868	29630	334	2842	155	2787	174	86.6	0.3	10.9	0.1	1.3	0.1	1.2	0.1

Table 4.1 X-Ray Data

		Fe		Cr		Si		P		Wt %							
Thick	Pos	Cnts	Error	Cnts	Error	Cnts	Error	Cnts	Error	Fe	Error	Cr	Error	Si	Error	P	Error
152	-10	227825	885	22191	298	2571	149	112	140	90.5	0.4	8.3	0.1	1.2	0.1	0.1	0.1
152	10	205301	838	20254	282	2286	141	524	144	90.2	0.4	8.3	0.1	1.2	0.1	0.3	0.1
80	-50	48547	405	5161	140	536	71	13	70	90.0	0.8	9.0	0.2	1.0	0.1	0.0	0.1
80	50	41177	375	4500	132	733	70	-179	68	89.6	0.8	9.2	0.3	1.7	0.2	-0.4	0.1
80	0	39582	366	5536	144	787	72	495	77	85.9	0.8	11.2	0.3	1.8	0.2	1.1	0.2
80	-2.5	44509	388	4809	137	543	68	148	69	89.5	0.8	9.1	0.3	1.1	0.1	0.3	0.1
80	-5	43972	388	4596	133	596	67	142	67	89.7	0.8	8.8	0.3	1.3	0.1	0.3	0.1
80	-7.5	43609	382	4372	132	529	66	76	65	90.1	0.8	8.6	0.3	1.1	0.1	0.2	0.1
80	-10	43353	385	4376	131	518	64	53	63	90.3	0.8	8.5	0.3	1.1	0.1	0.1	0.1
80	-25	42769	381	4405	132	527	65	106	64	90.0	0.8	8.7	0.3	1.2	0.1	0.2	0.1
80	2.5	31689	328	3929	122	597	64	22	67	88.0	0.9	10.2	0.3	1.7	0.2	0.1	0.2
80	5	51102	418	4999	141	918	79	-77	79	90.2	0.7	8.3	0.2	1.7	0.1	-0.1	0.1
80	7.5	43219	384	4619	133	886	74	-139	72	89.5	0.8	9.0	0.3	1.9	0.2	-0.3	0.2
80	10	41217	373	4170	129	777	70	-144	68	90.0	0.8	8.5	0.3	1.8	0.2	-0.3	0.1
80	25	44193	387	4665	136	848	73	-142	73	89.7	0.8	8.9	0.3	1.8	0.2	-0.3	0.1
92	-50	108121	606	11239	211	1403	104	-219	95	90.2	0.5	8.8	0.2	1.2	0.1	-0.2	0.1
92	50	98514	580	10392	202	897	98	85	97	90.2	0.5	8.9	0.2	0.9	0.1	0.1	0.1
92	0	79380	522	12851	216	1284	98	1377	111	84.3	0.6	12.8	0.2	1.4	0.1	1.5	0.1
92	-2.5	93341	563	10246	198	1406	98	156	93	89.3	0.5	9.2	0.2	1.4	0.1	0.2	0.1
92	-5	89812	552	9413	190	1311	95	81	91	89.7	0.6	8.8	0.2	1.4	0.1	0.1	0.1
92	-10	87350	545	8952	186	1006	94	-65	89	90.3	0.6	8.7	0.2	1.1	0.1	-0.1	0.1
92	-25	85125	539	8853	186	1152	93	-90	86	90.0	0.6	8.8	0.2	1.3	0.1	-0.1	0.1
92	2.5	83566	534	9346	188	858	91	191	93	89.5	0.6	9.4	0.2	1.0	0.1	0.2	0.1
92	5	84347	537	8597	186	838	90	156	89	90.3	0.6	8.6	0.2	1.0	0.1	0.2	0.1
92	10	82636	530	8121	181	824	89	115	88	90.6	0.6	8.3	0.2	1.0	0.1	0.1	0.1
92	25	80853	525	8286	181	781	89	62	87	90.3	0.6	8.7	0.2	0.9	0.1	0.1	0.1

Table 4.1 X-Ray Data

		Fe		Cr		Si		P		Wt %							
Thick	Pos	Cnts	Error	Cnts	Error	Cnts	Error	Cnts	Error	Fe	Error	Cr	Error	Si	Error	P	Error
195	-50	247586	923	25383	316	1934	139	-10	136	90.4	0.3	8.7	0.1	0.9	0.1	0.0	0.0
195	50	238234	906	23670	306	2123	136	189	130	90.5	0.3	8.4	0.1	1.1	0.1	0.1	0.1
195	0	236138	902	32568	350	2973	147	1576	151	86.7	0.3	11.2	0.1	1.4	0.1	0.7	0.1
195	-2.5	239834	910	25157	314	2351	138	351	136	89.9	0.3	8.8	0.1	1.1	0.1	0.2	0.1
195	-5	236733	901	23494	305	2002	137	111	134	90.5	0.3	8.4	0.1	1.0	0.1	0.1	0.1
195	-10	302441	1022	29553	343	2414	154	30	152	90.7	0.3	8.3	0.1	0.9	0.1	0.0	0.1
195	-25	307635	1034	30778	349	2432	154	68	152	90.6	0.3	8.5	0.1	0.9	0.1	0.0	0.0
195	2.5	262068	950	28661	335	2969	148	703	144	89.3	0.3	9.1	0.1	1.3	0.1	0.3	0.1
195	5	259335	942	25758	319	2560	144	212	138	90.4	0.3	8.4	0.1	1.2	0.1	0.1	0.1
195	10	251168	929	23975	311	2274	141	161	132	90.8	0.3	8.1	0.1	1.1	0.1	0.1	0.1
195	25	24547	918	24177	308	2227	140	75	132	90.5	3.4	8.4	0.1	1.1	0.1	0.0	0.1
Alloy S25 Data																	
60	0	550537	1616	72580	624	8011	320	1414	329	87.9	0.1	10.8	0.1	1.2	0.1	0.2	0.1
60	25	590767	1604	63502	577	5452	294	334	295	90.1	0.1	9.1	0.1	0.8	0.0	0.0	0.0
60	-25	568640	1576	61256	563	5874	394	400	318	89.6	0.1	9.0	0.1	0.9	0.0	0.0	0.0
60	0	592289	1676	78427	650	8675	333	1616	342	87.8	0.1	10.8	0.1	1.2	0.0	0.2	0.0
60	25	639998	1738	68794	625	5906	318	362	320	90.2	0.1	9.0	0.1	0.8	0.0	0.0	0.0
60	-25	616027	1707	66361	610	6363	319	300	344	89.0	0.1	9.0	0.1	0.9	0.0	0.0	0.0
143	0	1402259	2586	157854	939	17917	473	1835	461	89.4	0.1	9.4	0.1	1.1	0.0	0.1	0.0
143	25	1631055	2568	164950	935	16921	482	762	452	90.3	0.1	8.4	0.1	0.9	0.0	0.0	0.0
143	-25	1264207	2403	123339	835	11552	399	501	430	90.7	0.1	8.4	0.1	0.8	0.0	0.0	0.0
143	0	1522665	2695	170359	975	19353	496	1979	471	89.5	0.1	9.3	0.1	1.1	0.0	0.1	0.1
143	25	1768039	2907	178757	1013	18228	513	826	487	90.6	0.1	8.5	0.1	0.9	0.0	0.0	0.0
143	-25	1370858	2555	133617	875	12578	438	543	465	90.9	0.1	8.2	0.1	0.8	0.0	0.0	0.0
50	0	195863	968	29665	399	2895	201	795	191	86.4	0.2	12.2	0.2	1.2	0.1	0.3	0.1
50	25	211480	951	22696	341	2320	189	525	225	89.8	0.2	8.8	0.1	0.9	0.1	0.1	0.1
50	-25	232484	1023	24882	359	2021	197	570	218	90.1	0.2	9.0	0.1	0.7	0.1	0.1	0.1
50	0	209661	1001	31738	414	3077	209	859	197	86.4	0.2	12.1	0.2	1.1	0.1	0.3	0.1

Table 4.1 X-Ray Data

		Fe		Cr		Si		P		Wt %							
Thick	Pos	Cnts	Error	Cnts	Error	Cnts	Error	Cnts	Error	Fe	Error	Cr	Error	Si	Error	P	Error
50	25	229163	1046	24638	377	2510	205	574	250	89.9	0.2	9.0	0.1	0.9	0.1	0.1	0.1
50	-25	251851	1103	27414	397	2207	221	617	251	90.0	0.2	9.1	0.1	0.7	0.1	0.1	0.1

Key to Table 4.1

Thick	Thickness of sample at analysis position
Pos	Distance from grain boundary or interface of interest
Cnts	Number of x-ray counts present fom element of interest
Error	Error determined by analysis routine
Wt%	Concentration of element in weight percent

Table 4.1 X-Ray Data

Acquisition Number	1	2	3	4	5	6
P/Fe Peak Height Ratio	64.8	58.5	47.8	50.9	50.2	49.3

Table 4.2 Variation of phosphorus to iron peak height ratio during successive acquisitions from the same facet using a 10nA beam current

Acquisition Number	Type of Facet	Beam Curent nA	P/Fe Peak Height Ratio
1	TG	5	0.00
2	IG	5	0.57
3	TG	5	0.00
4	IG	10	0.57
5	TG	5	0.31

Table 4.3 Phosphorus to iron peak height ratios obtained using 5nA and 10nA beam currents

Monolayers Removed	P Signal	Cr Signal	Fe Signal	P/Fe	Cr/Fe
0	804	718	1420	0.57	0.51
0.5	663	823	2012	0.33	0.41
1	329	1014	2387	0.14	0.42
1.5	204	641	1754	0.12	0.37
2	146	640	2070	0.07	0.31
2	152	648	1976	0.08	0.33
4	111	780	2495	0.04	0.31

Table 4.4 Ratios of phosphorus and chromium collected during depth profile experiment

Alloy S560 Data							
P	CR	FE	P/FE	P BG	Fe Bg	PBg/FeBg	Adj P/Fe
1,029	816	1,649	0.62	32676	32949	0.99	0.63
568	469	1,022	0.56	20664	22740	0.91	0.61
997	923	1,739	0.57	36811	37933	0.97	0.59
1,115	910	1,739	0.64	38095	37525	1.02	0.63
921	727	1,511	0.61	28121	30636	0.92	0.66
430	362	788	0.55	14947	16861	0.89	0.62
341	286	601	0.57	11855	13360	0.89	0.64
1,047	830	1,805	0.58	32518	35148	0.93	0.63
635	493	1,015	0.63	18607	21624	0.86	0.73
963	783	1,766	0.55	17888	18501	0.97	0.56
828	615	1,378	0.60	27040	28594	0.95	0.64
433	460	1,062	0.41	18376	20587	0.89	0.46
561	1	1,050	0.53	20127	20936	0.96	0.56
619	561	1,481	0.42	26112	28128	0.93	0.45
498	371	981	0.51	17979	21356	0.84	0.60
593	459	969	0.61	18951	20673	0.92	0.67
645	593	1,439	0.45	23548	25808	0.91	0.49
712	557	1,132	0.63	20879	23862	0.87	0.72
394	356	689	0.57	15505	16785	0.92	0.62
488	373	736	0.66	16727	18135	0.92	0.72
926	740	1,759	0.53	33805	34167	0.99	0.53
731	672	1,376	0.53	27840	28116	0.99	0.54
1,252	1027	2,427	0.52	42157	40348	1.04	0.49
609	529	1,152	0.53	20922	22837	0.92	0.58
866	771	1,613	0.54	28877	30813	0.94	0.57
857	1	2,118	0.40	37430	36103	1.04	0.39
524	711	950	0.55	16837	17954	0.94	0.59
404	352	725	0.56	15242	16036	0.95	0.59
691	558	1,341	0.52	23967	25692	0.93	0.55
666	529	1,104	0.60	21700	22751	0.95	0.63
641	483	930	0.69	19646	21478	0.91	0.75
667	611	1,469	0.45	24963	26215	0.95	0.48
1,110	1173	1,757	0.63	33593	35321	0.95	0.66
856	745	1,611	0.53	28750	30289	0.95	0.56
696	680	1,352	0.51	25284	25845	0.98	0.53
378	327	651	0.58	12084	13277	0.91	0.64
679	619	1,352	0.50	25291	26819	0.94	0.53
723	589	1299	0.56	23174	25433	0.91	0.61
508	450	851	0.60	18521	18999	0.97	0.61
440	387	1001	0.44	18398	19595	0.94	0.47
501	479	1228	0.41	24280	25004	0.97	0.42
384	335	849	0.45	17134	18036	0.95	0.48
575	435	1067	0.54	20351	21472	0.95	0.57
872	755	1949	0.45	33017	32631	1.01	0.44
628	540	1074	0.58	20465	22014	0.93	0.63
435	351	565	0.77	13800	14653	0.94	0.82
341	1	529	0.64	11466	12322	0.93	0.69
372	326	548	0.68	13002	13922	0.93	0.73
454	340	696	0.65	15485	16323	0.95	0.69

Table 4.5 AES Data

P	CR	FE	P/FE	P BG	Fe Bg	PBg/FeBg	Adj P/Fe
338	1	520	0.65	11852	12434	0.95	0.68
564	501	1030	0.55	19627	20557	0.95	0.57
364	276	628	0.58	12707	14071	0.90	0.64
265	207	421	0.63	10070	11007	0.91	0.69
726	586	1218	0.60	25264	26893	0.94	0.63
670	572	1172	0.57	21977	22532	0.98	0.59
351	297	619	0.57	12470	13251	0.94	0.60
560	511	1062	0.53	19683	20228	0.97	0.54
729	659	1391	0.52	24872	26226	0.95	0.55
971	838	1607	0.60	31545	31625	1.00	0.61
1034	878	1653	0.63	31881	31773	1.00	0.62
1124	981	1989	0.57	35409	34220	1.03	0.55
367	289	756	0.49	14762	16038	0.92	0.53
316	299	651	0.49	12204	13394	0.91	0.53
418	322	521	0.80	14902	15368	0.97	0.83
397	447	743	0.53	14665	16205	0.90	0.59
479	447	725	0.66	17409	17860	0.97	0.68
793	862	1428	0.56	27984	27459	1.02	0.54
963	896	1611	0.60	28358	29426	0.96	0.62
1233	967	2179	0.57	40632	40165	1.01	0.56
818	597	1418	0.58	25843	27753	0.93	0.62
295	1	450	0.66	11517	12014	0.96	0.68
482	364	737	0.65	14751	16531	0.89	0.73
564	449	1024	0.55	18109	20192	0.90	0.61
873	647	1252	0.70	25004	24824	1.01	0.69
Alloy S300 data							
453	515	1181	0.38	19601	27061	0.72	0.53
547	729	1664	0.33	25482	34508	0.74	0.45
710	911	2227	0.32	33715	43678	0.77	0.41
524	606	1537	0.34	23239	31103	0.75	0.46
621	792	1688	0.37	30661	33475	0.92	0.40
615	698	1724	0.36	26450	36055	0.73	0.49
622	666	1866	0.33	28767	37635	0.76	0.44
598	683	1928	0.31	29164	37711	0.77	0.40
396	487	1123	0.35	18592	25529	0.73	0.48
657	743	1998	0.33	32781	38799	0.84	0.39
371	552	2177	0.17	28900	39816	0.73	0.23
514	547	1550	0.33	23727	31764	0.75	0.44
454	502	1063	0.43	21409	26006	0.82	0.52
718	842	2219	0.32	35697	46547	0.77	0.42
493	605	1587	0.31	28157	35254	0.80	0.39
448	622	1422	0.32	24188	31437	0.77	0.41
566	656	1617	0.35	28806	36811	0.78	0.45
535	561	1298	0.41	28121	28386	0.99	0.42
565	655	1759	0.32	25830	37305	0.69	0.46
619	696	1717	0.36	27553	36427	0.76	0.48
706	872	2255	0.31	35243	44554	0.79	0.40
603	723	1893	0.32	30102	39380	0.76	0.42
624	752	2135	0.29	31944	43116	0.74	0.39
404	530	1244	0.32	20627	29070	0.71	0.46

Table 4.5 AES Data

P	CR	FE	P/FE	P BG	Fe Bg	PBg/FeBg	Adj P/Fe
459	696	1544	0.30	23547	31307	0.75	0.40
676	844	2273	0.30	35129	45745	0.77	0.39
634	823	1897	0.33	30801	40468	0.76	0.44
384	490	1212	0.32	20299	28686	0.71	0.45
429	477	1090	0.39	19857	27354	0.73	0.54
548	675	1759	0.31	29341	45661	0.64	0.48
607	711	1308	0.46	27561	29876	0.92	0.50
673	817	2331	0.29	38328	50638	0.76	0.38
492	588	1551	0.32	26996	34708	0.78	0.41
772	892	2494	0.31	37871	48938	0.77	0.40
848	1134	2853	0.30	40765	56525	0.72	0.41
790	1030	2826	0.28	39218	53836	0.73	0.38
628	846	2065	0.30	32734	43946	0.74	0.41
517	654	1527	0.34	21628	32985	0.66	0.52
523	686	1594	0.33	24282	34105	0.71	0.46
357	551	1493	0.24	19053	31544	0.60	0.40
151	284	1351	0.11	17749	26752	0.66	0.17
276	320	2959	0.09	13943	20797	0.67	0.14
373	532	1459	0.26	19760	29831	0.66	0.39
381	532	1400	0.27	18958	27583	0.69	0.40
326	357	942	0.35	13381	19945	0.67	0.52
701	967	2287	0.31	35626	45755	0.78	0.39
431	459	1371	0.31	23000	30661	0.75	0.42
634	917	2593	0.24	37257	51787	0.72	0.34
700	906	2111	0.33	34635	46455	0.75	0.44
772	914	2340	0.33	37279	45960	0.81	0.41
715	909	2056	0.35	33879	44397	0.76	0.46
501	635	1563	0.32	26860	33690	0.80	0.40
575	693	1724	0.33	26112	35471	0.74	0.45
361	493	1153	0.31	19172	25810	0.74	0.42
455	623	1384	0.33	23587	33494	0.70	0.47
676	788	2068	0.33	32344	42348	0.76	0.43
318	391	1328	0.24	21654	29417	0.74	0.33
467	614	1503	0.31	24962	33223	0.75	0.41
401	524	1111	0.36	19987	26375	0.76	0.48
435	518	1477	0.29	24191	32087	0.75	0.39
Alloy S120 Data							
238	615	1641	0.15	30912	39171	0.79	0.18
475	654	1983	0.24	35139	46524	0.76	0.32
435	757	1907	0.23	36904	45534	0.81	0.28
653	1223	2979	0.22	52777	58789	0.90	0.24
763	1210	2490	0.31	42801	50491	0.85	0.36
663	1141	2944	0.23	45904	56427	0.81	0.28
1440	1898	3829	0.38	79826	77591	1.03	0.37
1450	1498	4276	0.34	89552	85062	1.05	0.32
664	1298	3042	0.22	67583	67655	1.00	0.22
687	1486	4082	0.17	82032	80108	1.02	0.16
1363	2554	4062	0.34	101866	95352	1.07	0.31
833	963	2733	0.30	62183	54525	1.14	0.27
964	1516	4227	0.23	95829	84985	1.13	0.20

Table 4.5 AES Data

P	CR	FE	P/FE	P BG	Fe Bg	PBg/FeBg	Adj P/Fe
797	1318	3380	0.24	79341	71605	1.11	0.21
689	1085	2860	0.24	55651	52336	1.06	0.23
956	1742	3950	0.24	85837	82157	1.04	0.23
1199	1814	4396	0.27	101115	80787	1.25	0.22
666	937	2440	0.27	53541	50821	1.05	0.26
460	820	2496	0.18	61490	59257	1.04	0.18
490	868	1755	0.28	41922	42392	0.99	0.28
1342	1409	3491	0.38	78502	68939	1.14	0.34
814	1009	2838	0.29	64463	59809	1.08	0.27
1299	1695	4232	0.31	88124	80004	1.10	0.28
1104	1333	2950	0.37	64152	60841	1.05	0.35
1014	1714	3600	0.28	82520	78850	1.05	0.27
1054	1483	3477	0.30	72577	72180	1.01	0.30
620	913	2896	0.21	67284	63623	1.06	0.20
1242	1900	4356	0.29	86503	81069	1.07	0.27
732	1079	2228	0.33	46897	46466	1.01	0.33
1121	1214	3679	0.30	66472	62133	1.07	0.28
1129	1622	2553	0.44	60791	59997	1.01	0.44
750	1119	2363	0.32	54265	54385	1.00	0.32
1080	1633	3350	0.32	64619	62088	1.04	0.31
985	1484	2579	0.38	61797	59114	1.05	0.37
519	621	1633	0.32	43674	41518	1.05	0.30
477	731	1550	0.31	40819	39755	1.03	0.30
958	1251	3384	0.28	65740	63782	1.03	0.27
795	1419	3781	0.21	78972	76062	1.04	0.20
687	699	2362	0.29	50030	47627	1.05	0.28
833	1091	2872	0.29	58700	61424	0.96	0.30
963	1577	4140	0.23	77131	77640	0.99	0.23
814	1174	3100	0.26	54279	61157	0.89	0.30
564	688	1746	0.32	32351	36686	0.88	0.37
865	1711	3837	0.23	73921	76553	0.97	0.23
1138	1511	4083	0.28	79270	77484	1.02	0.27
956	1177	2734	0.35	59330	63161	0.94	0.37
753	914	1705	0.44	35430	39603	0.89	0.49
680	942	2735	0.25	50750	57149	0.89	0.28
781	1241	3297	0.24	56947	62427	0.91	0.26
1123	1080	3277	0.34	61645	66398	0.93	0.37
905	1572	3381	0.27	64219	72539	0.89	0.30
862	1324	3345	0.26	57849	68729	0.84	0.31
772	1020	2503	0.31	54383	55364	0.98	0.31
809	1075	2951	0.27	60837	56933	1.07	0.26
926	1500	3281	0.28	71416	70272	1.02	0.28
1237	1552	3516	0.35	68067	69342	0.98	0.36
846	1109	3030	0.28	59187	59709	0.99	0.28
919	1508	4154	0.22	77965	70829	1.10	0.20
973	1048	3047	0.32	62558	61133	1.02	0.31
691	1482	4094	0.17	81172	77909	1.04	0.16
931	1509	2446	0.38	61217	56686	1.08	0.35
1098	1809	4420	0.25	90354	88637	1.02	0.24
1832	2329	6177	0.30	117686	109534	1.07	0.28
823	1256	2484	0.33	56916	54661	1.04	0.32

Table 4.5 AES Data

P	CR	FE	P/FE	P BG	Fe Bg	PBg/FeBg	Adj P/Fe
828	1127	3185	0.26	62478	62871	0.99	0.26
339	660	1958	0.17	43147	41870	1.03	0.17
690	1367	2819	0.24	60440	64481	0.94	0.26
1190	1956	3317	0.36	73223	70658	1.04	0.35
558	783	2105	0.27	37705	44548	0.85	0.31
520	1026	1937	0.27	38671	42890	0.90	0.30
561	1055	2137	0.26	42119	46959	0.90	0.29
1228	1919	3973	0.31	84410	79407	1.06	0.29
778	1307	2952	0.26	67487	65015	1.04	0.25
840	1592	3663	0.23	68455	69670	0.98	0.23
433	955	3246	0.13	59257	59608	0.99	0.13
866	1059	2838	0.31	57401	61973	0.93	0.33
659	912	2451	0.27	52608	53981	0.97	0.28
1355	2470	4577	0.30	84768	88073	0.96	0.31
889	2707	3757	0.24	82469	83974	0.98	0.24
653	1245	2238	0.29	43589	48838	0.89	0.33
Alloy S25							
96	739	2204	0.04	40852	45171	0.90	0.05
95	1139	3892	0.02	66389	69822	0.95	0.03
0	885	3110	0.00	52321	55961	0.93	0.00
101	1305	4104	0.02	75730	76039	1.00	0.02
111	878	2948	0.04	52018	56284	0.92	0.04
77	914	3312	0.02	61996	60780	1.02	0.02
99	690	2267	0.04	41119	45906	0.90	0.05
124	1743	5493	0.02	101159	95216	1.06	0.02
126	883	2497	0.05	51327	51190	1.00	0.05
150	1075	3175	0.05	58963	63478	0.93	0.05
77	715	2362	0.03	47895	50552	0.95	0.03
75	828	2692	0.03	53953	54790	0.98	0.03
79	857	2423	0.03	41640	47387	0.88	0.04
103	1358	3780	0.03	66164	71846	0.92	0.03
75	830	2013	0.04	39577	43419	0.91	0.04
103	1206	3851	0.03	74293	71688	1.04	0.03
180	1342	3470	0.05	67021	67666	0.99	0.05
129	948	2619	0.05	45302	51273	0.88	0.06
130	1070	2837	0.05	54808	59503	0.92	0.05
158	1121	3777	0.04	66538	70521	0.94	0.04
220	1433	4380	0.05	74936	79926	0.94	0.05
85	910	2752	0.03	54996	57289	0.96	0.03
146	1025	3751	0.04	61542	65872	0.93	0.04
45	337	929	0.05	24239	26050	0.93	0.05
83	678	2042	0.04	43777	44926	0.97	0.04
64	942	3129	0.02	55253	59513	0.93	0.02
76	801	2263	0.03	43943	47554	0.92	0.04
70	705	2281	0.03	42169	46016	0.92	0.03
124	726	1741	0.07	37004	39258	0.94	0.08
129	851	2219	0.06	45434	48008	0.95	0.06
138	576	1927	0.07	34817	41382	0.84	0.09
90	586	1377	0.07	27882	30730	0.91	0.07
0	452	1609	0.00	31167	35199	0.89	0.00

Table 4.5 AES Data

P	CR	FE	P/FE	P BG	Fe Bg	PBg/FeBg	Adj P/Fe
102	1238	3949	0.03	58201	67459	0.86	0.03
110	622	1556	0.07	30239	36505	0.83	0.09
112	515	2086	0.05	34717	43710	0.79	0.07
0	973	2912	0.00	49849	57542	0.87	0.00
133	732	2231	0.06	41163	48047	0.86	0.07
0	699	2557	0.00	45713	52894	0.86	0.00
71	368	1133	0.06	23603	27122	0.87	0.07
66	531	2143	0.03	45900	40095	1.14	0.03
203	931	3399	0.06	62788	61898	1.01	0.06
294	1322	4064	0.07	70621	67569	1.05	0.07
187	1313	3832	0.05	66570	67588	0.98	0.05
0	532	2047	0.00	41657	41733	1.00	0.00
0	1685	5061	0.00	95083	86722	1.10	0.00
93	1544	3469	0.03	71280	65786	1.08	0.02
160	623	2004	0.08	38133	40833	0.93	0.09
256	906	2826	0.09	58822	53434	1.10	0.08
150	958	3040	0.05	62465	59952	1.04	0.05
217	1156	3574	0.06	68193	67821	1.01	0.06
129	858	2959	0.04	53782	54529	0.99	0.04
0	534	2160	0.00	48160	44326	1.09	0.00
187	919	3810	0.05	70175	67779	1.04	0.05
130	1003	3543	0.04	69698	62822	1.11	0.03
153	915	3160	0.05	63911	61287	1.04	0.05
115	334	1237	0.09	31860	30981	1.03	0.09
86	523	1294	0.07	32485	33509	0.97	0.07
75	342	909	0.08	21948	22509	0.98	0.08
0	391	1402	0.00	30642	33656	0.91	0.00

Table 4.5 AES Data

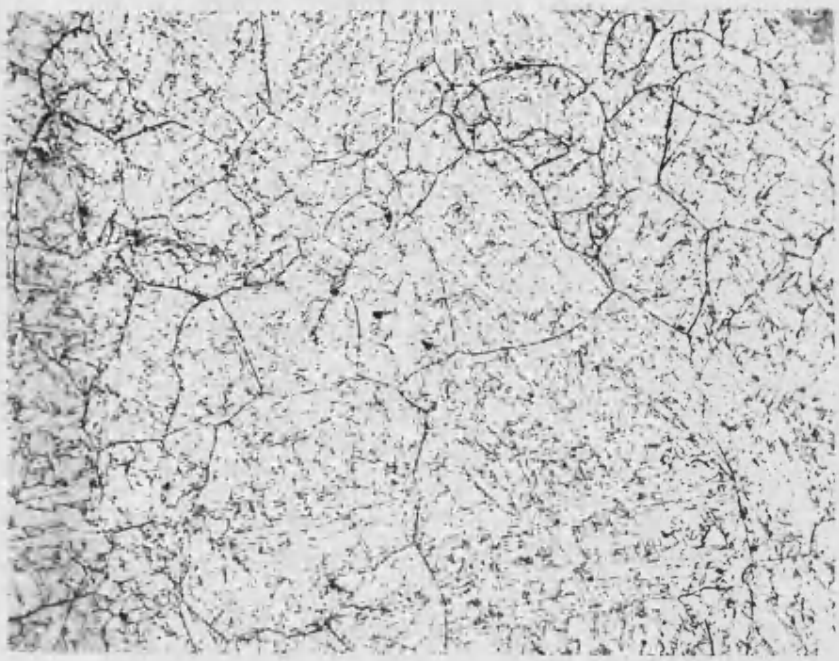

Figure 4.1 Optical micrograph of alloy S560

0.1mm

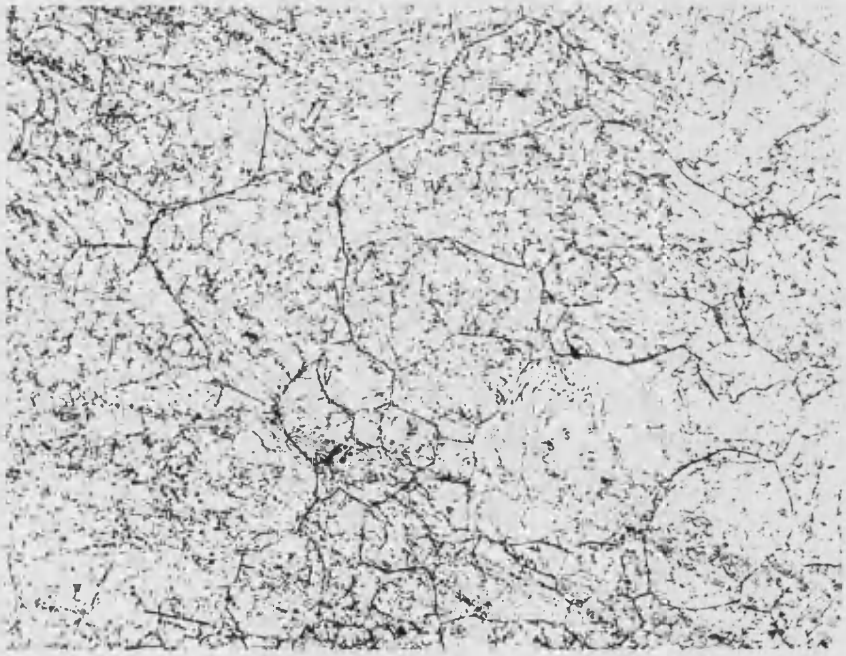

Figure 4.2 Optical micrograph of alloy S300

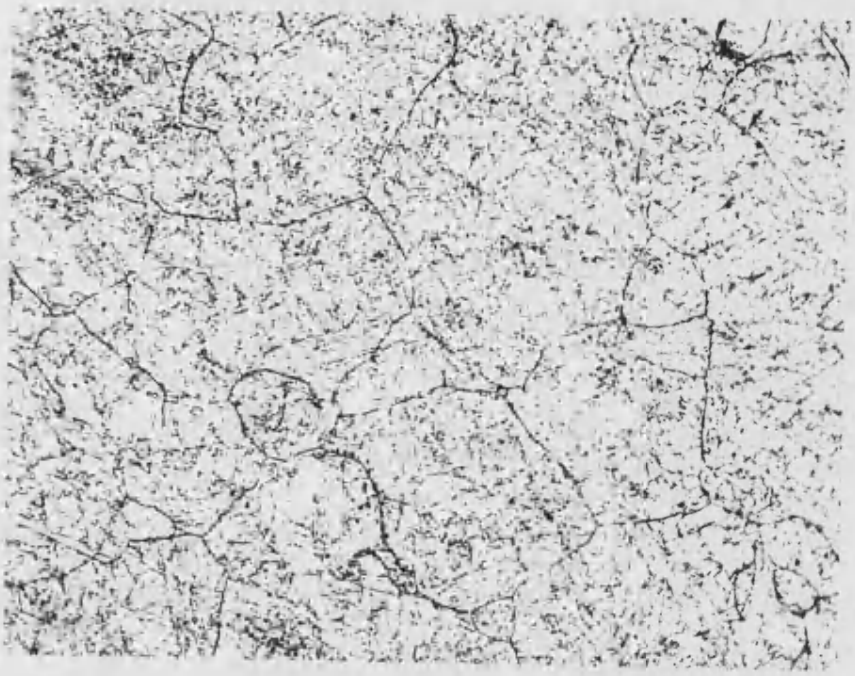

Figure 4.3 Optical micrograph of alloy S120

0.1mm

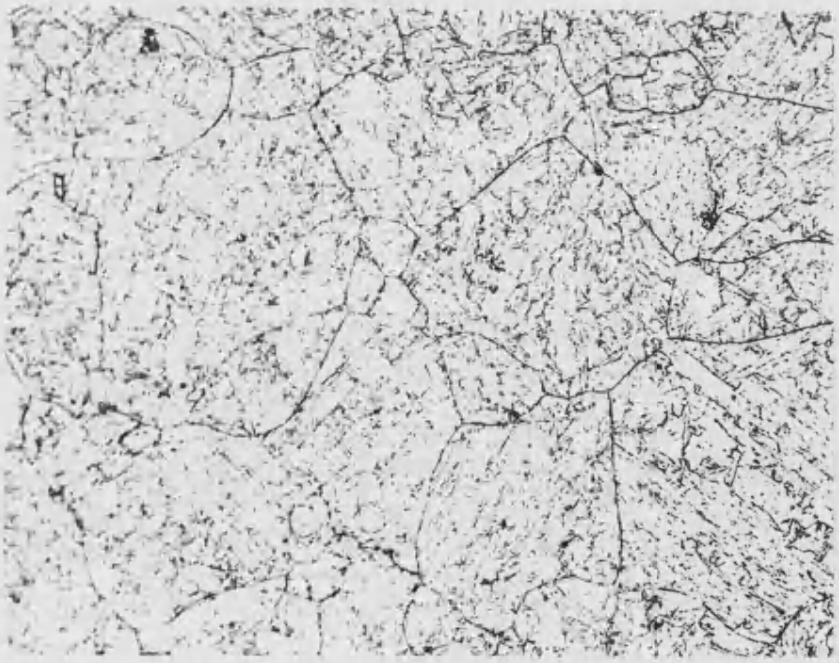

Figure 4.4 Optical micrograph of alloy S25

Figure 4.5 SEM micrograph of low temperature fracture, transgranular cleavage

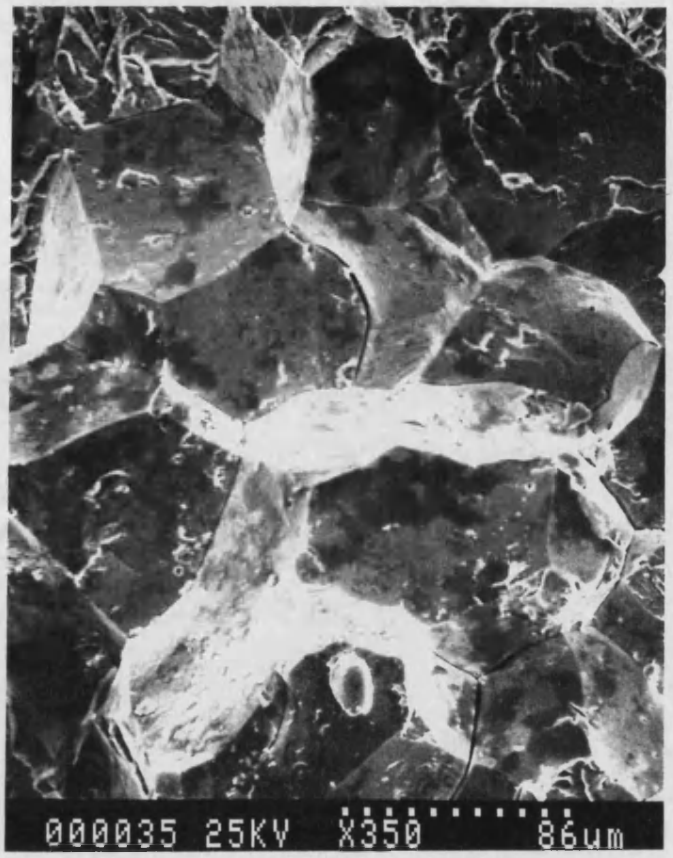

Figure 4.6 SEM micrograph of low temperature fracture, intergranular fracture

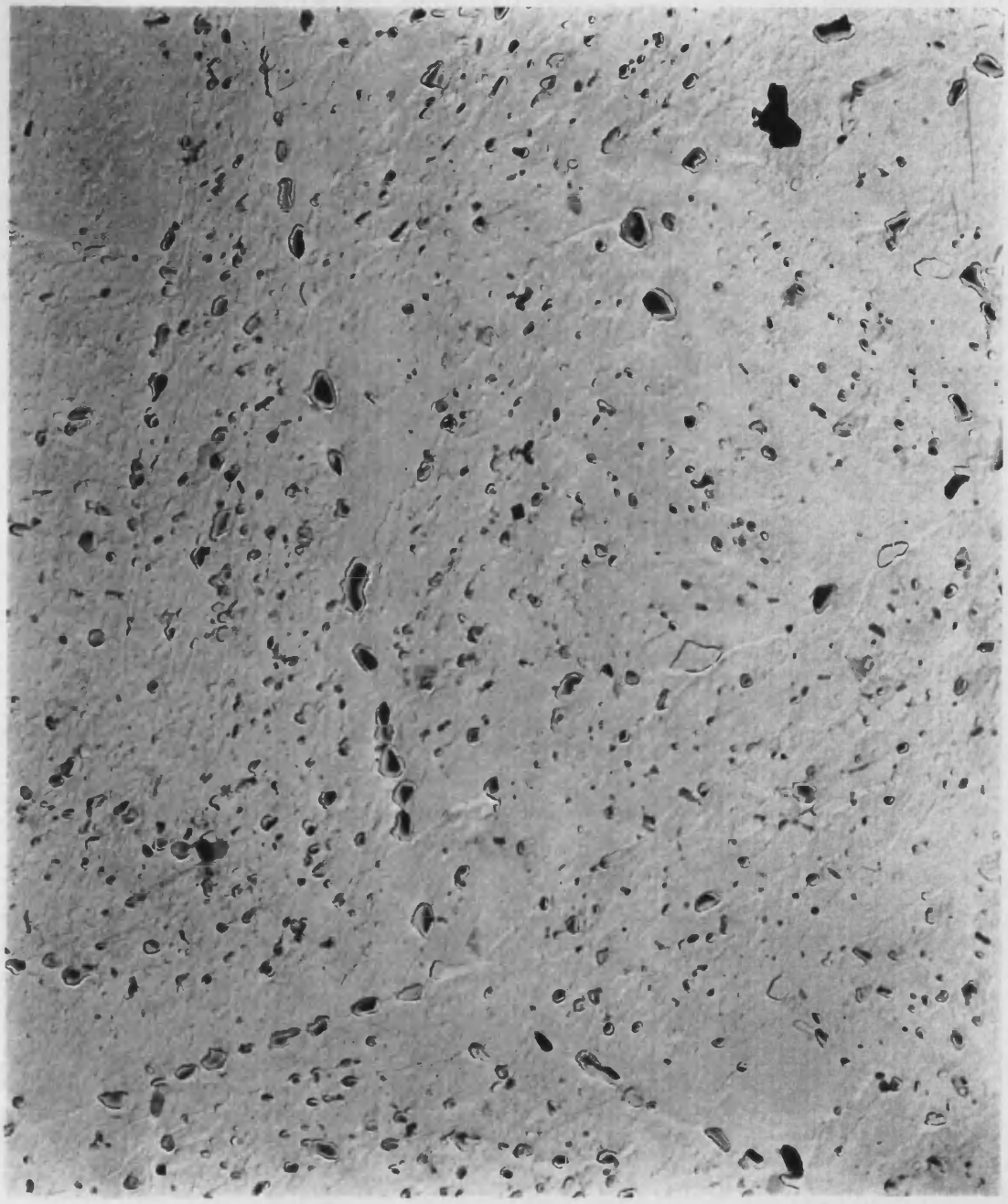

Figure 4.7 Electron micrograph of carbon extraction replica

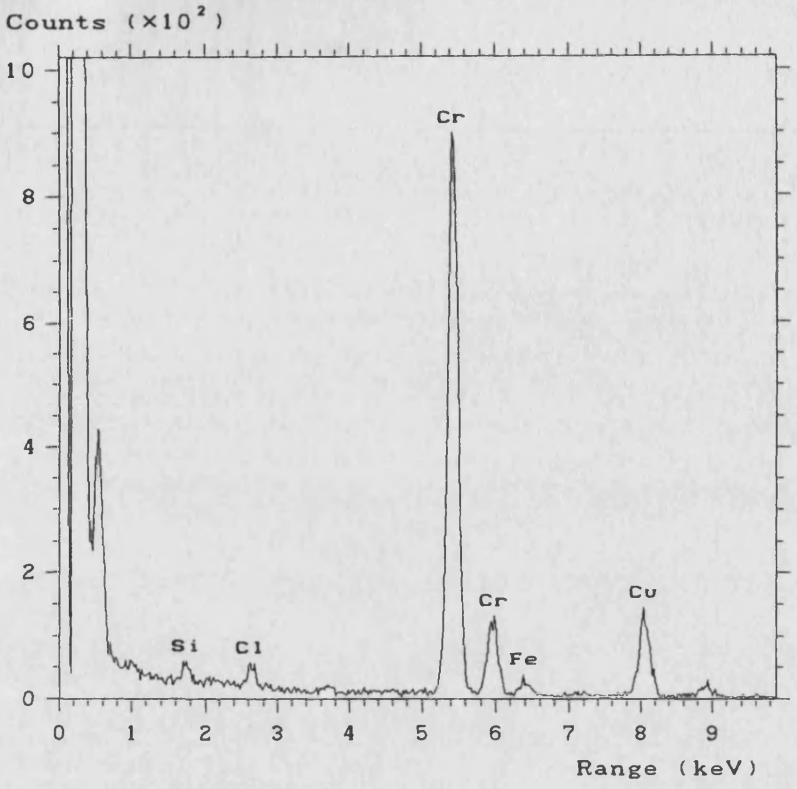

Figure 4.8 EDX spectrum collected from a precipitate on carbon extraction replica

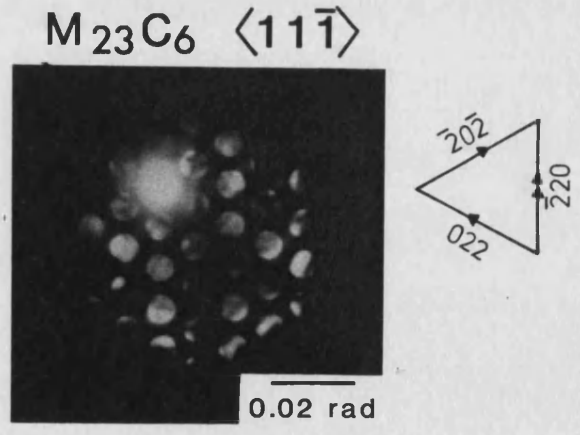

Figure 4.9 Convergent electron beam diffraction pattern of $M_{23}C_6$ precipitate

Figure 4.10 Low magnification electron micrograph of TEM sample

Figure 4.11 Increased magnification electron micrograph of TEM sample

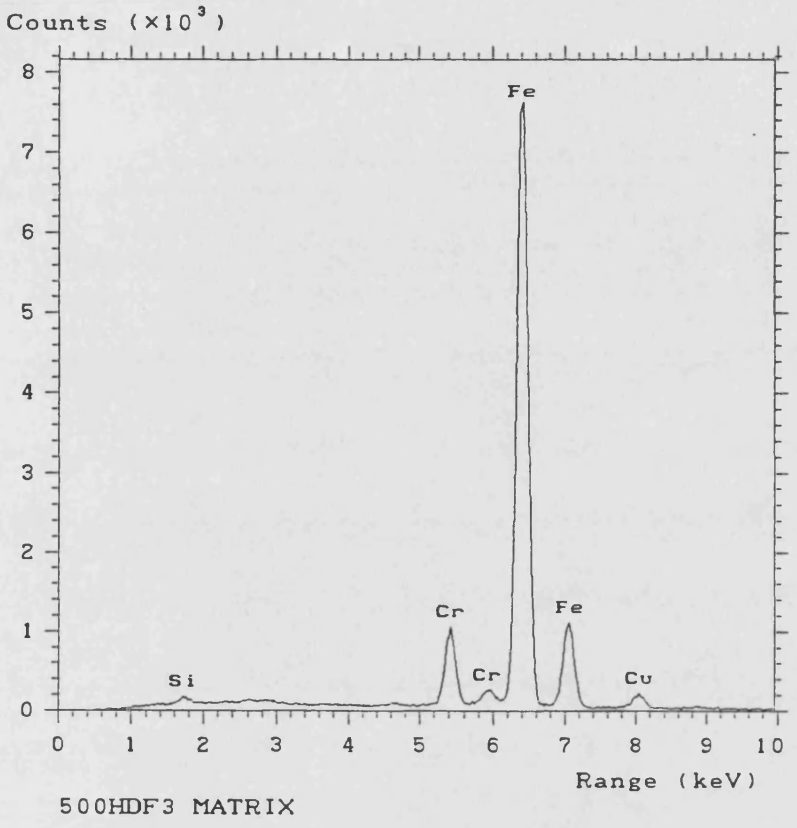

Figure 4.12 EDX spectrum of matrix

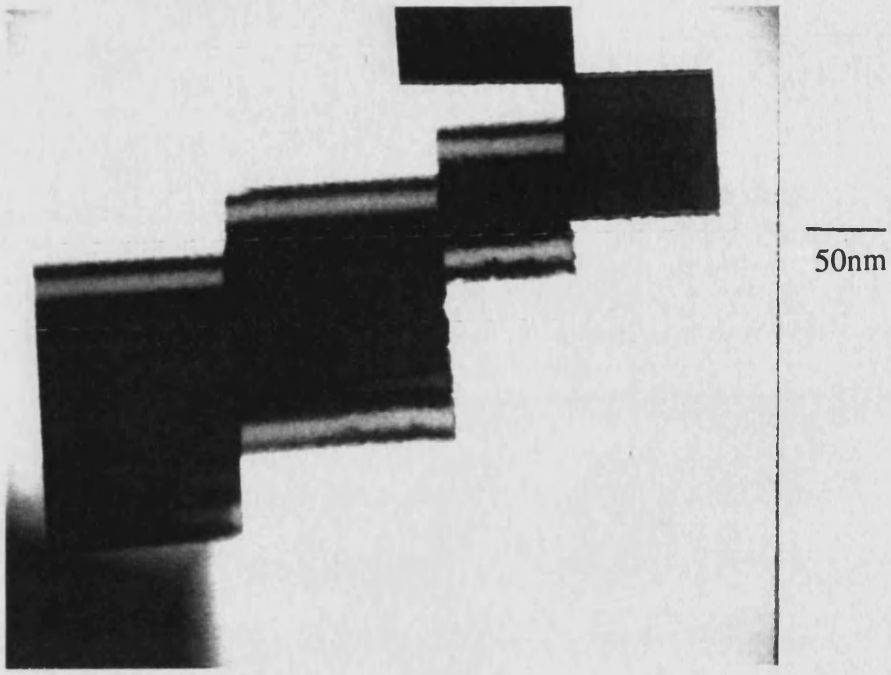

Figure 4.13 Well oriented magnesium oxide crystals

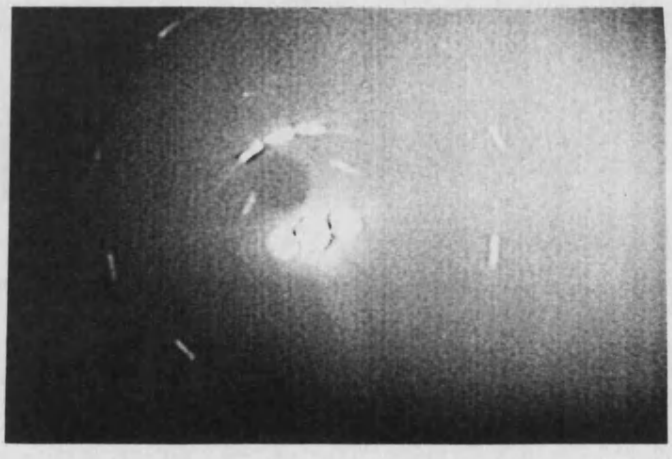

Figure 4.14 Diffraction pattern from magnesium oxide crystals

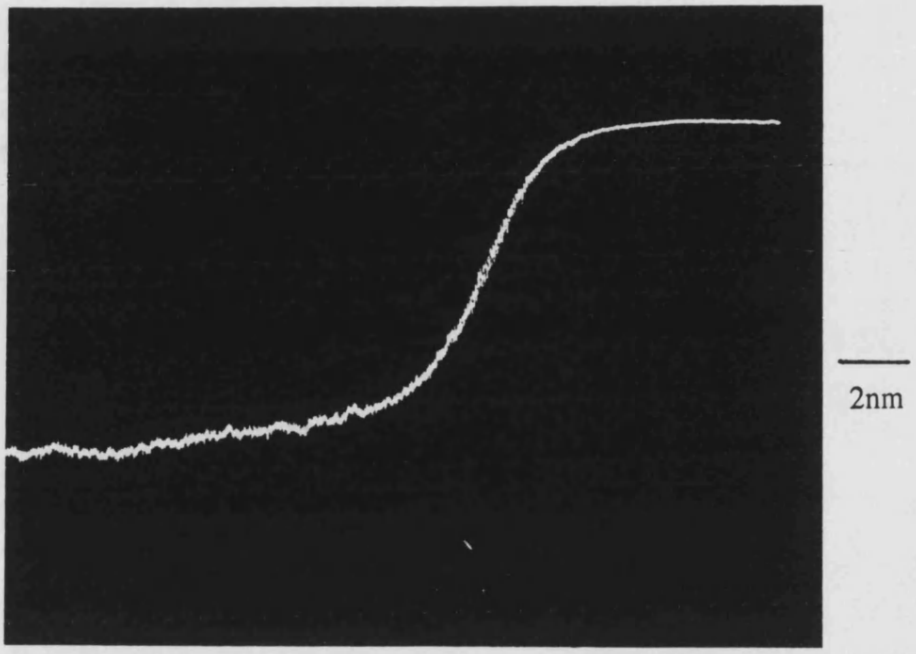

Figure 4.15 Dark-field electron intensity profile obtained by scanning across edge of magnesium oxide crystal

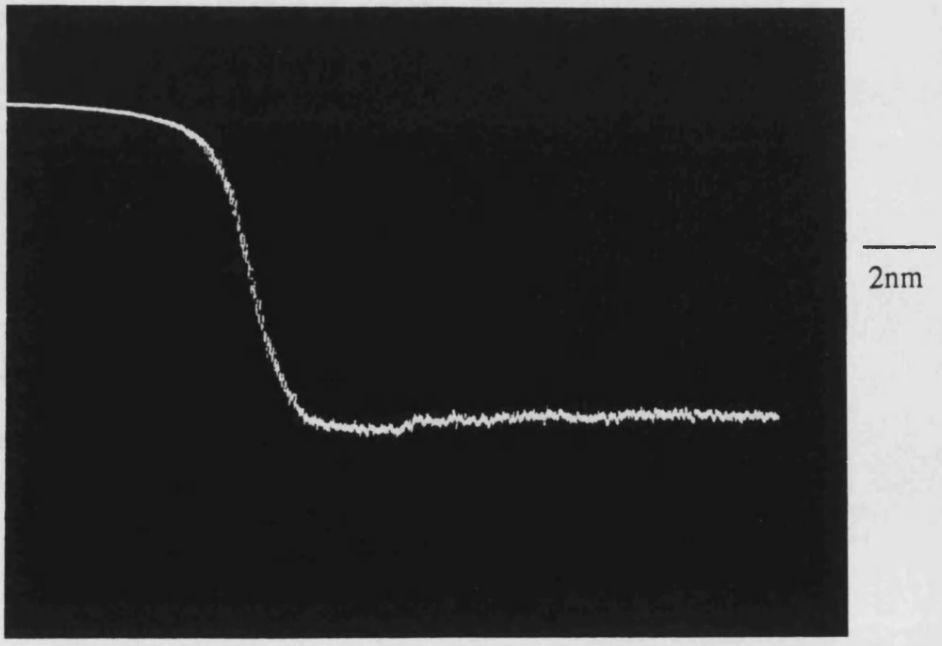

Figure 4.16 Dark-field electron intensity profile obtained by scanning across edge of magnesium oxide crystal

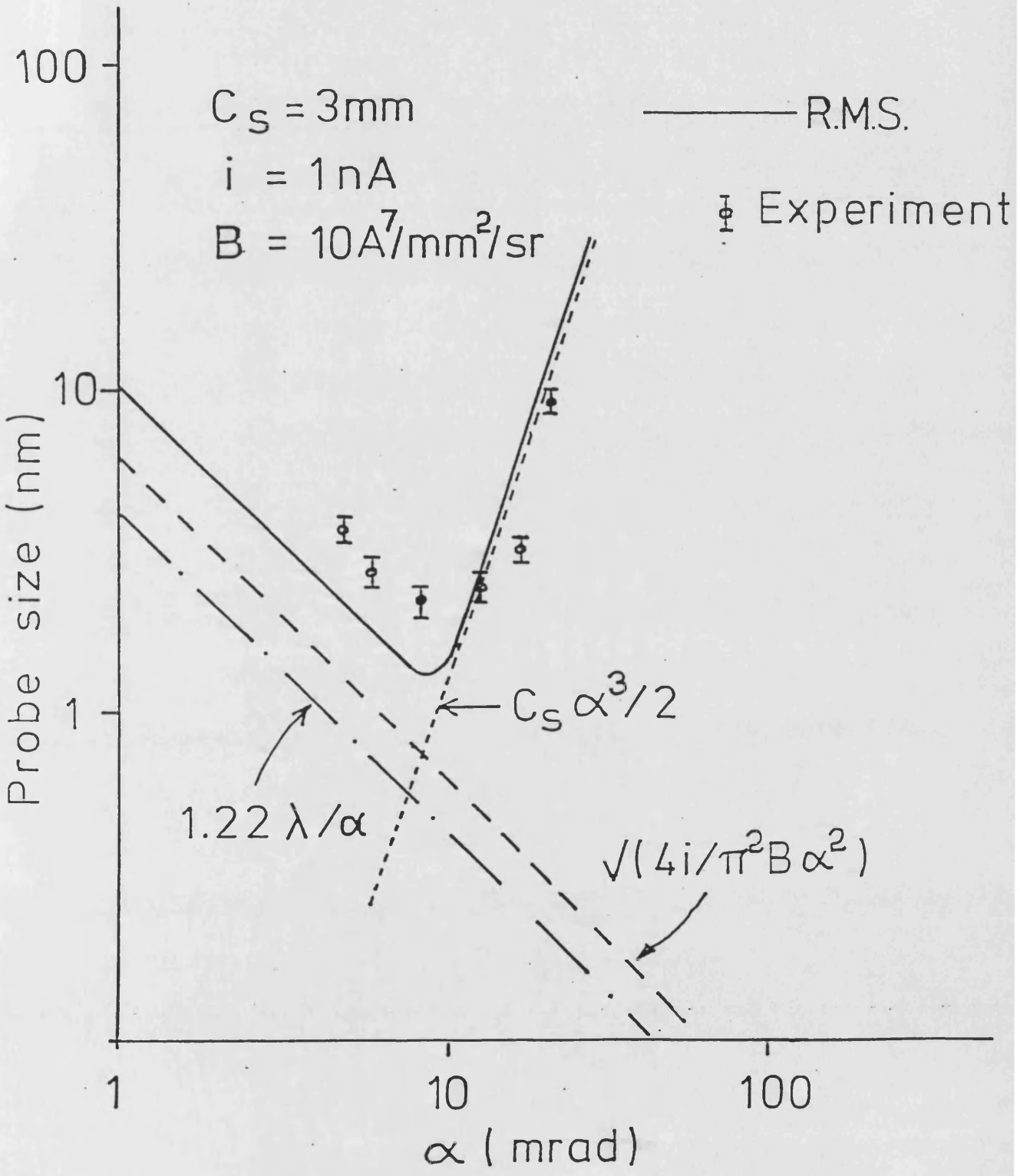

Figure 4.17 Variation in diameter of electron probe as a function of convergence angle

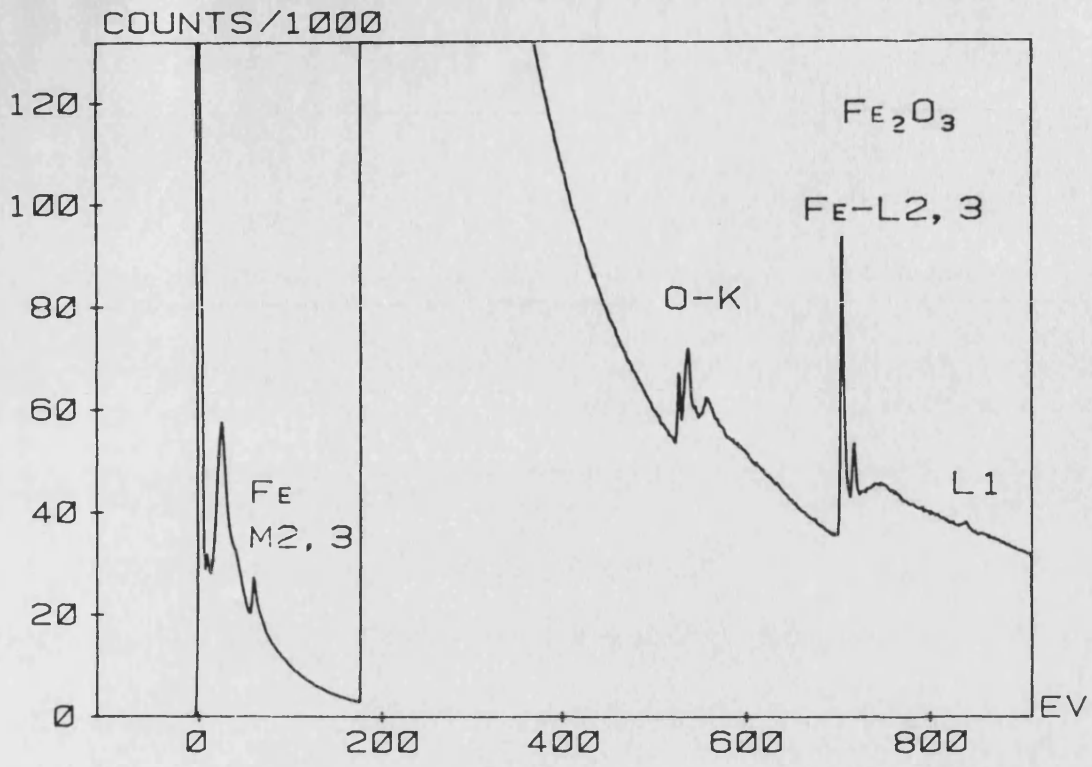

Figure 4.18 Typical EELS spectrum

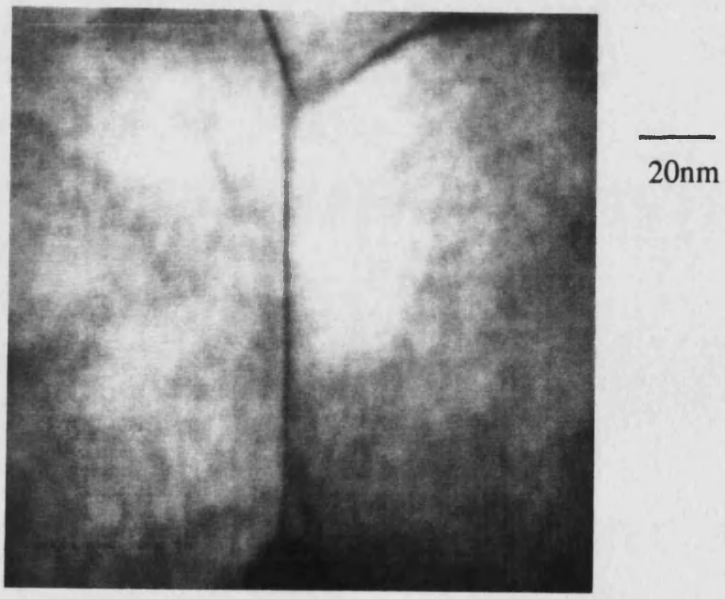

Figure 4.19 Prior austenite grain boundary in alloy S560 suitable for analysis

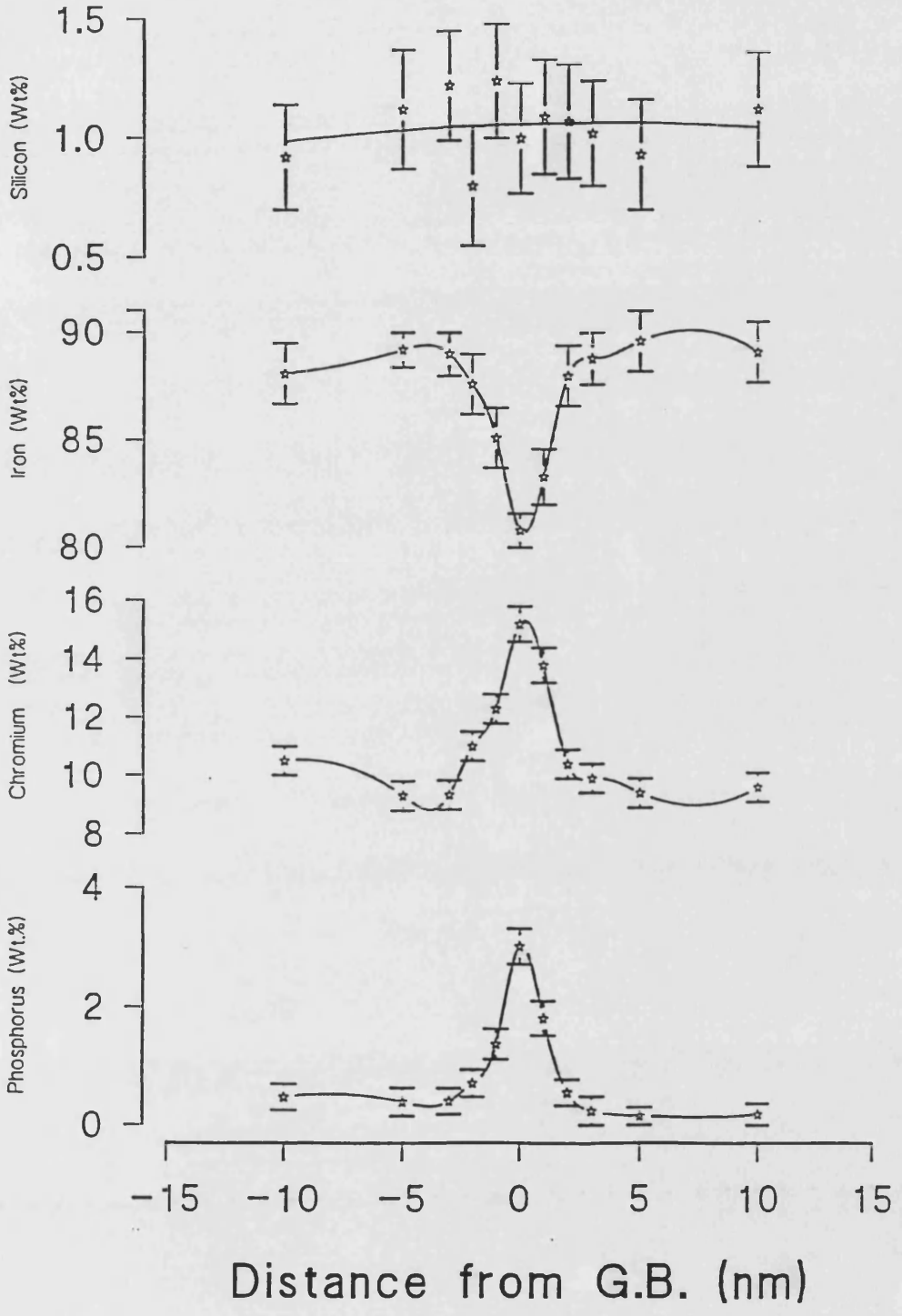

Figure 4.20 Chemical composition profile measured across a prior austenite grain boundary in alloy S560

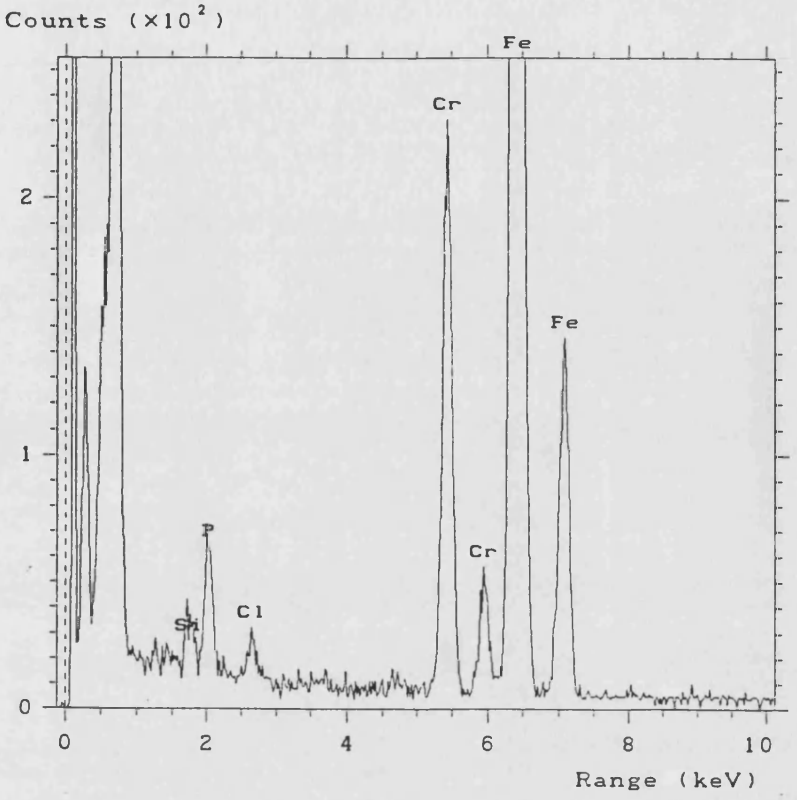

Figure 4.21a EDX spectrum collected with electron probe centred on grain boundary

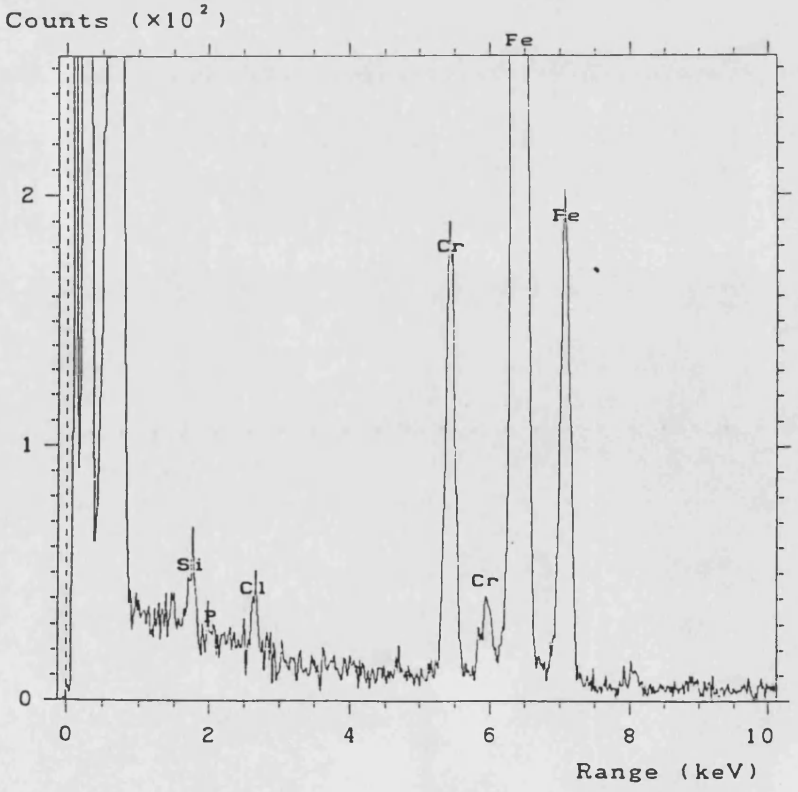

Figure 4.21b EDX spectrum collected with electron probe placed in matrix 5nm from grain boundary

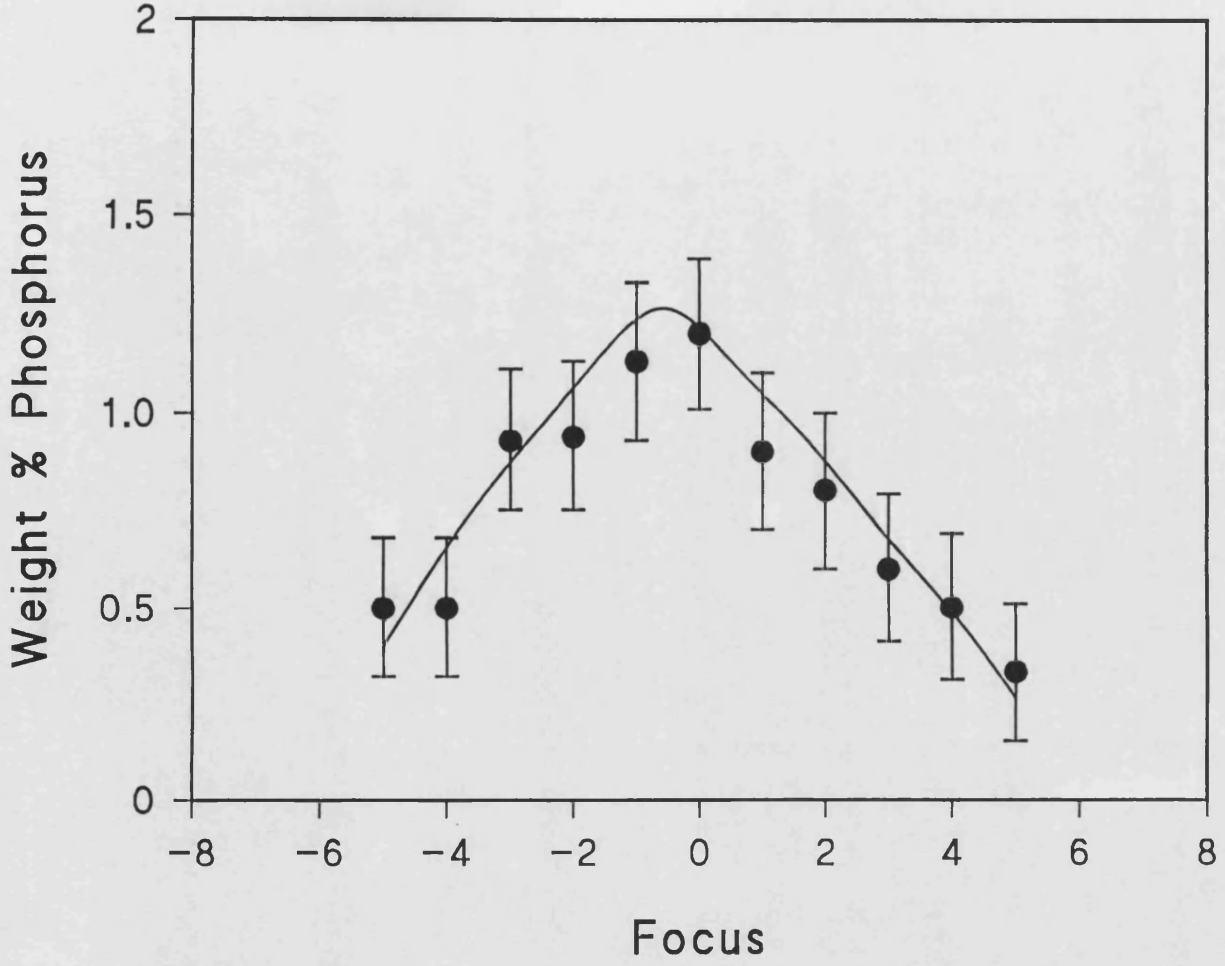

Figure 4.22 Variation of detected phosphorus signal as a function of focus

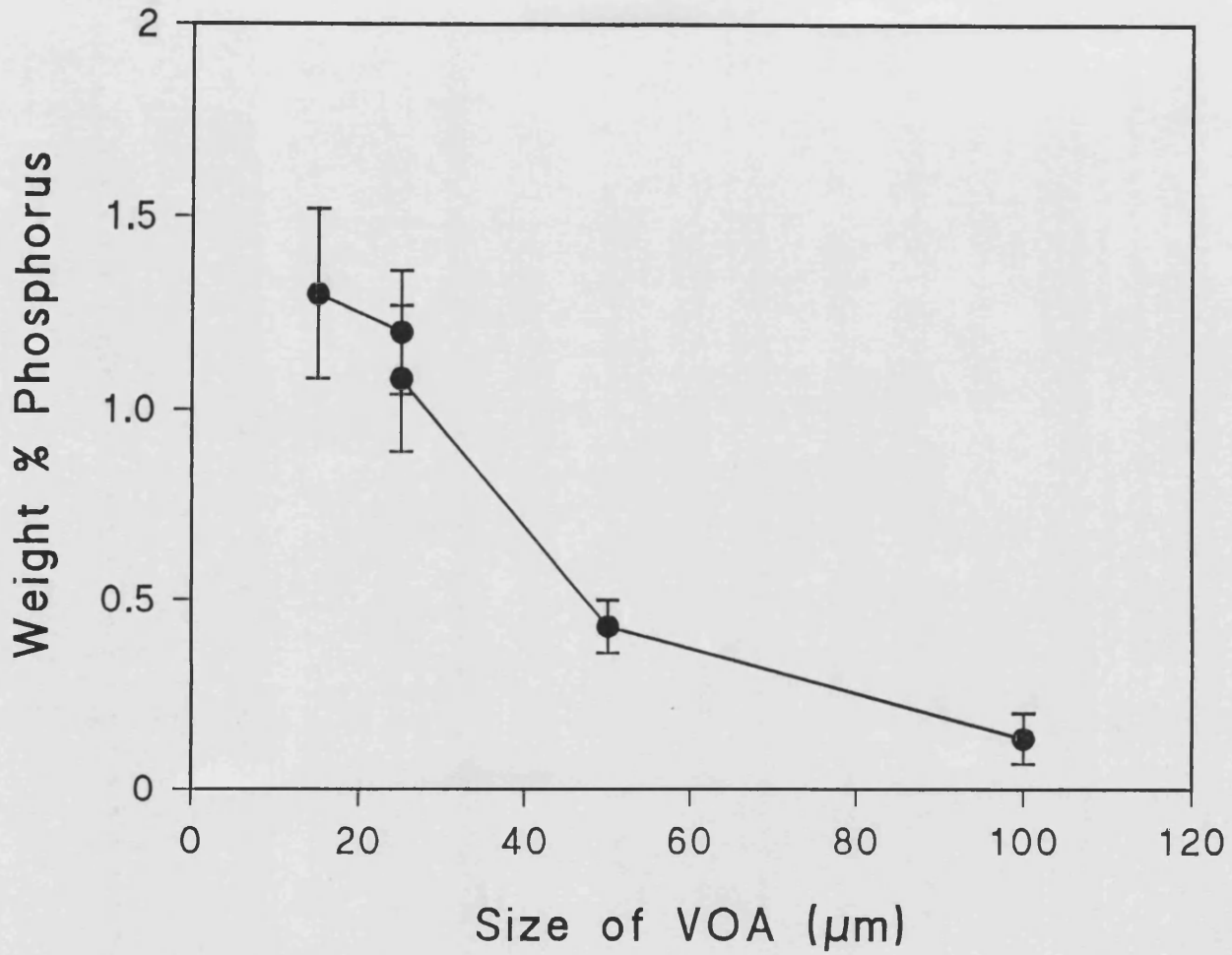

Figure 4.23 Variation of detected phosphorus signal as a function of electron beam diameter defining aperture

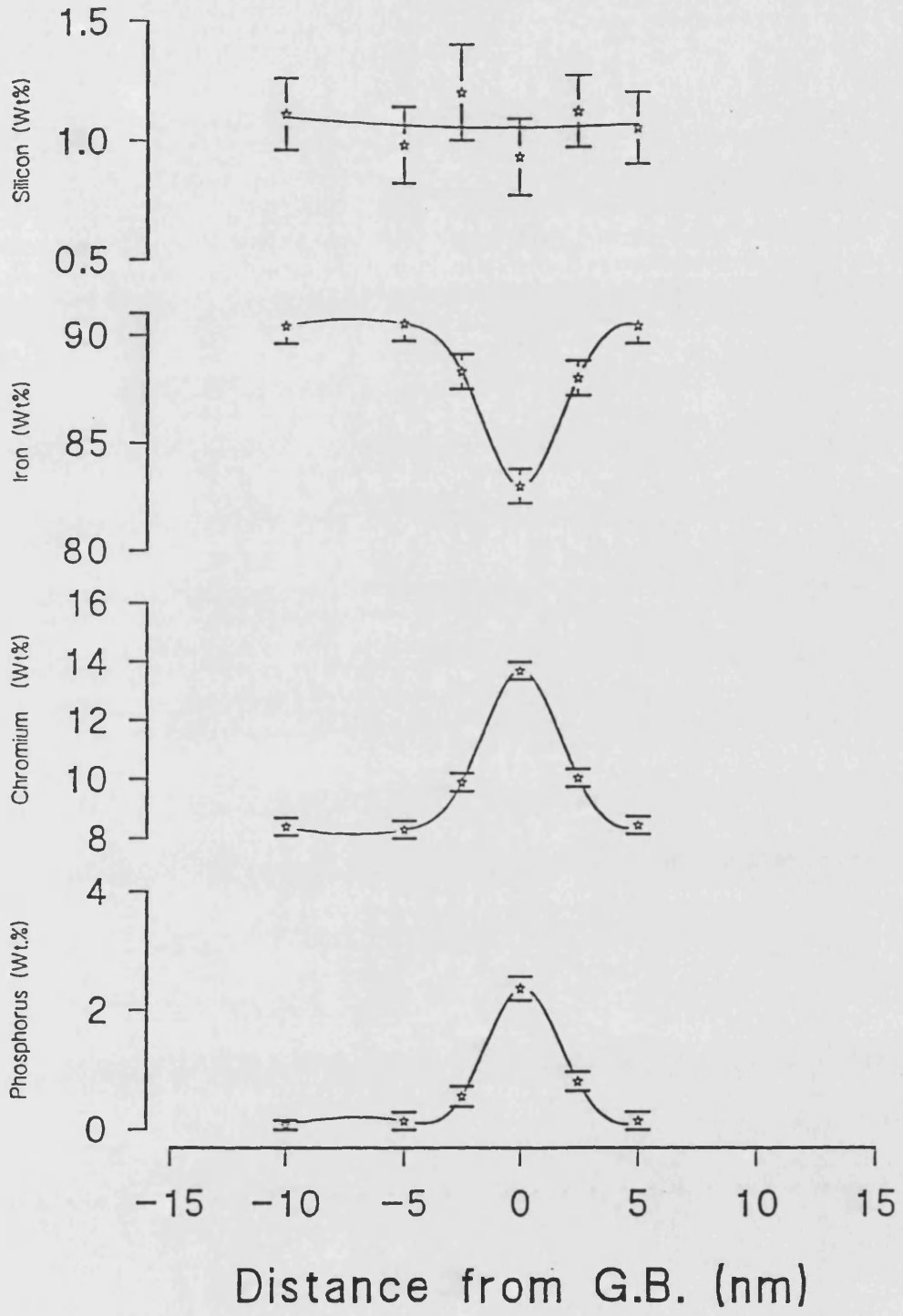

Figure 4.24a Chemical composition profile measured across a well oriented prior austenite grain boundary

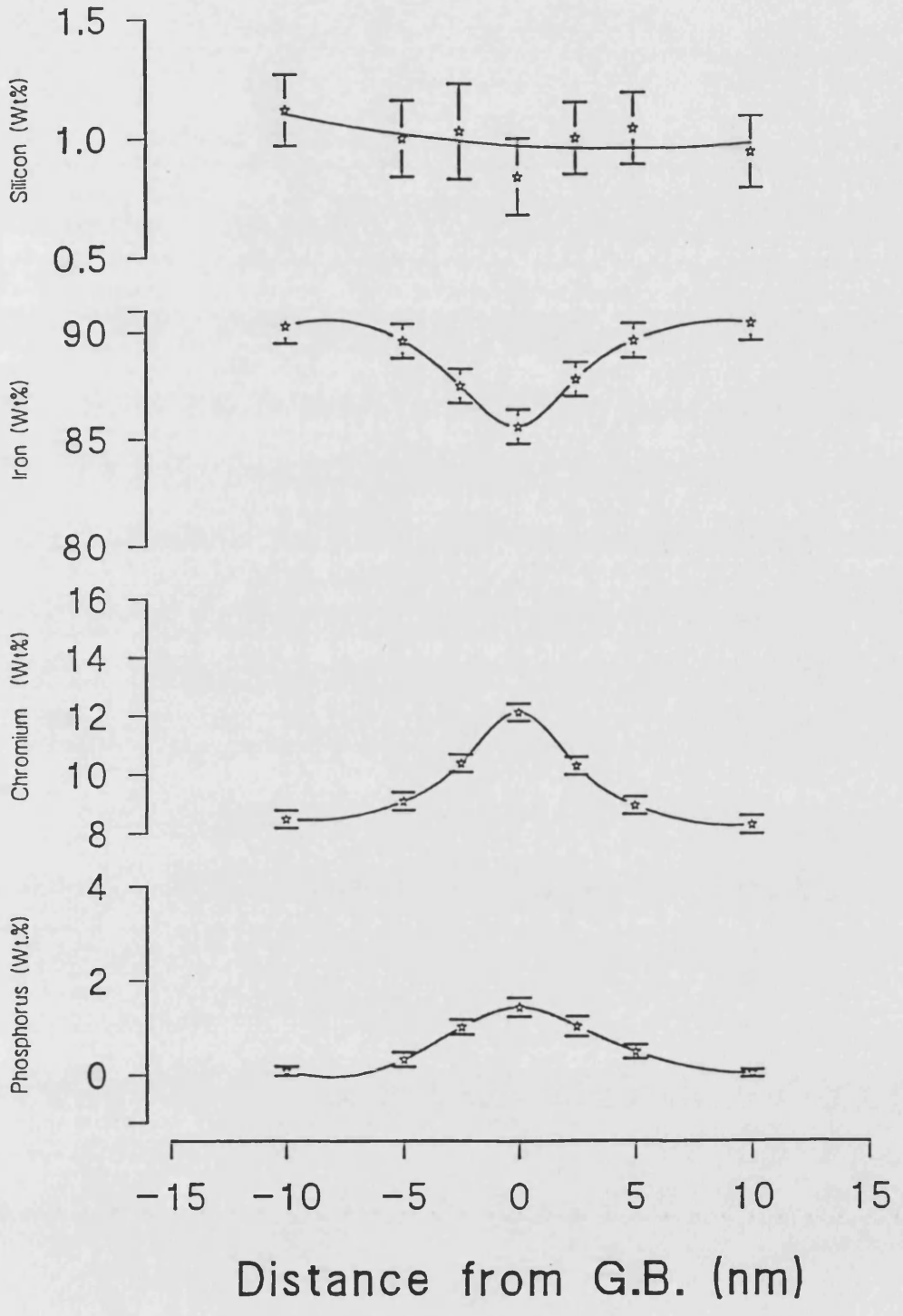

Figure 4.24b Chemical composition profile measured across a prior austenite grain boundary tilted 2.5° from ideal

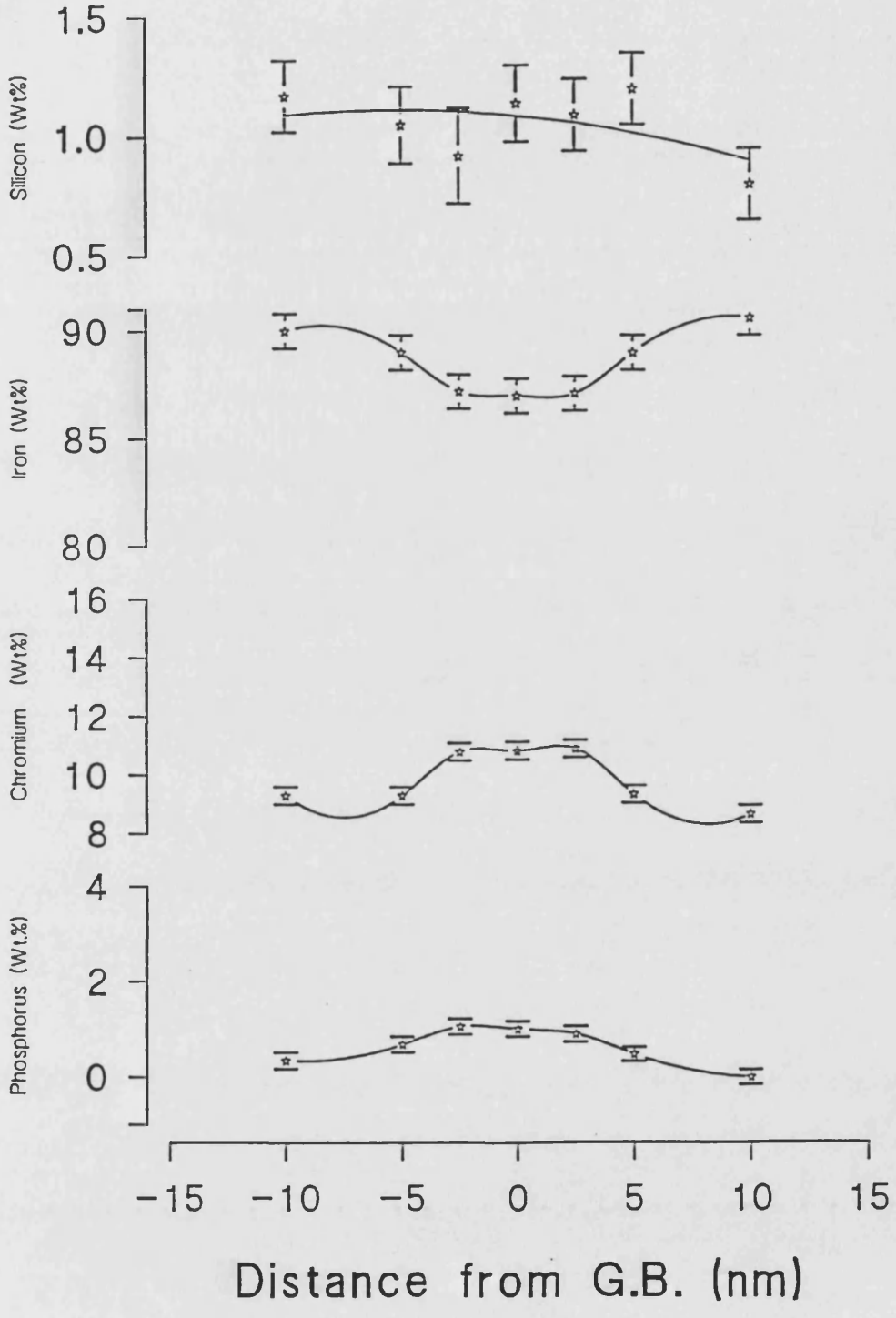

Figure 4.24c Chemical composition profile measured across a prior austenite grain boundary tilted 4° from ideal

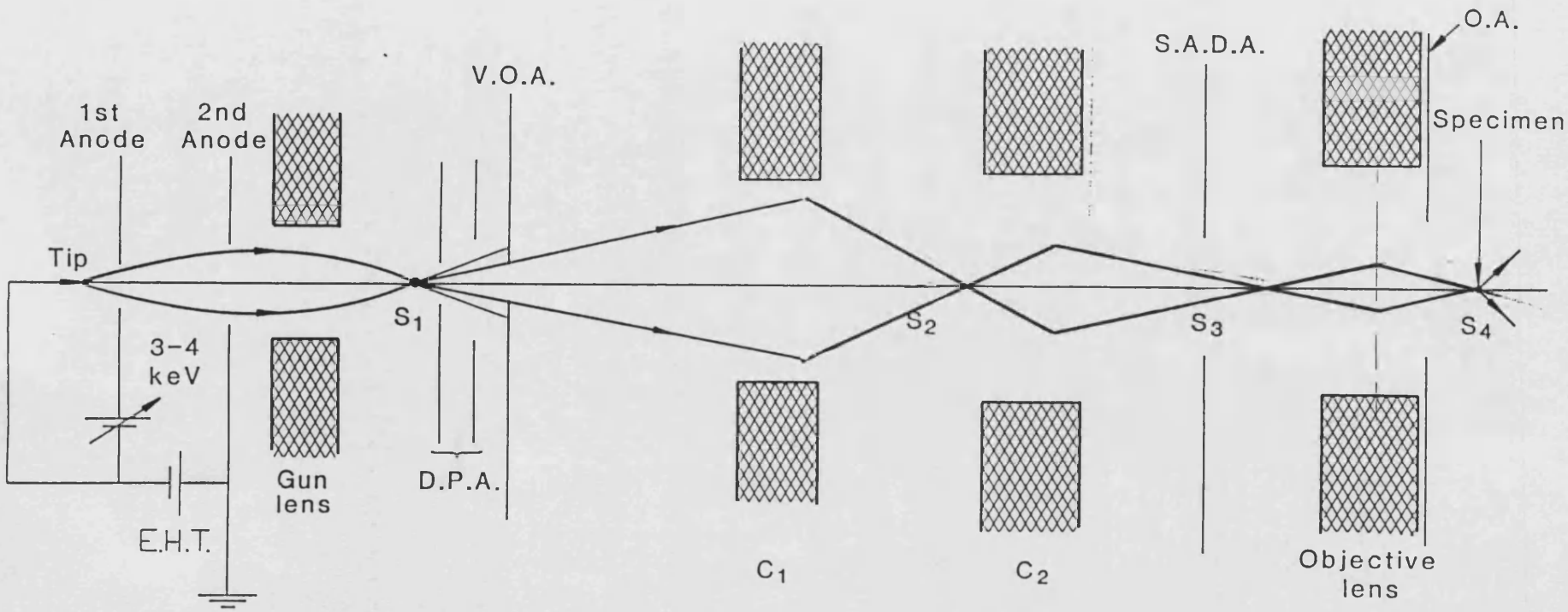

Figure 4.25 Electron ray diagram of STEM operating with reduced excitation of first condenser lens

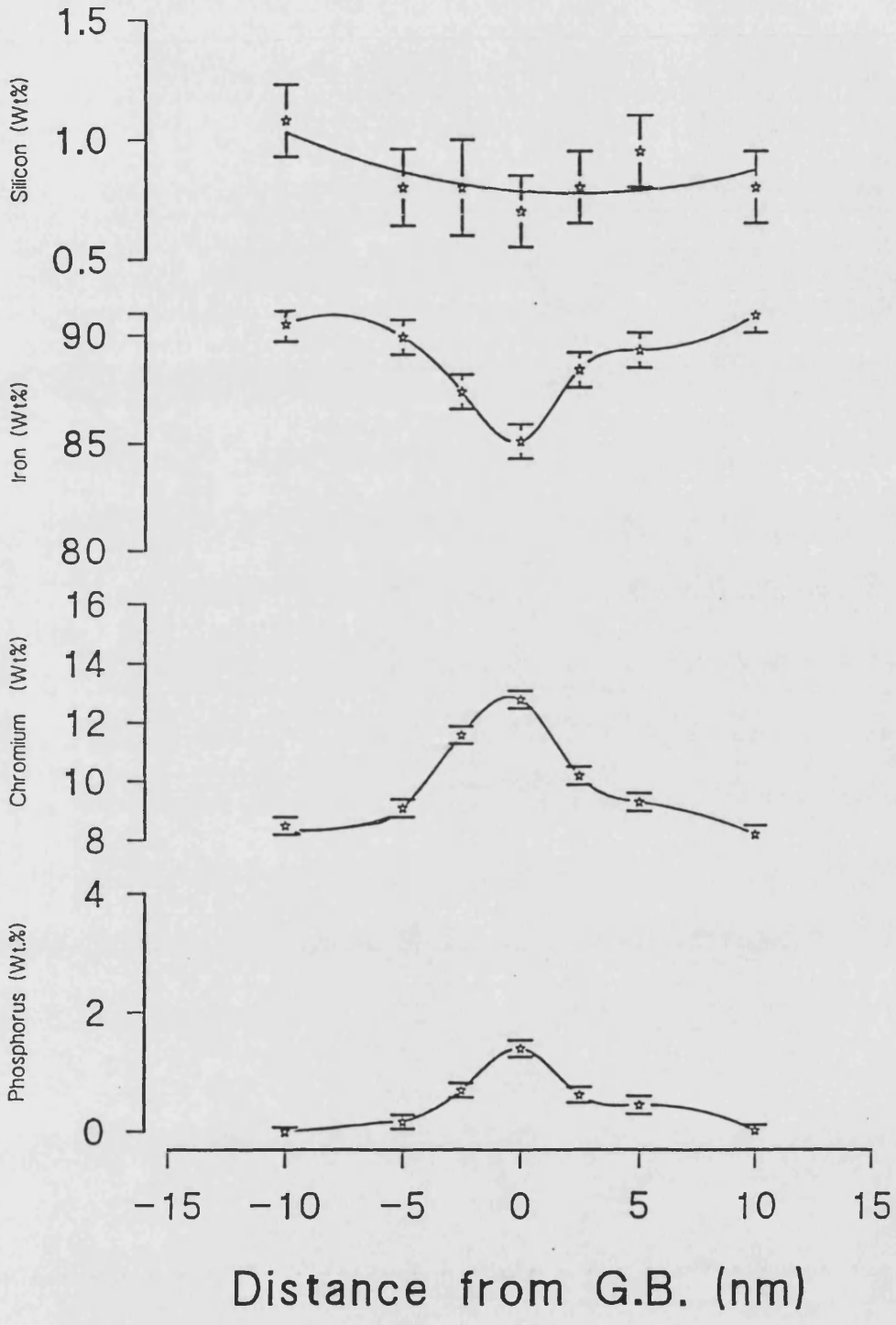

Figure 4.26 Chemical composition profile measured across a well oriented prior austenite grain boundary with reduced excitation of first condenser

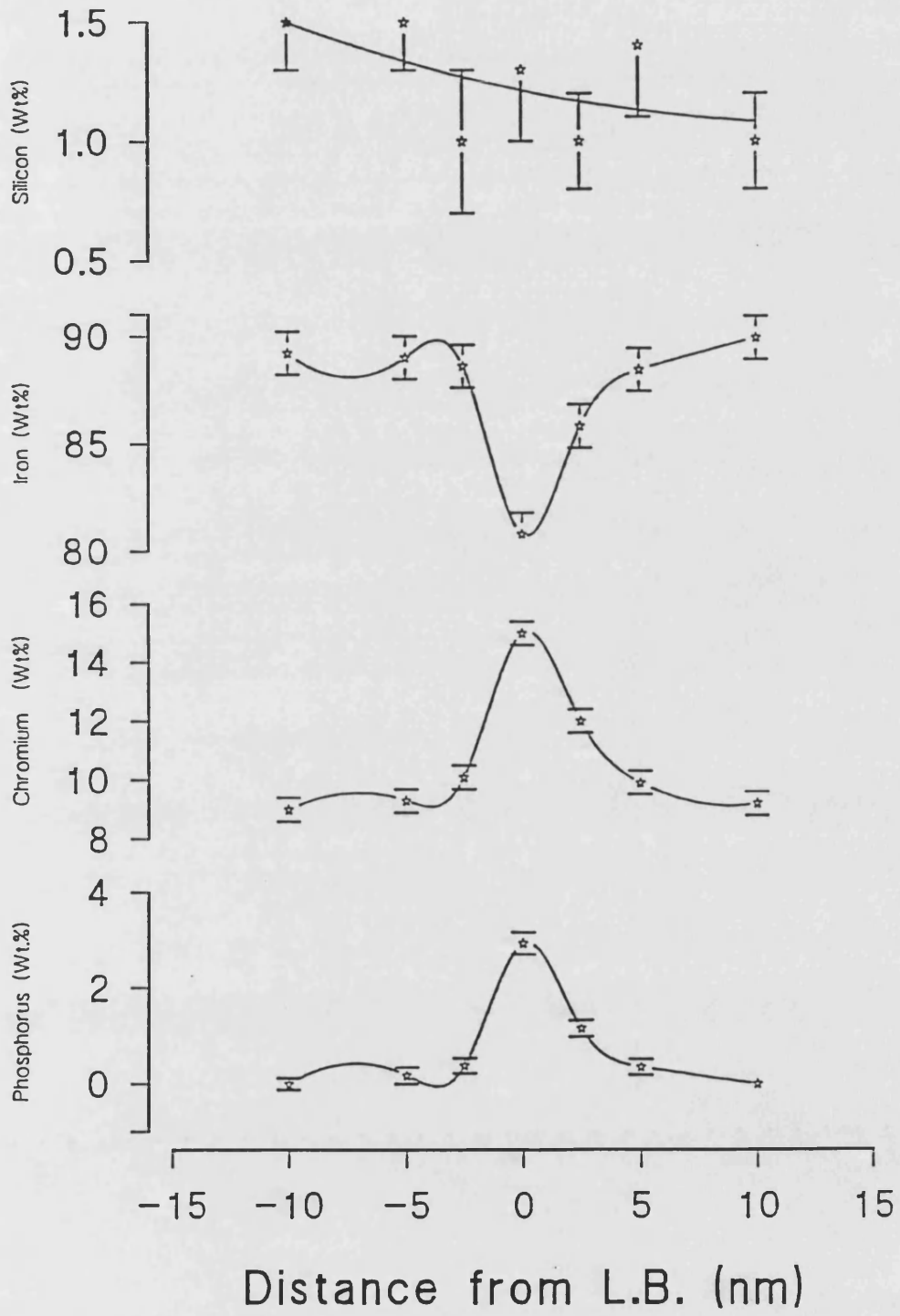

Figure 4.27 Chemical composition profile measured across a lath boundary in alloy S560

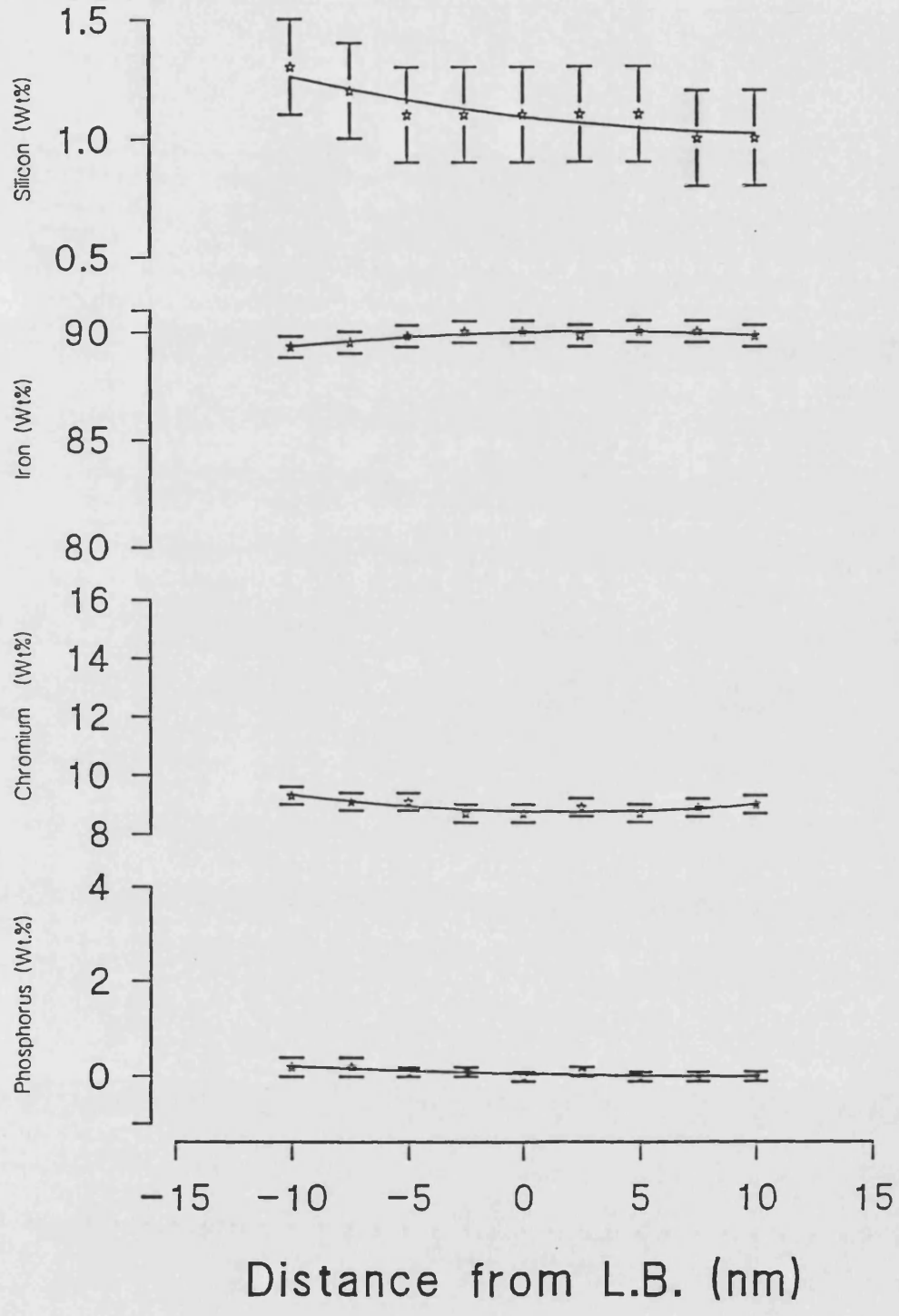

Figure 4.28 Chemical composition profile measured across a lath boundary in alloy S300

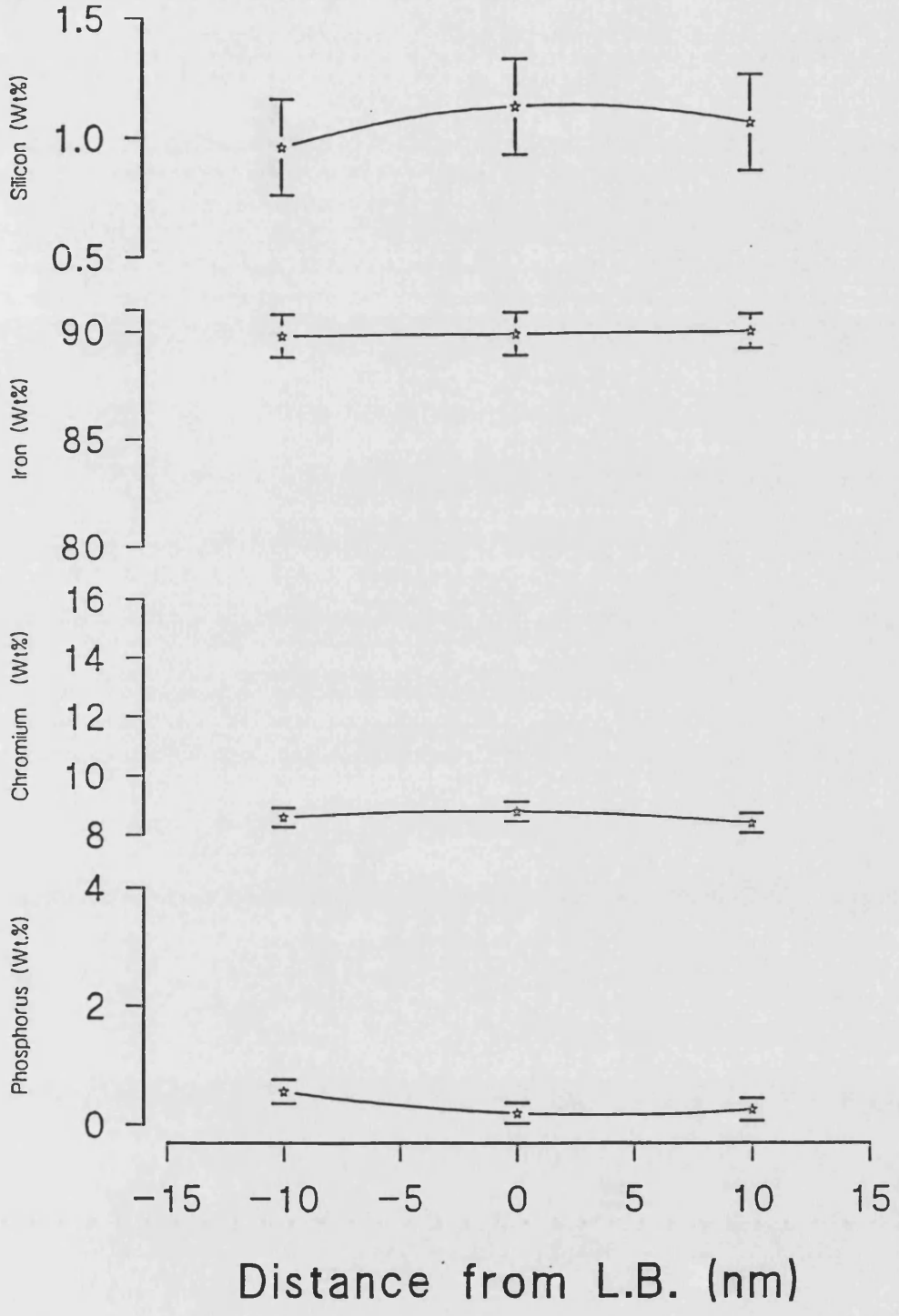

Figure 4.29 Chemical composition profile measured across a lath boundary in alloy S120

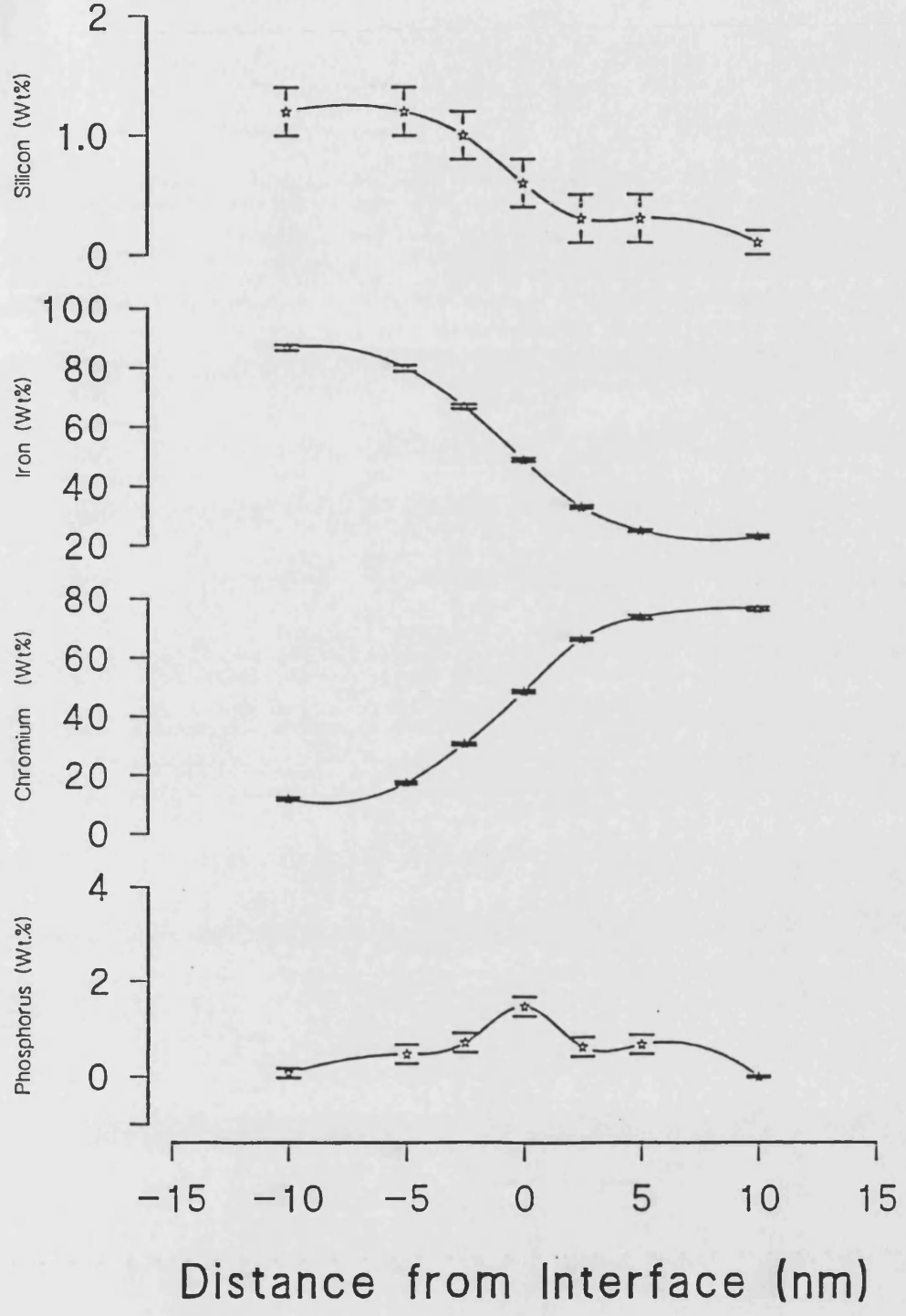

Figure 4.30 Chemical composition profile measured across a precipitate matrix boundary in alloy S560

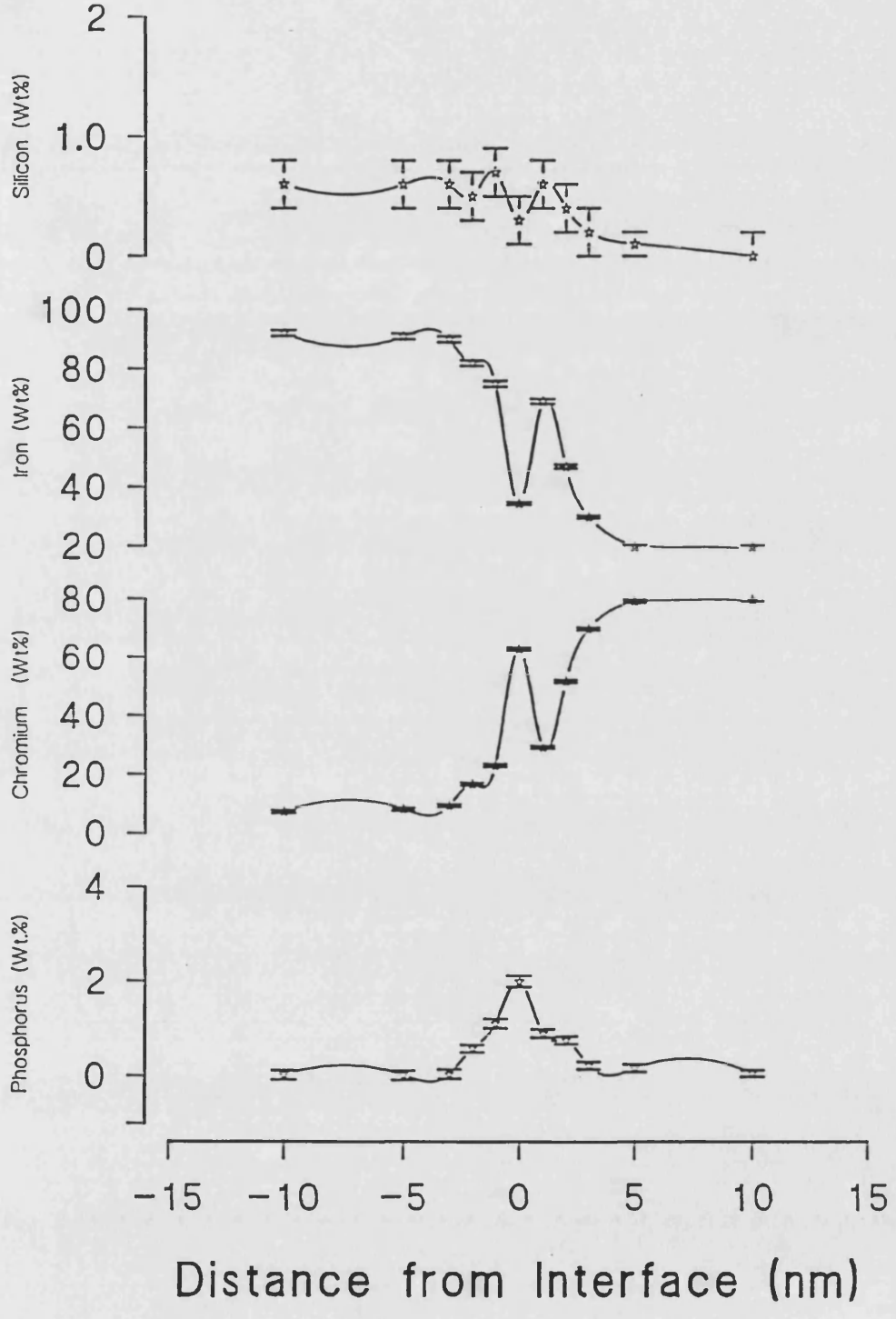

Figure 4.31 Chemical composition profile measured across a precipitate matrix boundary in alloy S300

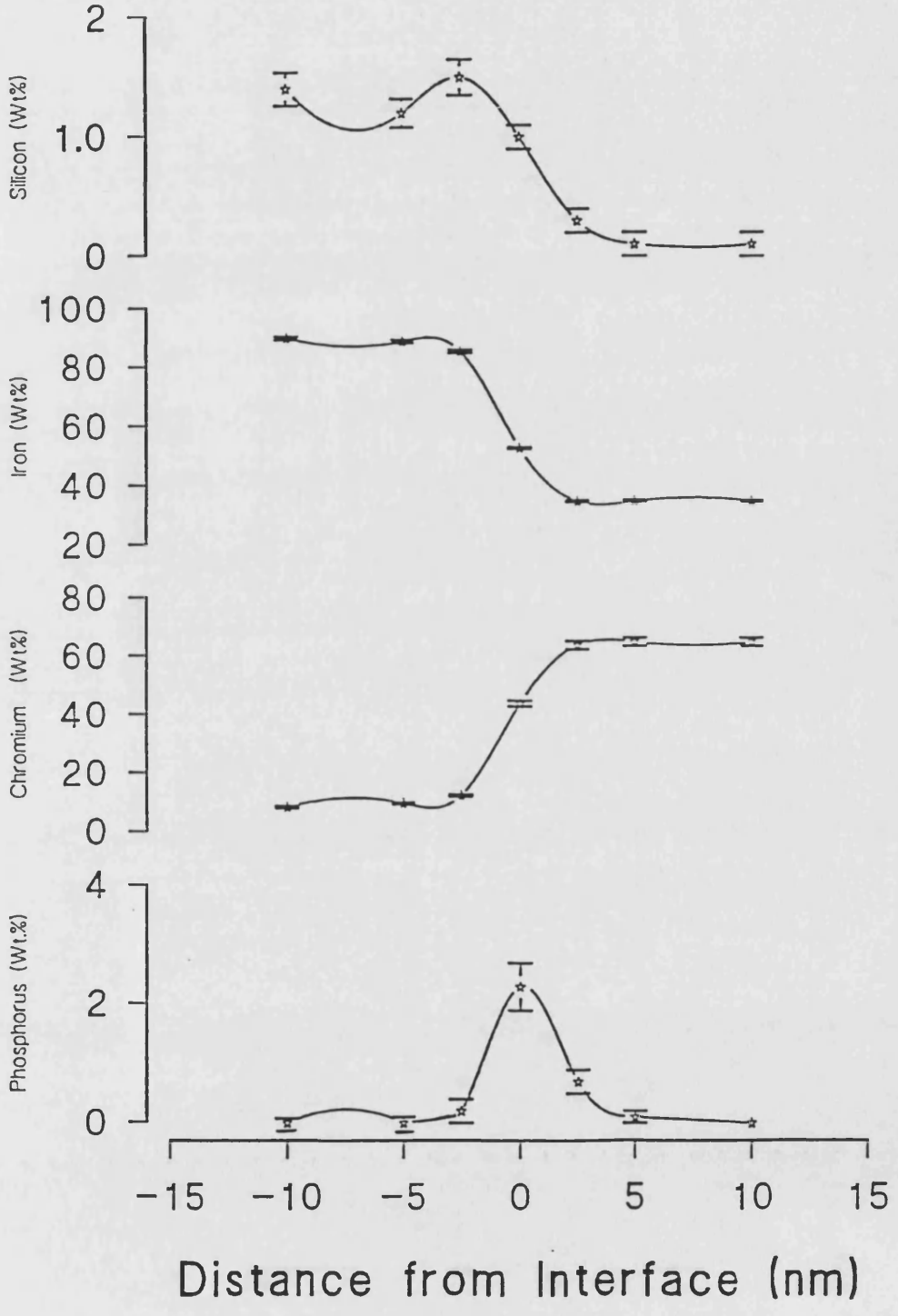

Figure 4.32 Chemical composition profile measured across a precipitate matrix boundary in alloy S120

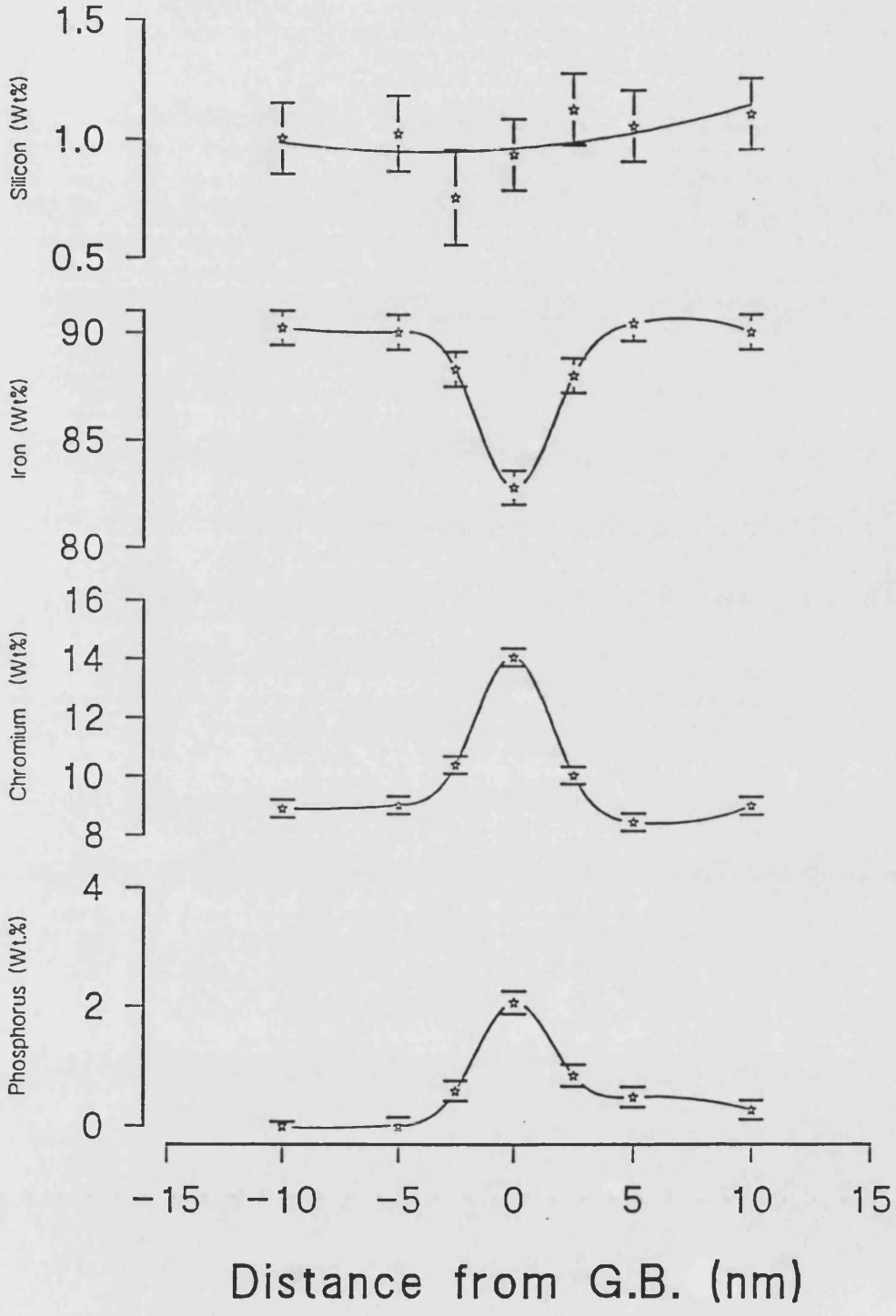

Figure 4.33 Chemical composition profile measured across a prior austenite grain boundary 15nm from a chromium rich precipitate

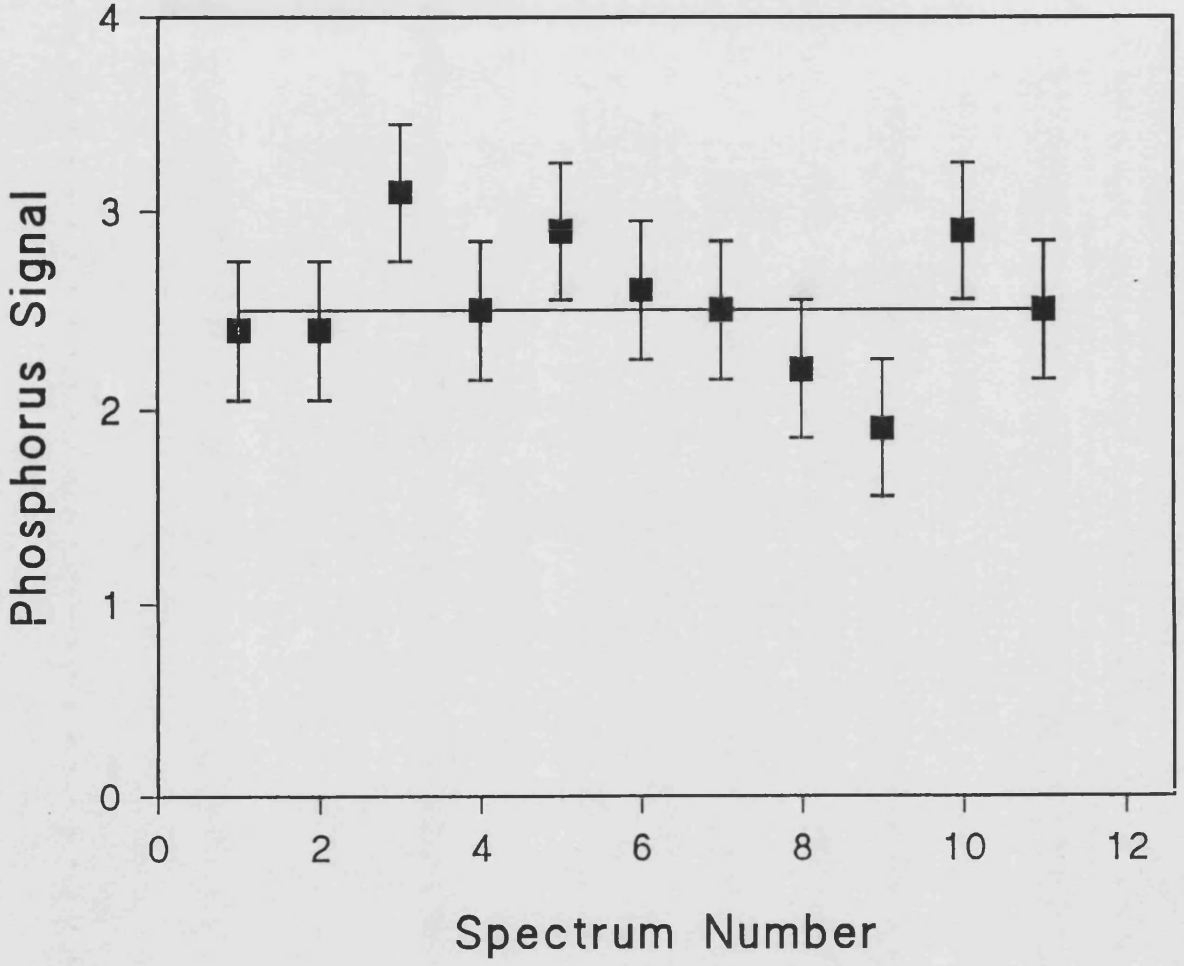

Figure 4.34 Variation of phosphorus signal detected as a function of electron exposure time

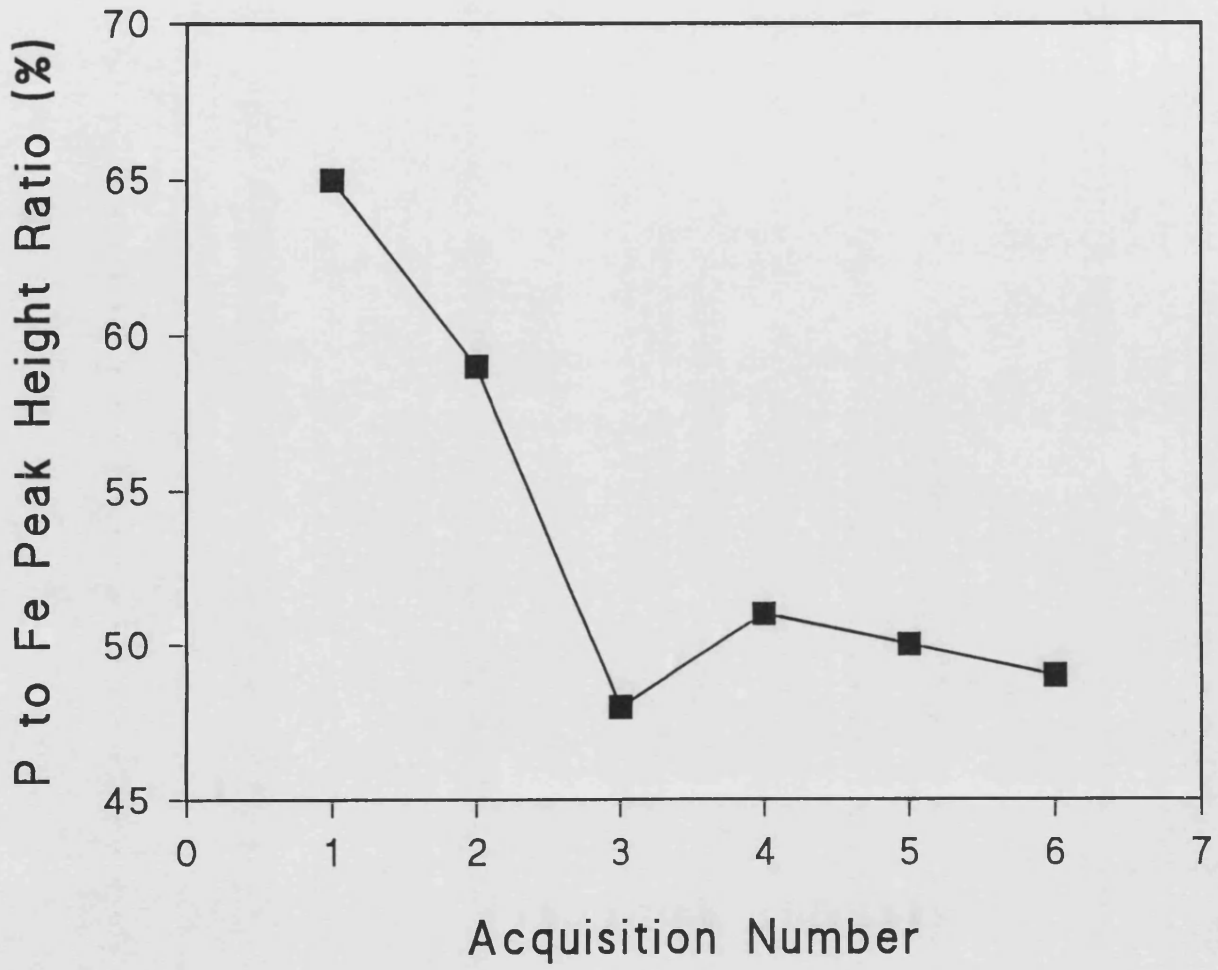

Figure 4.35 Variation of phosphorus-to-iron peak height ratio as a function of exposure to 10nA beam

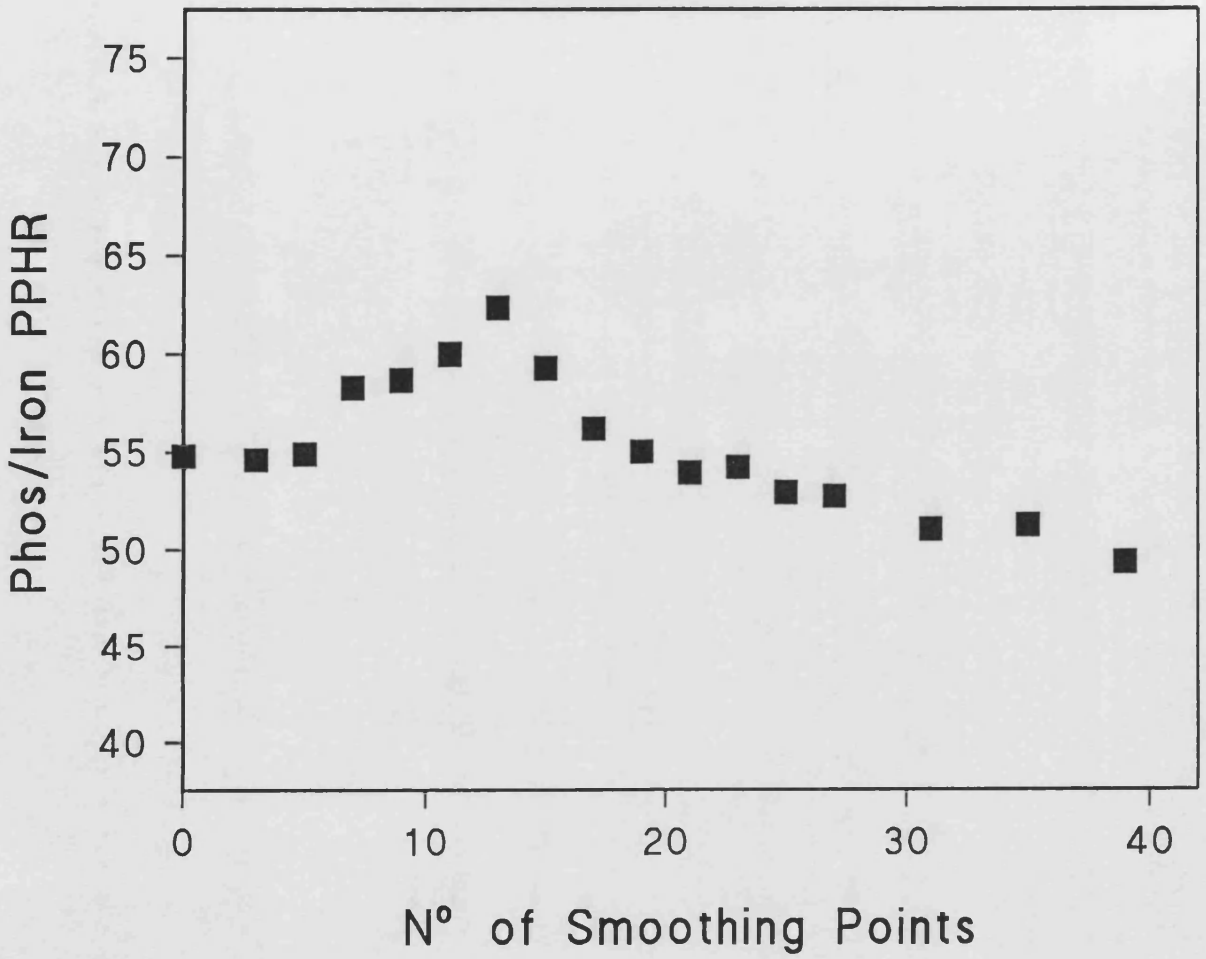

Figure 4.36 Variation of phosphorus-to-iron peak height ratio as a function of the number of smoothing points

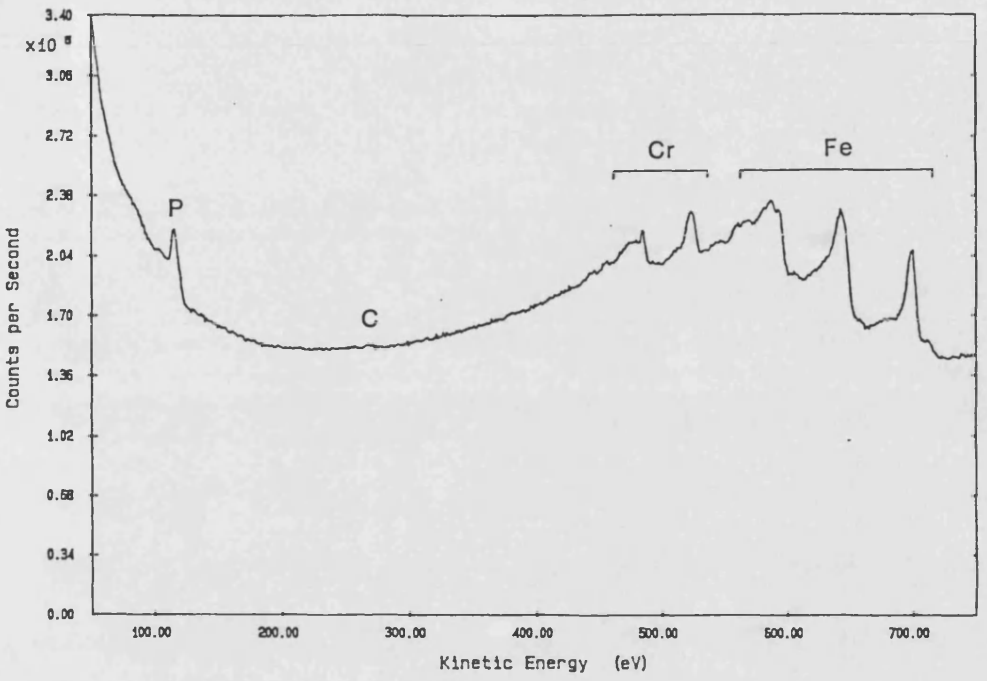

Figure 4.37a Direct Auger electron spectrum collected from intergranular facet

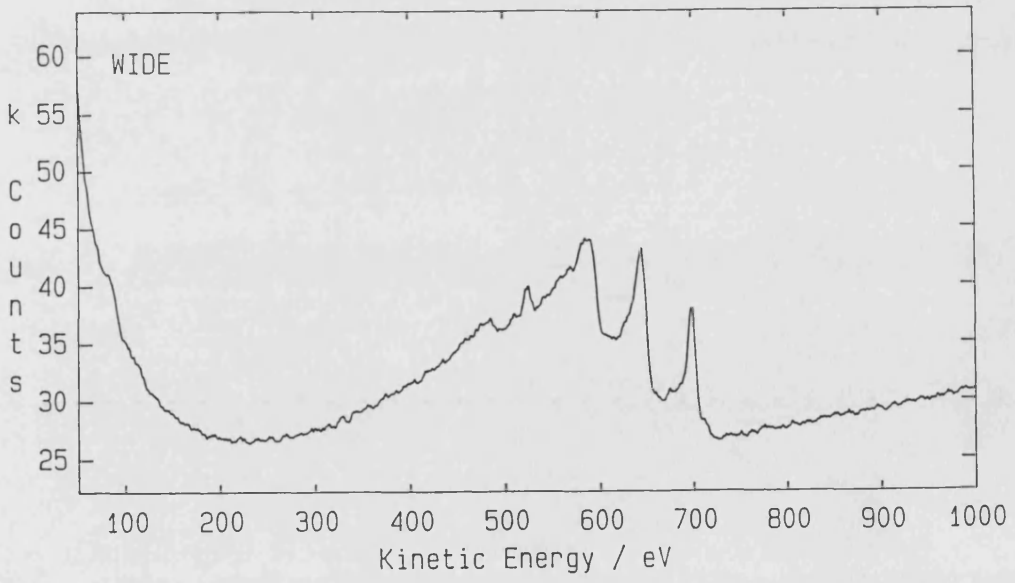

Figure 4.37b Direct Auger electron spectrum collected from transgranular cleavage

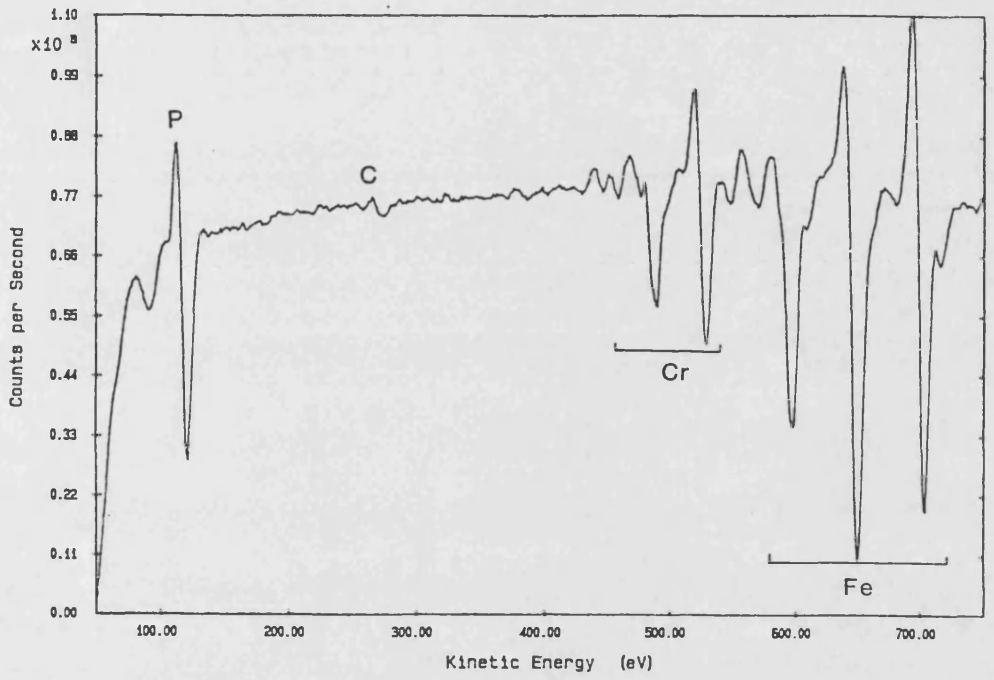

Figure 4.38a Differential Auger electron spectrum collected from intergranular facet

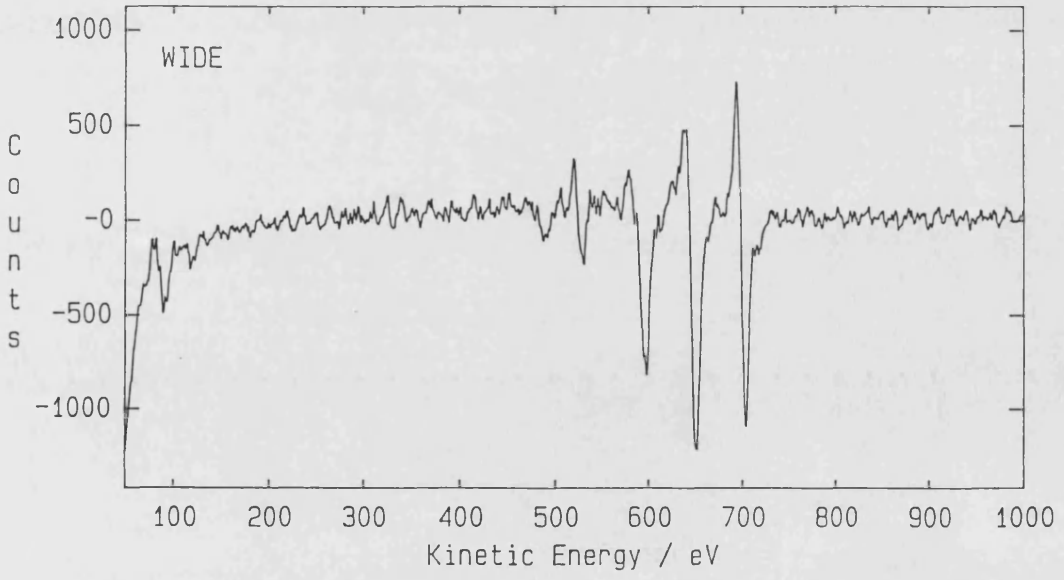

Figure 4.38b Differential Auger electron spectrum collected from transgranular cleavage

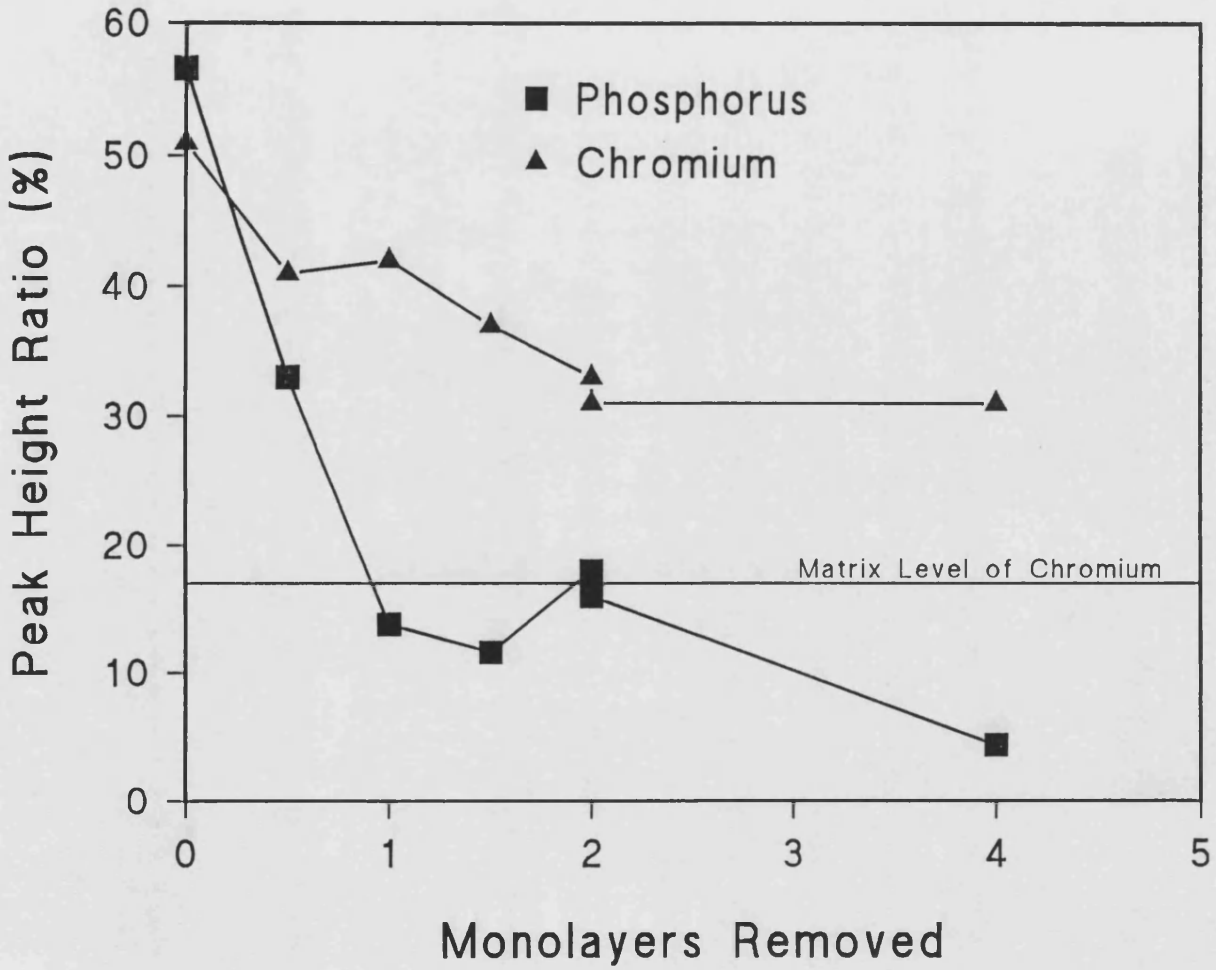

Figure 4.39 Variation in phosphorus and chromium signals as a function of depth perpendicular to the sample surface

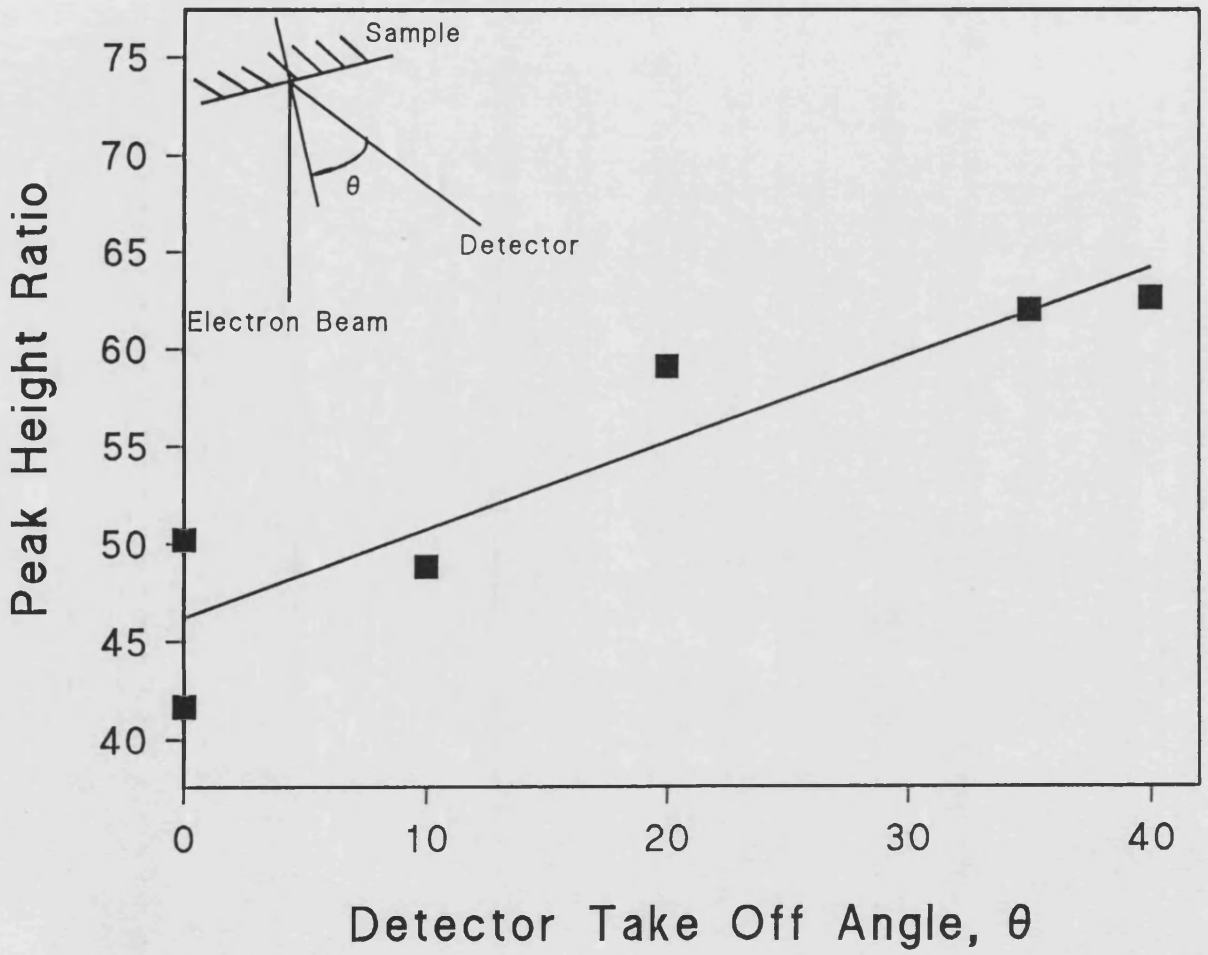

Figure 4.40 Variation of phosphorus to iron peak height ratio as a function of specimen tilt angle

Chapter 5 Processing of Data to Obtain Monolayer Coverages

This chapter develops and discusses the quantification routines used for converting the raw experimental data reported in chapter 4 into equivalent monolayer coverage of the interface by the segregating specie. When quantification is complete it will permit a comparison of the two techniques.

5.1 Monolayer Determination from Analytical Electron Microscopy Data

As stated in section 3.4.4 the quantification of x-ray emission spectra collected in the AEM produces a composition which is an average of the material through which the electron beam has passed. If the sample is not homogeneous on the scale of examination further processing of the data is required to arrive at the true distribution of elements within the sample. The experimental determination of equilibrium segregation to interfaces is such a case. This type of segregation occurs within one or two atom planes of the interface, i.e. <0.5nm (McLean 1957), whereas the electron probe in the HB501 used to determine the chemical composition is a minimum of 2.5nm in diameter as reported in section 4.2. The chemical composition profiles obtained using the HB501 have been converted into equivalent monolayer coverages using two different approaches. The first is a simple deconvolution of the electron beam intensity distribution with an assumed impurity concentration profile. The second approach utilises Monte Carlo calculations to model the interaction between the electron beam and a sample containing a thin layer of segregant.

5.1.1 Simple Deconvolution

For equilibrium segregation, such as the thermal segregation of phosphorus in iron, it is reasonable to assume that all of the segregated specie is concentrated at the interface under examination. The chemical composition profile measured in the AEM can then be approximated by a simple convolution of the electron distribution within the probe with the segregant which is assumed to form a delta function at the grain boundary. The electron distribution within the focused probe can be described by the Gaussian formula shown below.

$$i(x) = \frac{1}{\sigma \sqrt{(2\pi)}} .\exp(-x^2/2.\sigma^2) \qquad 5.1$$

It can be confirmed that this expression has the two essential mathematical properties of the Gaussian: (1) there is unit integrated intensity between $\pm\infty$, and (2) the second moment of the expression equals σ^2, where σ is the standard deviation. If the electron probe is positioned symmetrically on a segregated interface the proportion of the electron flux contained in the probe which passes through the segregant layer, and therefore capable of exciting characteristic signals, is the product of the width of the segregated layer and the height of the Gaussian probe. This is shown diagramatically in Figure 5.1. The full width at half maximum of the electron beam is determined by drawing a Gaussian through the experimentally determined chemical composition profile. The fractional path length of the electrons in the segregant is determined from the x-ray spectrum collected with the electron beam positioned on the interface. The electron path length calculated by this method is in terms of atomic percent, it is therefore necessary to ensure that the x-ray data are similarly atomic percent in preference to the usual weight percent. These parameters allow the effective thickness of the segregant layer to be calculated from the following equations.

$$\sigma = \frac{FWHM}{2.35} \qquad 5.2$$

$$d = P\,\sigma\,\sqrt{(2\,\pi)} \qquad \text{assuming } P \ll 1 \qquad 5.3$$

where P = Fractional path length of electrons in segregant

d = Width of segregant layer

This gives a measure of the effective width of the segregant layer at the interface. If the atomic density at the interface is assumed to be similar to that of the matrix and the segregation occurs by the substitution of phosphorus or chromium for iron at the interface. The equivalent percentage coverage of the interface by segregant can then be calculated by dividing the thickness of the segregant layer by the close packed interplanar spacing of iron.

The procedure outlined above does not directly include corrections for the effects of beam broadening. However, beam broadening will have a tendency to produce an experimentally determined profile with a more extensive FWHM and a lower peak value. The simple quantification technique is in part limited by the accuracy with which a Gaussian can be drawn through the experimentally determined points and the confidence in the peak segregation signal collected with the electron probe centred on the interface. When reduced profiles have been collected an average value of FWHM of the electron distribution has been used to allow calculation of segregant coverage at the interface.

This simple convolution procedure can be used to determine the interfacial coverage of both phosphorus and chromium. In the case of chromium the boundary enrichment has been calculated by subtracting the matrix concentration measured remote from the boundary from the level measured on the boundary. X-ray spectra collected from the matrix in each alloy did not exhibit phosphorus peaks with statistical significance, therefore to determine phosphorus enrichment the matrix

level of phosphorus was assumed to be zero. The distribution of monolayer coverages calculated for each of the alloys are shown in figures 5.2 to 5.5 for phosphorus and figures 5.6 to 5.9 for chromium. The mean level of phosphorus coverage of boundaries is 0.79 (σ=0.25) monolayers in alloy S560, 0.68 (σ=0.24) in alloy S300, 0.32 (σ=0.14) in alloy S120 and 0.08 (σ=0.04) in alloy S25. The figure in brackets represent the standard deviation of the experimental points. The average enrichment of the boundaries by chromium is 0.89 (σ=0.16) monolayers in alloy S560, 0.87 (σ=0.29) in alloy S300, 0.43 (σ=0.28) in alloy S120 and 0.44 (σ=0.22) in alloy S25.

5.1.2 Monte Carlo Calculations

One of the drawbacks of the simple deconvolution method is that it does not implicitly or explicitly address the effects of beam broadening but assumes that the probe size at the exit side of the foil is the same as the initial probe size. In reality this is not true. The primary beam of energetic electrons undergoes scattering as it interacts with the atoms in the sample. The consequent spreading of the electron beam is a factor which limits the spatial resolution for chemical analysis when using the AEM technique. The extent to which beam broadening occurs in the thin samples used in transmission electron microscopy is much reduced from that experienced in bulk samples, as examined in the SEM, due to the reduced number of scattering events which occur before the electron beam exits the lower surface of the AEM sample.

The extent of beam broadening is dependant upon the atomic number of the sample, the thickness of the sample and the energy of the electron beam. Electron scattering increases with increasing atomic number of the sample, specimen thickness and decreasing electron energy. A simple estimate of beam broadening can be obtained from the following equation (Goldstein et al 1977).

$$b = 6.25x10^{-5} (Z/E_o) t^{3/2} (\rho/A)^{1/2} \quad 5.4$$

where b is the beam diameter on the exit side of the electron transparent sample (cm), E_o the primary beam energy (eV), t the sample thickness (cm), ρ the sample density g/cm^3, and Z and A are the atomic number and atomic weight of the sample respectively.

The electron scattering can alternatively be modelled using a computer to conduct a Monte Carlo simulation. In Monte Carlo calculations the passage of each electron is modelled at each stage of its passage through the foil. This is achieved using various simple equations. The equations calculate the distance between elastic scattering events, as these are the events which result in large angular deviations, and the polar and azimuthal angles of deviation of the electron from its previous trajectory. This is shown schematically in figure 5.10. The proportion of energy which is lost by the electron as a consequence of inelastic scattering along the trajectory during its passage through the TEM sample is small due to the relatively low number of inelastic scattering events encountered by the beam. This is confirmed by observing the EELS spectrum obtained from a thin foil in which the current in the low loss region (e.g. below 200eV) greatly exceeds the current in the remainder of the spectrum. The programme, therefore, assumes a constant electron energy for all scattering events. A large number of electron trajectories are modelled to predict the behaviour of the electron beam. The accuracy of this technique is dependent on the accuracy of the equations used to model the electron-sample interaction.

The Monte Carlo programme used has been developed by Titchmarsh and is similar to that described by Newbury and Myklebust (1981). The elastic collisions between electrons and atoms in the sample are calculated using the relativistic, screened Rutherford elastic scattering cross-sections. The calculation incorporates a two-dimensional Gaussian current distribution in the incident probe. The probe

diameter, foil thickness and foil orientation can all be independently varied. The results of this Monte Carlo code have been independently verified by Hosoi (1989).

A knowledge of the trajectory of each electron can be utilised in the study of segregation in the AEM. If the sample through which the electron trajectories are modelled contains a thin layer of segregant on which the probe is centred, the path length of each electron in the segregant and in the matrix can be determined. Using the ionisation cross sections and the relative x-ray efficiencies for the relevant atoms the number of x-rays produced from each region can be calculated. This is compared to the experimentally determined chemical composition and the width of the segregant region in the model adjusted until the calculated value gives good agreement. The Monte Carlo experiment is repeated with the electron probe displaced from the boundary to construct a theoretical chemical composition profile which can be compared to the experimental data. Monte Carlo techniques can also be used to investigate the effect of altering the foil thickness, probe size and tilting the interface to determine theoretically the effect of these parameters on the detection of grain boundary segregants. The distributions of monolayer coverages calculated by Monte Carlo fitting are shown in figures 5.11 to 5.14 for phosphorus segregation and figures 5.15 to 5.18 for chromium segregation. The average levels of coverage of the boundaries by phosphorus are 0.79 (σ=0.16), 0.75 (σ=0.17), 0.51 (σ=0.29) and 0.07 (σ=0.03) monolayers in alloys S560 to S25 respectively. The average levels of chromium segregation calculated for each of the alloys are 0.88 (σ=0.16) monolayers in alloy S560, 0.78 (σ=0.22) in alloy S300, 0.61 (σ=0.25) in alloy S120 and 0.64 (σ=0.2) in alloy S25.

5.2 Monolayer Determination from Auger Electron Spectroscopy Data

The quantification routines for AES data outlined in section 3.6.4 assume chemical homogeneity in a direction perpendicular to the sample surface. In this study the composition of the surfaces studied are not homogeneous but consist of overlayers of phosphorus and chromium segregant on the matrix and more extensive quantification is therefore required to deconvolute the experimental data to obtain equivalent monolayer coverages.

5.2.1 Quantification of the Extent of Interfacial Coverage

Before tackling the complex case of a two-component overlayer it is first necessary to consider the effect of a single component overlayer on the surface of a sample, shown schematically in figure 5.19, on the Auger signals detected. This situation has been considered in detail by Seah (1983).

The segregant may form either a continuous layer with a thickness d, or a discontinuous monolayer of fractional coverage ϕ. For equilibrium segregation the latter of these is most commonly encountered. Due to the inhomogeneity of the sample in the direction of the beam the signal detected from the matrix and segregant undergo markedly different absorption.

After exposure by fracture, Auger electrons are produced in the segregant layer by interaction with the primary electron beam as it enters the sample. When the primary electrons are scattered by atoms in the matrix some of the electrons will be deflected through sufficiently large angles for them to leave the sample, i.e. backscattered. These backscattered electrons pass through the segregant layer for a second time and can interact with the segregant atoms to produce further Auger emission. The equation used to calculate the Auger signal originating from the segregant therefore necessarily contains backscattering terms to account for this

additional source of Auger electrons. The Auger electrons produced in the segregant layer undergo attenuation within the layer; the magnitude of the attenuation is dependant upon their path length in the direction of the detector. The Auger signal from the segregated phosphorus, I_P, can be represented as:

$$I_P = \phi_P I_P^{\infty} \left[\frac{1+r_{Fe}(E_P)}{1+r_P(E_P)}\right] \{1-\exp[-a_P/\lambda_P(E_P)\cos\theta]\} \qquad 5.5$$

Where

ϕ_P = fractional coverage of segregated phosphorus

I_P^{∞} = sensitivity factor of phosphorus

$r_{Fe}(E_P)$ = Backscattering factor in matrix

$r_P(E_P)$ = backscattering factor in segregant

a_P = atom size of phosphorus

$\lambda_P(E_P)$ = inelastic mean free path of segregant Auger electrons in the segregant

θ = angle of Auger electron emission to the surface normal

The signal detected from the iron matrix, in the simple case of iron covered by a fractional monolayer, ϕ, of phosphorus, consists of two components. The first component is from the exposed matrix and the second component is the matrix signal attenuated through the overlayer of segregant. The matrix signal can thus be represented as:

$$I_{Fe} = I_{Fe}^{\infty} \{1-\phi_P + \phi_P \exp[-a_P/\lambda_P(E_{Fe})\cos\theta]\} \qquad 5.6$$

where

$\lambda_p(E_{Fe})$ = inelastic mean free path of matrix Auger electrons in the segregant

Taking the ratio of these signals gives

$$\frac{\phi_p \{1-\exp[-a_p/\lambda_p(E_p)\cos\theta]\}}{1-\phi_p \{1-\exp[-a_p/\lambda_p(E_{Fe})\cos\theta]\}} = \frac{1+r_p(E_p)}{1+r_{Fe}(E_p)} \frac{I_p / I_p^{\infty}}{I_{Fe} / I_{Fe}^{\infty}} \qquad 5.7$$

It is assumed that upon fracture the segregant is equally divided between the two surfaces created. The monolayer coverage of the original interface is therefore twice the calculated value of fractional coverage, ϕ. The intensities (I) are measured from the experimental spectra and are the peak to peak height ratios determined from the derivative spectrum. The relative sensitivity factors are those for the particular experimental conditions (i.e. accelerating voltage and angle of incidence). The atomic size of phosphorus is calculated from an equation suggested by Seah (1983), based upon the density and packing of elemental phosphorus. $\lambda_p(E_p)$ and $\lambda_p(E_{Fe})$ are the inelastic mean free paths of the phosphorus and iron Auger electrons in phosphorus; these are used to account for the attenuation of the Auger electrons as they pass through the segregant layer. The inelastic mean free paths are calculated from the formulations of Seah and Dench (1979). The cosine θ term refers to the take-off angle of the detector and accounts for the increased path length of the Auger electrons at any given depth in the sample due to their path to the detector not being perpendicular to the sample surface. The terms containing r_p are backscattering factors. These account for the Auger electrons which are produced by the passage of backscattered primary electrons through the surface layer. The backscattering factors used in this study have been obtained from the work of Shimizu and Ichimura (1981).

The inelastic mean free path of an Auger electron has been studied by Seah and Dench (1979) and they have produced several empirical fits to the available experimental data, the exact form of which is dependent upon the class of material being investigated: elemental samples, organic and inorganic compounds. For an elemental sample:

$$\lambda_m = 0.41\ a_m^{1.5}\ E_m^{0.5} \qquad 5.8$$

λ_m = inelastic mean free path (nm)

a_m = atom size of element (nm)

E_m = Energy of Auger electron (eV)

The atom size is derived from the following equation

$$a_m^3 = \frac{A_m}{1000\ \rho_m\ N} \qquad 5.9$$

where A_m = Average atomic weight

ρ_m = Density (kg/m^3)

N = Avogadro's number

These equations have been used to calculate the atomic size of phosphorus and the inelastic mean free path of phosphorus Auger electrons in a matrix of phosphorus.

$$a_p = \frac{31.07}{1000 \times 1830 \times 6.023 \times 10^{23}}$$

$$= 3.04 \times 10^{-10}\text{m}$$

$$\lambda_m = 0.41 \times 0.304^{1.5} \times 115^{0.5}$$

$= 0.737\text{nm}$

A slight correction to equation 5.8 has been proposed by Seah and Dench (1979)

$$\lambda_m = \frac{538\, a_m}{E^2} + 0.41\, a_m^{1.5}\, E_m^{0.5} \qquad 5.10$$

This correction is largest for low energy Auger electrons. For phosphorus Auger electrons with an energy of 115eV the correction is less than 2%. Examination of figure 3.10 which shows the variation of inelastic mean free paths of Auger electrons with energy demonstrates that this correction is insignificant in comparison to the experimental scatter.

Equation 5.8 gives values of 1.18 and 1.82 nm for the inelastic mean free path of iron Auger electrons in an iron matrix and iron Auger electrons in a matrix of phosphorus, respectively. This latter value is required in order to calculate the attenuation of iron Auger electrons when passing through an overlayer of phosphorus.

An alternative formula for calculating inelastic mean free paths has been suggested by Penn (1976):

$$\lambda = E / [a\,(\ln E + b)] \text{ Angstrom} \qquad 5.11$$

E	energy of Auger electron, eV
a and b	constants dependant on electron configuration of host material and core levels of constituent atoms

Values of these constants can be obtained from tabulated data (Penn 1976).

e.g. for iron Auger electrons in an iron matrix the inelastic mean free path is given as

$$\lambda_{Fe}(E_{Fe}) = 700 / [\,21.1\,(\ln 700 - 3)]$$
$$= 9.34\text{Å} = 0.934\text{nm}$$

This compares with a value of 1.18nm calculated using the formulation of Seah and Dench amounting to a difference of 20%. Although larger, this is again below the experimental variation displayed in figure 3.10. In this study the inelastic mean free path values calculated from the formulations of Seah and Dench have been used.

The backscattering of electrons is dependent upon the material through which the electron beam is travelling, the energy of the electron and its angle of incidence with the sample. The value of backscattering factors has been evaluated by several authors using Monte Carlo calculations and empirical approximations. The most complete calculations are considered to be those of Shimizu and Ichimura (1981) who used Monte Carlo calculations to model the passage of electrons in samples. The value of the backscattering factor, 'r', increases with increasing atomic number of the sample, decreases with the depth of the core level, $E_{ax,}$ which is ionised and varies with angle of incidence and electron beam energy.

For a primary beam energy of 10keV and an angle of incidence of 30° Shimizu and Ichimura have produced the following parametric fit to their Monte Carlo data.

$$r = (0.462 - 0.777\,Z^{0.2})\,U^{-0.32} + (1.15\,Z^{0.2} - 1.05) \qquad 5.12$$

U = The overvoltage ratio $= \dfrac{\text{Primary beam energy}}{\text{Ionisation energy of x-shell electron}}$

Z = Atomic number or material

The value for the angle θ has been selected as 30°. In the standard configuration of the MA500 the sample is oriented such that the sample axis bisects

the angle between the electron gun and the concentric hemispherical analyser, nominally 60°, thus giving an angle of incidence of the electron beam and a detector take-off angle of 30°.

As has already been discussed, the equations for determining the chemical composition, be it the bulk composition or the determination of the extent of coverage by an overlayer, require the input of elemental sensitivity factors. Those used in this study were a combination of experimentally determined and literature values.

A literature value for the iron sensitivity factor of 0.21 (Sekine et al 1984) was used throughout the study. A first approximation for the sensitivity factor of chromium was obtained from the literature ($I_{Cr}^{\infty}=0.42$) (Sekine et al 1984). To validate this, spectra obtained from regions of transgranular fracture in the experimental programme which should not include signals from segregated chromium and only minimal contributions from the chromium rich carbides, were examined. The spectra collected from the transgranular regions can therefore be expected to reflect the bulk composition of the alloy. The literature values for sensitivity factors of iron, 0.21, and chromium, 0.42, were used to determine the matrix composition using the following equation.

$$C_A = \frac{I_A/I_A^{\infty}}{\Sigma_i I_i/I_i^{\infty}} \qquad 5.13$$

This gives an average experimental value of chromium concentration of 8 atomic percent, compared to a bulk composition determined (Wall 1987) for this alloy of 9.6 atomic percent (a discrepancy of approximately 20%). The sensitivity factor for chromium was therefore adjusted to compensate and the value of 0.34 used in the subsequent quantification. The phosphorus-to-iron sensitivity factor was determined experimentally using a sample of ferro-phosphorus which had been

previously characterised in the EPMA, as described in section 3.6.3. Using the collected data in equation 5.13 gave a value of I_P^{∞} of 0.54.

A variable introduced to the Auger spectra collected in this study, was the magnetic field which is produced by the ferritic steel of the samples examined. This introduction of additional magnetic flux into the analysis chamber can influence the trajectory of the Auger electrons which escape from the sample. The most susceptible of the Auger electrons are those with the lowest kinetic energy. The consequence of this additional magnetic field was to decrease the low energy Auger signal detected. To compensate for this the Auger signal at an energy of 10 eV was optimised using a variable strength lens which is positioned close to the entrance aperture of the spectrometer and if necessary the positioning of an external magnet. These adjustments counterbalanced the majority of the magnetic field introduced by the specimen, allowing spectra to be collected without excessive low energy attenuation. As a further check the background signals were compared at an energy slightly above the phosphorus and iron peaks. The ratios of these two background measurements were found to vary in the range 0.8 to 1.1 with the majority being close to unity. This variation will affect the relative height of the phosphorus peak recorded. It is expected that for the same detector, primary beam energy and sample orientation, the ratio of these measured backgrounds should remain constant and that the experimental variation discovered is probably induced by the residual magnetic field of the sample which had not be corrected by the measures detailed above. For this reason the phosphorus-to-iron peak height ratio has been normalised using the measured background ratio for each individual spectrum. The only segregation figures to be significantly affected by this normalisation procedure were the data for alloy S300 containing 300 wt ppm phosphorus where an increase of 33% was recorded. This was due to particularly poor low energy response of the spectrometer at the time of analysis of these samples. This normalisation procedure

was also conducted on the spectra collected during the determination of elemental sensitivity factors.

The phosphorus and iron signals, adjusted for background ratios, collected from alloys S560 to S25 were used in equation 5.7 to calculate the effective coverage of the boundaries by phosphorus. The results are shown in figures 5.20 to 5.23. For alloy S560, containing the highest level of phosphorus (560 wtppm) the Auger data gives a distribution of monolayer coverage which peaks at 1.0 monolayers with a distribution ranging from 0.6 - 1.2 monolayers. The mean value is 1.01 with a standard deviation of 0.13. Alloy S300 containing 300 wt ppm phosphorus has a skewed distribution of measured monolayer coverages and very few facets with a phosphorus coverage of 0.5 or less. In this case the mean is 0.73 with a standard deviation of 0.12. As the phosphorus content of the alloy was further reduced to 80 wtppm, alloy S120, the measured segregation fell to a mean value of 0.50 with a standard deviation of 0.1 and in alloy S25 with the lowest concentration of phosphorus (25 wtppm) the level of segregation detected was 0.08 monolayers with a standard deviation of 0.05.

The above calculations of monolayer coverage of phosphorus take no account of the presence of chromium either as a segregant, a major constituent of the $M_{23}C_6$ precipitates, which are known to be present on the grain boundaries, or as a matrix component. This causes an overestimation of the level of phosphorus coverage as not all of the matrix signal is being recorded and used in the analysis. The correction for the presence of chromium is described in the following section.

5.2.2 Quantification of the Extent of Interfacial Coverage by a Two Component Overlayer

The quantification procedure discussed in the previous section gives an overestimate of the level of phosphorus segregation. This overestimate is due to only the phosphorus and iron signals being considered in the calculation and no account being made for the presence of the enhanced chromium signal observed. The additional chromium signal arises from the presence of segregated chromium and chromium-rich grain-boundary precipitates as determined from the STEM examination.

The enhanced chromium signal can be included in the analysis by extending the scope of the segregation equations given in the previous section. The signal detected from the overlayer of phosphorus is unchanged. The signal from a fractional overlayer of chromium, I_{Cr}, can be represented in a similar manner to the phosphorus overlayer as described in section 5.2.1 as:

$$I_{Cr} = \phi_{Cr} I_{Cr}^{\infty} \left[\frac{1+r_{Fe}(E_{Cr})}{1+r_{Cr}(E_{Cr})} \right] \{1-\exp [-a_{Cr} / \lambda_{Cr}(E_{Cr}) \cos \theta]\} \quad 5.14$$

Where

ϕ_{Cr} = fractional coverage of segregated chromium

I_{Cr}^{∞} = relative sensitivity factor

$r_{Fe}(E_{Cr})$ = Backscattering factor in matrix

$r_{Cr}(E_{Cr})$ = backscattering factor in segregant

a_{Cr} = atom size of chromium

$\lambda_{Cr}(E_{Cr})$ = inelastic mean free path of chromium Auger electrons in the segregant

θ = angle of Auger electron emission to the surface normal

The signal from the iron matrix is now considered to consist of three components

(i) A signal attenuated through the overlayer of phosphorus

(ii) A signal attenuated through the overlayer of chromium

(iii) An unattenuated signal from the uncovered matrix

This gives the following form for the signal from the matrix:

$$I_{Fe} = I_{Fe}^{\infty}(1 - \phi_P \{1- \exp [-a_P /\lambda_p(E_{Fe}) \cos \theta]\} - \phi_{Cr} \{1- \exp [-a_{Cr} /\lambda_{Cr}(E_{Fe}) \cos \theta]\}) \quad 5.15$$

Equations 5.14 and 5.15 can be combined to give the following equations which can be used to calculate the level of segregation of phosphorus and chromium over the steel surface.

$$\frac{I_p / I_p^{\infty}}{I_{Fe} /I_{Fe}^{\infty}} \frac{[1+r_p(E_p)]}{[1+r_{Fe}(E_p)]} = \frac{\phi_p \{1-\exp [-a_p /\lambda_p(E_p) \cos \theta]\}}{1-\phi_p\{1-\exp[-a_p/\lambda_p(E_{Fe}) \cos \theta]\}-\phi_{Cr}\{1-\exp[-a_{Cr}/\lambda_{Cr}(E_{Fe})\cos\theta]\}} \quad 5.16$$

and

$$\frac{I_{Cr} / I_{Cr}^{\infty}}{I_{Fe} / I_{Fe}^{\infty}} \frac{[1+r_{Cr}(E_{Cr})]}{[1+r_{Fe}(E_{Cr})]} = \frac{\phi_{Cr} \{1-\exp [-a_{Cr} /\lambda_{Cr}(E_{Cr}) \cos \theta]\}}{1-\phi_p\{1-\exp[-a_p/\lambda_p(E_{Fe}) \cos \theta]\}-\phi_{Cr}\{1-\exp[-a_{Cr}/\lambda_{Cr}(E_{Fe})\cos\theta]\}} \quad 5.17$$

These two equations in two unknowns, ϕ_p (the fractional coverage of phosphorus), and ϕ_{Cr} (the fractional coverage of chromium) can be solved once all the constants have been evaluated. The values for all of the required constants have been evaluated using the equations given in section 5.2.1 and are listed below.

$$I_{Fe}^{\infty} = 0.21$$
$$I_{Cr}^{\infty} = 0.34$$
$$I_{P}^{\infty} = 0.54$$

$$1+r_P(E_P) = 1.681$$
$$1+r_{Fe}(E_P) = 1.867$$
$$1+r_{Cr}(E_{Cr}) = 1.693$$
$$1+r_{Fe}(E_{Cr}) = 1.718$$

$$a_p = 0.304\text{nm}$$
$$a_{Cr} = 0.229\text{nm}$$

$$\lambda_p(E_P) = 0.737\text{nm}$$
$$\lambda_p(E_{Fe}) = 1.819\text{nm}$$
$$\lambda_{Cr}(E_{Fe}) = 1.19\text{nm}$$
$$\lambda_{Cr}(E_{Cr}) = 1.03\text{nm}$$

$$\cos\theta = 0.866$$

Not all of the chromium signal in the AES spectrum comes from segregant. The proportion of the boundary chromium signal which arises from the matrix has been estimated by analysing spectra from transgranular cleavage. These areas exhibit no segregation and only a small amount of precipitation. The ratio of chromium to iron in these spectra was found to be 0.17. This proportion can be subtracted from the chromium signal measured on the grain boundary to give a

matrix-corrected, chromium-enhanced signal from the grain boundary. The matrix signal does not consist solely of iron as assumed in the previous calculations, but iron and chromium. The magnitude of the composite matrix signal is calculated by summing the iron counts and the proportion of chromium, assumed to come from the matrix, both divided by their respective sensitivity factors. The grain boundary coverages of chromium calculated by this procedure for each of the alloys are shown in figures 5.24 to 5.27. The mean monolayer coverage of chromium calculated for each alloy are 1.22 (σ=0.23) in alloy S560, 0.90 (σ=0.22) in alloy S300, 1.04 (σ=0.30) in alloy S120 and 0.67 (σ=0.20) in alloy S25. The phosphorus coverages for each alloy calculated from equation 5.16 and 5.17 are reduced from those obtained in section 3.2.1 due to the inclusion of chromium in the matrix signal. The effect of this on the distribution of calculated phosphorus monolayer coverages is shown in figures 5.28 to 5.31. Alloy S560 now has a mean coverage of 0.83 (σ=0.11) monolayers, alloy S300 0.60 (σ=0.09), alloy S120 0.41 (σ=0.08) and alloy S25 a mean monolayer coverage of 0.07 (σ=0.04). In the above case the calculated chromium segregation level will be an overestimate of the true value due to the enhancement in chromium on the grain boundary coming from a combination of segregation and chromium rich precipitates. In order to obtain a better estimate of chromium segregation it is necessary to estimate the signal from the precipitates and the matrix and subtract this from the detected grain boundary signal. The chromium signal arising from matrix and chrome rich precipitates can be estimated from spectra obtained during the depth profile experiment. In this experiment the chromium and phosphorus segregation is removed leaving behind exposed precipitates and matrix. A depth profile obtained from alloy S560 is shown in figure 4.39; as has been described previously, the levels of chromium and phosphorus fall sharply as the outer layers of the sample are removed. This leaves a chromium level which is in excess of the matrix value determined from the analysis of transgranular cleavage. This difference is related to the segregated phosphorus and chromium being removed, leaving the chromium-rich precipitates and matrix.

When the final spectrum from the depth profile is analysed, the ratio of chromium to iron detected from the effective matrix is calculated to be 0.31. This value can be used to apportion more accurately the chromium signal detected on a grain boundary facet between segregant and matrix plus precipitates, and the segregant portion of the chromium signal used as inputs for equations 5.16 and 5.17 to re-calculate the levels of segregated phosphorus and chromium. The matrix signal used is again the sum of the iron and chromium signals divided by their respective sensitivity factors. This modified analysis gives very little change in the calculated levels of segregated phosphorus ($<1\%$) but reduces the calculated chromium levels in the following manner. Alloy S560 reduced from a fractional coverage of 1.22 to 0.67 (σ=0.24), alloy S300 down from 0.90 to 0.35 (σ =0.18), alloy S120 down from 1.04 to 0.46 (σ =0.31) and alloy S25 down from 0.67 to 0.11 (σ =0.15). Histograms of the distribution of chromium segregation corrected for matrix and precipitate contributions to the chromium signal are shown in figures 5.32 to 5.35. The AES data quantified to give monolayer coverage by each of the procedures described in the previous sections is listed in table 5.1.

Alloy S560 Data				
Phos 1	Phos 2	Chrome 1	Phos 3	Chrome 2
1.06	0.85	1.25	0.86	0.73
1.03	0.84	1.13	0.85	0.60
1.00	0.79	1.38	0.80	0.86
1.06	0.84	1.35	0.85	0.83
1.11	0.89	1.20	0.91	0.68
1.04	0.84	1.13	0.85	0.60
1.07	0.87	1.19	0.88	0.66
1.05	0.86	1.13	0.87	0.60
1.20	0.97	1.21	0.98	0.69
0.96	0.78	1.08	0.79	0.54
1.07	0.87	1.08	0.88	0.55
0.79	0.64	1.06	0.65	0.51
0.78	0.65	0.86	0.66	0.29
1.02	0.85	0.84	0.86	0.28
1.12	0.90	1.18	0.91	0.65
0.84	0.69	0.98	0.70	0.42
1.19	0.96	1.23	0.97	0.71
1.04	0.83	1.33	0.84	0.81
1.19	0.95	1.28	0.96	0.77
0.91	0.75	1.00	0.76	0.46
0.91	0.73	1.25	0.74	0.71
0.85	0.69	1.02	0.70	0.47
0.98	0.79	1.14	0.80	0.60
0.97	0.78	1.20	0.79	0.67
0.99	0.72	2.05	0.73	1.58
0.99	0.80	1.23	0.81	0.70
0.94	0.77	0.99	0.78	0.44
1.06	0.86	1.20	0.87	0.67
1.24	0.99	1.32	1.00	0.81
0.82	0.67	0.99	0.68	0.44
1.11	0.83	1.80	0.84	1.32
0.95	0.77	1.15	0.78	0.62
0.90	0.71	1.30	0.72	0.77
1.07	0.85	1.28	0.87	0.76
0.91	0.74	1.14	0.74	0.60
1.03	0.84	1.11	0.85	0.58
1.03	0.81	1.37	0.82	0.85
0.81	0.67	0.88	0.68	0.32
0.73	0.61	0.90	0.61	0.34
0.82	0.68	0.91	0.69	0.35
0.96	0.80	0.95	0.81	0.40
0.76	0.64	0.89	0.64	0.33
1.06	0.84	1.28	0.85	0.76
1.34	1.03	1.63	1.04	1.15
1.20	0.93	1.57	0.94	1.07
1.15	0.92	1.22	0.93	0.70
0.97	0.78	1.23	0.79	0.70
1.08	0.88	1.06	0.89	0.52
1.15	0.92	1.23	0.93	0.71

Table 5.1 Monolayer coverages determined from AES Data (key at end of table)

Phos 1	Phos 2	Chrome 1	Phos 3	Chrome 2
1.07	0.86	1.21	0.87	0.68
0.99	0.79	1.24	0.80	0.71
1.02	0.82	1.21	0.83	0.68
0.92	0.74	1.22	0.75	0.69
0.94	0.76	1.19	0.77	0.66
1.02	0.81	1.35	0.82	0.83
1.05	0.83	1.38	0.84	0.86
0.93	0.74	1.26	0.75	0.73
0.90	0.75	0.86	0.76	0.30
0.91	0.74	1.14	0.74	0.61
1.35	1.04	1.62	1.05	1.14
1.00	0.77	1.61	0.78	1.11
1.13	0.87	1.64	0.88	1.15
0.93	0.71	1.63	0.72	1.12
1.04	0.82	1.46	0.83	0.95
0.95	0.77	1.08	0.78	0.54
1.04	0.86	0.99	0.87	0.45
1.21	0.97	1.24	0.99	0.72
1.03	0.85	1.06	0.86	0.52
1.15	0.92	1.32	0.93	0.80
Alloy S300 Data				
0.90	0.74	1.06	0.75	0.52
0.77	0.63	1.08	0.63	0.53
0.72	0.59	0.98	0.60	0.42
0.79	0.65	0.92	0.66	0.35
0.70	0.56	1.20	0.57	0.65
0.83	0.69	0.95	0.70	0.40
0.75	0.64	0.77	0.64	0.20
0.70	0.59	0.77	0.60	0.19
0.83	0.68	1.06	0.69	0.51
0.68	0.57	0.84	0.57	0.26
0.42	0.37	0.36	0.37	-0.26
0.77	0.65	0.76	0.66	0.18
0.89	0.71	1.19	0.72	0.66
0.73	0.61	0.86	0.62	0.30
0.68	0.56	0.87	0.57	0.30
0.71	0.58	1.08	0.59	0.53
0.77	0.64	0.96	0.65	0.40
0.72	0.59	1.06	0.60	0.51
0.80	0.67	0.83	0.68	0.26
0.82	0.68	0.95	0.69	0.40
0.69	0.57	0.89	0.58	0.33
0.72	0.60	0.87	0.61	0.31
0.69	0.58	0.76	0.59	0.18
0.79	0.65	1.03	0.65	0.48
0.69	0.56	1.13	0.56	0.58
0.67	0.56	0.84	0.57	0.26
0.76	0.62	1.06	0.63	0.51
0.77	0.64	0.95	0.65	0.40
0.92	0.75	1.06	0.76	0.52
0.83	0.69	0.87	0.70	0.31

Table 5.1 Monolayer coverages determined from AES Data (key at end of table)

Phos 1	Phos 2	Chrome 1	Phos 3	Chrome 2
0.86	0.67	1.44	0.68	0.92
0.67	0.56	0.75	0.57	0.18
0.71	0.59	0.86	0.60	0.29
0.70	0.59	0.78	0.59	0.21
0.72	0.59	0.93	0.60	0.37
0.67	0.56	0.81	0.57	0.23
0.71	0.58	0.98	0.59	0.42
0.88	0.72	1.03	0.73	0.49
0.79	0.65	1.05	0.66	0.50
0.69	0.58	0.83	0.58	0.25
0.30	0.27	0.17	0.28	-0.47
0.25	0.24	-0.33	0.24	-1.01
0.67	0.56	0.81	0.57	0.23
0.69	0.57	0.87	0.58	0.30
0.88	0.74	0.85	0.75	0.29
0.69	0.56	1.03	0.57	0.47
0.73	0.62	0.69	0.63	0.11
0.60	0.50	0.77	0.51	0.19
0.77	0.63	1.05	0.64	0.49
0.71	0.59	0.91	0.59	0.34
0.79	0.64	1.09	0.65	0.54
0.70	0.58	0.97	0.58	0.41
0.78	0.65	0.94	0.65	0.39
0.73	0.60	1.04	0.60	0.49
0.80	0.65	1.12	0.66	0.58
0.74	0.62	0.87	0.63	0.30
0.57	0.49	0.53	0.50	-0.07
0.72	0.59	0.97	0.60	0.41
0.82	0.66	1.20	0.67	0.66
0.68	0.57	0.75	0.58	0.18
Alloy S120 Data				
0.33	0.27	0.87	0.28	0.28
0.56	0.48	0.68	0.48	0.09
0.50	0.41	0.95	0.42	0.37
0.43	0.36	1.00	0.36	0.43
0.63	0.50	1.26	0.51	0.72
0.49	0.41	0.91	0.41	0.33
0.64	0.51	1.30	0.51	0.76
0.57	0.48	0.76	0.48	0.18
0.39	0.32	1.07	0.32	0.50
0.30	0.25	0.83	0.25	0.24
0.55	0.42	1.75	0.42	1.24
0.47	0.40	0.77	0.40	0.19
0.36	0.30	0.80	0.31	0.21
0.38	0.31	0.93	0.32	0.35
0.40	0.34	0.88	0.34	0.30
0.41	0.33	1.12	0.34	0.56
0.39	0.32	1.01	0.32	0.44
0.46	0.38	0.90	0.39	0.32
0.32	0.27	0.68	0.27	0.08
0.50	0.40	1.31	0.40	0.76

Table 5.1 Monolayer coverages determined from AES Data (key at end of table)

Phos 1	Phos 2	Chrome 1	Phos 3	Chrome 2
0.59	0.49	0.96	0.49	0.40
0.47	0.40	0.79	0.40	0.20
0.49	0.41	0.96	0.41	0.39
0.62	0.50	1.14	0.51	0.59
0.48	0.38	1.24	0.39	0.69
0.53	0.43	1.06	0.44	0.49
0.36	0.31	0.63	0.31	0.02
0.47	0.39	1.10	0.39	0.53
0.57	0.46	1.26	0.46	0.72
0.50	0.43	0.68	0.43	0.09
0.75	0.57	1.75	0.58	1.25
0.56	0.45	1.23	0.45	0.68
0.55	0.43	1.28	0.44	0.73
0.64	0.49	1.57	0.50	1.05
0.53	0.44	0.88	0.45	0.30
0.53	0.42	1.22	0.43	0.67
0.49	0.41	0.84	0.41	0.26
0.36	0.30	0.87	0.31	0.29
0.49	0.42	0.54	0.43	-0.06
0.54	0.45	0.88	0.45	0.30
0.42	0.35	0.89	0.35	0.31
0.52	0.44	0.87	0.44	0.30
0.64	0.53	0.92	0.54	0.36
0.42	0.34	1.14	0.34	0.58
0.48	0.40	0.84	0.41	0.26
0.65	0.53	1.06	0.54	0.50
0.85	0.66	1.41	0.67	0.89
0.50	0.42	0.74	0.42	0.15
0.46	0.38	0.87	0.39	0.29
0.64	0.55	0.67	0.56	0.09
0.53	0.43	1.20	0.43	0.65
0.54	0.45	0.94	0.45	0.37
0.55	0.46	0.98	0.46	0.42
0.46	0.38	0.82	0.39	0.24
0.49	0.40	1.17	0.40	0.62
0.63	0.51	1.10	0.52	0.55
0.50	0.42	0.83	0.42	0.24
0.36	0.30	0.82	0.31	0.23
0.55	0.46	0.73	0.47	0.15
0.29	0.24	0.82	0.25	0.23
0.62	0.47	1.71	0.47	1.20
0.43	0.36	1.00	0.36	0.43
0.49	0.41	0.87	0.41	0.29
0.56	0.44	1.34	0.45	0.80
0.46	0.39	0.78	0.40	0.19
0.30	0.26	0.72	0.26	0.12
0.46	0.37	1.28	0.37	0.73
0.61	0.46	1.62	0.47	1.10
0.55	0.46	0.85	0.47	0.27
0.53	0.41	1.43	0.42	0.89
0.52	0.41	1.30	0.42	0.76
0.51	0.41	1.26	0.41	0.72

Table 5.1 Monolayer coverages determined from AES Data (key at end of table)

Phos 1	Phos 2	Chrome 1	Phos 3	Chrome 2
0.45	0.37	1.12	0.37	0.56
0.42	0.34	1.10	0.34	0.53
0.24	0.21	0.54	0.21	-0.07
0.58	0.48	0.85	0.49	0.27
0.49	0.41	0.85	0.41	0.27
0.54	0.42	1.46	0.43	0.93
0.43	0.31	2.05	0.31	1.56
0.57	0.45	1.51	0.45	0.99
Alloy S25 Data				
0.09	0.07	0.73	0.08	0.12
0.05	0.04	0.55	0.04	-0.08
0.00	0.00	0.51	0.00	-0.12
0.05	0.04	0.65	0.04	0.04
0.07	0.06	0.57	0.07	-0.06
0.04	0.04	0.47	0.04	-0.16
0.09	0.08	0.59	0.08	-0.03
0.04	0.03	0.65	0.03	0.03
0.09	0.08	0.80	0.08	0.20
0.09	0.08	0.74	0.08	0.13
0.06	0.05	0.59	0.05	-0.03
0.05	0.04	0.61	0.05	-0.01
0.07	0.06	0.80	0.06	0.20
0.05	0.05	0.83	0.05	0.22
0.08	0.06	1.04	0.06	0.45
0.05	0.04	0.63	0.04	0.01
0.10	0.08	0.93	0.08	0.34
0.10	0.09	0.83	0.09	0.23
0.09	0.08	0.90	0.08	0.30
0.08	0.07	0.56	0.07	-0.06
0.10	0.08	0.69	0.08	0.08
0.06	0.05	0.71	0.05	0.09
0.08	0.07	0.46	0.07	-0.17
0.10	0.08	0.84	0.08	0.24
0.08	0.06	0.71	0.07	0.10
0.04	0.03	0.58	0.04	-0.04
0.07	0.06	0.80	0.06	0.20
0.06	0.05	0.62	0.05	0.00
0.14	0.11	1.05	0.11	0.47
0.11	0.09	0.92	0.09	0.33
0.16	0.13	0.57	0.14	-0.05
0.13	0.11	1.08	0.11	0.50
0.00	0.00	0.50	0.00	-0.14
0.06	0.05	0.63	0.05	0.02
0.16	0.13	0.98	0.13	0.40
0.12	0.11	0.34	0.11	-0.30
0.00	0.00	0.73	0.00	0.11
0.13	0.11	0.69	0.11	0.08
0.00	0.00	0.46	0.00	-0.17
0.13	0.11	0.68	0.11	0.07
0.05	0.04	0.35	0.04	-0.30
0.11	0.09	0.46	0.09	-0.17

Table 5.1 Monolayer coverages determined from AES Data (key at end of table)

Phos 1	Phos 2	Chrome 1	Phos 3	Chrome 2
0.13	0.11	0.68	0.11	0.07
0.09	0.08	0.76	0.08	0.15
0.00	0.00	0.40	0.00	-0.24
0.00	0.00	0.72	0.00	0.11
0.05	0.04	1.17	0.04	0.59
0.16	0.13	0.62	0.13	0.00
0.15	0.13	0.66	0.13	0.05
0.09	0.07	0.64	0.08	0.02
0.11	0.09	0.67	0.10	0.06
0.08	0.07	0.53	0.07	-0.09
0.00	0.00	0.35	0.00	-0.30
0.09	0.08	0.32	0.08	-0.33
0.06	0.05	0.50	0.05	-0.13
0.09	0.07	0.53	0.07	-0.10
0.17	0.14	0.44	0.15	-0.19
0.13	0.10	1.00	0.10	0.41
0.15	0.13	0.89	0.13	0.29
0.00	0.00	0.49	0.00	-0.15

Table 5.1 Monolayer coverages determined from AES Data

Phos1 Monolayer coverage of phosphorus adjusted for background ratio

Phos2 Monolayer coverage of phosphorus corrected for matrix chromium

Phos3 Monolayer coverage of phosphorus corrected for matrix and precipitate chromium

Chrome 1 Monolayer coverage of chromium corrected for matrix chromium

Chrome 2 Monolayer coverage of chromium corrected for matrix and precipitate chromium

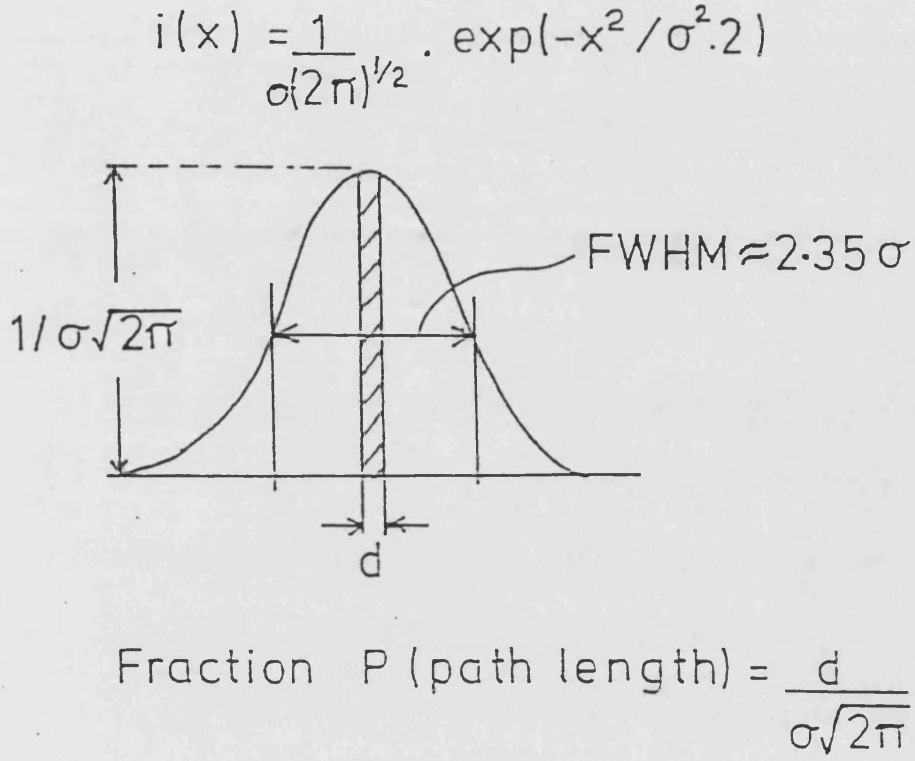

Figure 5.1 Simple deconvolution method of converting STEM data to monolayer coverage

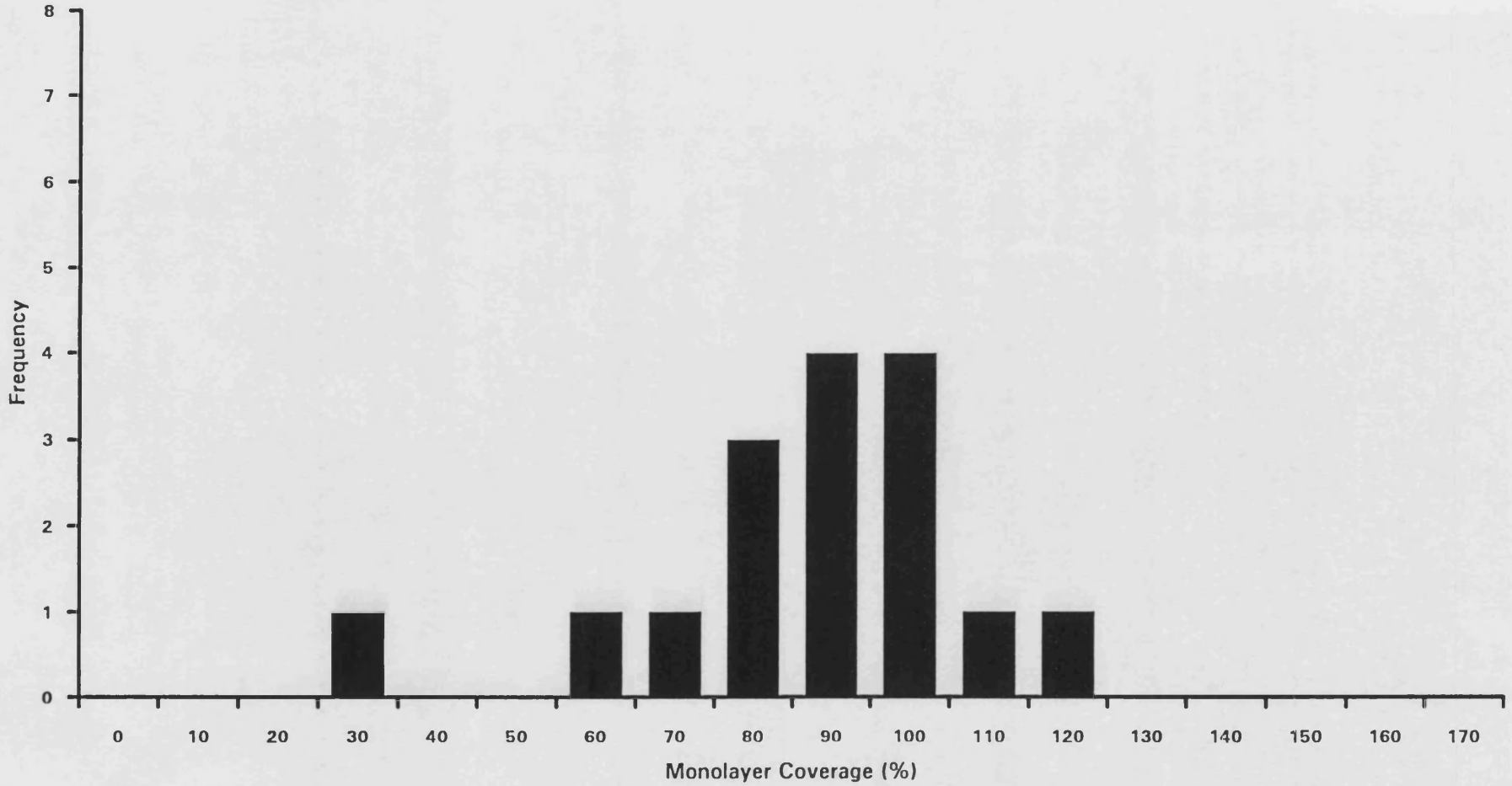

Figure 5.2 Distribution of monolayer coverage of phosphorus detected in alloy S560 calculated by the simple deconvolution method

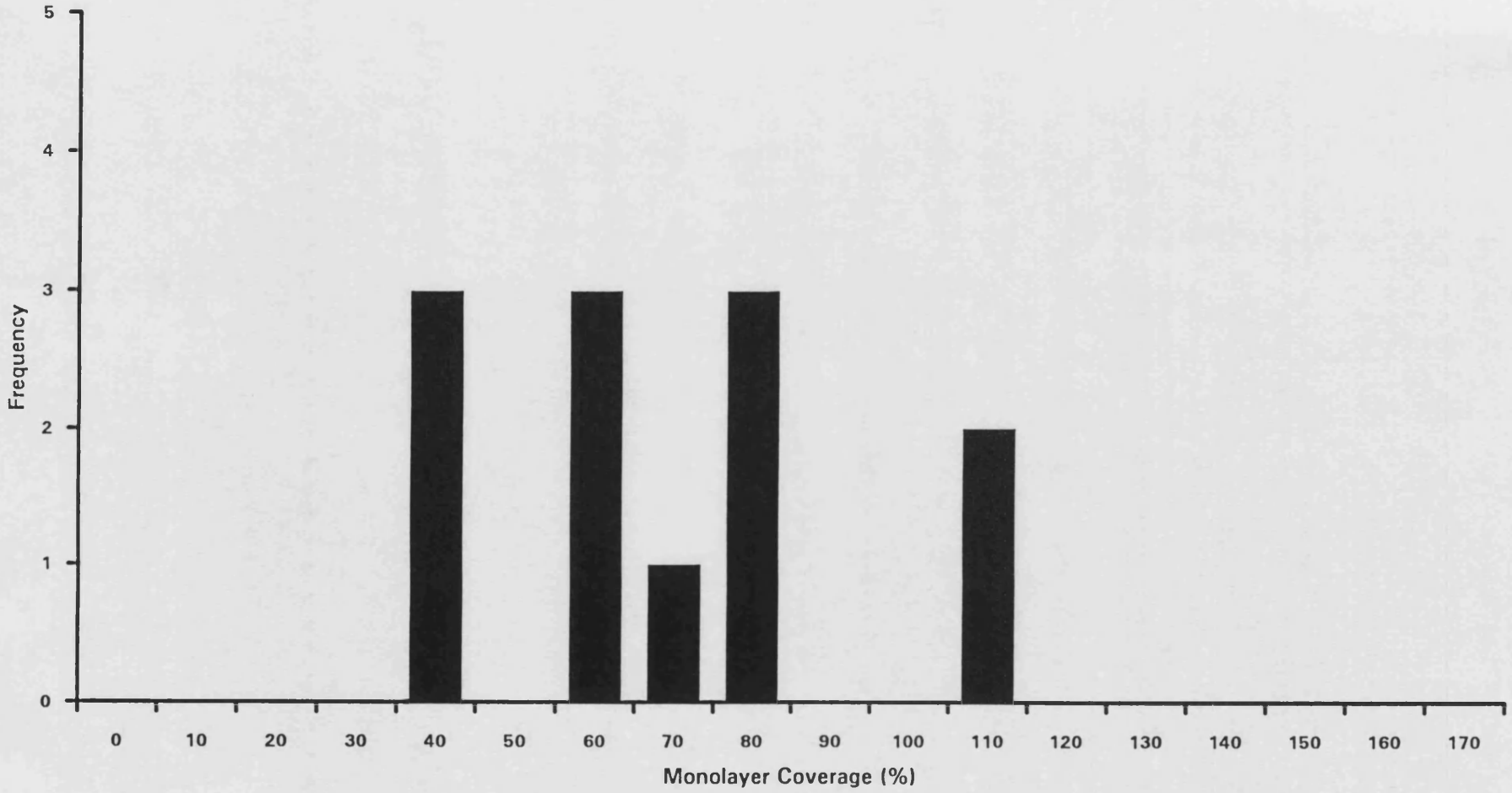

Figure 5.3 Distribution of monolayer coverage of phosphorus detected in alloy S300 calculated by the simple deconvolution method

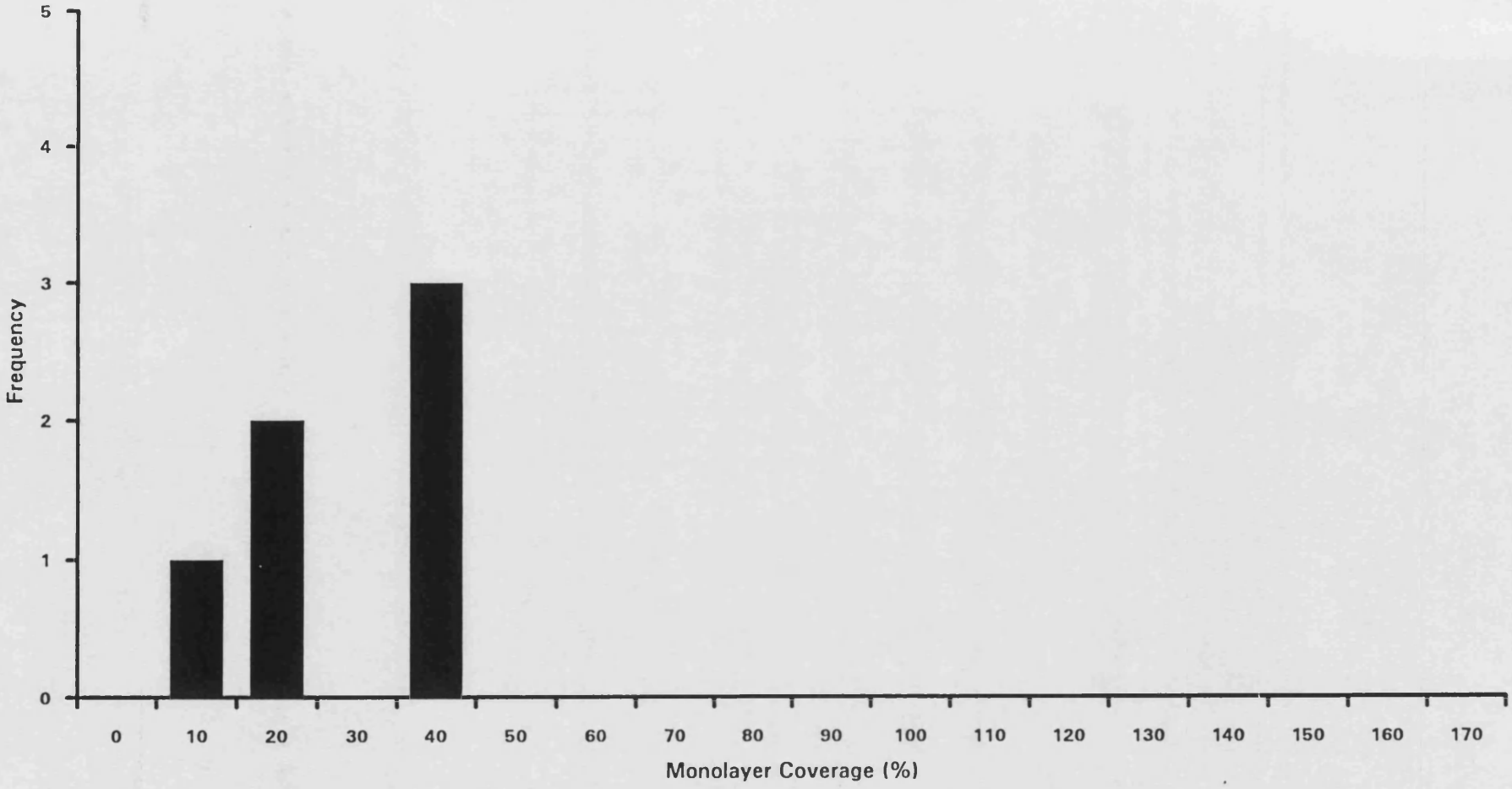

Figure 5.4 Distribution of monolayer coverage of phosphorus detected in alloy S120 calculated by the simple deconvolution method

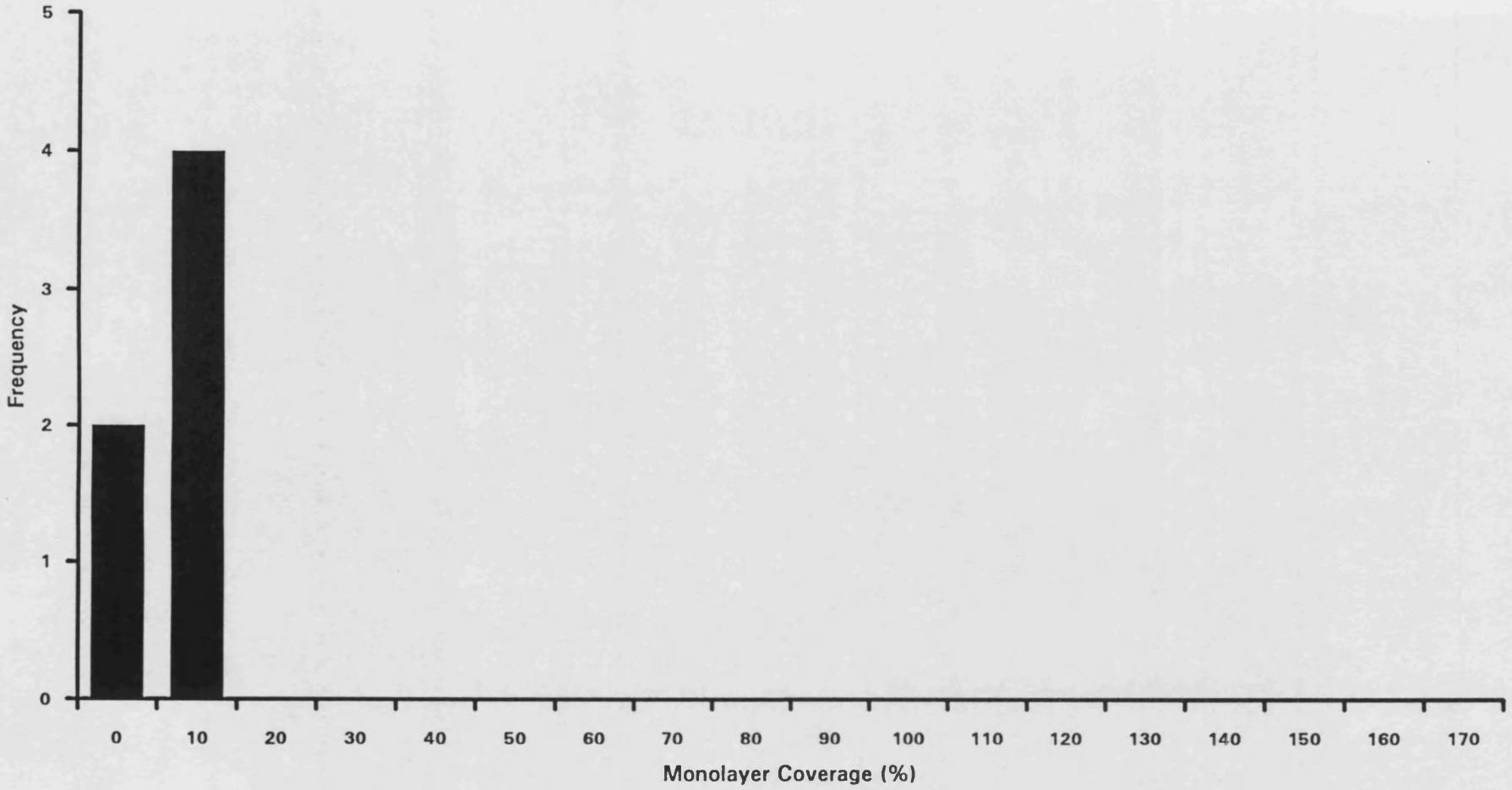

Figure 5.5 Distribution of monolayer coverage of phosphorus detected in alloy S25 calculated by the simple deconvolution method

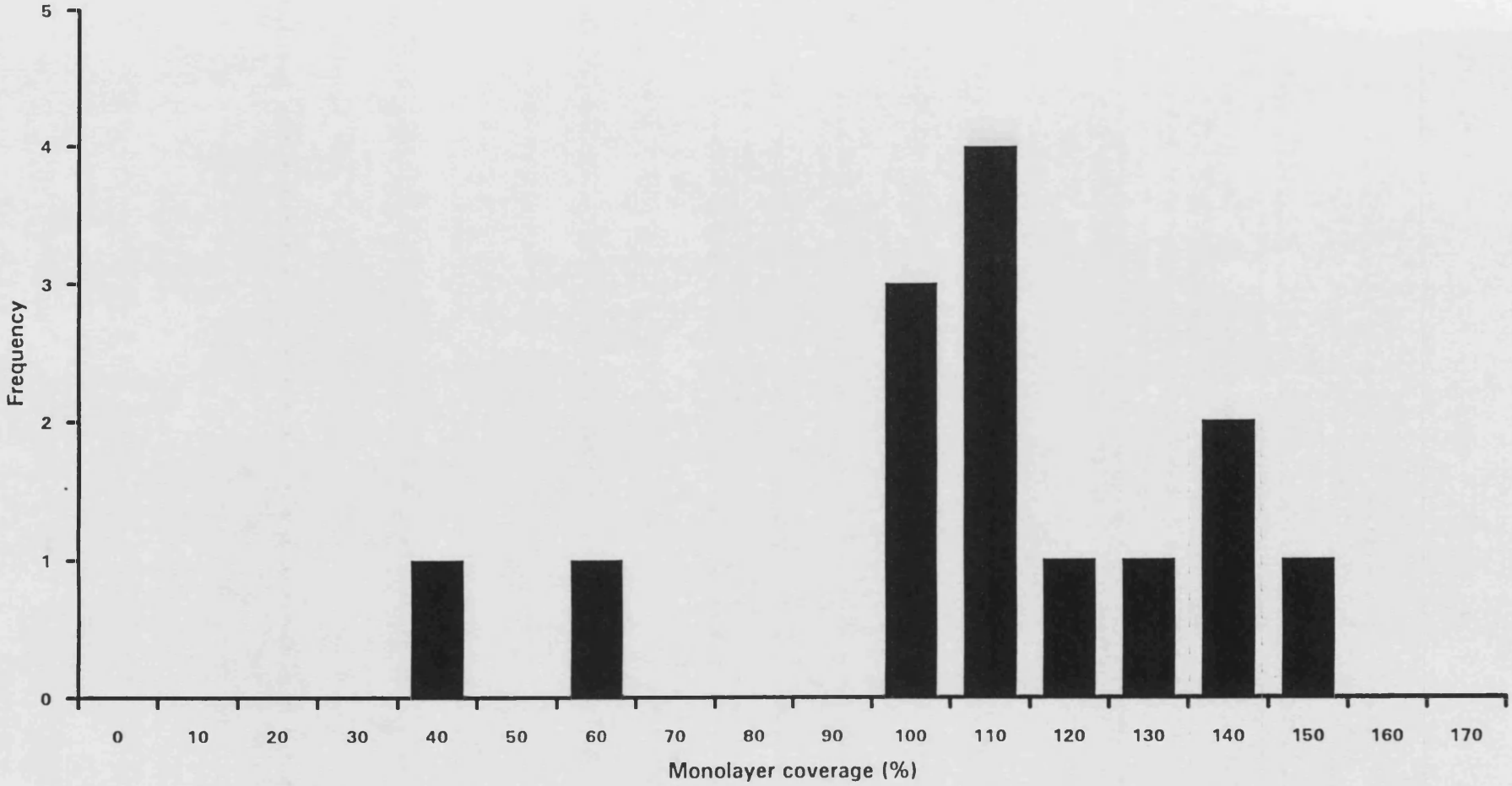

Figure 5.6 Distribution of monolayer coverage of chromium detected in alloy S560 calculated by the simple deconvolution method

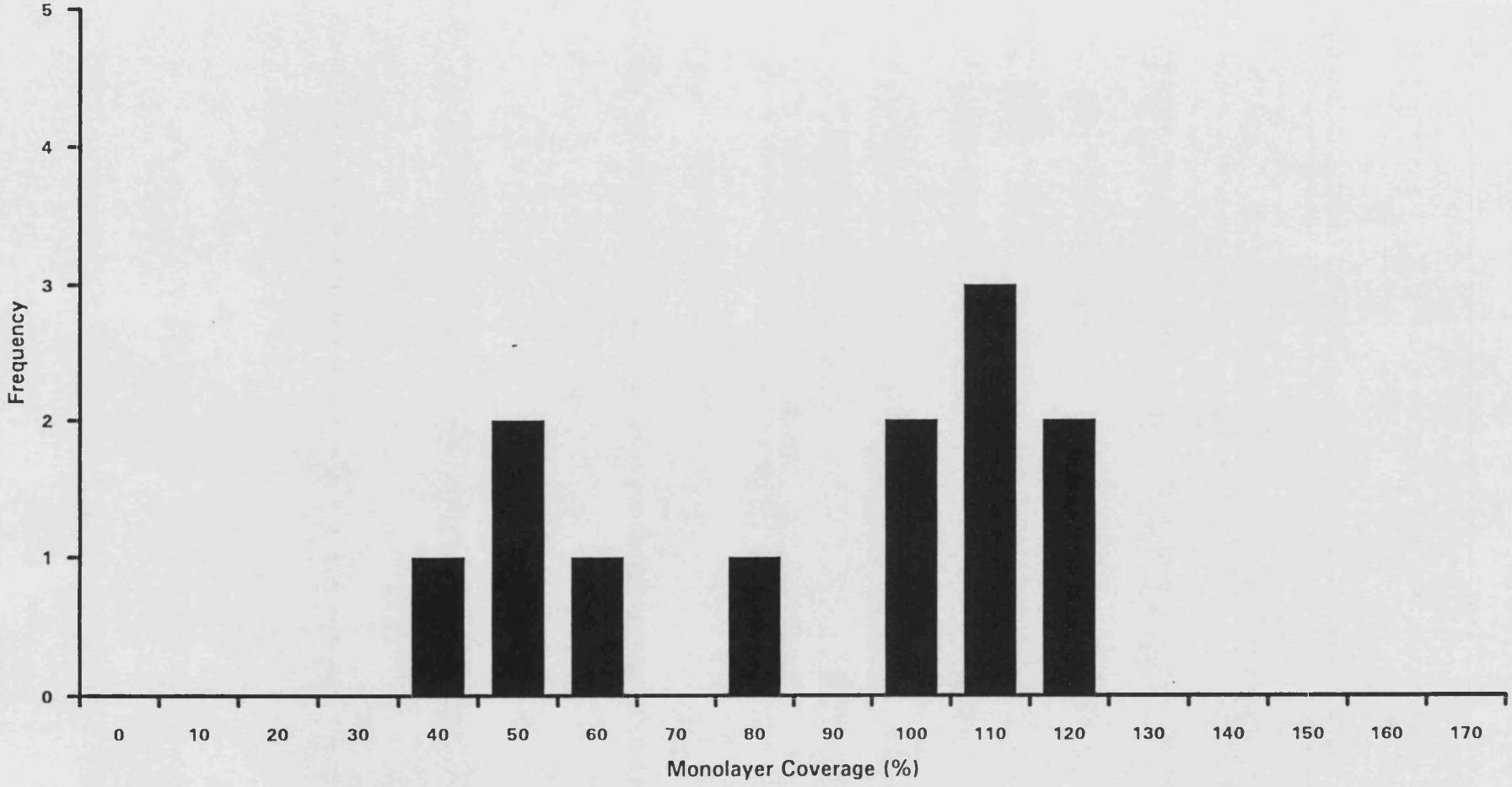

Figure 5.7 Distribution of monolayer coverage of chromium detected in alloy S300 calculated by the simple deconvolution method

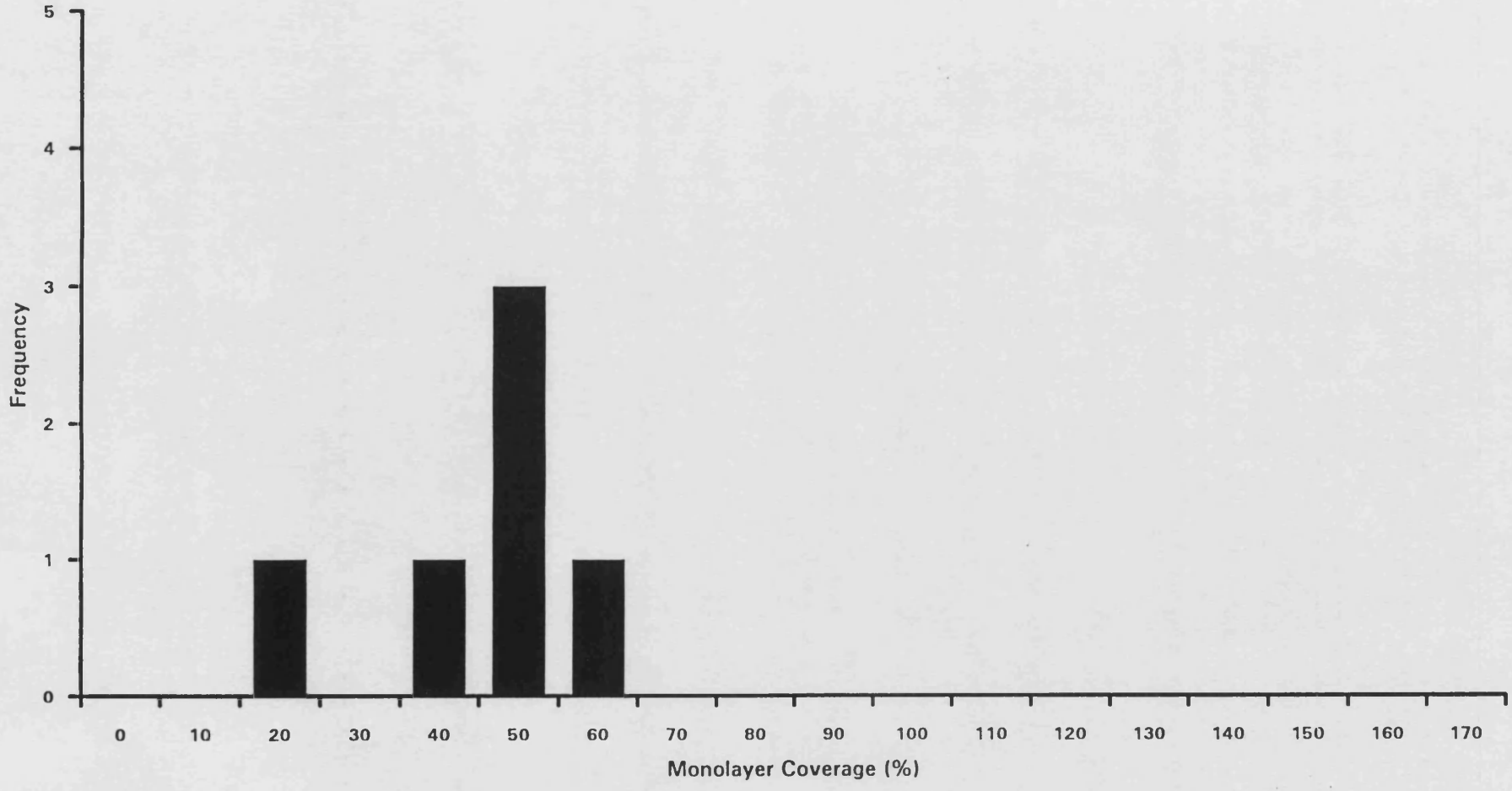

Figure 5.8 Distribution of monolayer coverage of chromium detected in alloy S120 calculated by the simple deconvolution method

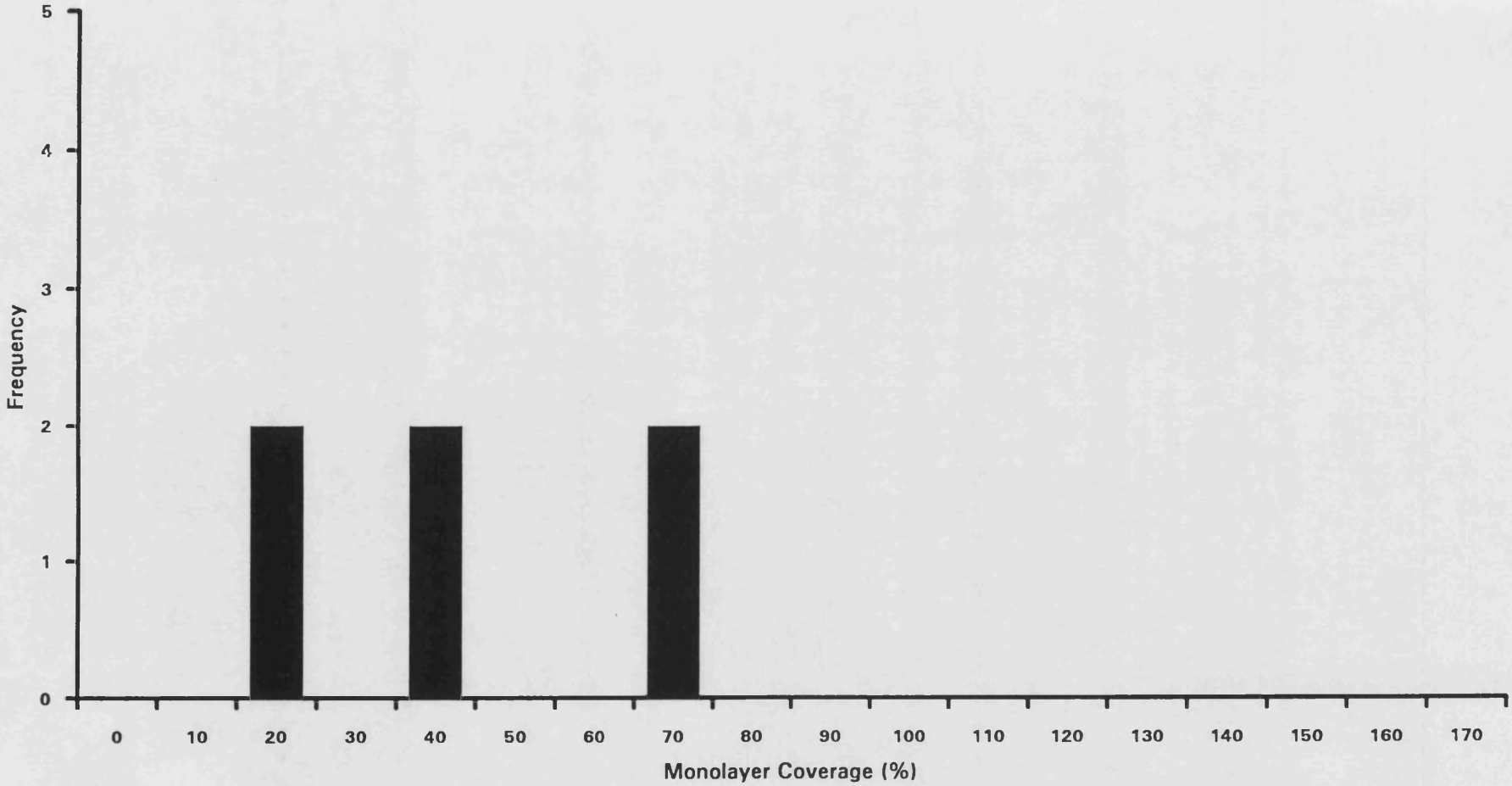

Figure 5.9 Distribution of monolayer coverage of chromium detected in alloy S25 calculated by the simple deconvolution method

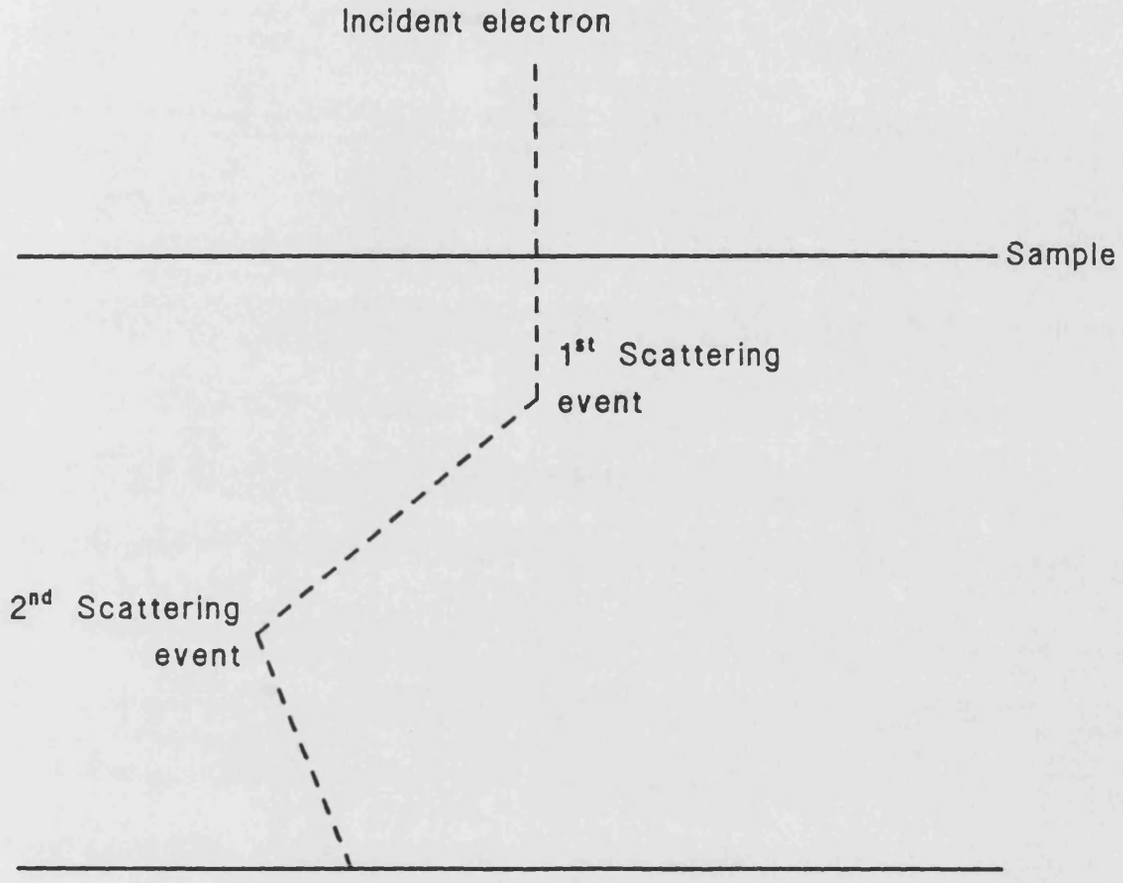

Figure 5.10 Schematic representation of electron passage through a thin foil

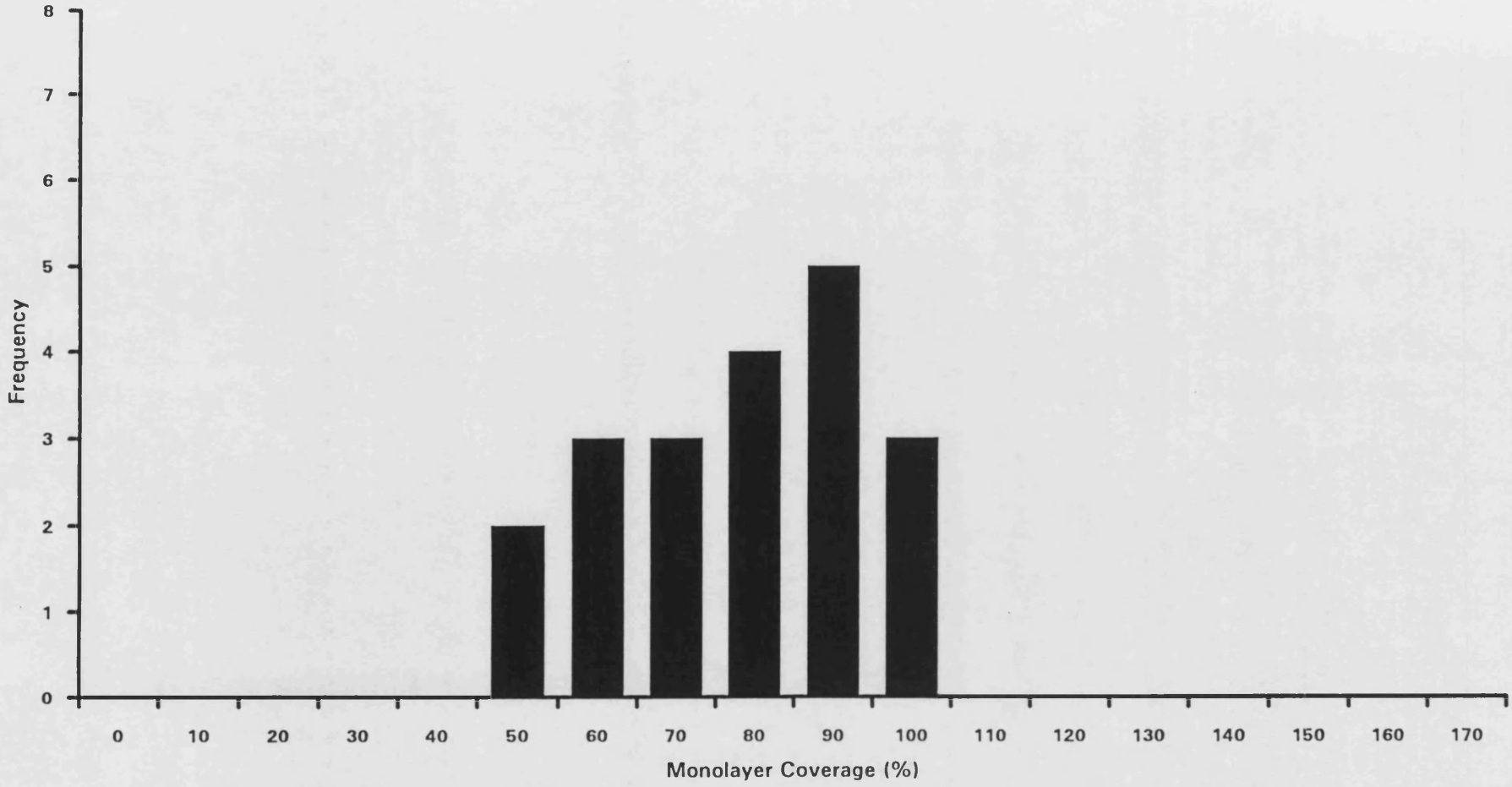

Figure 5.11 Distribution of monolayer coverage of phosphorus detected in alloy S560 calculated by the Monte Carlo method

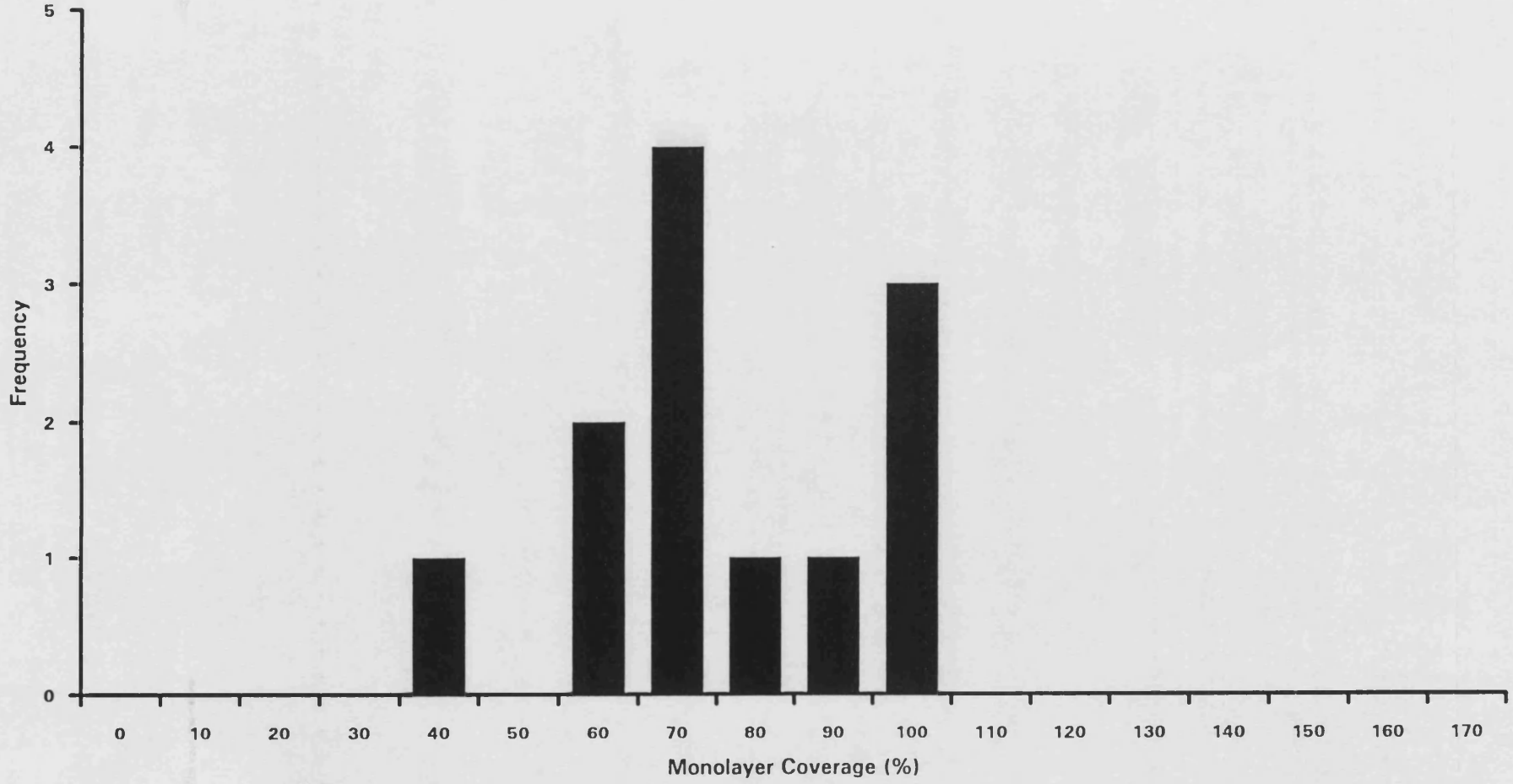

Figure 5.12 Distribution of monolayer coverage of phosphorus detected in alloy S300 calculated by the Monte Carlo method

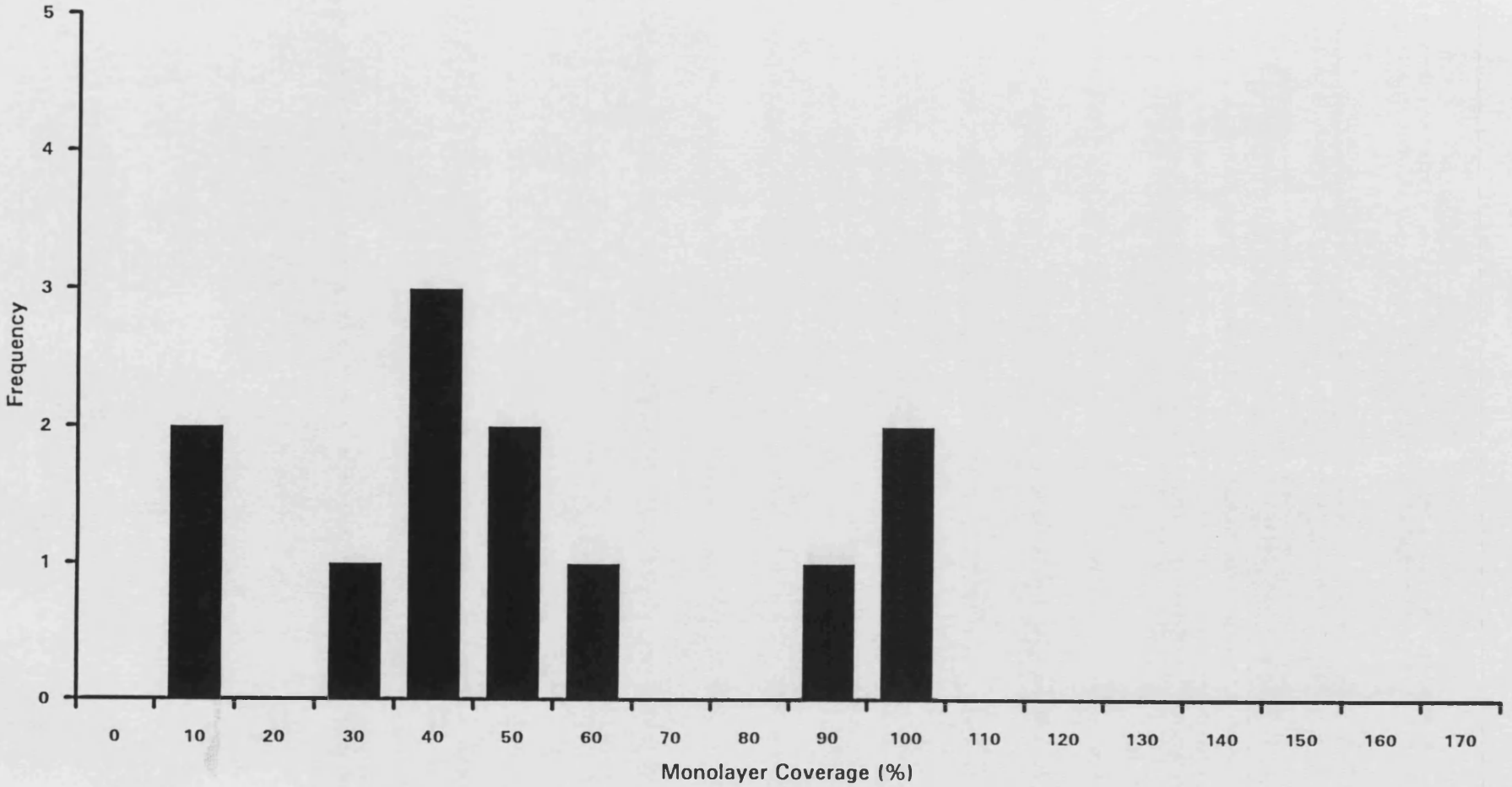

Figure 5.13 Distribution of monolayer coverage of phosphorus detected in alloy S120 calculated by the Monte Carlo method

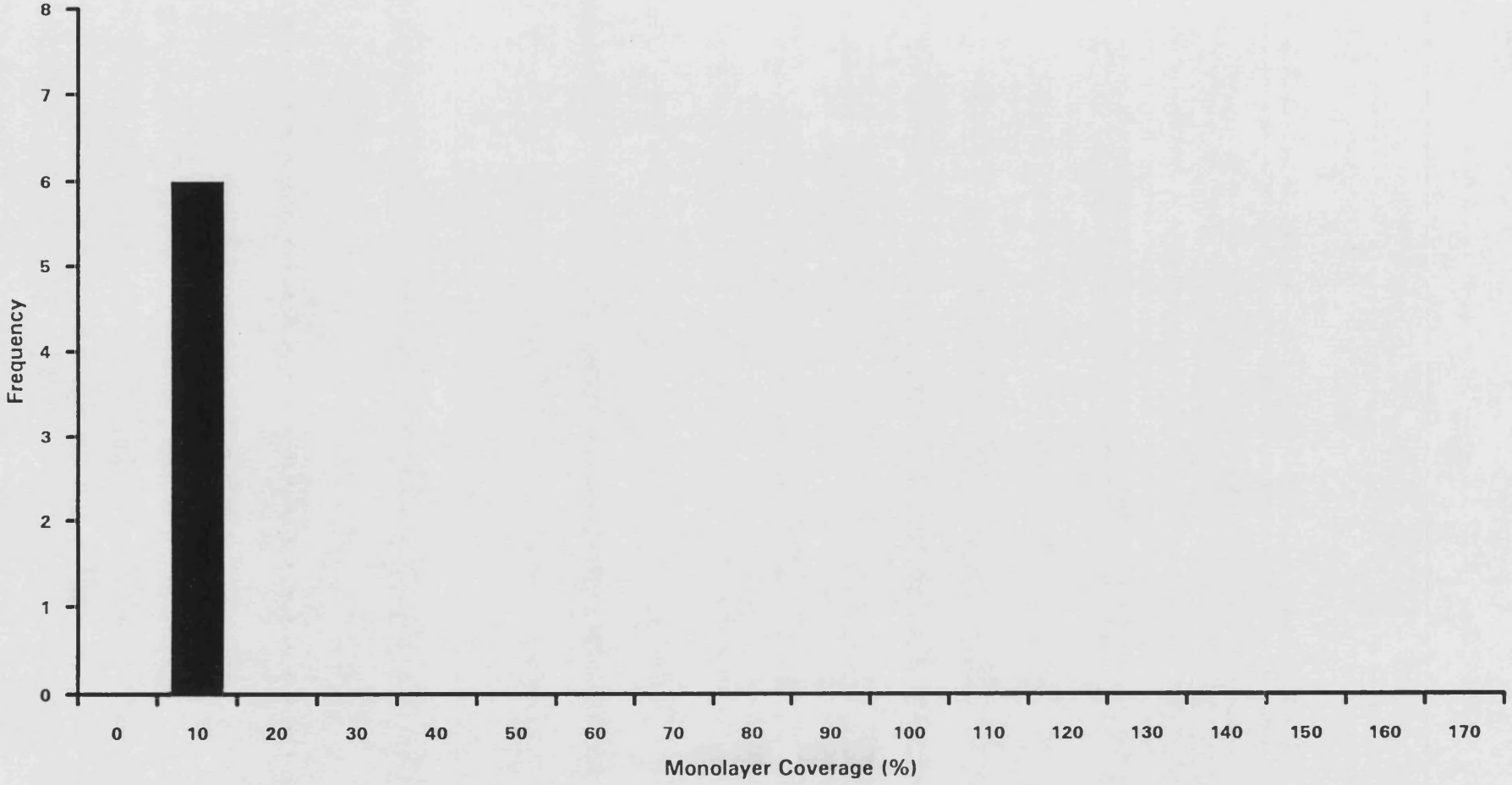

Figure 5.14 Distribution of monolayer coverage of phosphorus detected in alloy S25 calculated by the Monte Carlo method

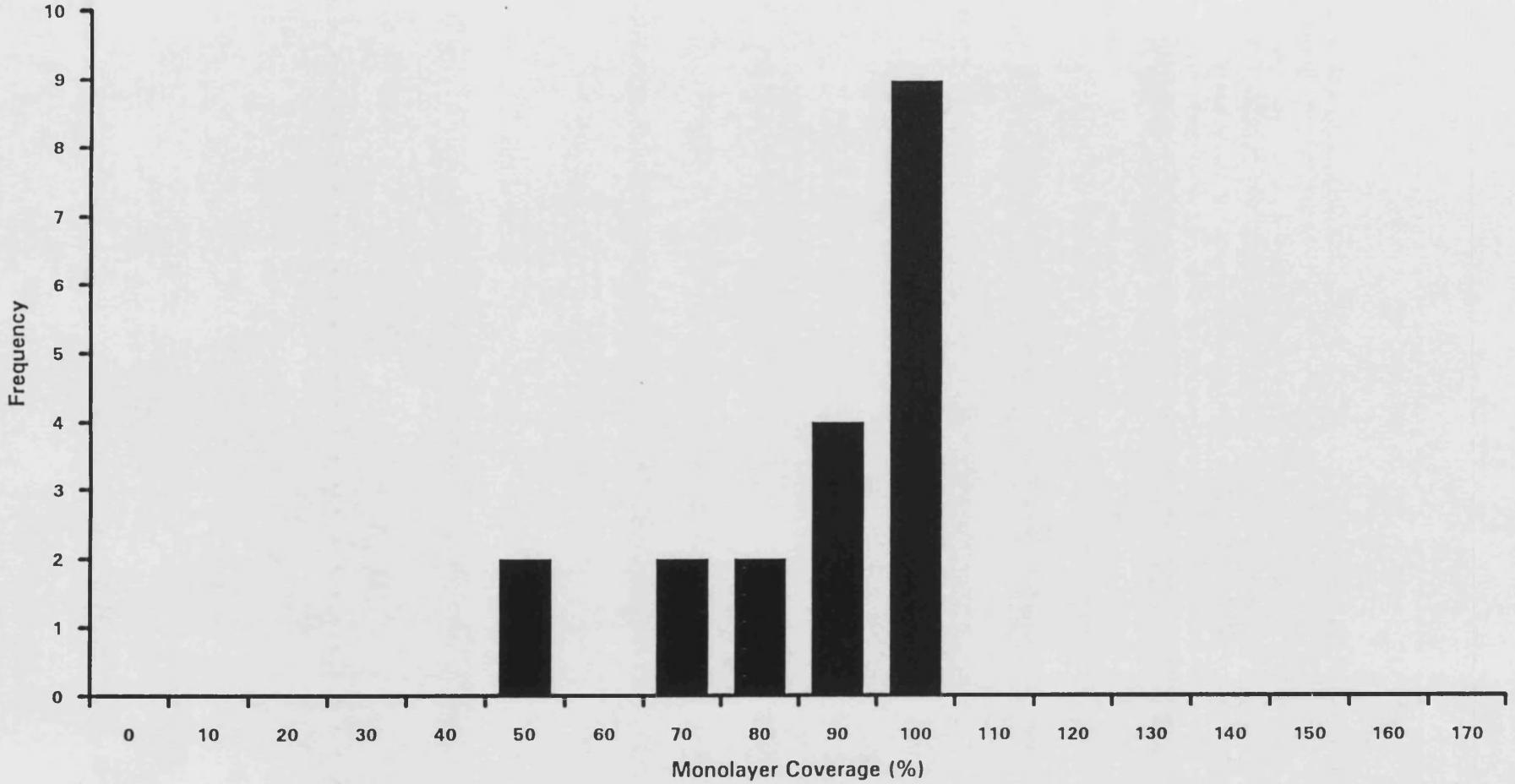

Figure 5.15 Distribution of monolayer coverage of chromium detected in alloy S560 calculated by the Monte Carlo method

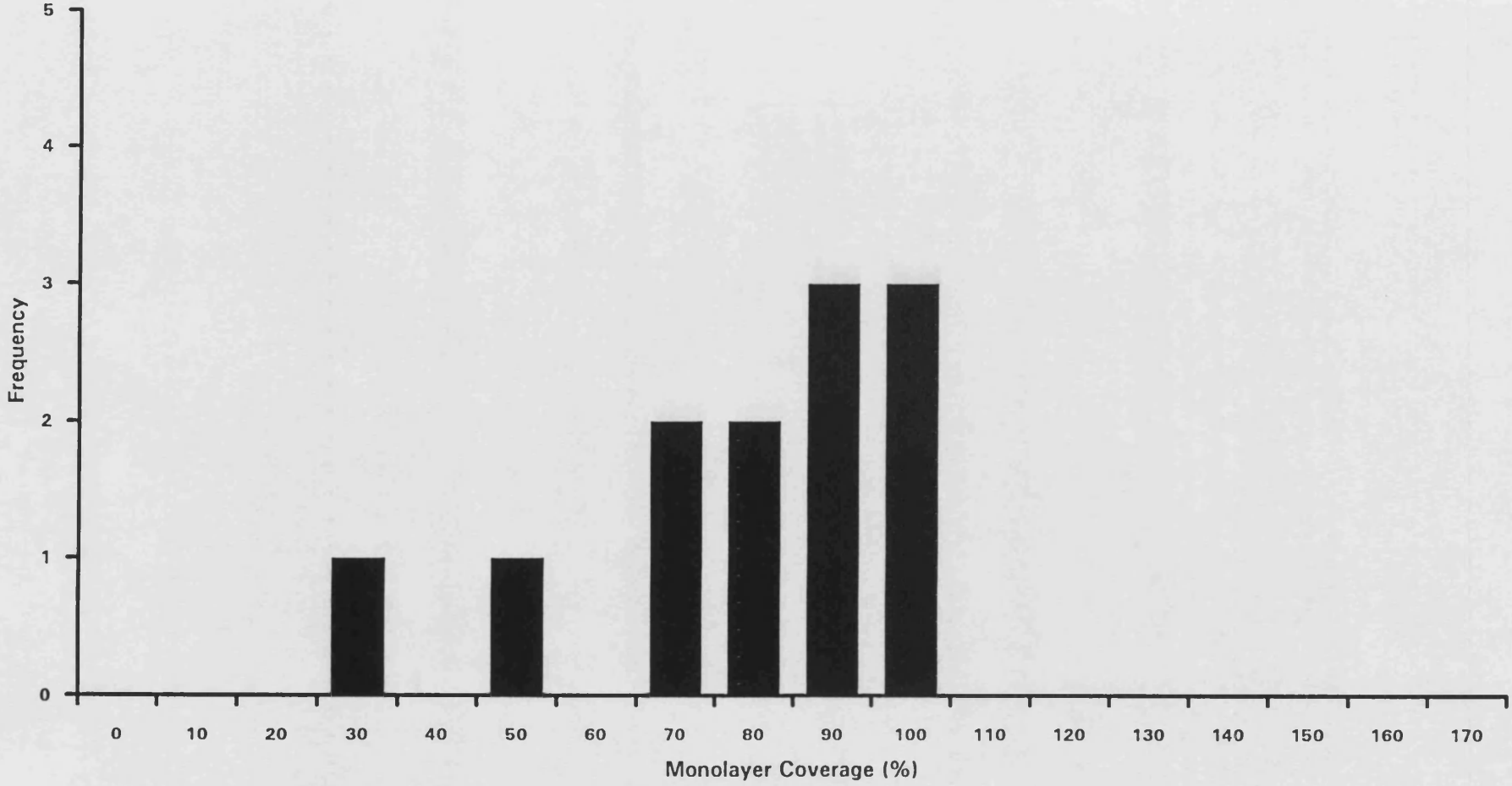

Figure 5.16 Distribution of monolayer coverage of chromium detected in alloy S300 calculated by the Monte Carlo method

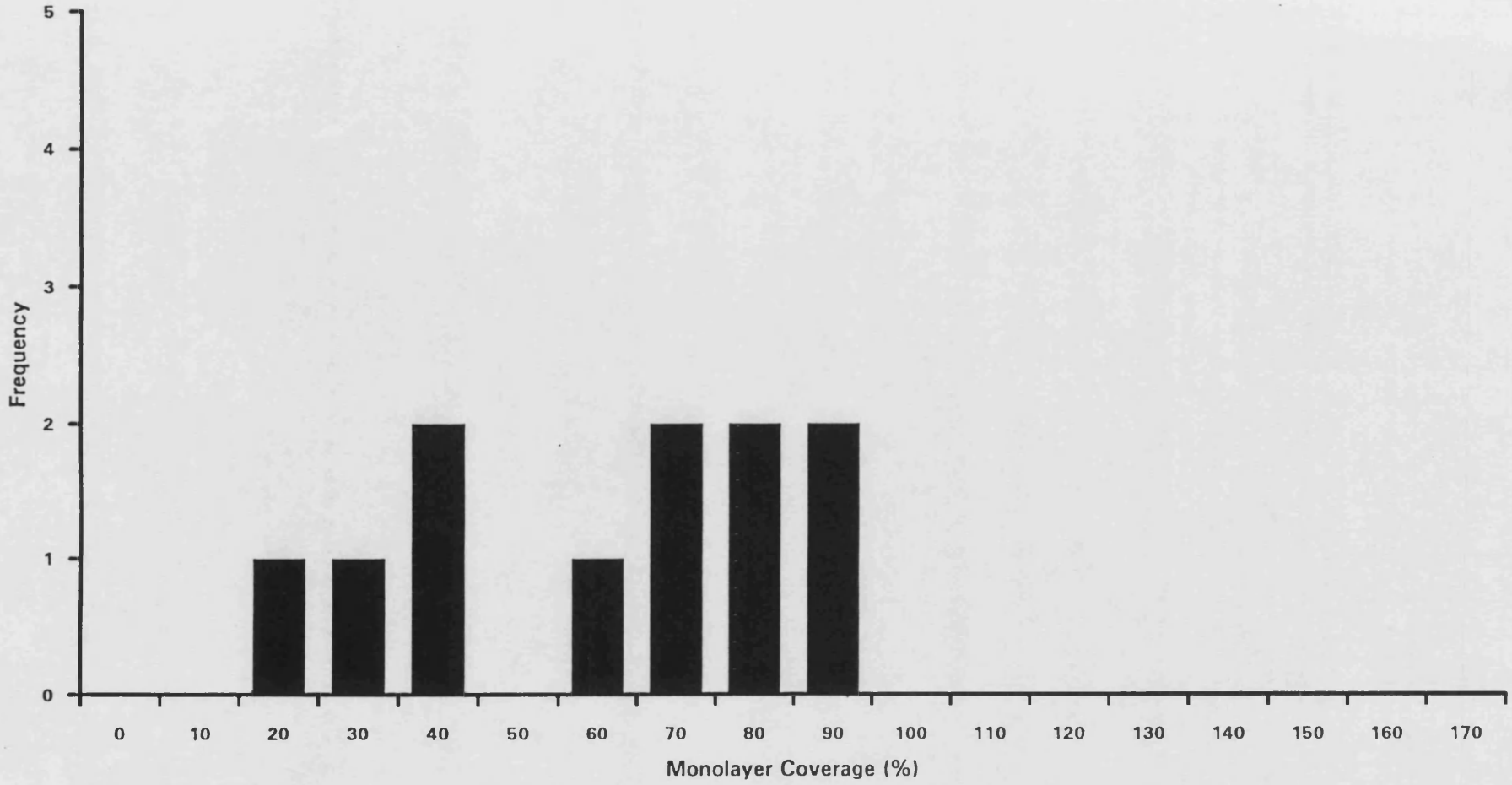

Figure 5.17 Distribution of monolayer coverage of chromium detected in alloy S120 calculated by the Monte Carlo method

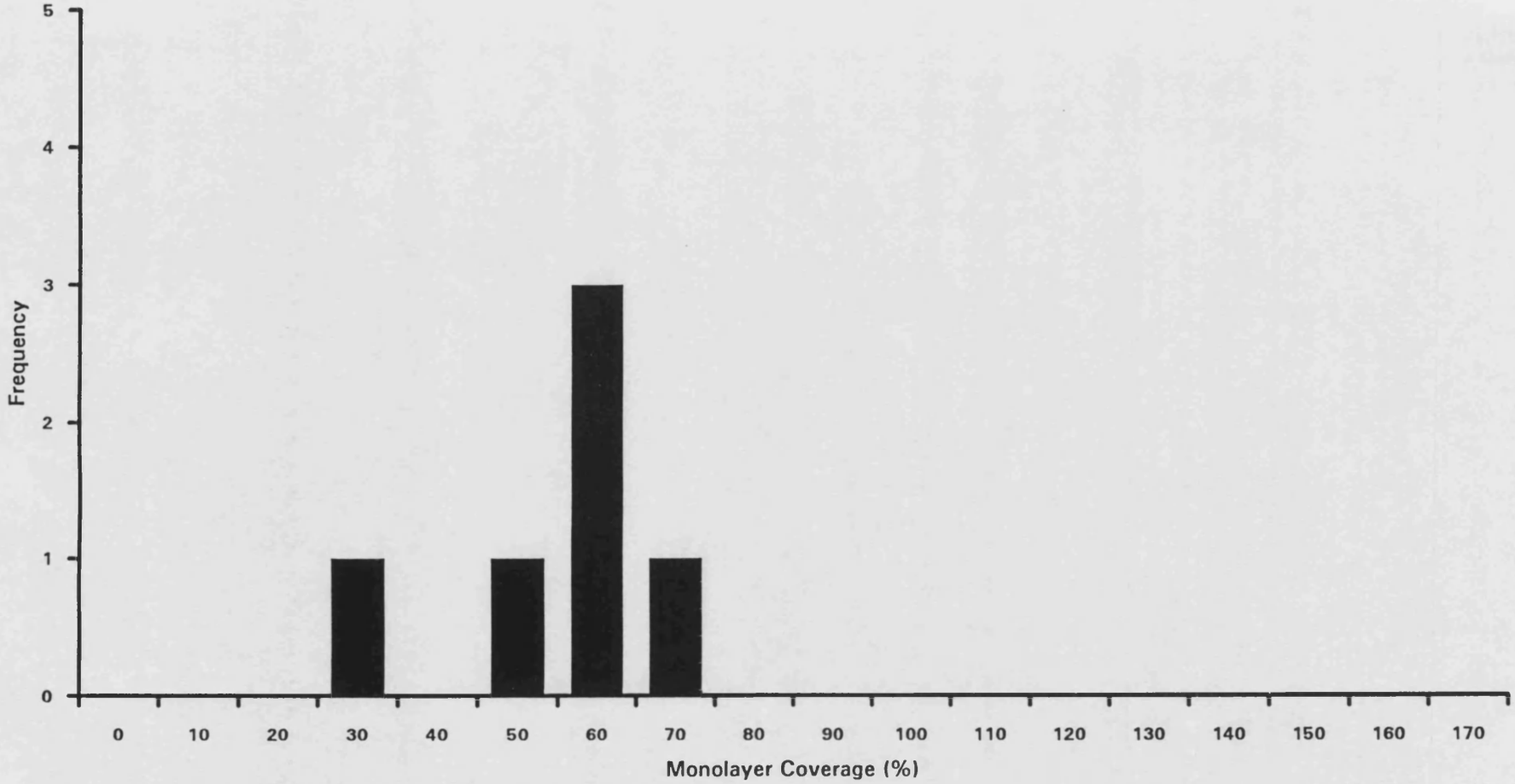

Figure 5.18 Distribution of monolayer coverage of chromium detected in alloy S25 calculated by the Monte Carlo method

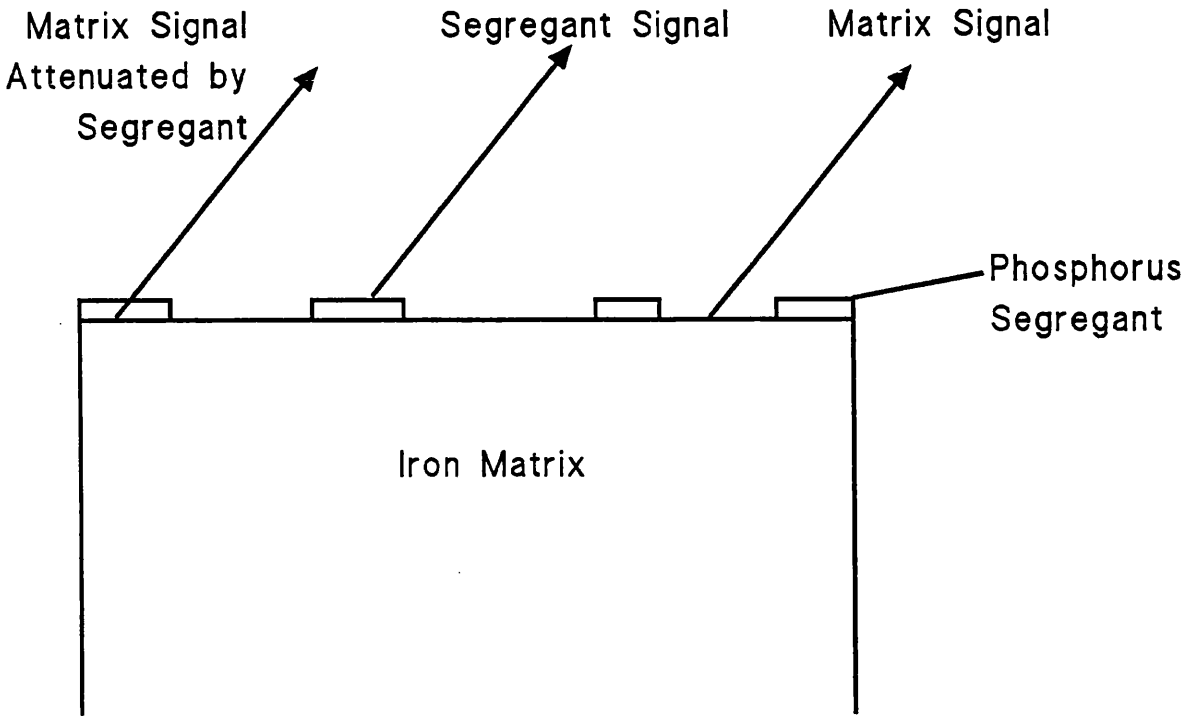

Figure 5.19 Schematic representation of single component overlayer of segregation

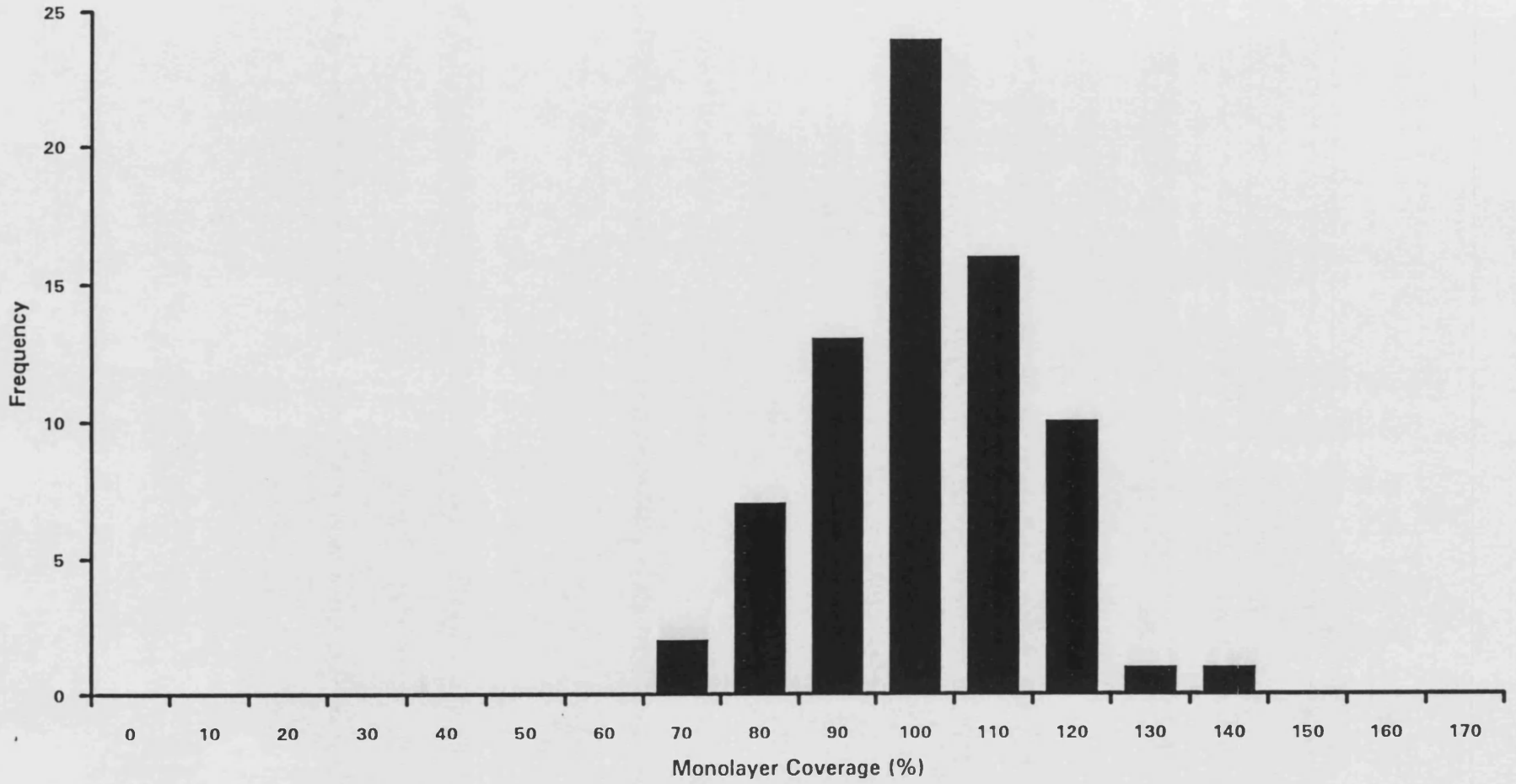

Figure 5.20 Distribution of monolayer coverage of phosphorus detected in alloy S560 calculated from AES data, not corrected for chromium content

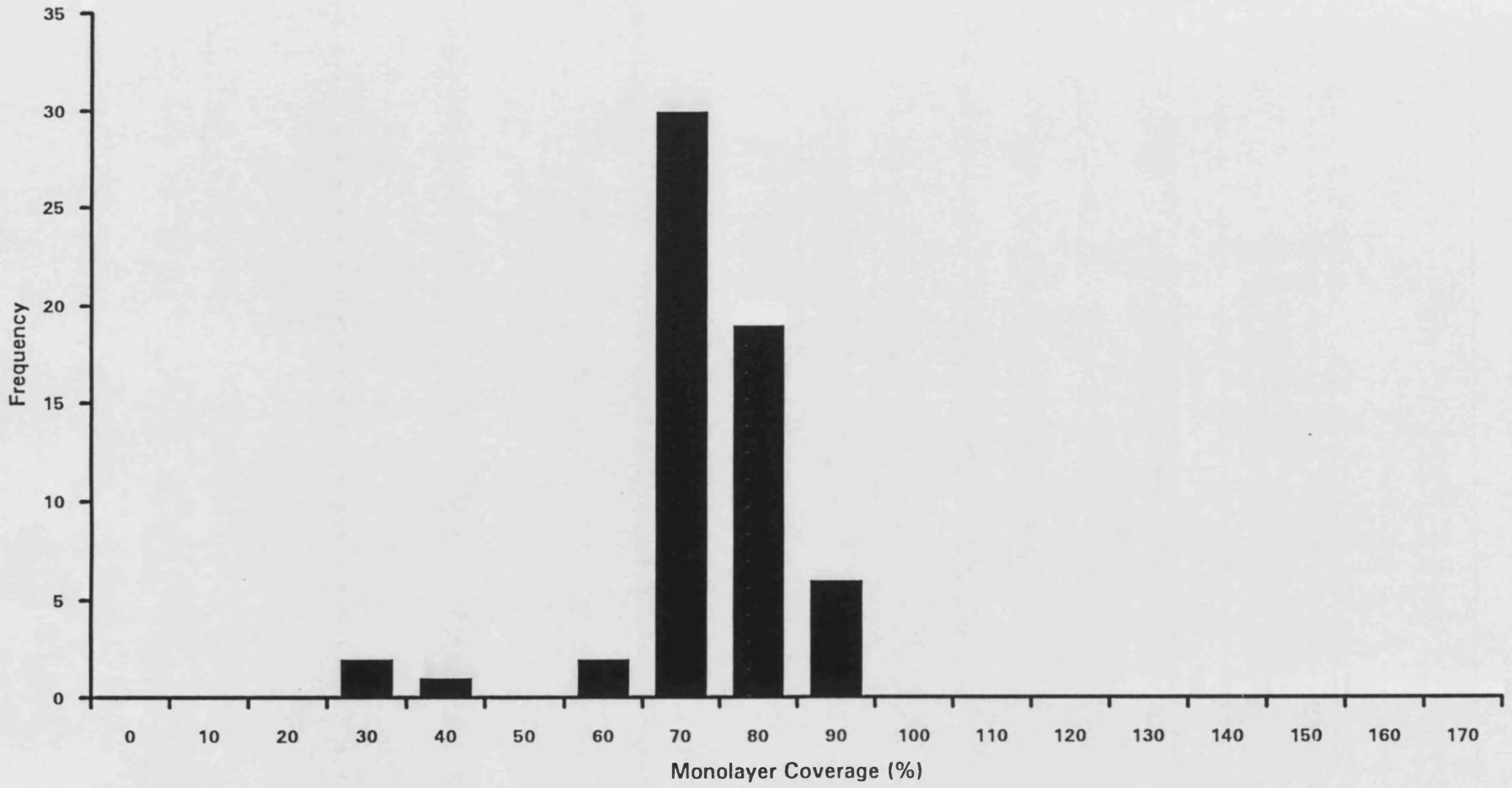

Figure 5.21 Distribution of monolayer coverage of phosphorus detected in alloy S300 calculated from AES data, not corrected for chromium content

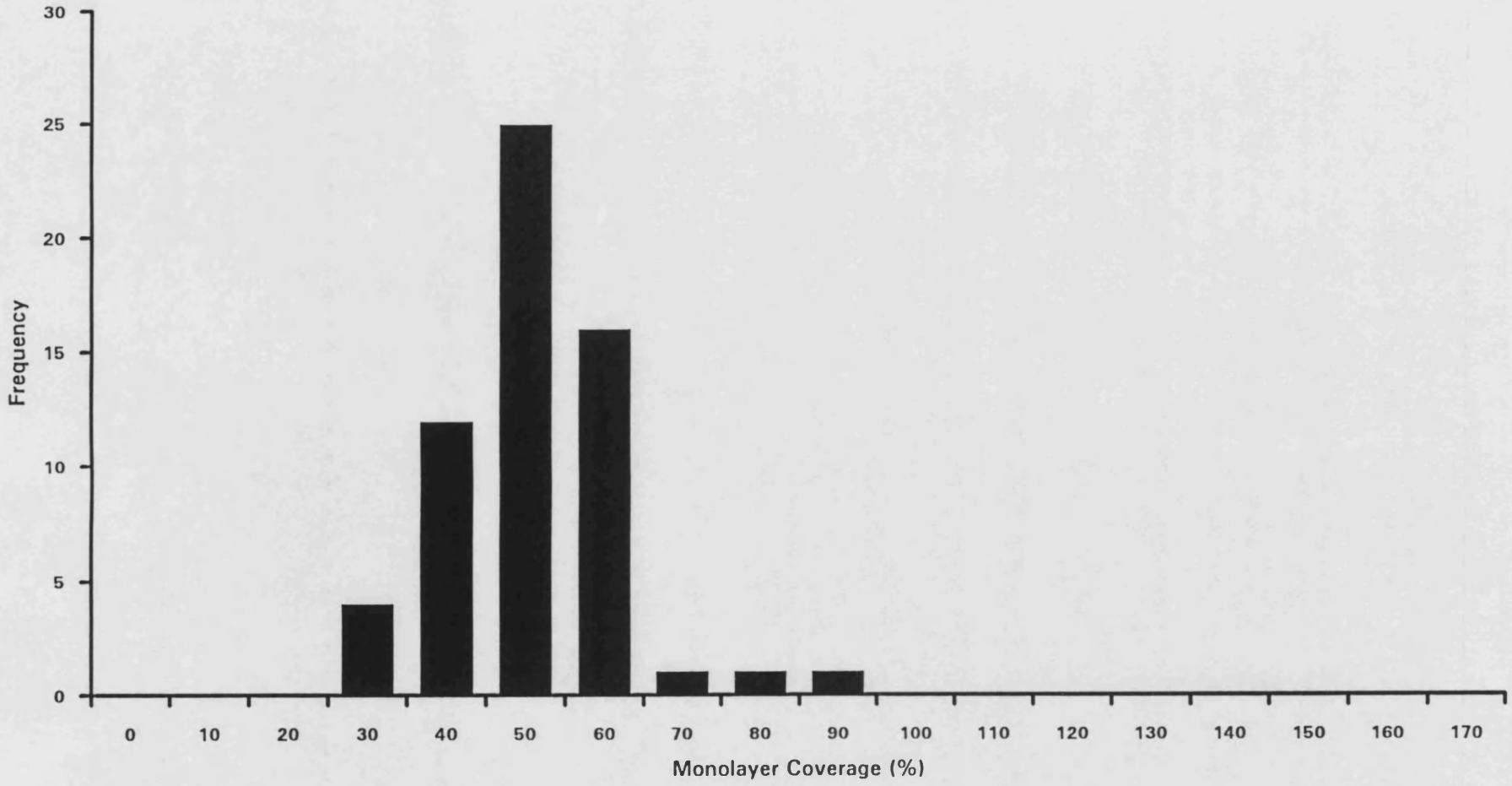

Figure 5.22 Distribution of monolayer coverage of phosphorus detected in alloy S120 calculated from AES data, not corrected for chromium content

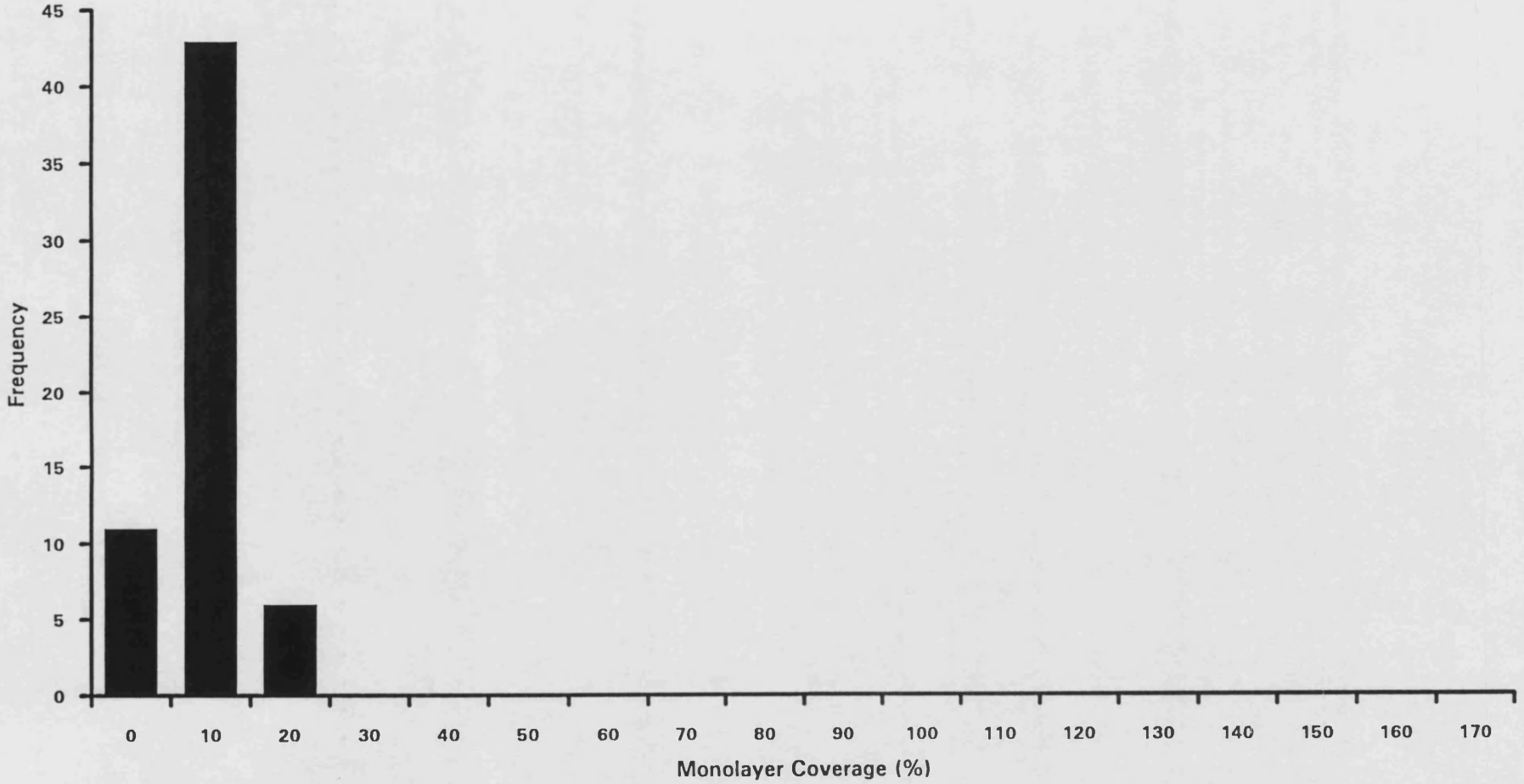

Figure 5.23 Distribution of monolayer coverage of phosphorus detected in alloy S25 calculated from AES data, not corrected for chromium content

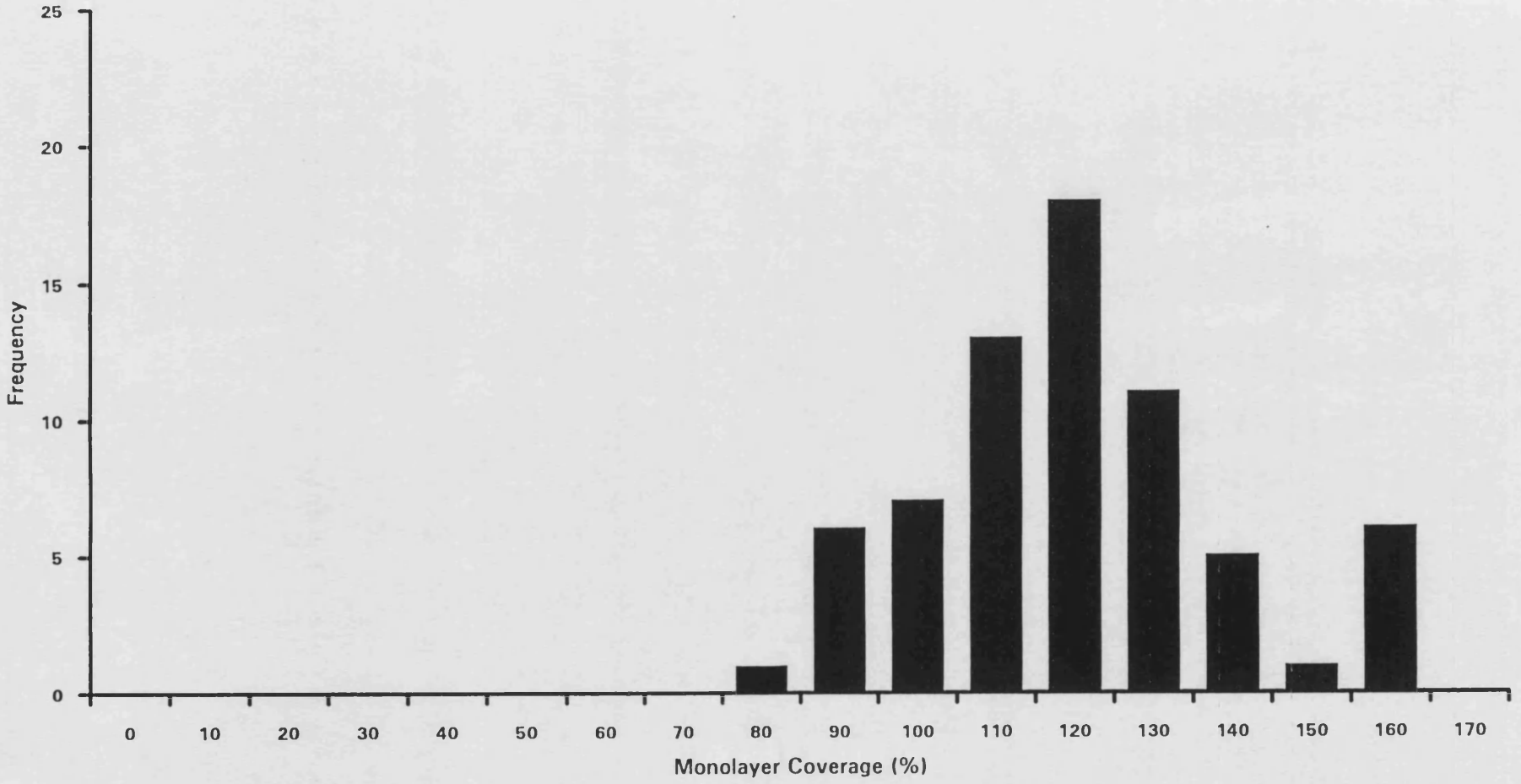

Figure 5.24 Distribution of monolayer coverage of chromium detected in alloy S560 calculated from AES data, corrected for matrix chromium

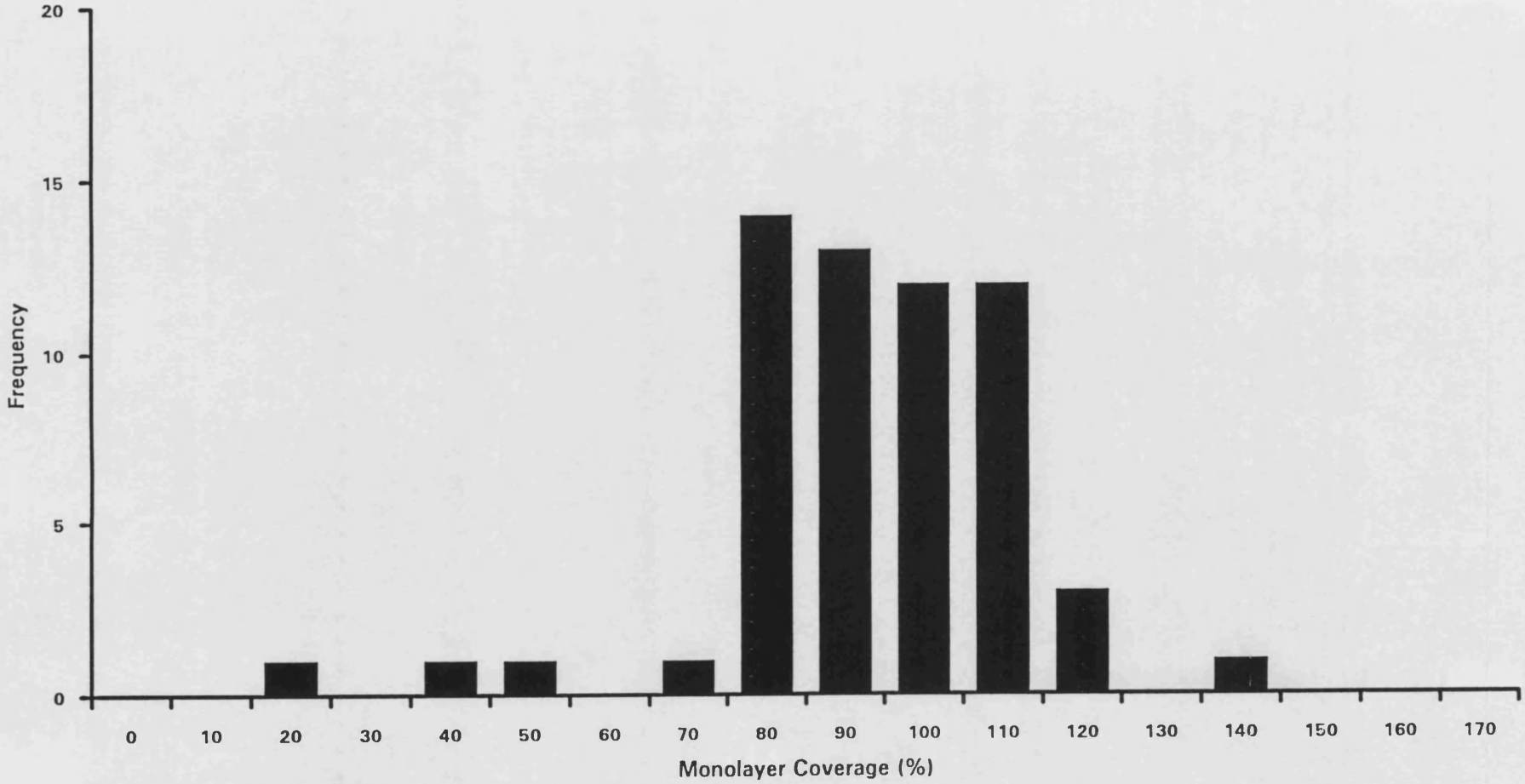

Figure 5.25 Distribution of monolayer coverage of chromium detected in alloy S300 calculated from AES data, corrected for matrix chromium

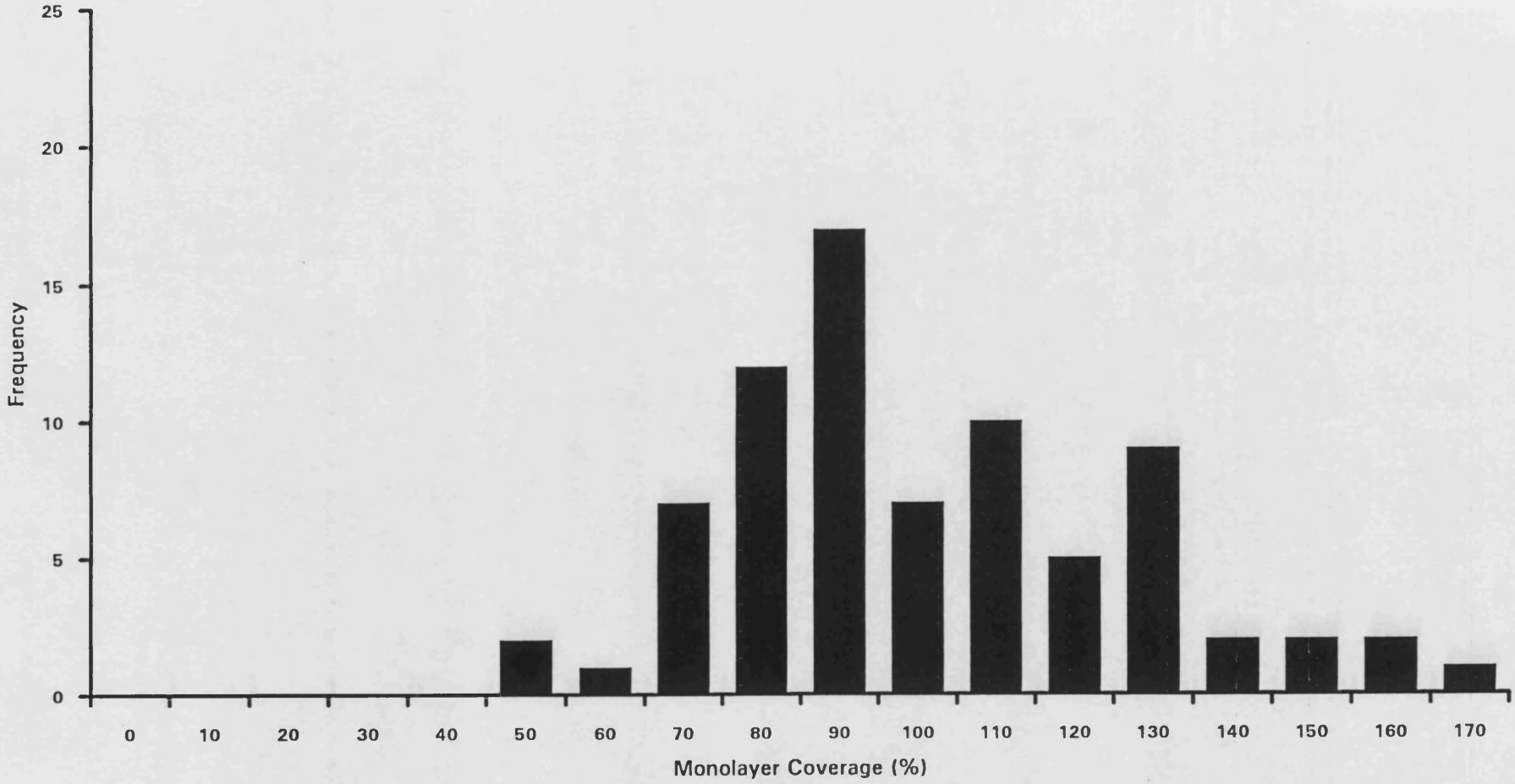

Figure 5.26 Distribution of monolayer coverage of chromium detected in alloy S120 calculated from AES data, corrected for matrix chromium

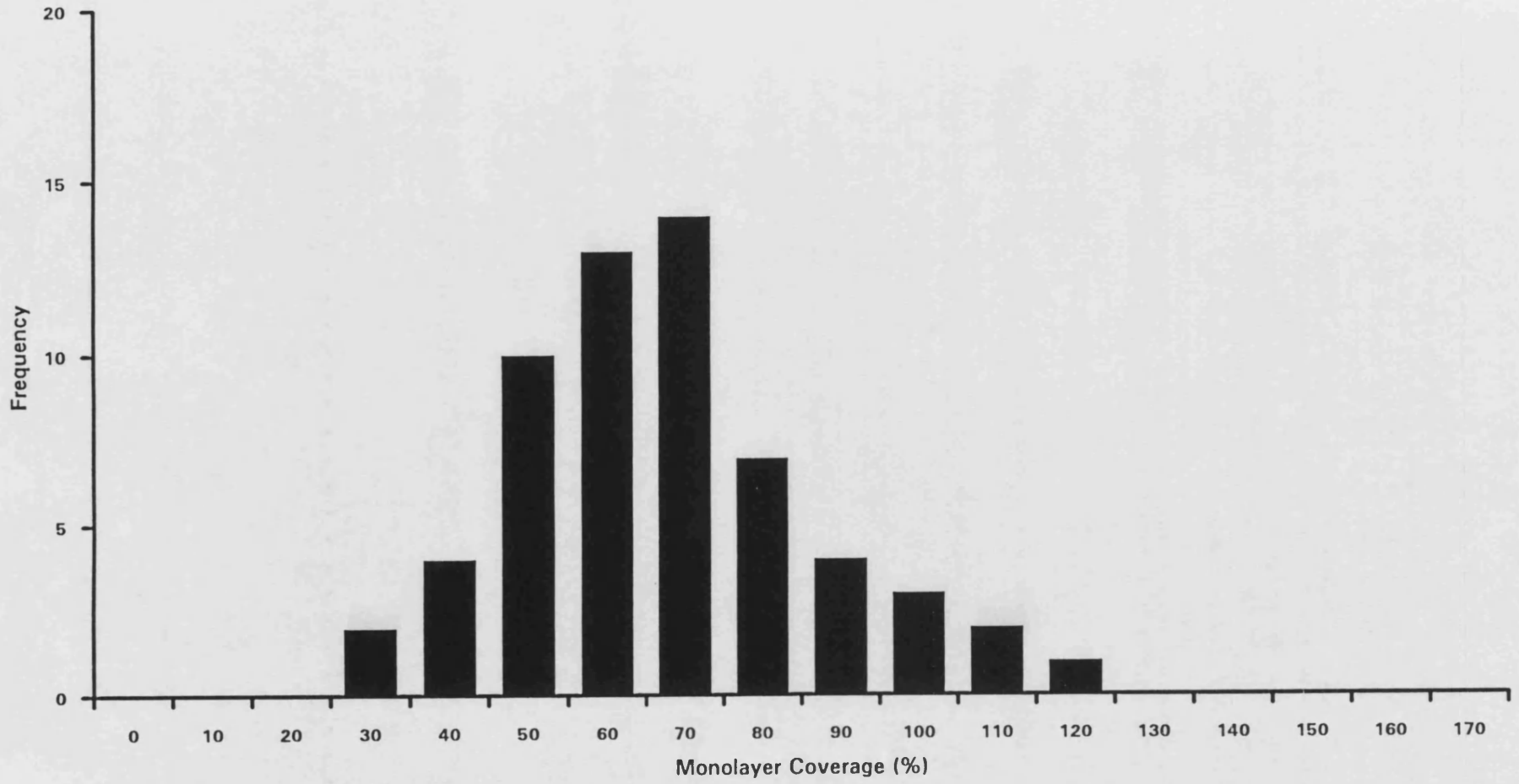

Figure 5.27 Distribution of monolayer coverage of chromium detected in alloy S25 calculated from AES data, corrected for matrix chromium

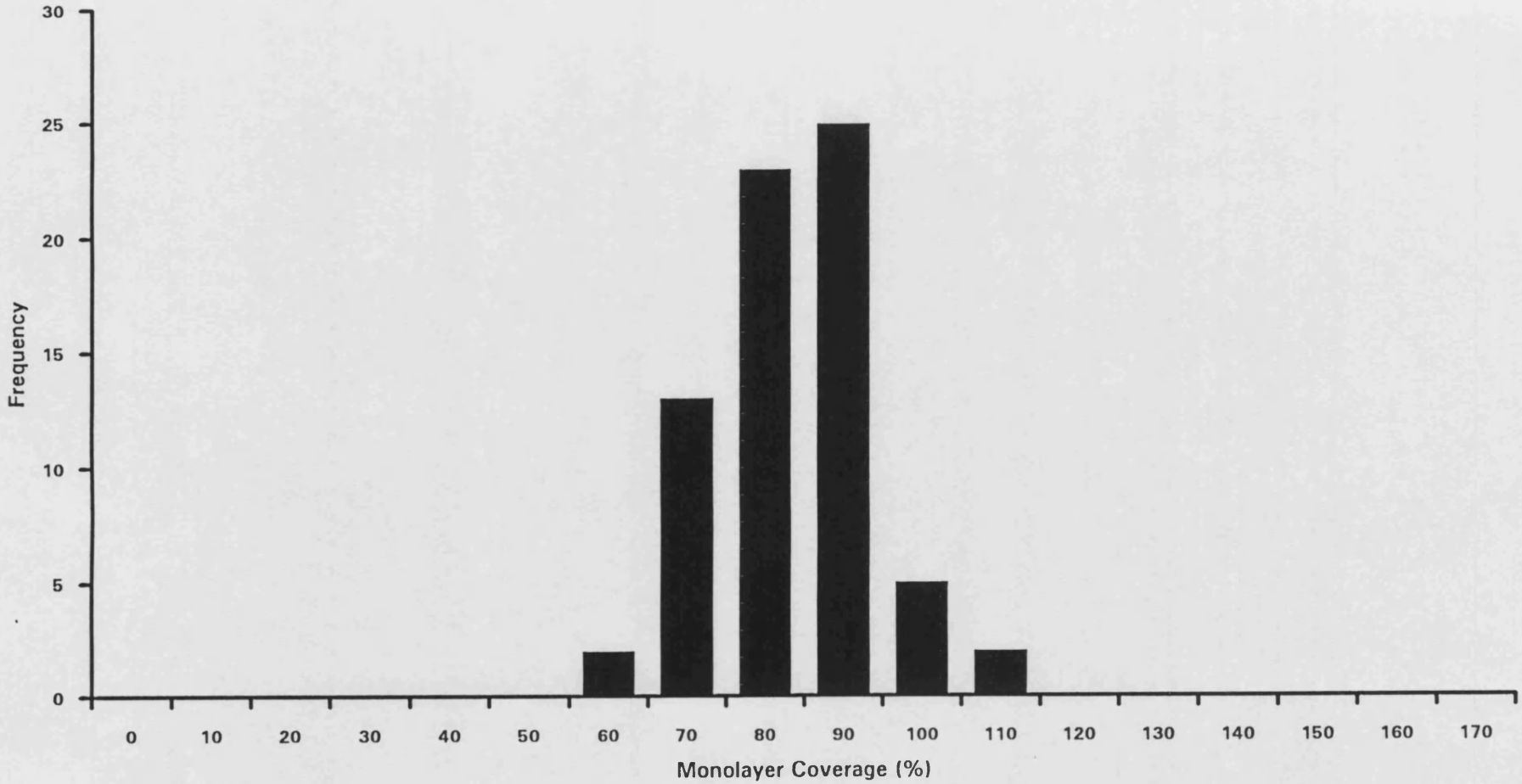

Figure 5.28 Distribution of monolayer coverage of phosphorus detected in alloy S560 calculated from AES data, corrected for matrix chromium

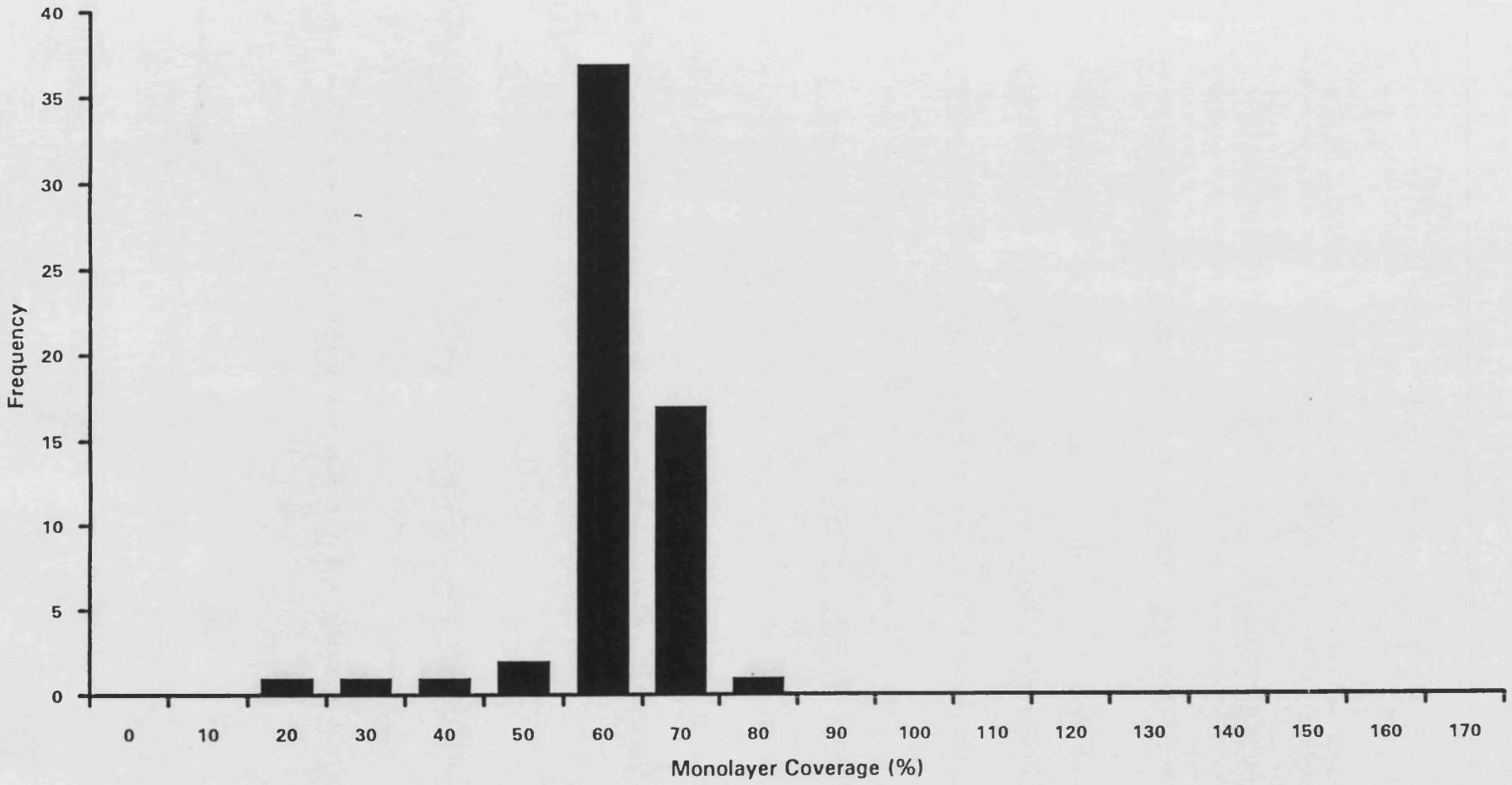

Figure 5.29 Distribution of monolayer coverage of phosphorus detected in alloy S300 calculated from AES data, corrected for matrix chromium

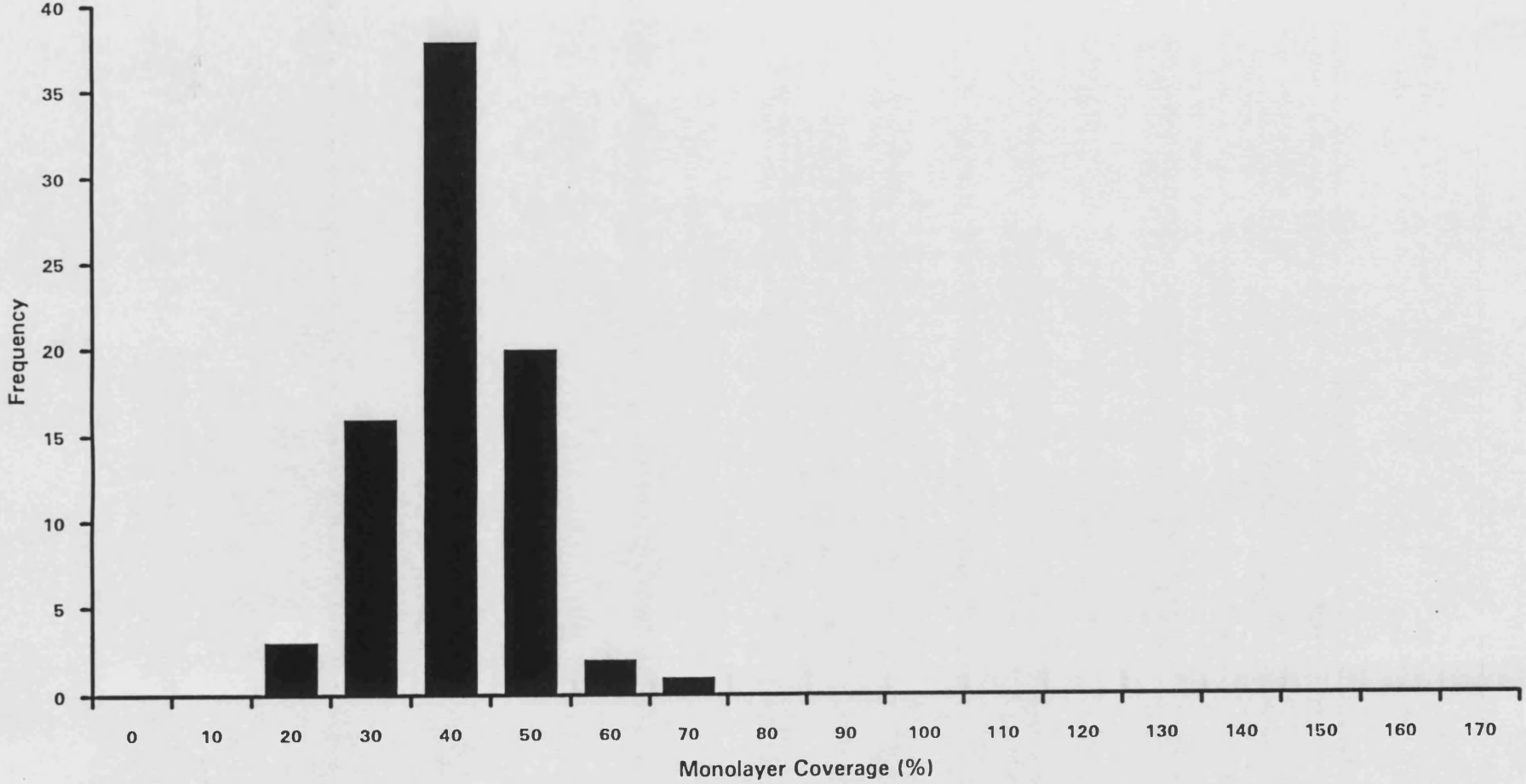

Figure 5.30 Distribution of monolayer coverage of phosphorus detected in alloy S120 calculated from AES data, corrected for matrix chromium

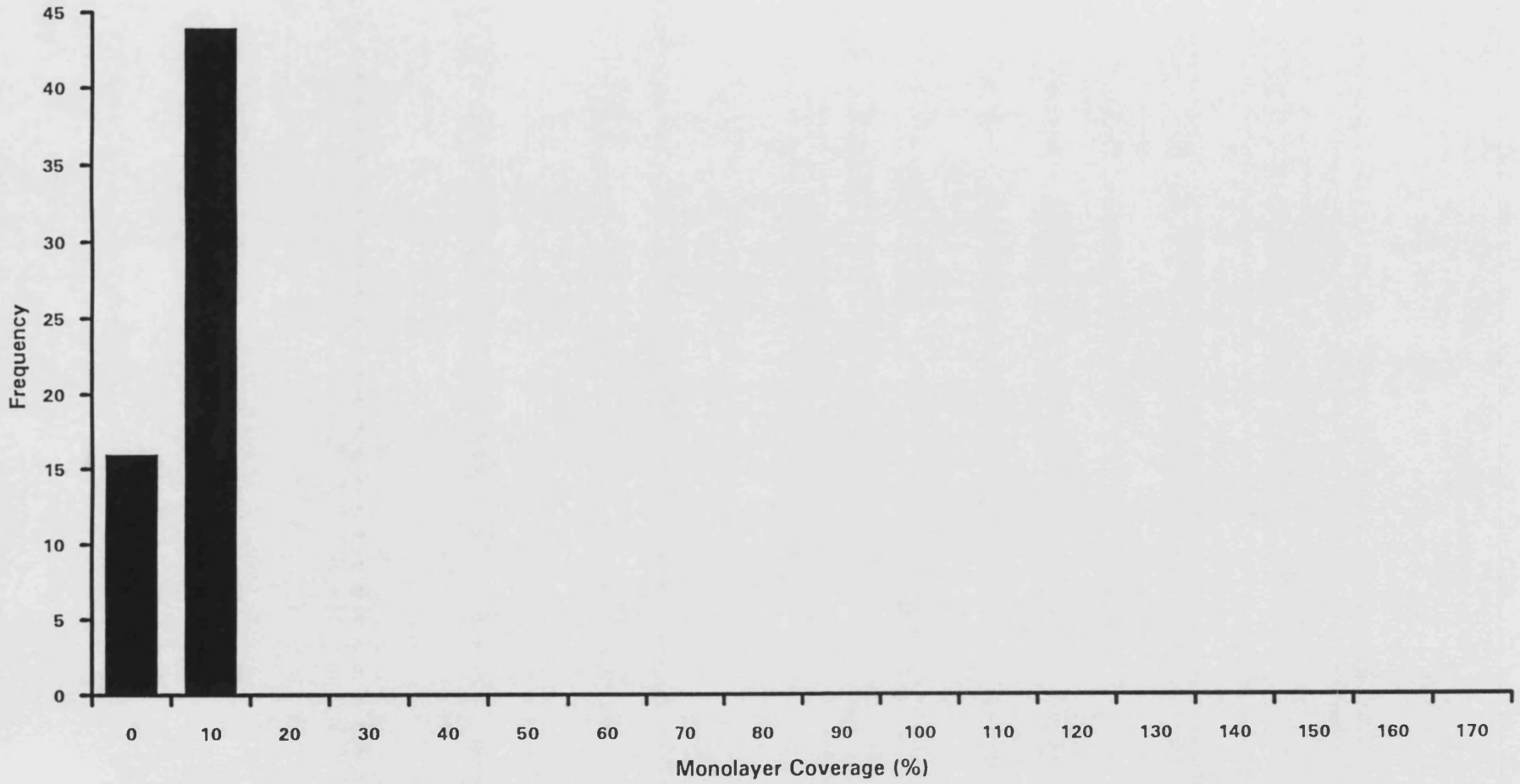

Figure 5.31 Distribution of monolayer coverage of phosphorus detected in alloy S25 calculated from AES data, corrected for matrix chromium

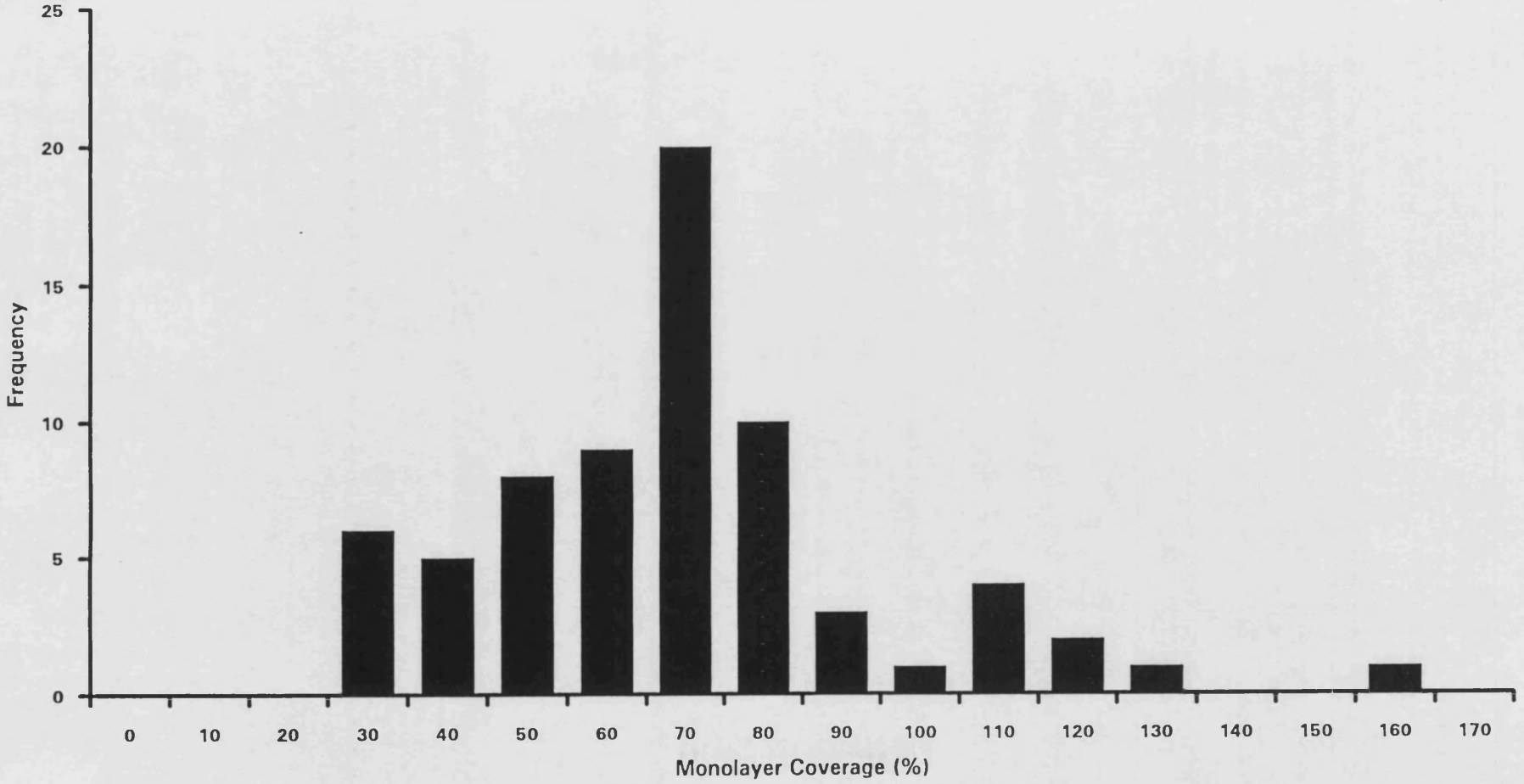

Figure 5.32 Distribution of monolayer coverage of chromium detected in alloy S560 calculated from AES data, corrected for matrix and precipitate contributions to chromium signal

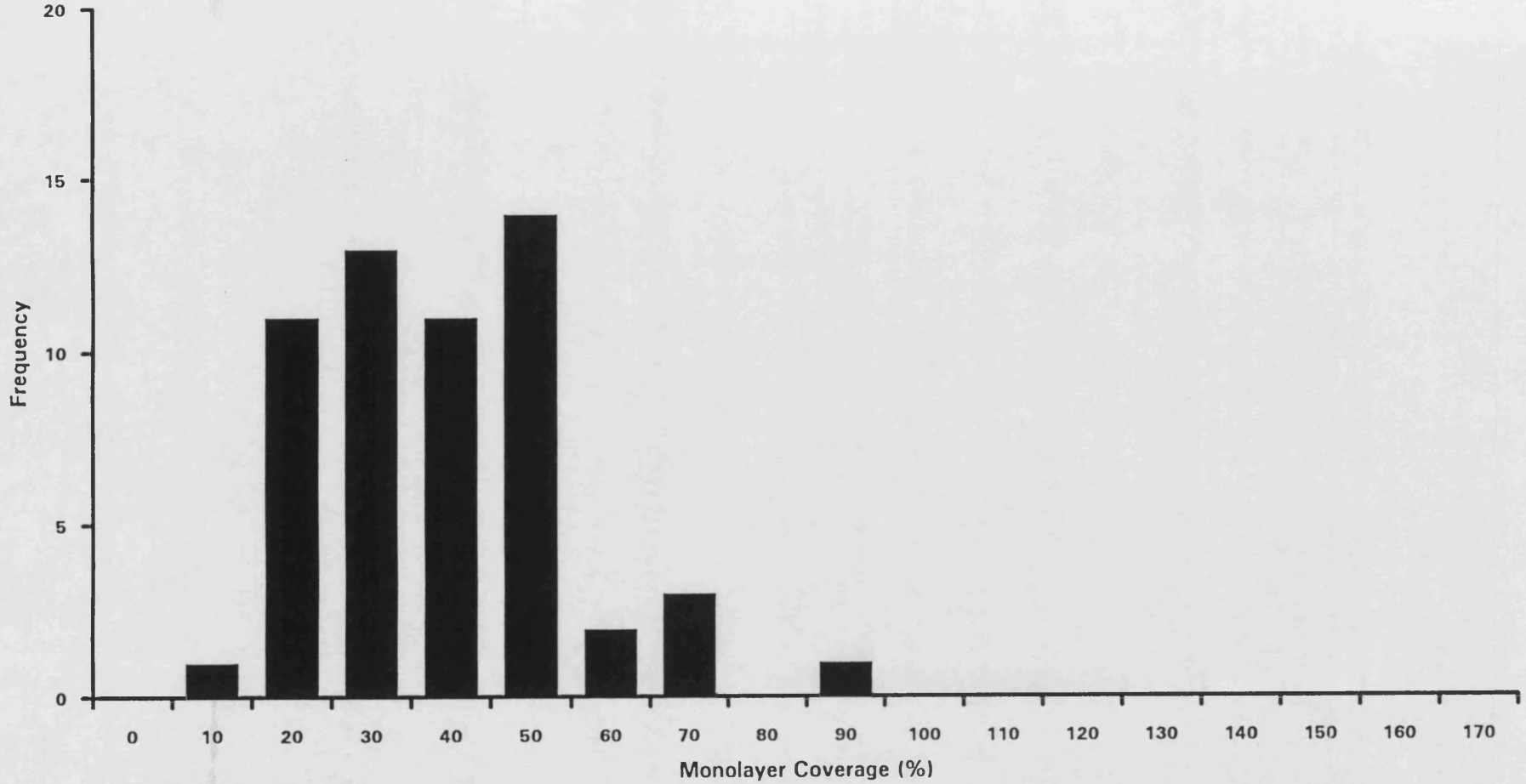

Figure 5.33 Distribution of monolayer coverage of chromium detected in alloy S300 calculated from AES data, corrected for matrix and precipitate contributions to chromium signal

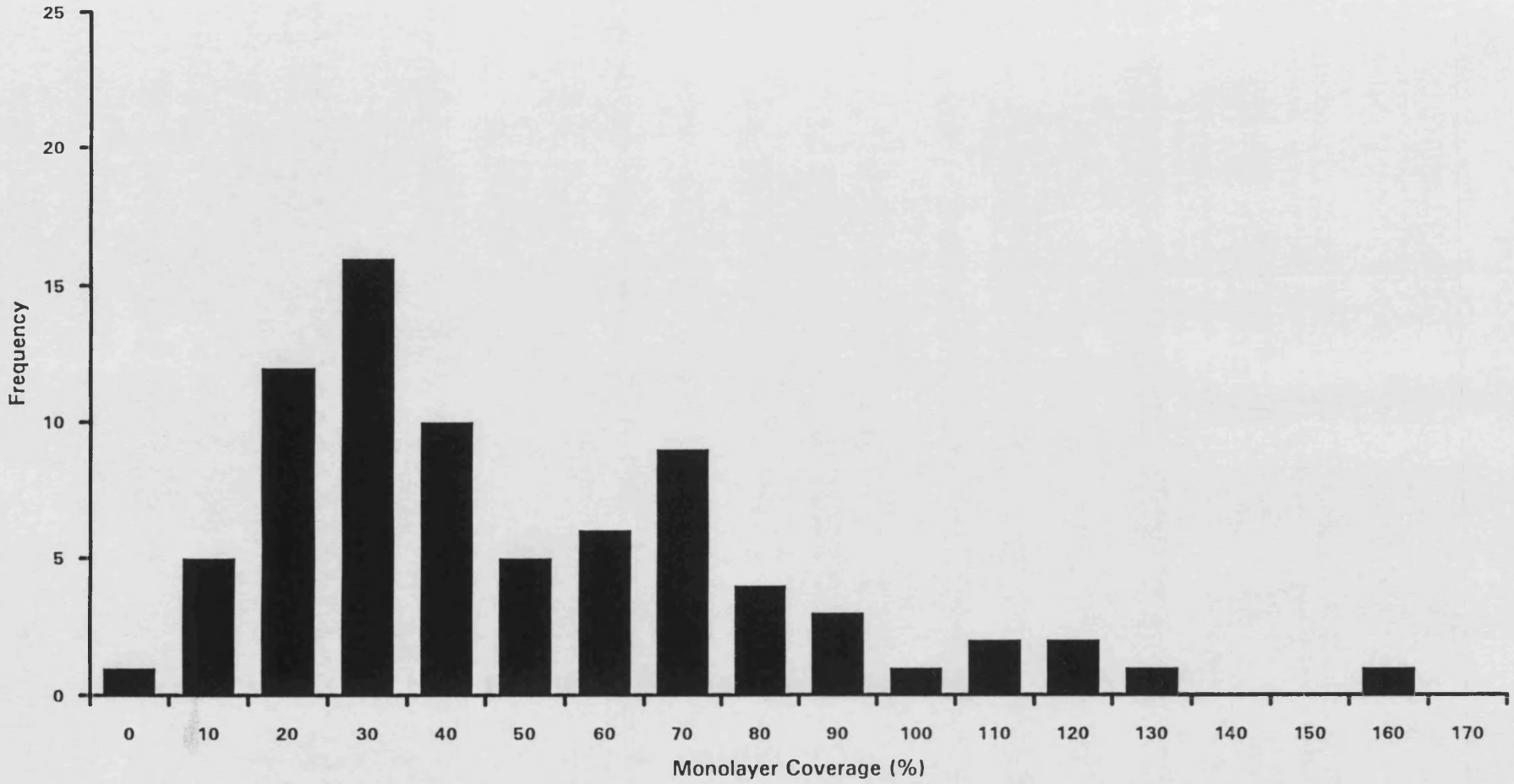

Figure 5.34 Distribution of monolayer coverage of chromium detected in alloy S120 calculated from AES data, corrected for matrix and precipitate contributions to chromium signal

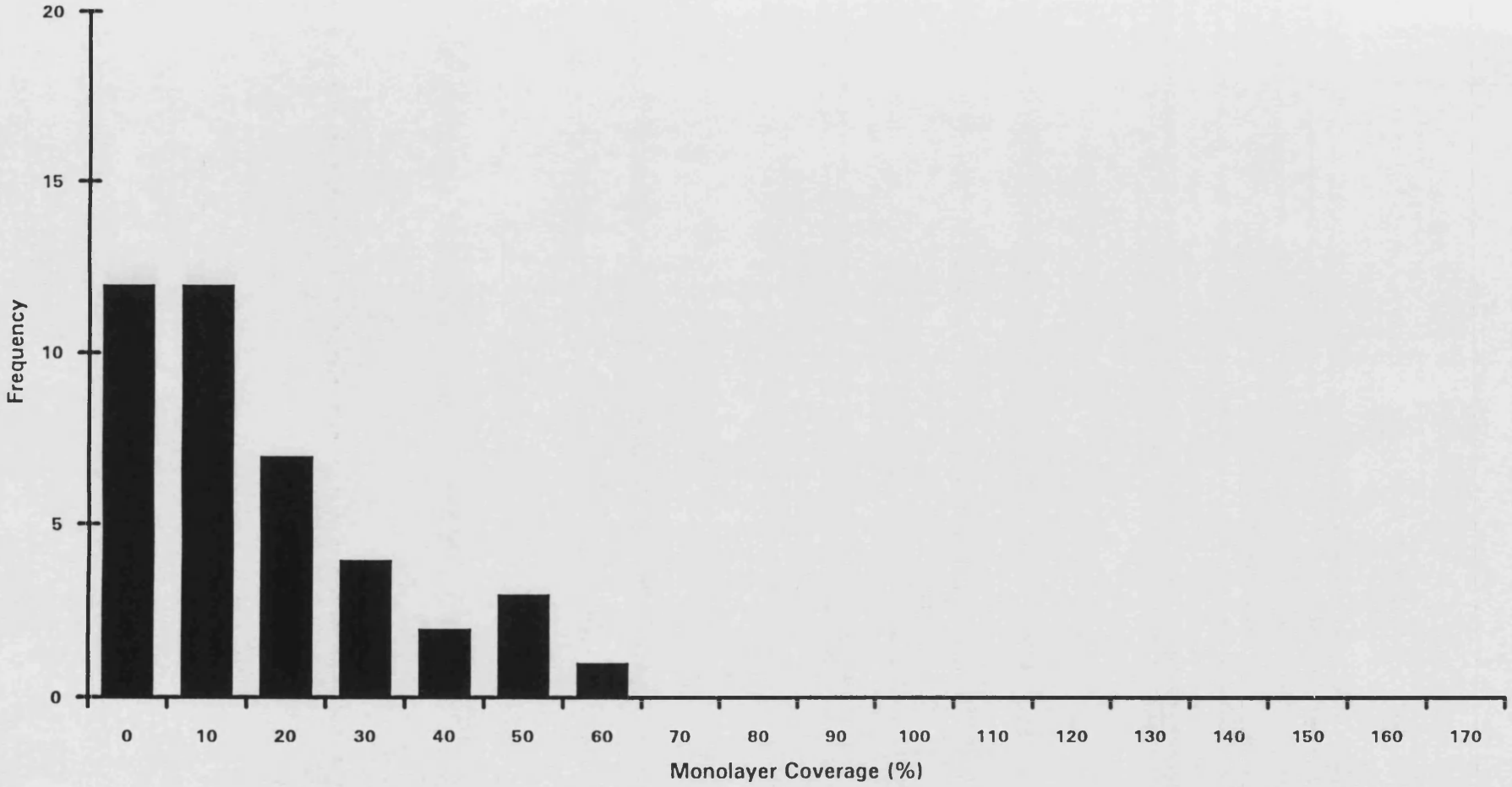

Figure 5.35 Distribution of monolayer coverage of chromium detected in alloy S25 calculated from AES data, corrected for matrix and precipitate contributions to chromium signal

Chapter 6 Discussion

This chapter discusses the methods of quantification which were developed in the previous chapter and used to convert the experimental data collected by AEM and AES from the phosphorus doped 9% chromium steel to equivalent monolayer coverages. The limitations and errors associated with each technique are discussed and the minimum detectable mass and number of atoms of segregant are determined for both of the techniques. Finally the monolayer coverages determined by the two techniques are compared and the conditions under which each is superior discussed.

6.1 Quantification of Data

6.1.1 Quantification of EDX Spectra

The technique of x-ray analysis in the AEM using EDX imposes limitations on the data which can be acquired. A major limitation is the poor response of the EDX detector with respect to light element detection. Several factors contribute to this problem. First although the ionisation cross-section of an atom increases with decreasing atomic number the fluorescence yield for x-rays decreases, consequently the light elements which are ionised are more likely to result in the production of an Auger electron than an x-ray photon. In addition the response of the silicon crystal is not constant with respect to x-ray energy as shown in figure 6.1. The efficiency of the EDX detector is relatively constant from 3 - 20keV but decreases as the incident x-ray energy falls below 3keV. Therefore the overall efficiency of EDX detection fall with decreasing atomic number. In addition, the x-rays which are produced from low atomic number elements are of low energy and therefore suffer greater absorption than higher energy x-rays, both prior to their exit from the sample and in any 'window' placed between the microscope chamber and the

detector. The lower limit for element detection using an EDX detector equipped with a beryllium window is approximately Z=10. This atomic number cut-off can be reduced by using a thin window of organic material in place of the beryllium or, if the vacuum in the AEM specimen chamber is good enough, removing the window completely. Such measures allow the passage of low energy x-rays from the sample to the detector. In the 'windowless' configuration low energy detector efficiency is determined by x-ray absorption in the gold contact and silicon dead layer which are present on the surface of the detector crystal. Under favourable conditions the 'windowless' detector interfaced to the HB501 can be used to detect x-rays from boron, the latest generation of EDX detectors are now demonstrating their capability to detect beryllium x-rays. The above factors combine to limit the usefulness of the EDX technique for detecting the presence of low atomic number elements particularly in low concentrations at interfaces.

Quantification of the x-ray spectrum imposes additional constraints. Factors which have the capacity to limit the accuracy of analysis include background subtraction, the deconvolution of overlapping peaks and the separation of the characteristic x-ray signals emitted by the sample from spurious x-ray signals which can arise from; the microscope environment, as a consequence of the sample preparation technique or the sample itself.

The accuracy of background subtraction can be enhanced and made more objective by the use of software routines, such as the digital filtering methods developed by Statham (1976a), or the shape of the background can be modelled using theoretical techniques. The latter technique requires a knowledge of the specimen composition and its use in the quantitative analysis of x-ray spectra is therefore necessarily iterative. Software routines are also used extensively in the identification and deconvolution of x-ray peak overlap.

In addition to the characteristic x-ray peaks several artefacts may also appear in the x-ray spectrum. The most important artefacts in relation to this study are sum peaks, escape peaks, tails on the low energy side of characteristic peaks due to incomplete charge collection, and coherent Bremsstrahlung.

Sum peaks occur when two x-ray photons enter the silicon crystal detector too close together for the electronics to distinguish them as separate events and hence the energy dissipated in the crystal is recorded as the sum of the two photons. The probability of occurrence of such dual events increases with x-ray count rate. Sum peaks are most commonly seen associated with the major elements present in a spectrum, e.g. iron in a spectrum collected from a steel. However, if the count rate is high enough, sum peaks for all of the constituents, as well as any combination of them, may occur. In cases of extremely high count rates triple or even higher order sum peaks may be found. However such events are more likely to be encountered in x-ray fluorescence experiments than electron microscopy, due to the significantly higher x-ray count rates encountered in the former technique.

At an energy of 1.74 KeV below a characteristic peak there may be found a smaller peak. This is the associated silicon escape peak. A count appears in the escape peak if an x-ray photon enters the detector and ionises a silicon atom by displacing a K shell electron, a process which requires 1.74 KeV of the incoming photon's energy. If the ionised silicon atom relaxes by the emission of an x-ray which is not absorbed within the detector then the resultant pulse measured will be reduced by 1.74 KeV from the energy of the incident x-ray photon. If the silicon x-ray is itself absorbed within the detector crystal then the electron-hole pairs produced are added to the original pulse (in a manner analogous to sum peak production) and the energy of the original photon is correctly recorded. The probability of the escape of the fluoresced silicon x-ray is a function of the depth within the detector crystal at which the silicon atom was ionised. Consequently the size of the escape peak, relative to the parent peak, is a function of the incident x-

ray energy as this controls the average depth at which the x-ray photon is absorbed in the detector and, hence, the escape probability of the silicon x-ray. Statham (1976b) calculated the size of the escape peak, for photons of normal incidence on the detector, to be:

$$0.0202 / (1+(mE+b)\,E^2) \qquad 6.1$$

where $m = 0.0144$

$b = 0.169$

E = x-ray energy in keV

Therefore for an iron kα peak (6.4 keV) the escape peak will contain approximately 0.2% of the number of counts in the parent peak. The size of the escape peak increases as the energy of the x-ray photon decreases down to approximately 1.9 keV where the escape peak contains approximately 1% of the number of counts within the parent peak. Below an energy of 1.9keV the incident x-rays no longer have sufficient energy to ionise a silicon atom. If the detector crystal is fabricated from a material other than silicon, germanium for example, the energy separation of the parent and escape peaks will be altered.

Tails which can appear on the low energy side of peaks are caused by incomplete charge collection. This occurs when some of the electrons, or holes, produced by the x-ray incident on the detector are not included in the output charge pulse These losses can be caused by trapping of the electrons, or holes at imperfections and surface states in the detector crystal, or by the decreased mobility of electrons and holes in the surface regions of the detector. Both of these mechanisms result in the incomplete collection of the charge produced within the detector by the incoming x-ray and the recording of an energy for the incident photon below its true value. The magnitude of these low energy tails varies with x-ray energy and also the quality of the detector crystal.(Craven et al 1985)

The spectrum shown in figure 6.2 was collected on the VG HB501 STEM and exhibits some of the above artefacts. The output count rate from the pulse processor was 21,000 counts per second, which is significantly higher than the 2,500 counts per second typically used when acquiring chemical composition data in the present investigation. The increase in count rate was achieved by firstly increasing the current contained in the electron probe by using a larger beam defining aperture and secondly placing the probe on a thick region of the sample. The spectrum is taken from a low-alloy ferritic steel containing iron, chromium, nickel and silicon. Easily visible are sum peaks of FeKα + FeKα (12.8keV) and FeKα + FeKβ (13.4 keV); much smaller will be the FeKβ + FeKβ (14.1 keV). The peak at an energy 17.4keV is due to the presence of a small amount of molybdenum in the steel, as confirmed by the L series of peaks at an energy of 2.302 KeV. The small peak 1.74 KeV below the FeKα peak is the FeKα escape peak. The characteristic peaks are symmetrical, evidencing very little incomplete charge collection. This is due to a high-quality detector crystal containing few trapping defects being used and good collimation of the incoming x-rays away from the edges of the detector crystal. The low energy region of the spectrum comprises L peaks from the transition elements, K peaks from carbon and oxygen, and Bremsstrahlung background radiation. The presence of characteristic x-rays in this region is due to the "windowless" configuration of the detector on the HB501.

An additional artefact, which may appear in x-ray spectra collected from crystalline samples, is coherent Bremsstrahlung or CB. This is a component of the Bremsstrahlung radiation which appears as a series of regularly spaced peaks, generally in the energy range 0 - 5 KeV, superimposed on the normal spectrum background. The CB peaks are strongest when the electron beam is parallel to a zone axis of the crystal. The energy of these additional peaks, (E keV), can be determined using the following formula (Spence et al 1983).

$$E = \frac{12.4\ (v/c)}{(1 - (v/c)\cos\theta)\ .\ L} \qquad 6.2$$

v = electron velocity

c = speed of light

θ = angle between beam and detector

L = interplanar spacing in nm

for E_0 = 100 keV and $\theta = 110°$

$E = 0.573/L$

As many materials have interplanar spacings in the range 0.2 to 0.5 nm, CB peaks commonly have energies in multiples of approximately 1-2 keV. The presence of CB peaks can be confirmed by tilting the specimen, upon which a series of CB peaks would either disappear or shift in energy. An EDX spectrum showing the presence of coherent Bremsstrahlung peaks is shown in Figure 6.3a. Figure 6.3b shows an x-ray spectrum from the same area of the sample after the foil had been tilted by a few degrees, this has caused the CB peaks to disappear. The presence of coherent Bremsstrahlung close to the phosphorus characteristic x-ray peak of 2.015 keV can cause problems for accurate quantification. To confirm the absence of a CB contribution to an interfacial x-ray spectrum, which might adversely affect quantification, x-ray spectra were always collected from the grains on both sides of the interface. Due to the change in crystallographic orientation across the interface, it is possible for one grain to exhibit CB peaks which are absent in the other grain, alternatively both grains can show peaks at different energies. It should be noted that at general crystallographic orientations no CB peaks are observed.

In addition to the spectral artefacts mentioned above, there are other artefacts which may be produced by the sample itself. These include oxide films, which increase the sample thickness and consequently increase beam broadening, and may also be preferentially enriched in one or more of the constituents within the

sample. Other surface films may be formed containing elements from the polishing solution, e.g. chlorine from perchloric acid electropolishing solution. The use of ion milling as a final stage of sample preparation can be used to remove both of these variants of surface films. However, ion milling produces a sample implanted with atoms of the gas used, characteristic x-rays from which will also contribute to the x-ray spectrum.

All of these artefacts need to be taken into consideration when identifying elements present in a sample and especially when conducting quantitative analysis.

In addition to the above detector and specimen-induced artefacts, the microscope can also be a source of x-ray signals. As the electron beam travels down the microscope column there are various apertures through which it must pass. At each of these, x-rays are produced characteristic of the aperture material. Electrons scattered by these apertures or by the sample itself can excite x-rays from the material they subsequently encounter. After scattering, the electrons may impinge on other portions of the sample, the specimen holder, the lens pole piece or other material in the vicinity of the scattering event. Without adequate collimation and shielding of the x-ray detector these additional x-rays can appear in the spectrum. A measure of the spurious x-ray signal present in a microscope can be made by collecting a "hole count". The "hole count" spectrum is collected with the electron beam focused through the hole in the specimen. The hole count does not represent all of the spurious x-ray signal present in spectra collected from the sample, as it does not include the signal produced by electrons scattered by the specimen. To investigate the magnitude of all of the spurious x-rays produced it is necessary to analyse an x-ray spectrum collected under standard analysis conditions, from a pure elemental sample, of similar atomic number to the sample being investigated. Provided that the sample being analysed is adequately pure, any x-rays detected from other elements can be attributed to spurious sources.

6.1.2 Interfacial Analysis in the STEM

Having ascertained that a boundary of interest was a prior austenite grain boundary by tracing it to a triple point, the next stage was to locate a section of the boundary suitable for chemical composition analysis. The procedure used to characterise interfaces in this study requires that the boundary is parallel to the incident electron beam. This maximises the segregant with which the electrons interact during their passage through the foil. The effect of tilting the grain boundary on the excited segregant signal is shown schematically in figure 6.4. When the grain boundary is parallel to the incident beam all of the segregant, with an assumed width of 0.2 nm (i.e. one atom plane), is intercepted by the two nanometre diameter electron beam. For a foil thickness of 75nm a tilt of the boundary of two degrees away from vertical produces a projected width of 2.6nm. Neglecting beam broadening, the proportion of the segregant with which the electron beam can interact is reduced to 0.77. If the tilt of this theoretical boundary is increased to four degrees from the vertical its projected width increases to 5.2nm and the proportion of segregant through which an unbroadened electron beam passes is reduced to 0.4 of its original value. This tilting of the grain boundary reduces the number of x-rays generated by the segregant and so degrades the characteristic signal detected, making it more difficult to determine the presence of small quantities of segregant. The preceding simple calculation demonstrates the requirement for accurately aligned boundaries. The criterion used to determine the suitability for analysis of an interface in this study was that its projected width in the bright field image must not exceed 2nm. In practice very few boundaries were observed to have a projected width of significantly less than 2nm. This criterion ensures that the boundary width is less than the 90% electron probe diameter and places an upper limit for deviation from the vertical of approximately 1.5° for a foil thickness of 75nm. As the foil increases in thickness the alignment with the electron

beam becomes more critical, and for a foil of thickness greater than 115nm the allowable deviation of the grain boundary from the vertical is less than 1°.

Monte Carlo simulations have been conducted in which the incoming electron beam has been deviated from the normal of the sample surface to predict the effect of misalignment of the boundary on the chemical composition profile collected. These calculations are equivalent to altering the angle of the grain boundary within a TEM sample. The Monte Carlo calculations have been conducted for the case of the electron beam positioned on the grain boundary and also stepped along a line perpendicular to the boundary to produce a theoretical chemical composition profile. The path length of electron trajectories in the segregant is plotted as a function of probe position in figure 6.5 for the two cases of 0° (vertical boundary) and 5° tilt. As the angle of tilt between the electron beam and grain boundary is increased the peak segregant signal predicted with the electron beam positioned on the grain boundary falls and the FWHM of the profile increases. Also at a tilt of 5° the profile can be seen to be asymmetric. This asymmetry is caused by beam broadening and the process is shown schematically in figure 6.6. Two probes with identical initial width and beam broadening characteristics are placed an equal distance either side of the centre of a segregated boundary, which is tilted away from the vertical. Due to beam spreading, probe 'A' intercepts a higher proportion of segregant towards the exit side of the foil than does beam 'B' at the entrance side of the foil, thus giving a higher signal from the segregant and leading to asymmetry in the profile. The characteristics of reduced maximum signal and profile asymmetry are exhibited by the experimental profiles shown in figures 4.24a - c. These profiles were taken from a well oriented boundary, a boundary tilted by 2.5° (4nm projected width in a 71nm thick foil) and 4° (projected width 5nm in foil of same thickness) respectively. The FWHM of the composition profiles has increased from 3.8nm to 11.8nm. This increase of approximately 200% in FWHM, for a tilt of 4°, indicates the sensitivity of this parameter to deviation of the

boundary from the vertical. The other consequence of carrying out chemical composition analysis of a misaligned boundary, reduction in the peak signal detected with the probe positioned on the boundary can also be seen. In the example shown in figure 4.24 the reduction in the detected signal is from 2.4 wt.% (4.1at.%) to 1.0 wt.% (1.8at.%), a decrease of more than 50%, for a tilt of 4°. The need for accurate boundary alignment is particularly important for quantification of reduced profiles, where assumptions need to be made about the probe shape.

The profile generated by stepping the fine electron probe perpendicular to a well oriented boundary typically exhibits a FWHM of approximately 3nm. However equilibrium segregation of phosphorus, as being investigated in this steel, occurs on a much finer scale, typically within one or two atom planes of the grain boundary (2-5Å). The segregation is therefore evidently occurring on a much finer scale than the x-ray profile produced. This can be explained with reference to figure 6.7. As the electron beam is traversed across the grain boundary, the first signal from the segregant is detected when the tail of the electron distribution in the probe intercepts the segregant layer. As the peak of the probe approaches the segregant layer the detected signal increases. The detected signal falls again as the electron probe recedes from the boundary. If the proportion of segregant intercepted by the beam is calculated (neglecting beam broadening) at each point of its traverse the resultant plot, also shown in figure 6.7, reflects the electron current distribution within the probe rather than the true spatial distribution of the segregant.

6.1.3 Quantification of AES Spectra

Having calculated the inelastic mean free path (imfp) of Auger electrons using equation 5.8 quoted in section 5.2.1, this value can be used to predict the depth into the sample from which the Auger electrons will contribute to the detected

spectrum. The Auger electron flux decays due to absorption as exp (-t/λ), where t is the distance into the sample that the Auger electron is produced and λ is the imfp of the Auger electron in the matrix. Therefore Auger electrons produced at a depth of 1λ into the material have a probability of 0.37 of escaping from the surface. This decreases to 0.13 and 0.05 for depths of 2λ and 3λ respectively and Auger electrons produced at a depth of 5λ have a probability of escaping from the surface of less than 0.01. Figure 6.8 demonstrates how this attenuation affects the proportion of Auger electrons being emitted from a surface when they are produced at varying depths into the sample. As the distances involved are very small, a few nanometres, it is possible to ignore the loss of energy from the primary electron beam and the number of Auger electrons produced can be considered constant with depth. If it is assumed that 100 Auger electrons are produced by the primary beam at depths of 0.5, 1.5, 2.5, 3.5 and 4.5λ into the sample, all of which are emitted in the direction of the surface. The number of these which escape from the surface is 60, 22, 8, 3 and 1 from each layer respectively. This gives a total flux of 94 Auger electrons of the 500 emitted in the direction of the surface. From this simplified approximation it can be seen that 67% of the Auger electrons detected are produced within one inelastic mean free path, and 96% within three inelastic mean free paths of the sample surface. For bulk iron this converts to 96% of the detected Auger electrons being emitted from the outermost 3.5nm of the sample. Using equation 5.9 the atom size of iron is calculated to be 0.228nm. X-ray diffraction measurement of the interplanar spacing of the close packed planes in iron gives a value of 0.202nm, which is not inconsistent with the calculated atom size. Using the interplanar spacing to calculate the depth from which Auger electrons are detected in terms of atoms planes reveals that 67% originate from the outermost 6 atom layers and 96% from the outermost 18 atom layers. This depth is further reduced by the fact that the detector is rarely able to be placed so that its axis lies normal to the surface being analysed. A more realistic take-off angle for the detector is 30° from the surface normal. This reduces the depth from which Auger electrons will be detected by a

factor of cos (30°), equal to 0.866. Thus the escape depths are reduced to 1nm (67%) and 3nm (96%), or represented as atom layers 5 and 16 respectively. From this it can be seen that the Auger signal whilst being surface specific in origin it is not surface exclusive. The collected Auger spectrum will therefore contain some information from the underlying material in a segregation study.

The dependence of backscattering factors on the incidence angle of the electron beam and the inclusion of the detector take-off angle ($\cos\theta$) in the formulae for determination of the effective path length, requires that some thought be given to the measurement of the angle of orientation of the sample in the Auger electron microprobe. For a flat specimen it is possible to calculate the angle of incidence and the take-off angle to the detector from geometric considerations. For the standard configuration used in the MA500 the specimen is tilted such that it bisects the angle between the electron gun and the Auger electron spectrometer, nominally 60°, thus giving an angle of incidence and detector take-off angle of 30°. However when examining a fracture surface the situation becomes considerably more complex as each facet presents a different angle to both the electron beam and the detector. Calculation of the exact angle is very difficult and consequently the average value of 30° has been used for the calculation of backscattering factor and path length. The effect of this approximation on the accuracy of monolayer coverage determination is discussed in a later section.

The experimental effect of varying the tilt angle was investigated by repeatedly collecting spectra from a single facet in alloy S560, altering the angle of the sample between each acquisition. The beam current was maintained at 5nA. Initially the specimen was tilted directly towards the detector; for collection of subsequent spectra the specimen was progressively tilted in the direction of the primary electron beam. The recorded phosphorus to iron ratios are plotted as a function of detector take-off angle, θ, in figure 4.40. As the angle, θ, between the specimen normal and the detector was increased the intensity of Auger electron

signal detected fell, but the phosphorus to iron peak to peak height ratio increased. The decrease in phosphorus and iron signals as the angle to the detector was increased is due to the effective path length for Auger electrons increasing with the tilt angle. This increase in path length should affect the attenuated signal from the matrix to a greater extent than the signal from the segregant, due to the Auger electrons from the former having to pass through the segregant layer. The effective thickness of the segregant layer, in the direction of the detector, is increased by the process of tilting. Therefore the ratio of phosphorus to iron would be expected to rise, as confirmed by this experimental data. The extent of the variation in the phosphorus to iron ratio is approximately $\pm 13\%$ on the mean value of 0.54. The range of angles presented to the detector in this experiment, 40°, exceeds the range of angles presented by the facets examined during this study. This level of uncertainty in the phosphorus to iron ratio also gives an indication of the limits of the possible errors introduced during the quantification of the data due to the uncertainty of the tilt angles.

In the early experiments conducted during this study there was doubt as to the stability of segregated phosphorus on the intergranular facets. The conditions used to collect the initial spectra were a magnification of x5,000, primary beam current of 10nA and an accelerating voltage of 10 keV. The beam was scanned at TV rate across the surface of a facet while the Auger spectrum was collected over the energy range 50 - 1000eV, a process which took approximately seven minutes to complete. This process was repeated 6 times over a period of an hour, maintaining the same area under the scanned beam. The phosphorus to iron ratios of the spectra were compared and found to have reduced by approximately 25% during the collection of the six spectra. The reduction in the recorded phosphorus to iron ratio observed with repeated examination of a facet of alloy S560 may be explained in one of two ways. Firstly the signal from the segregant may be reduced due to the formation of a contaminant overlayer which would mask the signal from the

underlying sample. This overlayer would reduce the signal detected from both the matrix and the segregant but would be expected to have a greater effect on the lower energy phosphorus Auger electrons relative to the higher energy iron Auger electrons, thus leading to a reduction in the phosphorus to iron ratio. The magnitude of the iron signal detected was reduced by approximately 14% and the phosphorus signal by approximately 34% between the first and last spectra. The imfp of iron and phosphorus Auger electrons in carbon are calculated, using equation 5.8, to be 0.414nm and 1.02nm respectively. The formula for the attenuation of Auger electrons was used to calculate the thickness of carbon contamination that would be required to cause the observed level of reduction in Auger electron signal. The required coverage is calculated to be 0.148nm to reduce the iron signal by the observed amount, and 0.173nm to bring about the required attenuation in the phosphorus signal. Using a value of atomic size for carbon calculated from equation 5.9, this converts to 0.71 and 0.84 monolayers of carbon film respectively. This is a difference in predicted coverage of approximately 15%, which is reasonable considering the level of uncertainty in the calculated values of Auger electron inelastic mean free paths. This amount of carbon contamination, although feasible, is unlikely to have built up during the relatively short period of time during which the data was collected. Also a subsequent spectrum collected from the area under investigation after the specimen had been held in the vacuum for a further hour did not show any marked decrease in the signals detected, as would have been expected if a carbon overlayer was continuing to be deposited on the surface of the sample. A further factor against the theory of contamination build-up is the absence of a large carbon peak in the subsequent wide scan spectra collected. A sizeable carbon peak would be expected if approximately 75% of the surface were covered by a carbon overlayer.

An alternative explanation for the reduction in phosphorus to iron ratio is that some of the phosphorus overlayer is being displaced by the electron beam. This

could occur by either a sputtering mechanism or enhanced surface diffusion of the phosphorus atoms. If either of these mechanisms is operating it should be possible to detect an increase in the phosphorus signal from areas surrounding the facet being analysed. An experiment to determine whether this was occurring was conducted using a sample which contained intergranular facets and adjacent regions of transgranular cleavage. The chemical composition of a region of transgranular cleavage was analysed before and after analysis of an adjacent intergranular facet. Initially a 5nA beam current was used to analyse both the intergranular facet and the transgranular cleavage, the same intergranular area was then analysed using an increased beam current of 10nA. Finally the transgranular region was re-examined using a 5nA beam current. The spectra collected from the transgranular cleavage region before and after analysis of the intergranular facet using a 5nA beam showed no evidence of a phosphorus peak. However after analysing the intergranular facet with the higher beam current of 10nA (and consequently higher current density) a phosphorus signal was detected from the transgranular region. The phosphorus to iron differential peak to peak height ratio in the final transgranular spectrum was approximately 30%, this compares to a value of approximately 60% initially detected on the intergranular facet. These results prove that although the phosphorus on the surface on intergranular facets is stable under a 5nA beam, increasing the current density of the electron probe by increasing the current to 10nA causes migration from under the beam to adjacent regions of the specimen. It can be stated that the movement of phosphorus is not occurring by a sputtering mechanism, as this would be dependent upon the energy of the incident electrons and not the current density of the electron beam. Thus if sputtering occurred under the influence of the 10nA beam it would also occur with the 5nA beam but at half the rate. The actual cause of the migration of phosphorus atoms from under the beam has not been identified in this study. One possibility is that surface diffusion has been enhanced by local heating of the sample surface by the electron beam. However, any temperature rise is likely to be slight due to the large heat sink provided by the

bulk of the sample. Although the mechanism has not been identified it is an important point to note that the analysis of regions using a high beam current density could lead to spurious results, due both to removal of phosphorus from the area being analysed, giving a reduced segregation measurement, and deposition of phosphorus onto areas yet to be analysed, leading to increased segregation measurement. Consequently all subsequent analyses in this study were conducted using a beam current of 5nA, also the spectra collected with a beam current of 10nA were not used to calculate monolayer coverages of phosphorus and chromium.

These results demonstrating the mobility of phosphorus under the action of an increased electron current density are a cause for concern in that previous studies have often used much higher beam currents, to overcome lower detector efficiencies, which may have resulted in the segregated species under investigation becoming mobile.

6.2 Discussion of Errors

6.2.1 Errors in EDX analysis

Errors in the calculation of chemical composition from an x-ray spectrum can arise from the following areas:

Random statistical fluctuation in the rate of x-ray production from an element; the magnitude of this fluctuation varies with the square root of the number of counts within the peak being measured and can be represented as $\sqrt{N}/N$. As a consequence of this the percentage error in the determination of the size of the iron peak will be significantly less than the error in the phosphorus peak even in the case of heavily segregated boundaries. In addition the error in determining the number of characteristic counts is also affected by the process of background subtraction and deconvolution of any peak overlap which may be present. Russ (1984) has proposed

that the error in the number of counts in a peak is no longer simply $\sqrt{N}/N$ as predicted by Gaussian probability, but is increased to $\sqrt{(N + 2(BG + OV))} / N$. Where BG represents the number of counts in the background and OV the number of counts contributed by an overlapping peak. This has a minor effect on the accuracy of determination of major non-overlapped peaks, such as iron in this study, which lie in portions of the spectrum where the background is relatively low and do not suffer from peak overlap. However the effect is significant for minor peaks where the background may be a significant proportion of the counts contained in the peak energy range. This is particularly the case at low energies where the background is rising rapidly. This contribution to the uncertainty from the large background further increases the error in the determination of the small phosphorus peak. For a typical spectrum collected from a boundary in alloy S560 containing 560 ppm phosphorus the relative errors calculated by the Link systems quantitative software (RTS-2) are $\pm 10\%$ for the phosphorus peak and $\pm 1.3\%$ for the iron peak. This difference is a consequence of the iron peak containing ~30 times as many counts as the phosphorus peak, and being superimposed on a lower background. As the peak phosphorus signal detected from a boundary decreases due to lower phosphorus content of the alloy or non-optimum conditions being used the relative error increases, e.g. for the spectra collected from grain boundaries in alloy S120 containing 120 ppm phosphorus had an error associated with the phosphorus peak of 15-20%, compared to the $\pm 10\%$ error in the phosphorus peak detected on boundaries in alloy S560. As the error in the number of counts in a peak is related to the number of counts the peak contains, any measure which increases the number of counts in the characteristic peaks will increase the accuracy in the determination of the chemical composition of the material under the electron beam. Such methods include increasing the thickness of the foil, utilising electron probes containing a higher current and increasing the counting time for spectrum acquisition.

A second source of error in the quantification of x-ray data is the accuracy of the sensitivity factors used to convert the raw x-ray counts data measured from the spectrum into weight percentages of the elements present. These factors may be calculated from first principles, taken from data reported in the literature, or directly measured. Potentially the most accurate of these is direct measurement. The highest accuracy for direct measurement is dependent upon the sample used as a standard being well characterised, homogeneous on the scale of analysis and the data collected under the appropriate conditions of keV, tilt and beam current density. It must also be remembered that the x-ray data collected from the standards will be subject to the usual statistical errors. Consequently it must be ensured that the characteristic x-ray peaks of interest contain a sufficient number of counts so as to minimise error, e.g. $>10{,}000$ counts for accuracy to 1%. This can require long x-ray acquisition times if the element of interest is present as a minor component in the standard material. Literature values of sensitivity factors measured on other AEMs will be less accurate. Calculation of sensitivity factors from first principles is likely to be accurate to better than 10% in most cases, particularly for K-shell x-ray peaks, where the parameters required are relatively well known.

In addition to the errors associated with determining the chemical composition from the measured spectra are the errors associated with deconvoluting the determined 'average' composition to give an equivalent monolayer coverage of segregant at the grain boundary.

The standard quantification of x-ray spectra assumes that the volume of material with which the electron beam interacts is chemically homogeneous. If this is not true, additional measures are required to deconvolute the true spatial distribution of the detected elements.

In an SEM, The primary electrons are continually decelerated as they penetrate the sample until they are brought to rest. This variation in electron energy

results in a variation in the elemental ionisation cross-sections with depth. In the TEM the electrons in the primary beam lose, on average, only a very small fraction of their incident energy. Therefore, a single excitation voltage can be assumed giving constant ionisation cross-sections through the thickness of the TEM sample without introducing significant errors.

The degree of x-ray absorption in a foil can be calculated using the following equation (Zaluzec 1979):

$$I(E) = \frac{I_0(E)\ (\ 1 - \exp(-\mu/\rho\ .\ \rho L)\ )}{\mu/\rho\ .\ \rho L} \qquad 6.3$$

where

$I(E)$	=	x-ray intensity leaving foil
$I_0(E)$	=	x-ray intensity generated within foil
μ/ρ	=	mass absorption coefficient
ρ	=	specimen density
L	=	Distance in specimen in direction of x-ray detector

Using this formula it can be shown that the error introduced by assuming that all of the emitted x-rays are produced at the mid-point of the foil rather than uniformly distributed through the foil is less than 1% for foils below 200nm in thickness. This allows the use of a single x-ray path length in the absorption correction without significant loss of accuracy.

The inhomogeneity in sample composition encountered in segregation studies also means that the spectra collected are very sensitive to the position of the electron probe. Any variation in beam position or amount of beam broadening within the sample has a pronounced effect on the chemical composition as determined from the x-ray spectrum.

Drift of the electron beam during acquisition of spectra can have one of two possible affects. When the beam is nominally placed on the segregated boundary the

occurrence of drift away from the boundary will reduce the proportion of the electron beam that is interacting with the segregant layer resulting in the detection of a reduced signal. Alternatively when the electron probe is displaced from the boundary, drift could increase, decrease or have little effect on the signal detected from the segregant. If the drift is towards the boundary, the segregant signal will be artificially enhanced, if the drift is away from the boundary the signal detected will be reduced, the third case occurs if the drift should be cyclic and centred on the nominal probe position. In such a case the signal is enhanced as the probe drifts toward the boundary and then reduced as the probe subsequently drifts away from the boundary. During this study when collecting spectra from the grain boundary the probe was accurately positioned in the following manner. The boundary is displayed in the bright field image as a region of reduced intensity. The probe can be accurately positioned on the grain boundary by monitoring the signal detected on the bright field photomultiplier and maintaining this signal at a minimum, thus compensating for drift in an on-line manner. It is not possible to use this procedure when acquiring data with the electron probe stepped away from the boundary due to the generally uniform contrast of the image in these areas. Therefore a different approach to controlling drift has to be adopted. Drift was minimised for these positions by interrupting the acquisition of the spectrum and repositioning the probe to correct for any drift which has occurred. The intervals between interruptions is varied according to the rate of drift being experienced during acquisition. Whenever severe drift had occurred between consecutive interruptions to spectrum acquisition, the acquisition was terminated, the data rejected, and analysis recommenced when the drift had reduced to a level where the following criteria could be satisfied. For data to be acceptable a limit in drift of $\pm 1/2$ nm for spectra collected within 5nm of a grain boundary and ± 1nm for spectra collected at distances in excess of 5nm from the boundary was imposed.

The occurrence of beam broadening increases the amount of material sampled by the electron beam as it passes through the foil. As with drift this can either increase or decrease the level of the segregant signal detected dependent upon the positioning of the electron beam. When the probe is positioned on the grain boundary beam broadening increases the proportion of matrix through which the electrons pass and decrease the proportion of segregant. As the probe is stepped away from the boundary the scattering processes increase the probability of electrons interacting with the segregant layer. Thus, the effect of beam broadening is to 'flatten' the profile by decreasing the peak value and increasing the tails of the distribution. However it has been shown, using Monte Carlo calculations, that beam broadening has only a minimal effect on the full width at half maximum value of the profile (Titchmarsh 1986). The extent of beam broadening varies with the foil thickness, atomic number of sample material and the build up of contamination on the entrance surface of the foil. Once an area of a sample has been selected for analysis nothing can be done about the first two of these but the latter can be minimised by careful specimen preparation, storage and examination. In addition to introducing errors associated with beam broadening, thick foils introduce further uncertainties in the absorption correction. These errors arise from the requirement to calculate the mass absorption coefficients for each element and consequently the degree of absorption that the x-rays will undergo during their passage to the exit surface the foil. Intrinsic in the calculation of absorption is a knowledge of the path length of the x-rays through the foil. This requires the detector take-off angle to be known and the tilt angle of the specimen to be ascertained. The take-off angle of the detector is the angle between the line of sight from the sample to the detector and the horizontal. The detector subtends quite a large angular range at the sample and the figure quoted for take-off angle is normally the angle between the centre of the detector and the sample. The range of take-off angles available for a given microscope is generally limited by the physical constraints of introducing the detector and its collimator through the objective lens to approach the sample. The

second requirement, knowledge of the tilt of the specimen in the microscope relative to the horizontal, is considerably more difficult to determine. The readouts provided on the microscope for each of the tilt axes can be used to calculate the overall tilt of the sample. However this equates to the tilt angle of the specimen holder and consequently the bulk of the sample, which may be quite different to the local tilt angle present in the thin, electron transparent areas of the sample adjacent to the hole. These areas can have differing angles of tilt to the bulk of the specimen due to local bending brought about by stresses induced during electropolishing, storage, loading or even examination of the sample. Due to the difficulties involved with determining this local tilt angle the bulk tilt has been used in calculating the extent of x-ray absorption in the specimen. This uncertainty in tilt angle introduces additional errors into the calculation of absorption correction; these are random and are likely to generate a similar number of over-estimates of tilt as underestimates, within the data set as a whole.

Once a chemical composition profile has been obtained from the raw data in as accurate manner as possible, the next stage in quantification which can introduce further errors is the conversion of the composition profile into an equivalent monolayer coverage of segregant at the grain boundary. As previously stated the measured shape of the compositional profile is assumed to be a convolution of the distribution of electron flux in the beam (in one dimension), with the distribution of the segregant, which is assumed to be present on a single atom plane at the interface. The simple method of deconvolution previously described requires the measurement of the peak signal from the boundary and the FWHM of the distribution. The error in the former can be estimated from the repeated acquisition of spectra from a grain boundary in alloy S300. The average value of phosphorus detected was 2.5% with a standard deviation of 0.35% (i.e. $\pm 14\%$). These spectra were each collected for 50 seconds and therefore suffer from a higher statistical uncertainty than the majority of x-ray spectra which were collected for 100 seconds.

However, the spectra do give an indication as to the likely magnitude of error. The accuracy of measurement of the FWHM from profiles will depend upon the confidence with which a continuous distribution can be drawn through the discrete points collected in the course of analysis. The accuracy of this depends in part upon the spacing of the data points, i.e. profiles collected with point spacings of 1nm will permit more accurate determination of FWHM than profiles collected with point spacings of 2.5nm. Additionally, the uncertainty of each data point both in terms of chemical composition and position relative to the boundary will affect the accuracy with which the FWHM may be determined.

The main components of the error in monolayer determination are therefore due to; absorption correction, statistics of x-ray production, drift, determination of sensitivity factors and the fitting of a Gaussian through the experimental points. The error introduced to the quantification due to the absorption correction is not expected to exceed 10%. The combined effect of x-ray statistics and drift on the phosphorus signal detected from a grain boundary in alloy S300 has been estimated from a series of spectra collected from a single grain boundary. This is the same data set as used to confirm the stability of phosphorus under the electron beam, shown in figure 4.34. The standard deviation on this data is $\pm 14\%$. The error in fitting a Gaussian to the experimental points is estimated to be ± 0.5nm. The average FWHM of the profiles collected in this study is 3.5nm. Therefore the average error in the Gaussian is $\pm 14\%$. The sensitivity factors, as has been stated above, are accurate to better than 10%. The error in monolayer determination can be obtained by adding the above components in quadrature, assuming that the effects are independent.

$$(\text{Fractional Error})^2 = \text{absorption}^2 + (\text{drift} + \text{x-ray statistics})^2 + \text{Gaussian}^2 + \text{sensitivity factors}^2$$

$$= 0.1^2 + 0.14^2 + 0.14^2 + 0.1^2$$

$$= 0.059$$

The fractional error in the monolayer coverage determined from the AES data is therefore 0.25

The other method of calculating the extent of monolayer coverage of a boundary from EDX data collected in the STEM is to utilise Monte Carlo calculations. These simulate the passage of a large number of electrons through a sample with a known level of grain boundary segregation to produce a theoretical composition profile. The predicted chemical composition profile obtained is compared with the experimental data and the extent of segregant is varied in the model to optimise the correlation between the two. The best fit between the theoretical and experimental profiles is determined using least squares analysis. The programme also produces a standard error on the level of monolayer coverage which it calculates to be present at the grain boundary, using statistical analysis. This error incorporates the statistical variation on the experimental points. Any uncertainty in cross sections used will introduce a systematic error and the use of a random number generator in the programme introduces a random error. The standard error calculated by the Monte Carlo programme was in the range of 10-15%.

6.2.2 Errors in AES analysis

The errors in the quantification of the Auger data to obtain monolayer coverages arise from uncertainties in the parameters used in the proposed segregation formulae and statistical fluctuations in the Auger electron signal recorded.

The parameters required by the segregation equations are; relative sensitivity factors, back scattering factors, atomic sizes, inelastic mean free paths of Auger

electrons, and angle of emission of the Auger electrons relative to the specimen normal.

The relative sensitivity factors used in this study were collected on the same equipment as was the experimental data. This reduces but does not entirely eliminate the errors present. When the phosphorus sensitivity factor was measured there was variation in the level of signals detected from the ferro-phosphorus. The mean phosphorus to iron ratio was 1.50 with a standard deviation on the results of ± 0.26, a relative error of 17%. This gives a value for the phosphorus sensitivity factor of 0.54 ± 0.092. For the determination of the sensitivity factor for chromium the variability was less and the determined value of 0.34 is subject to an uncertainty of 0.0065 or 4%.

The formula for the determination of backscattering factors, (eqn 5.12), proposed by Shimizu and Ichimura (1981) is based upon Monte Carlo modelling, the incident beam is assumed to slow down according to the Bethe stopping power equation, with elastic scattering calculated numerically by partial wave expansion with a Thomas-Fermi-Dirac atomic potential. These energetic electrons ionise core levels according to the Gryzinski cross section (1965). There are other proposed approximations for the backscattering factors (Jablonski 1980, El Gomati and Prutton 1978, Reuter 1972), however those of Shimizu and Ichimura are the most complete and generally accepted as describing the experimental results accurately. The use of ratios of the backscattering factors in the equations for determining monolayer coverage reduces the effect of any systematic errors in backscattering factors. The error in backscattering factors is therefore considered to be less than 10%.

The inelastic mean free path determination is a possible source of large errors in the calculation of the effective monolayer coverage of segregants. As discussed in section 3.5.1, the measurement of inelastic mean free path is difficult

and subject to errors. As can be seen in figure 3.10, where the inelastic mean free path of Auger electrons is plotted against the electron energy, the data to which Seah and Dench have fitted their empirical formula suffers from a large amount of scatter. This is particularly high in the energy range 100 - 1000eV, where the variation in inelastic mean free path can approach an order of magnitude. This experimental scatter exceeds the variation between the different formulae which have been suggested for calculating the inelastic mean free path.

Variations in the value of inelastic mean free path which are used in the equation for the calculation of monolayer coverage has the following effects.

If the value of inelastic mean free path of phosphorus Auger electrons in phosphorus, ($\lambda_P(E_P)$), is decreased by a factor of two (not unreasonable from the data in figure 3.11), the calculated monolayer coverage of phosphorus falls by approximately 35%. This is due to the reduction of phosphorus coverage required in order to attenuate the generated Auger signal to the recorded level. In a similar manner increasing the inelastic mean free path of phosphorus Auger electrons in phosphorus by a factor a two increases the value of monolayer coverage predicted by approximately 70%. Changes in the inelastic mean free path of phosphorus Auger electrons in phosphorus have no significant effect on the extent of the predicted monolayer coverage of chromium.

Varying the value of the inelastic mean free path of iron Auger electrons in phosphorus, ($\lambda_P(E_{Fe})$), over a similar range (x0.5 to x2) has a much weaker affect on the levels of phosphorus and chromium coverages predicted, giving rise to only a $\pm$10% variation. This is due to the signal from the iron matrix attenuated through the phosphorus overlayer comprising only one portion of the matrix signal which is detected, the remainder of the matrix signal consisting of the iron signal attenuated through the chromium overlayer and an unattenuated signal from matrix which is not covered by a segregant layer.

It is possible that the mean values of imfp to which the empirical fit has been performed are inappropriate and that either a higher or lower value for inelastic mean free paths used in the quantification routines may be required. If all four of the inelastic mean free paths appearing in the equations for the determination of monolayer coverages are reduced by a factor of two the effect on the predicted level of phosphorus and chromium segregation is a reduction of between 40 and 45%. This is again due to a lower percentage coverage of the surface being required to attenuate the excited signal by the observed amount. In a similar manner increasing the values of the inelastic mean free paths by a factor of two increases the predicted coverage by 80 to 90%. A contribution to the error in monolayer determination due to uncertainty in imfp has therefore been set at $\pm 75\%$.

The atomic size of species used in the monolayer coverage equations is derived from a simple formula (eqn 5.9) which calculates the size of the atoms assuming that they are close packing cubes. The error introduced by this approximation is not large. Calculation of the atomic size of iron ($\mathbf{a}_{Fe}$) using this equation gives a value for each cube of:

$$\mathbf{a}_m^3 = \frac{A_m}{1000\,\rho_m\,N} \qquad 5.9$$

where A_m = atomic weight

ρ_m = Density (kg/m^3)

N = Avogadro's number

$$55.85 / 1000 \times 7800 \times 6.023 \times 10^{23} = 2.3 \times 10^{-10}\text{m}$$

If a simple two dimensional array of atoms of this size are considered, as shown in figure 6.9, the interplanar spacing, d, is 2 r sin (60°), where r is the atomic radius. This gives an interplanar spacing of 2×10^{-10}m. In a three

dimensional structure this distance will be slightly reduced. This value of 2 x 10^{-10}m compares well with the interplanar spacing of ferritic iron (2.02 x 10^{-10}m) as measured by x-ray diffraction, thus showing that using the above formula is reasonable. Varying the value of atomic size of phosphorus used in the monolayer coverage equations by 10% effects a change of similar magnitude but opposite sign in the fractional monolayer coverage predicted. The change is due to the variation in attenuation caused by the thickness of the overlayer which varies with the value used for the atom size.

The errors associated with the value used for the atomic size also affect the determination of the inelastic mean free path as indicated by equation 5.8. However, the errors in the atomic size, as already stated, are small and the possible uncertainties in the inelastic mean free path are large. Therefore the additional error introduced into the calculation of inelastic mean free path due to the uncertainty in the atomic size is likely to be insignificant.

Errors covered in the previous discussion are all systematic and have the same effect on all the quantified data. Because of the random orientation of intergranular facets to the incoming electron beam Auger electrons are collected with a range of emission angles. Due to the difficulty of accurate determination for each facet the angle of electron incidence and Auger emission, used in the equation for determination of monolayer coverage has been fixed at 30°, introducing a random error to the data. The range of take-off angles has been estimated from the facets selected to be between 15° and 45°. A variation of $\pm$15° in the emission angle gives rise to a $\pm$15% variation in the value of cos θ, which gives a variation in the calculated monolayer coverage of $\pm$15%.

Random variations in the detected Auger signal will arise from statistical fluctuations in the Auger production rate. This has been assessed by collecting a series of spectra from a single facet in alloy S560. The standard deviation from the

mean was ±7%. Additional contributions to the uncertainty in the measured Auger signal come from variation in the height of the specimen causing mis-alignment with the spectrometer, and the accuracy with which magnetic trimming can be applied to counteract the effect of the magnetism of the specimen on the trajectory of low energy Auger electrons (see Chapter 4). The variation due to height, spectrometer alignment and the magnetic trim were minimised before each spectrum acquisition by optimising the Auger signal detected whilst varying these parameters. Any overall variation in the resultant magnetic field after correction with the magnetic trim available on the spectrometer entrance lens and placing of external magnets is compensated for by the background normalising procedure employed (discussed in section 5.2.1). An overall contribution to uncertainty due to the above factors has been estimated to be ±10% (which is dominated by the statistical fluctuation).

The statistical uncertainty in the Auger signal is related to the square root of the number of counts it contains, as in the case of an EDX peak. For this reason the uncertainty in the phosphorus signal will increase as the amount of phosphorus segregation is decreased. Ultimately a point will be reached when the random fluctuations in the spectrum background are of the same magnitude as any phosphorus peak which may be present. For the collection parameters used during narrow spectrum acquisition in this study, i.e. 50ms dwell per channel, 0.5eV per channel and 10 scans per acquisition, this limit was found to be approximately a phosphorus-to-iron ratio of 0.03. Below this level the peak was not easily distinguishable from the random noise present in the dN(E) spectrum.

The cumulative effect of the errors discussed above can be estimated by their addition in quadrature.

$$(\text{Fractional Error})^2 = \text{sensitivity factor}^2 + \text{backscattering factor}^2 + \text{imfp}^2 + \text{atom size}^2 + \cos\theta^2 + \text{statistics}^2$$

$$= (0.17)^2 + (0.1)^2 + (0.75)^2 + (0.1)^2 + (0.15)^2 + (0.1)^2$$

$$= 0.64$$

The fractional error in the monolayer coverage determined from the AES data is therefore 0.80. This is dominated by the potential error in the inelastic mean free path which has been discussed previously.

6.3 Statistics of Segregation Measurement

6.3.1 Statistics of STEM Analysis

In addition to the ability to quantify the level of segregation present, another important parameter to determine is the minimum amount of segregation which it is possible to detect using each of the techniques.

The statistics of detecting phosphorus in steel have been considered by Titchmarsh and Vatter (1989). For the EDX peak of phosphorus which falls on a large non-uniform background, as shown in figure 6.10, the number of counts (S) within the peak of interest is found by subtracting a best estimate of the background under the peak (B) from the total number of counts (T) within a window placed over the peak. The statistical variance of the signal (S), var(S), is then the sum of the variances of T and B.

Then:- $$\text{Var}(T) = T = S + B \cong B \qquad 6.4$$

when S is very small, so that

$$\text{Var}(S) \cong B + \text{Var}(B) \qquad 6.5$$

The signal to noise ratio, SNR, can be defined as

$$\text{SNR} = S / (B + \text{Var}(B))^{1/2} \qquad 6.6$$

The limit for detecting a peak on a background, with a confidence limit of >99% is given by 3≤SNR. By obtaining an estimate of the variance in the spectrum background it is therefore possible to determine the detection limit from any spectrum containing a statistically significant characteristic peak from a segregated specie.

An alternative to the above approach is to use theoretical considerations to calculate the detection limit for a uniformly distributed chemical species and including features specific to the process of EDX analysis. To facilitate this the simplified approximation of an x-ray spectrum shown in figure 6.11, will be used. The use of a peak placed on a steadily falling background allows the use of a linear extrapolation of the background under the peak, which is realistic approximation for many EDX peaks. The zero of the energy scale has been placed at the centre of the peak to simplify the algebra by eliminating co-variance terms from the statistical analysis. The terms for the peak and background are determined by optimising the interpolation of the background under the peak. The form of the background is written as:

$$B = a_o + a_1 E \qquad 6.7$$

so that

$$\text{Var}(B) = (dB / da_o)^2 \text{Var}(a_o) + (dB / da_1)^2 \text{Var}(a_1) \qquad 6.8$$

The background is interpolated over n channels under the peak using m adjacent background channels on each side of the peak. Statistical analysis then predicts:

$$\text{Var}(B) = n^2 \sigma^2 / 2m \qquad 6.9$$

Where σ^2 is the typical variance of a single channel (i.e. $\sigma^2 = B/n$ for a slowly varying background), so that when $n = m$

$$\text{Var}(B) = B / 2 \qquad 6.10$$

Combining equations 6.6 and 6.10 gives:

$$SNR = S / (1.5\ B)^{1/2} \qquad 6.11$$

For EDX spectra the value of 'S ' can be calculated using standard expressions for x-ray production and detection. Similarly, the background can be calculated using a suitable expression for Bremsstrahlung cross-section for the matrix composition. Alternatively, the Bremsstrahlung cross-section can be measured experimentally relative to the matrix cross-section for characteristic x-ray production and scaled expressions for matrix x-ray intensities used in equation 6.11. Thus:

$$S = n_s\ I\ \tau\ t\ \sigma_s\ w_s\ a_s\ e_s\ \Omega_s \qquad 6.12$$

and

$$B = n_m\ I\ \tau\ t\ \sigma^s_m\ e_s\ \Omega \qquad 6.13$$

where

I = incident electron flux

τ = analysis time

t = foil thickness

Ω = detector solid angle (as a fraction of 4π)

e_s = detector efficiency at energy of characteristic signal

a_s = partition function of signal characteristic energy

w_s = fluorescent yield for characteristic x-ray line

σ_s = ionisation cross section for ionisation of atom of interest

σ^s_m = cross section for Bremsstrahlung integrated under the peak

This can be combined with the profile obtained from grain boundary segregation as follows. In thin foils the amount of high angle scattering is negligible to such an extent where a simple analytical calculation can be used to estimate the amount of segregation present. Assuming all of the segregant is present at the grain boundary the measured profile is a simple convolution of the incident probe current.

This gives the probe current profile projected into a diametrical plane. For a radially symmetric probe with a Gaussian distribution this projection also has a Gaussian distribution which can be represented as:

$$i = (i_o / x_o (2\pi)^{1/2}) \exp (- x^2 / x_o^2) \qquad 6.14$$

where i = current

i_o = initial current

x_o = probe width

This has an integrated area of unity and a second moment (variance) of x_o^2. The fractional ratio, R, of the electron trajectory path lengths in the segregant and in the matrix can be written as:

$$R = (f \delta / x_o (2 \pi)^{1/2}) / (1-f \delta / x_o (2 \pi)^{1/2})) \qquad 6.15$$

$$\cong f\delta / x_o (2 \pi)^{1/2}$$

when $f < 1$ and $x_o >> \delta$

where f = fractional concentration of segregant

δ = boundary layer thickness

R can be related directly to the atomic concentrations derived from the analysis of the experimental spectrum to estimate f. Alternatively, the segregation can be equated to a uniform distribution of solute under the probe such that:

$$R = n_s / n_m \qquad 6.16$$

n_s = solute atomic density

n_m = matrix atomic density

combining equations- 6.11, 6.12, 6.13, 6.15 and 6.16-with the assumption that $3 \leq$ SNR is required for detection, and $R = n_s / n_m$, an expression is obtained for the

minimum detectable fraction of a monolayer, f_{min},which can be detected using EDX techniques.

$$f_{min} = 3\, x_o\, (2\, \pi\, h\, \sigma_m^s)^{1/2} / d\, \sigma_s\, w_s\, a_s\, (I\, \tau\, t_{nm}\, e_s\, \Omega)^{1/2} \qquad 6.17$$

The value of x_o can be estimated from a compositional profile as this represents the projection of the probe distribution as previously discussed; a value of x_o= 1.5nm can then be substituted into equation 6.17 along with the values given below.

symbol	units	value
σ_s	m^2	2×10^{-25}
w_s		0.07
a_s		1
δ	nm	0.2
h		1.5
n_m	m^{-3}	8×10^{-28}
t	nm	18
Ω		0.08
e_s		0.9
τ	sec	100
I	el/sec	5×10^9
σ_m^s	m^2	7×10^{-27}

This gives a theoretical limit of f_{min} of 0.06 atom layers. To determine an experimental value of f_{min} a set of x-ray spectra were collected from a well oriented boundary in alloy S300. The foil was 52nm thick, each spectrum was collected for 50 seconds, and each spectrum was recorded from the same portion of the grain boundary. Quantification of the phosphorus peak predicts a coverage of 50% of the boundary by segregant. The average SNR measured from these 13 spectra is 17.5.

This gives an experimental value of f_{min} of 0.086. For a counting time of 50 seconds and a foil thickness of 52nm the theoretical prediction of f_{min} is 0.047. The experimental value of f_{min} exceeds the theoretical value due to factors which reduce the magnitude of the detected signal from the segregant. These include specimen drift, beam broadening and focus fluctuations all of which are not allowed for in the theoretical calculation. The improvements in sensitivity achievable by increasing the collection time for the x-ray spectrum can be seen by summing the 13 spectra to give a composite spectrum with an effective collection time of 650 seconds. The SNR of this spectrum is 58, giving an f_{min} of 0.026; this compares to a theoretical estimate for these conditions of 0.013.

The value of f_{min} will vary with the relative sizes of the background and characteristic peak. Consequently segregated species whose characteristic lines lie in portions of the spectrum where the background is low will be detectable in smaller concentrations. An example of this is the study of zinc segregation in aluminium. A grain boundary spectrum from this system is shown in figure 6.12. The SNR of the zinc peak is ~40 and Monte Carlo modelling estimates a grain boundary coverage of 50%. From these figures a prediction of f_{min} equal to 2.3% can be made. The study of heavy element segregation in a lighter matrix also has the advantage of increased overall detector efficiency for the x-rays of the segregated element and significantly reduced absorption of the signal from the segregated specie.

The values of f_{min}can be reduced by improving the statistics of the x-ray spectrum by increasing the number of counts it contains. This can be achieved by extending the counting time, increasing the foil thickness or utilising an electron probe containing a larger current.

The current in the probe can be increased by using a higher brightness source or enlarging the beam defining aperture. In this study a field emission electron source has been used which has the highest brightness currently available

on an electron beam instrument. The current can be increased by selecting a larger virtual objective aperture, used to define the beam, which has the effect of increasing the beam diameter and decreasing the peak signal detected on a segregated grain boundary, as previously discussed. The thickness of foil and counting time can be easily varied. However increasing the counting time increases the problems encountered with drift and contamination; longer counting times also reduce the number of boundaries which can be analysed during a session on the microscope. Increasing the thickness of the foil increases the amount of beam-broadening and so reduces the peak signal detected. It is therefore necessary to optimise these various parameters in order to achieve the ultimate experimental f_{min} value.

This minimum detectable fraction of a monolayer can be used to predict the minimum detectable mass of phosphorus using the following geometric approximation.

Assume a beam diameter of 3.5nm and a foil thickness of 60nm. Neglecting beam broadening this gives the area of the grain boundary intercepted by the beam, when the boundary lies on a diametral plane of the probe, as 3.5 x 60 = 210nm^2. The close packed planes in iron have a spacing of 0.202nm. Therefore assuming that the atoms at the boundary have a similar spacing then the volume of the grain boundary is 0.202 x 210 = 42nm^3 of which, in the limiting case, 6% is segregant. Consequently the minimum detectable volume of phosphorus is 2.5nm^3. Seah's equation is used for calculating atomic volume. i.e.

$$A_p = 1000\,\rho_p\,N\,a_p^3 \qquad 6.18$$

where A_p = Atomic weight of phosphorus

ρ_p = Density kgm^{-3}

N = Avogadro's number

a_p^3 = Atomic volume of phosphorus = 2.8 x 10^{-29}m^3

This value is divided into the grain boundary volume of segregant to calculate the minimum number of atoms detectable.

$$\frac{2.5 \times 10^{-27}}{2.8 \times 10^{-29}} = 90$$

The mass of a single phosphorus atom is given by its atomic weight divided by Avogadro's number

$$30.97 / 6.023 \times 10^{23} = 5.14 \times 10^{-23} \text{ kg/atom}$$

Consequently the minimum detectable mass of phosphorus is

$$90 \times 5.14 \times 10^{-23} = 4.6 \times 10^{-21} \text{ kg}$$

6.3.2 Statistics of AES Analysis

The determination of the smallest significant phosphorus-to-iron peak height ratio may be used to determine the minimum detectable mass of phosphorus and minimum detectable number of phosphorus atoms in AES. The minimum phosphorus-to-iron ratio detectable with confidence in the differential spectra collected using the standard conditions adopted in this study is 0.03. This equates to an equivalent monolayer coverage of the boundary of 5%. Assuming that on fracture the segregation is uniformly distributed between the two fracture surfaces created, the minimum level of segregation under the beam in the Auger electron microprobe is 2.5% of a monolayer. The approximate area scanned by the beam at a magnification of X5,000 is 20 x 15 μm. This gives an area covered by phosphorus of 7.5μm^2. Given an atom size of phosphorus of 3.04×10^{-10}m, the area of a phosphorus atom is 9.24×10^{-20} m^2. This permits the approximate minimum number

of phosphorus atoms detected to be calculated as $7.5 \times 10^{-12} / 9.24 \times 10^{-20}$, equals 8.1×10^{7}. The mass of a single phosphorus atom is 5.14×10^{-23} Kg. This gives a minimum detectable mass of phosphorus, under the specific acquisition parameters stated, of 4.17×10^{-20} Kg. These figures can be reduced by scanning smaller areas and reach a limit for the microprobe when the focused electron beam is held stationary on the specimen. For a typical system, such as the MA500 used in this study, with a beam diameter of 100nm the area of the specimen on which the electrons are incident is 7.9×10^{-15} m^2. The area covered by phosphorus is therefore 2×10^{-16} m^2 and the number of phosphorus atoms contained in this area is approximately 2000 giving a minimum detectable mass of 1×10^{-19} Kg.

These values are approximately a factor of 20 above those derived from the FEG-STEM data. This is due to the considerably larger electron probes utilised in the AES. However the minimum detectable grain boundary coverage of phosphorus is very similar for both the AES and STEM techniques at between 5 and 6 percent of a monolayer.

6.4 Comparison of the AES and STEM Techniques

The purpose of this thesis is to compare the monolayer coverage of grain boundaries by segregation determined using the techniques of Auger electron spectroscopy and scanning transmission electron microscopy and the previously discussed quantification routines. This comparison can be conducted by examining the correlation of the mean value and spread of coverages calculated by each technique for each alloy. The means and standard deviations of the simple deconvolution and Monte Carlo modelling of the STEM data and the AES data are given in table 6.1. To allow direct visual comparison of the data the histograms showing the distribution of monolayer coverage determined by Monte Carlo analysis of the STEM data, figures 5.11 to 5.18 have been superimposed on the histograms

showing the distribution of monolayer coverage determined from the AES data corrected for matrix and precipitate contributions to the chromium signal, figures 5.28 to 5.35. These composite histograms are shown in figures 6.13 to 6.20. Both treatments of the STEM data gave similar results. The Monte Carlo treatment of the data is considered to be more accurate as it incorporates correction for beam broadening and this is therefore used for the comparison with the AES data

In alloy S560 the agreement between the monolayer coverages of phosphorus determined from the STEM data and the AES data is very good, shown in figure 6.13. Examination of the data obtained using the simple deconvolution routine, figure 5.2, shows one low data point, which moved into the bulk of the data when analysed by the Monte Carlo technique. This discrepancy is probably due to the local thickness being large in this instance. The monolayer coverages calculated for chromium in alloy S560 also show good agreement between the two techniques. Examination of figure 6.14 shows that the distribution of the STEM data is slightly higher than the AES data.

For alloy S300 the agreement between the data is again good for phosphorus, figure 6.15. An interesting observation is the sharp cut-off in frequency of facets exhibiting segregation of less than 60% coverage in the AES data, a similar cut-off is not seen in the STEM data (simple deconvolution or Monte Carlo analysis). The sharp cut-off could be due to a threshold level of segregation that aids selection of the boundary for intergranular fracture. Such pre-selection does not influence the analysis of boundaries in the STEM. The quantification of the chromium enrichment data determined by STEM gives similar results between the simple deconvolution routine and the Monte Carlo technique but both give a significantly higher value of monolayer coverage than the AES data, figure 6.16.

In alloy S120 there is reasonable agreement between the monolayer coverages of phosphorus determined from the STEM data and the AES data, figure

6.17. The mean of the AES data lies between the means of the simple deconvolution and Monte Carlo treatments of the STEM data. However, the presence of a small number of boundaries exhibiting high levels of segregation may be distorting the mean level of segregation determined from the STEM data. In the case of chromium the spread of the data is quite large and the agreement between the two treatments of the STEM data is not so good, figure 6.18. The AES data for chromium shows better agreement with the simple deconvolution of the STEM data than with the Monte Carlo analysis.

In alloy S25 the levels of phosphorus segregation are very low and approaching the detection limit of both techniques at 6-8% of a monolayer. The quantification of the small signals detected by both of the techniques gives a very similar level of monolayer coverage from each of the two techniques, figure 6.19. The quantification of the chromium data does not give such good agreement, figure 6.20, with the STEM data giving a much higher average level of segregation than the AES data.

To allow comparison of the individual techniques over the range of segregation levels investigated the data has been plotted on Youden plots in figures 6.21 to 6.26. The error bars on each data point indicate ± 1 standard deviation calculated from the distribution of the experimental data. The plot of phosphorus data obtained on the STEM and quantified by simple deconvolution and Monte Carlo techniques, figure 6.21, shows good agreement between the monolayer coverages calculated over the complete range of phosphorus levels. The largest deviation of the data from the 1 to 1 relationship is exhibited by the data from alloy S120. A possible explanation for this is that the average local thickness of grain boundaries examined in alloy S120 was the highest of the four alloys analysed in the STEM. The average thickness of alloy S120 boundaries was 117nm, compared to 70nm in alloy S560, 84nm in alloy S25 and 109nm in alloy S300. Alloy S300 also shows a lower level of segregation calculated by the simple deconvolution method.

Increased thickness of the sample increases the extent of beam broadening which decreases the signal detected from the segregant. This reduction is not accounted for in the simple deconvolution method thus lower levels of segregation are predicted. Comparison of the monolayer coverages of phosphorus determined from the STEM data, by either the simple deconvolution method, figure 6.22, or Monte Carlo technique, figure 6.23, with the AES data shows a good correlation with the 1:1 equivalence line passing through the majority of the error bars.

The chromium data does not show such a good agreement between the techniques as the phosphorus data. The agreement between the simple deconvolution method and the Monte Carlo technique used to quantify the STEM data, shown in figure 6.24, is still reasonably good. The comparison of AES data and STEM data is shown in figure 6.25 for the simple deconvolution method and figure 6.26 for the Monte Carlo technique. The agreement is not as good as between the data for phosphorus segregation. This reflects the greater difficulty in determining the proportion of the grain boundary signal which arises from enrichment by chromium from the matrix and precipitate contributions. The correlation is slightly better at the higher levels of chromium segregation due to the lower uncertainty in determining the larger grain boundary enrichment signals. However, the data do indicate that the level of chromium segregation decreases going from alloy S560 to alloy S25. This observation suggests that there is an interaction between the two segregating elements.

The choice of which of these two analytical techniques to use in any given situation is governed by many factors. As shown in the previous sections, with careful application both of the techniques give comparable results and have similar minimum detectable levels of segregation. The technique of Auger electron spectroscopy is well suited to collecting data from a large number of interfaces in a short period of time, providing that data is only required about the composition of the exposed surface. Information regarding the distribution of chemical elements in

a direction perpendicular to the surface of the sample can be obtained using AES but requires the collection of a depth profile. This is a more time consuming process and due to the large diameter of ion beams available on Auger electron microprobes, i.e. several mm, it is not possible to erode the surface of a single facet. Consequently, once a depth profile has been conducted further chemical analysis of other areas of the sample is no longer possible.

The application of the Auger technique is often limited by the spatial resolution of the image produced. The imaging capability of a general scanning Auger microprobe is adequate to locate features such as grain boundary facets but not for the discrimination of smaller features such as precipitates. The consequence of this is that the spectra collected from grain boundary facets can contain information from unresolved features on the interface which may distort the analysis of segregant level. These contributions must be accounted for when conducting subsequent analysis of the data. The formulae which have been used to calculate the equivalent monolayer coverage of a surface from the peak height ratio data are reasonably straight forward to apply for a single element segregating to the interfaces of a simple matrix. The use of these formulae requires that suitable values for the sensitivity factors, back scattering factors and inelastic mean free paths are known or determined. The study of multi-component systems greatly increases the complications of Auger quantification especially if more than one species is segregating. Further complications arise when a segregating specie is also present as a significant proportion of the matrix and/or grain boundary precipitates. Many of these complications have been encountered in this study and it has been necessary to attempt to strip away the contributions of matrix and precipitation from the interfacial chromium signal to ascertain boundary enrichment. These added complications increase the magnitude of errors in the determined monolayer coverage.

An advantage of the STEM technique for investigating interfacial segregation is that it permits both high resolution imaging and analysis. This imaging capability can be used to investigate the microstructure of the sample, including identification of precipitates, second phases and the analysis of dislocations. The high spatial resolution capability of the STEM technique enables interfacial precipitates to be imaged and subsequently avoided. Therefore, only contributions from the matrix need to be considered when calculating interfacial enrichment. The chemical composition of the matrix can also be easily ascertained in the STEM. Drawbacks of the STEM technique are that boundaries for analysis must be very well aligned to the incoming electron beam to optimise the signal detected from the segregant; in large grained material there will be a restricted number of boundaries within the electron transparent region of the sample; the boundaries present in a sample will be randomly oriented in the foil, the limited degree and fixed axes of tilt of STEM holders mean that it is not possible for many of these boundaries to be brought parallel to the electron beam. Consequently several samples may have to be examined to collect data from a sufficient number of boundaries to allow meaningful conclusions to be drawn regarding the levels of segregation in the material.

The criteria by which boundaries are selected for analysis in the STEM are orientation, and a freedom from visible precipitation and strong diffraction effects. The boundaries examined in the AES, however, are pre-selected by the process of fracture. The distribution of segregation measured in the STEM is, therefore, likely to be more representative of the true distribution within the sample, whereas the distribution measured in the AES will be biased towards those boundaries which are sufficiently embrittled to undergo intergranular fracture. This could be the cause of the skewed distribution of monolayer coverages of phosphorus observed in the AES data collected from alloy S300. It can be argued that in relation to a materials properties it is the most heavily embrittled boundaries that will control the fracture

process and determine the mechanical properties of the material, consequently these are the boundaries of most interest and their pre-selection by the process of fracture in the Auger microprobe may thus be considered to be an advantage.

The quantification of data to obtain monolayer coverages from the STEM is less complicated than the AES with less uncertainty in the required parameters. However, the time consuming nature of data collection in the STEM generally results in fewer boundaries being examined, with consequently poorer statistics on the STEM distribution of monolayer coverages. The time required to locate a grain boundary in the STEM, collect an eleven point composition profile and measure the local foil thickness can easily limit the number of boundaries examined to two per day. This is in comparison to the time required to collect an Auger spectrum which is approximately 7 to 10 minutes making it is feasible to collect data from 30 boundaries in a sample in a single session of 5-6 hours before contamination build-up becomes a problem. However if a depth profile is collected in the Auger microprobe, in order to determine the composition perpendicular to the sample surface, the time required for the experiment is approximately two hours, dependent upon the number of spectra collected and the length of time required for sputtering. The problems of data collection in the STEM are particularly acute when investigating low levels of segregation approaching the limit of detection, x-ray spectra acquisition times at each point of interest can exceed 15 minutes to give adequate statistics to enable detection of the characteristic peak from the segregant with statistical significance. Under these conditions the collection of full, 11 point compositional profiles becomes impractical; consequently in this situation only the boundary and matrix compositions are measured to give a reduced profile. Quantification of the reduced profile is subject to higher uncertainty due to the assumptions which have to be made regarding the width of the incident electron beam. Examination of samples exhibiting low levels of segregation in the Auger microprobe is not without problems either, these samples are commonly only

slightly embrittled and on breaking only a low proportion of the fracture will occur intergranularly. This is demonstrated by alloy S25 in this study which failed with 17% intergranular fracture compared to 75% in alloy S560 which received the same thermal treatment.

The sample itself may also influence the choice of analytical technique. If the available material is particularly limited or radioactive the reduced volume of a STEM sample compared to an AES sample can be very advantageous. For the examination of irradiated steel the limiting factor on the level of radioactivity is commonly imposed by the x-ray detector which can be inundated by gamma rays produced during the decay processes occurring in the sample.

The above considerations show that the choice of technique for detection and measurement of interfacial segregation is not clear-cut; it is dependent upon the prevailing circumstances. In general for samples which exhibit a high proportion of intergranular fracture the large number of boundaries which can be examined by AES favours this technique. For easier deconvolution of grain boundary enrichment in complex systems containing several segregating species and precipitation the high spatial resolution of the STEM technique means this becomes favoured. In addition materials which exhibit either no, or a very restricted proportion, of intergranular fracture, such as many austenitic steels, will have to be examined in the STEM. The decision on which technique to use to examine materials which fall between these extremes has to be made on a case by case basis weighing up the relative advantages which each technique offers. In many cases the two techniques supply complimentary data and there is good reason for both to be used.

6.5 Comparison with Previous Work

Other studies have been conducted to measure the extent of phosphorus segregation in steels (Doig and Flewitt 1978, Fukuya et al 1985, Youngbin 1987, Nakamura 1979, Okumura 1985). Due to the importance of segregation induced embrittlement, phosphorus segregation has also been extensively studied in the low alloy ferritic steels used to fabricate pressure vessels for nuclear reactors (Druce et al 1986, Vatter and Hippsley 1991a, Kameda et al 1991). In some studies the range of conditions investigated (phosphorus content, thermal ageing time and temperature) has been sufficiently extensive to enable the kinetics and thermodynamics of segregation to be calculated. The study by Vatter and Hippsley examined phosphorus segregation in alloys with bulk phosphorus content in the range 40 - 1300 wt ppm, a temperature range for thermal ageing of 325° - 525°C and ageing times of 100 -20,000 hours. The level of phosphorus segregation in the low alloy MnMoNi ferritic steel at each stage was measured using AES. The data was converted to percentage monolayer coverages using the formulations of Seah (1983) as outlined in section 5.2.1 of this thesis. The calculated monolayer coverages were applied in conjunction with the formulations of McLean (1957) to estimate the equilibrium levels of coverage and the diffusion coefficient for phosphorus in ferritic steel. This information was used to develop a computer model to predict the level of phosphorus segregation as a function of time, temperature and phosphorus content. The model was used to calculate the level of segregation expected during thermal ageing of a steel containing 560 wtppm phosphorus for 100 hours at 500°C and it predicted a coverage of approximately 45% assuming an initial coverage of 5%, typical for a steel in the quenched and tempered condition (Vatter and Hippsley, 1991b). The level of phosphorus segregation measured in the present study for alloy S560 after thermal ageing for 100 hours at 500°C was approximately double this, indicating that the behaviour of phosphorus in 9% chromium steel is different from its behaviour in the low alloy steel investigated by

Vatter and Hippsley (1991a). Chromium has previously been observed to increase the level of phosphorus segregation in Fe-Cr-C-P alloys (Erhart et al 1981) compared to a Fe-C-P alloy. One explanation for this is that the chromium rich carbides which form in the Fe-Cr-C-P alloy reduce the amount of carbon in solution. This reduces site competition between phosphorus and carbon and leads to enhanced phosphorus segregation. An alternative explanation is synergistic cosegregation (Guttman 1975) which depends upon the energetic interaction between phosphorus and chromium atoms and leads to enhanced segregation of both species. It is possible that a combination of these mechanisms were operating in the 9% chromium steel examined in the current work. The MnMoNi steel on which the segregation model was based contained less than 0.15% chromium. Evidence for an interaction between phosphorus and chromium can be seen from the lower levels of chromium segregation measured in the alloys with reduced phosphorus content.

Other comparisons between AES and STEM for quantitative analysis of phosphorus segregation are scarce. Breummer et al (1985) used a rotor steel to compare various analytical techniques for measuring phosphorus segregation. The grain boundaries in this steel were almost completely covered with precipitates and consequently there was very little grain boundary available for analysis in the STEM. The AES analysis of fracture surfaces produced from this material probably included phosphorus segregated to matrix/precipitate interfaces; these features are more difficult to examine in the STEM due to the curvature of the interface and also the small proportion of the total thickness of the specimen which is made up of matrix/precipitate interface. Another comparison between AES and STEM has been conducted by Partridge and Tatlock (1992). In their study they examined the segregation of phosphorus, molybdenum and chromium in a nimonic PE16 alloy. The quantitative routines used by Partridge and Tatlock were similar to those employed during this study, although the methods used to account for contributions in the AES spectra from matrix and grain boundary precipitates were not clearly

defined. Also the average levels of phosphorus detected by Partridge and Tatlock were 1.6% to 5% of a monolayer, a level at, if not below, the detection limits of both techniques, as discussed earlier. Consequently these are not the best data to use to compare AES and STEM for the detection of segregated phosphorus. Higher levels of segregation of molybdenum and chromium were detected in the PE16 samples and the levels determined by the two techniques showed reasonable agreement. Partridge and Tatlock encountered an additional problem due to the necessity for hydrogen charging of the AES samples to obtain intergranular fracture; this led to contamination of the facets adjacent to the edge of the sample with oxygen, arsenic and sulphur present in the charging solution.

Technique	Analysis	Alloy S560	Alloy S300	Alloy S120	Alloy S25
AES	Phosphorus, adjusted for background ratio	1.01(0.13)	0.73(0.12)	0.50(0.10)	0.08(0.05)
	Chromium, corrected for matrix signal	1.22(0.23)	0.90(0.22)	1.04(0.30)	0.67(0.20)
	Chromium, corrected for matrix and precipitate signal	0.67(0.24)	0.35(0.18)	0.46(0.31)	0.11(0.15)
	Phosphorus, corrected for chromium signal	0.82(0.11)	0.59(0.09)	0.40(0.08)	0.07(0.04)
STEM	Simple deconvolution, phosphorus	0.79(0.25)	0.68(0.24)	0.32(0.14)	0.08(0.04)
	Simple deconvolution, chromium	0.89(0.16)	0.87(0.29)	0.43(0.28)	0.44(0.22)
	Monte Carlo analysis, phosphorus	0.79(0.16)	0.75(0.17)	0.51(0.29)	0.07(0.03)
	Monte Carlo analysis, chromium	0.88(0.16)	0.78(0.22)	0.61(0.25)	0.56(0.14)

Table 6.1 Means and standard deviations of monolayer coverages determined by AES and STEM techniques

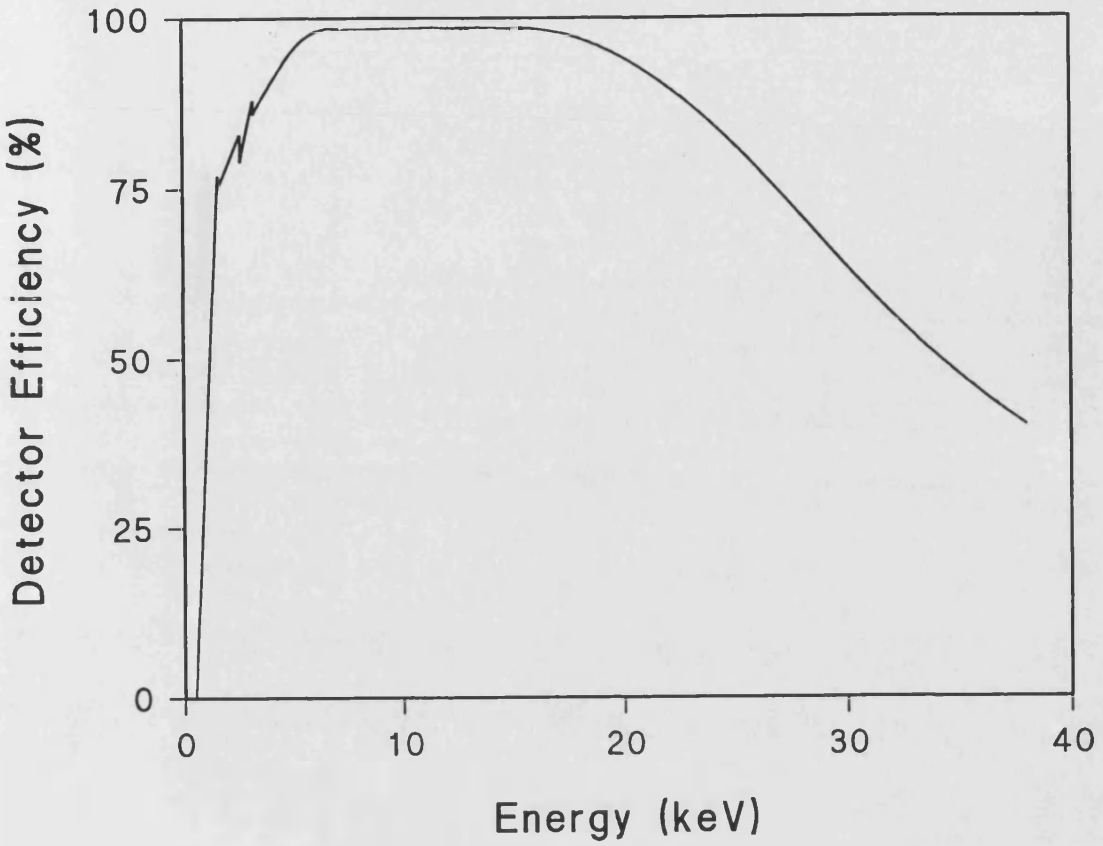

Figure 6.1 Response of lithium-drifted silicon crystal as a function of x-ray energy

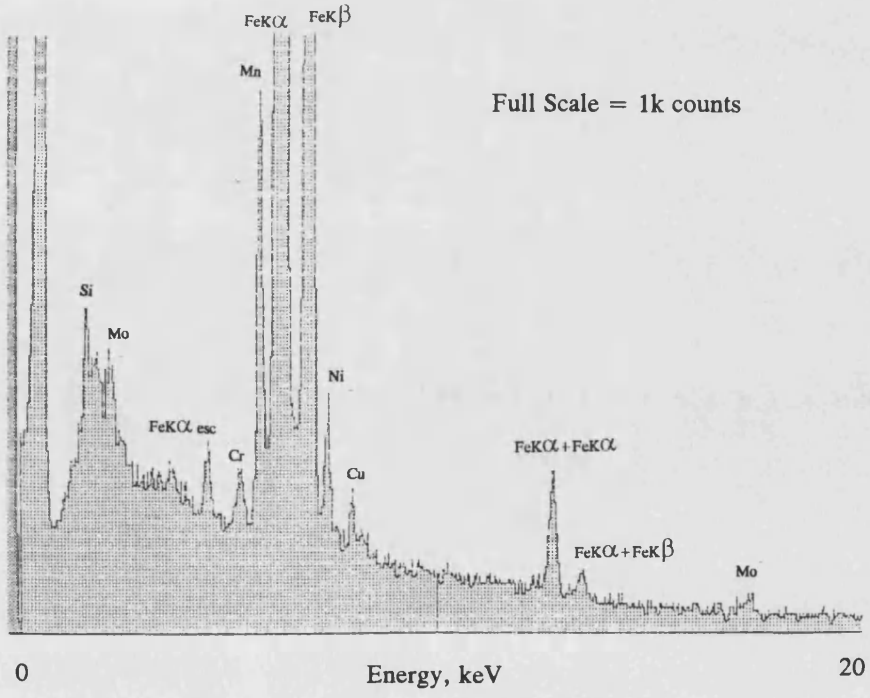

Figure 6.2 EDX spectrum displaying sum and escape peaks

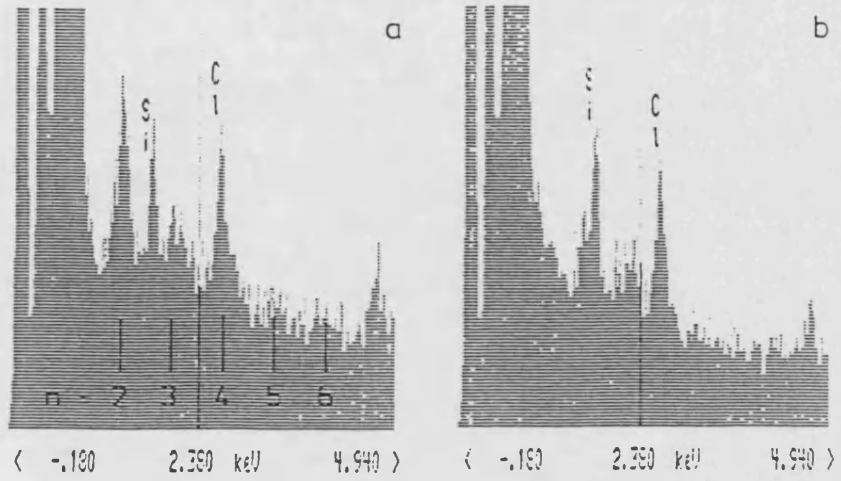

Figure 6.3 EDX spectra, a) Showing coherent Bremsstrahlung
b) After tilting to remove CB

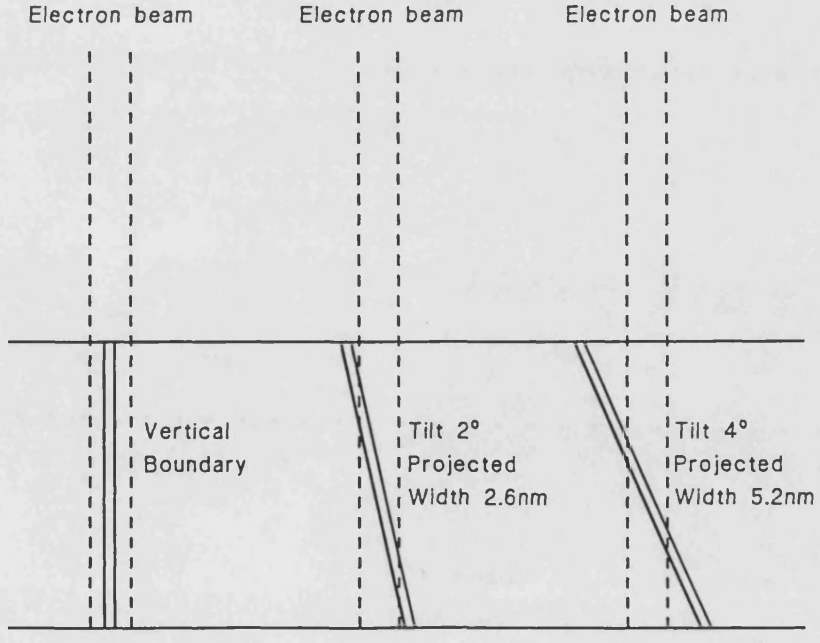

Figure 6.4 Schematic representation of effect of tilting a grain boundary on the detected segregant signal

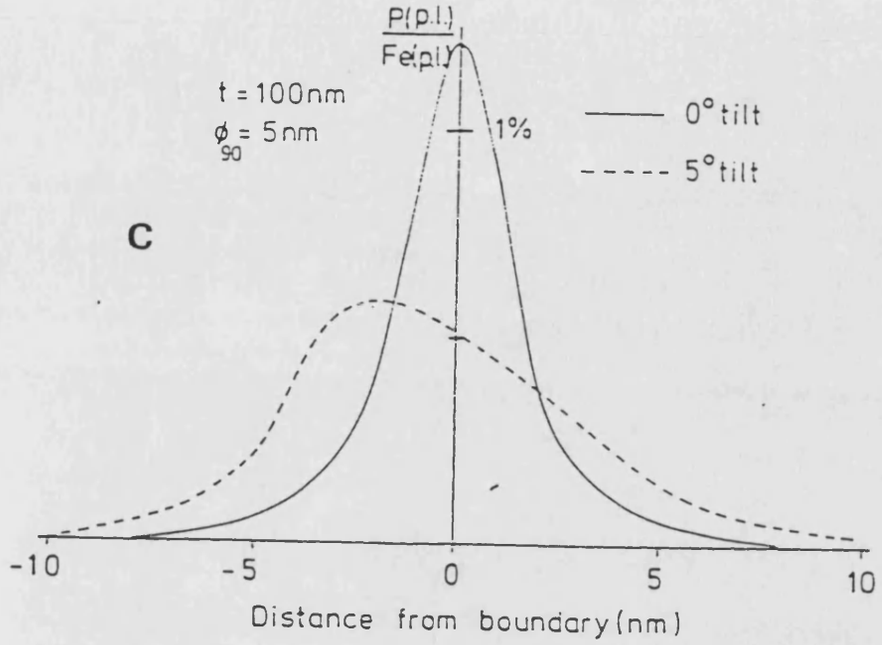

Figure 6.5 Theoretical chemical composition profiles from tilted grain boundaries

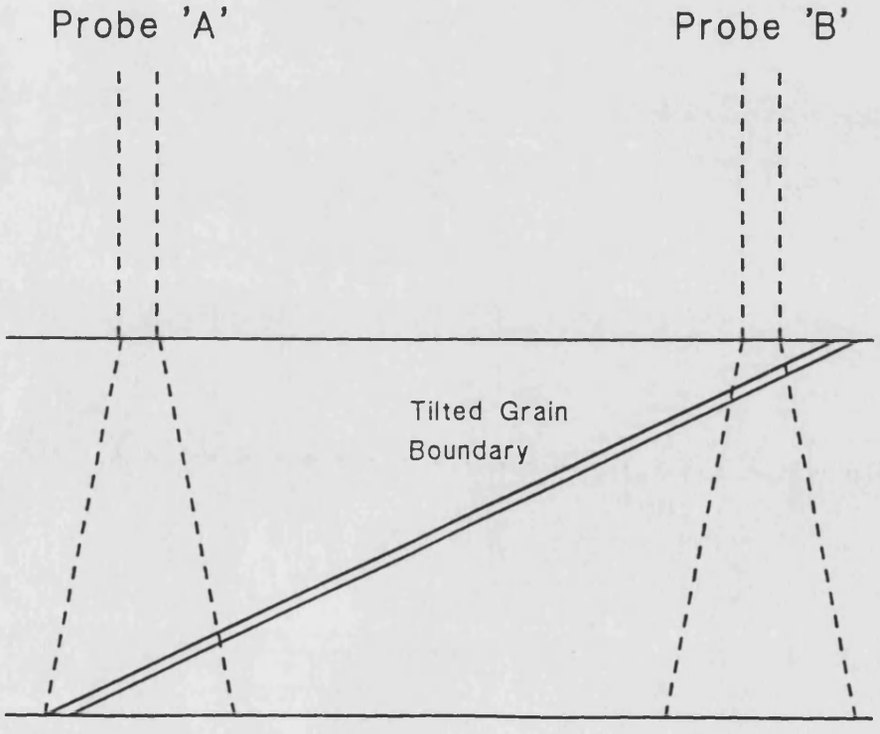

Figure 6.6 Production of asymmetric profiles from tilted grain boundaries

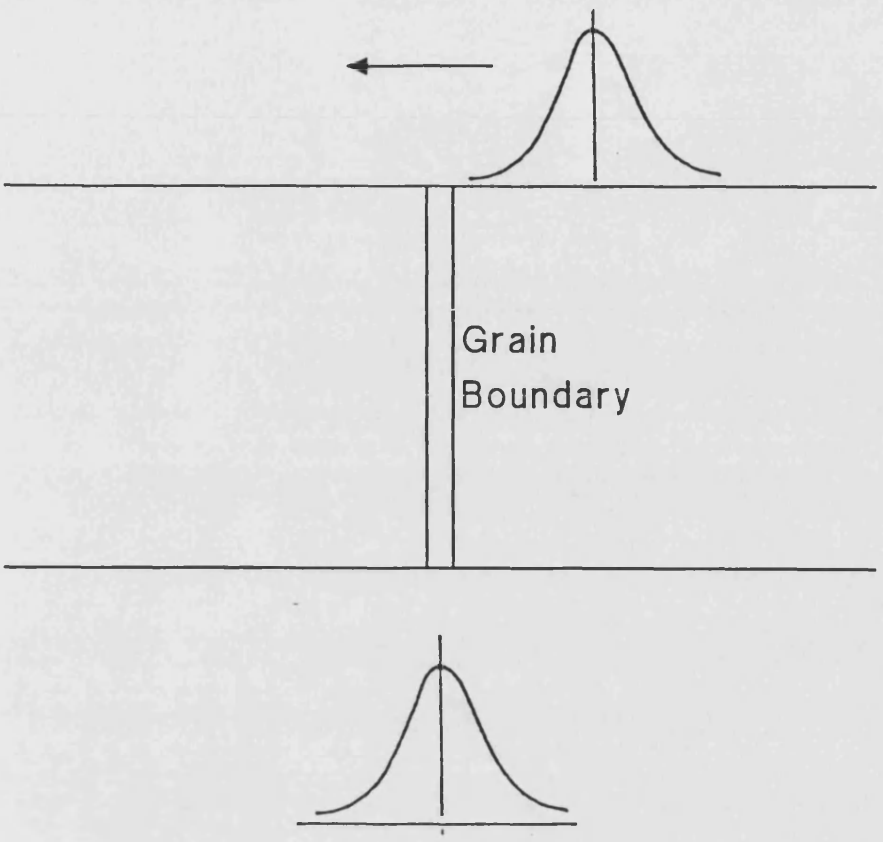

Figure 6.7 Production of x-ray profiles

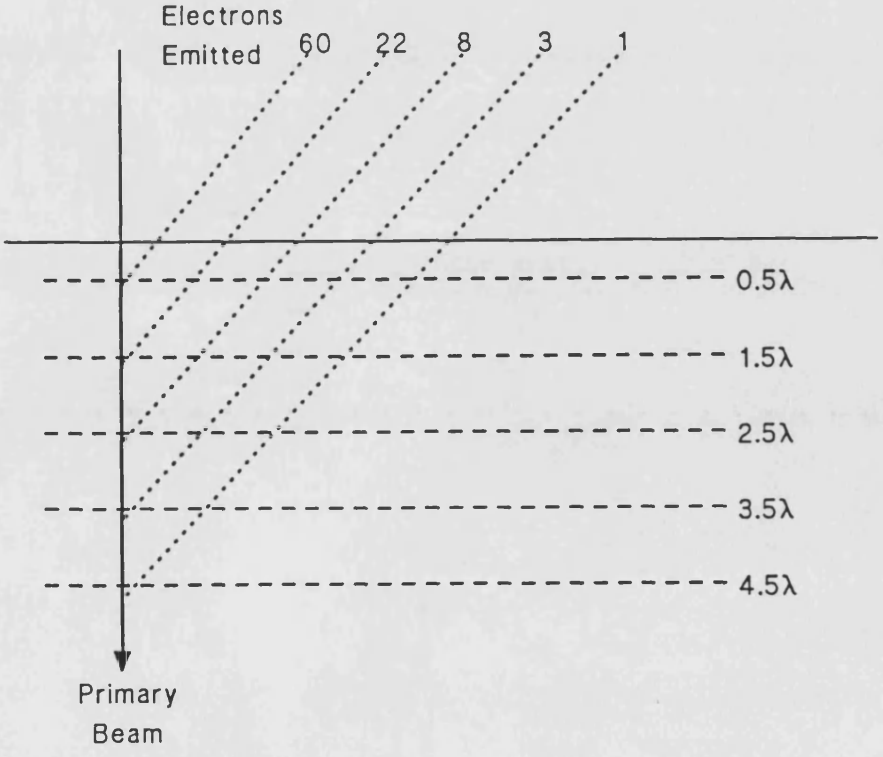

Figure 6.8 Effect of attenuation on Auger electrons

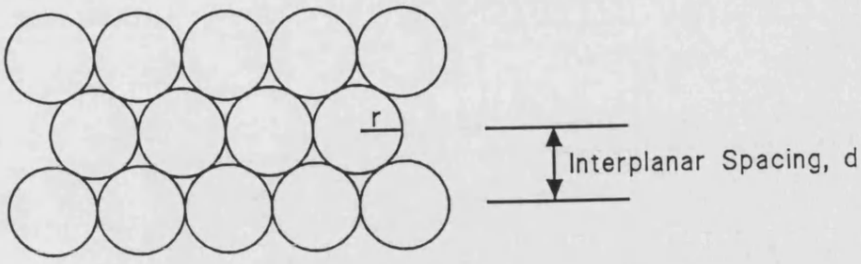

Figure 6.9 Two dimensional array of atoms

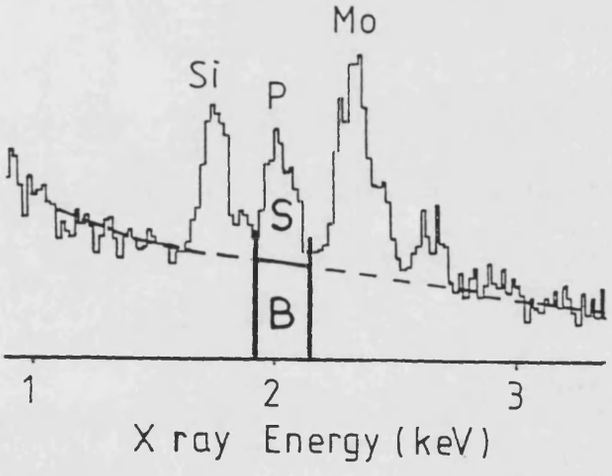

Figure 6.10 EDX peak of phosphorus on a large non-uniform background

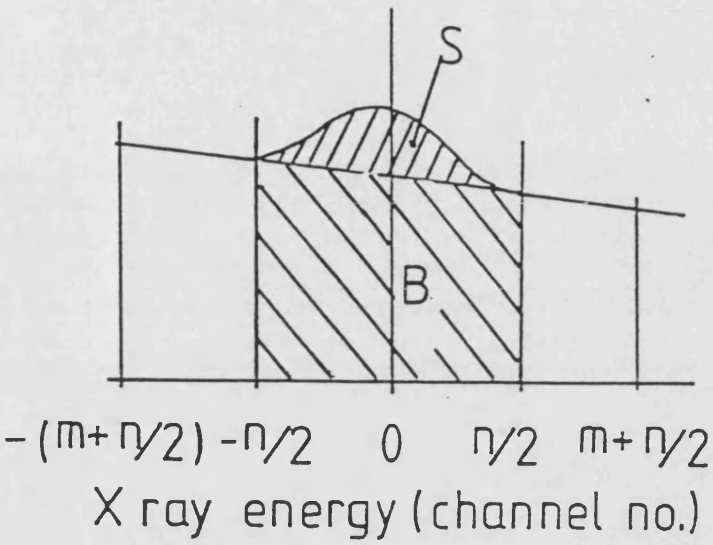

Figure 6.11 Simplified approximation of EDX spectrum

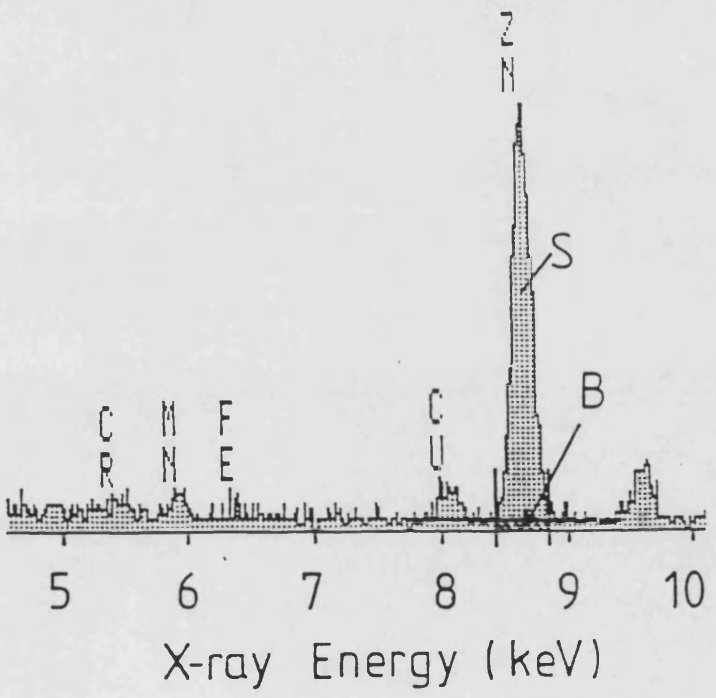

Figure 6.12 Grain boundary EDX spectrum showing zinc segregation in aluminium

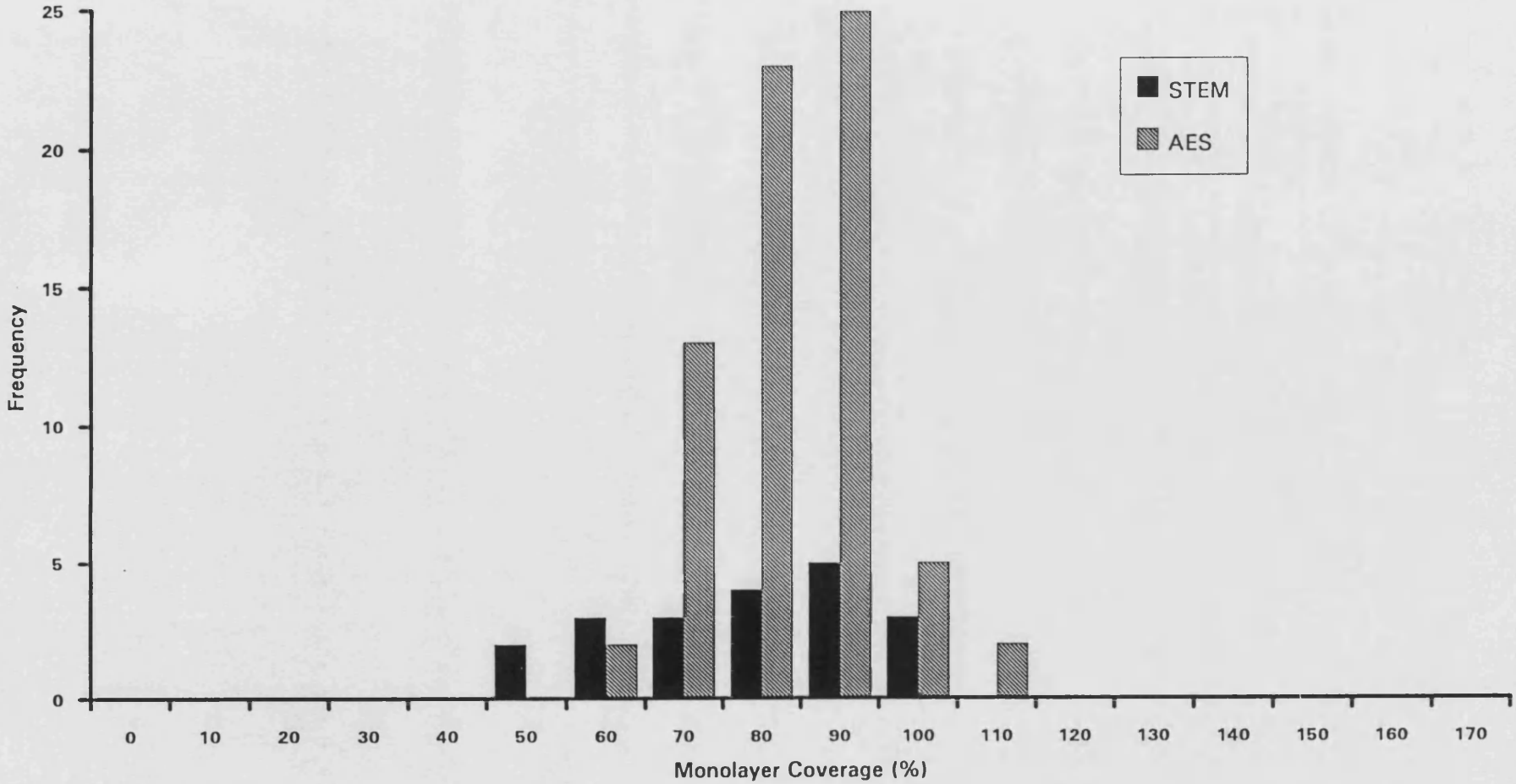

Figure 6.13 Histogram of phosphorus monolayer coverage in alloy S560, AES and STEM data

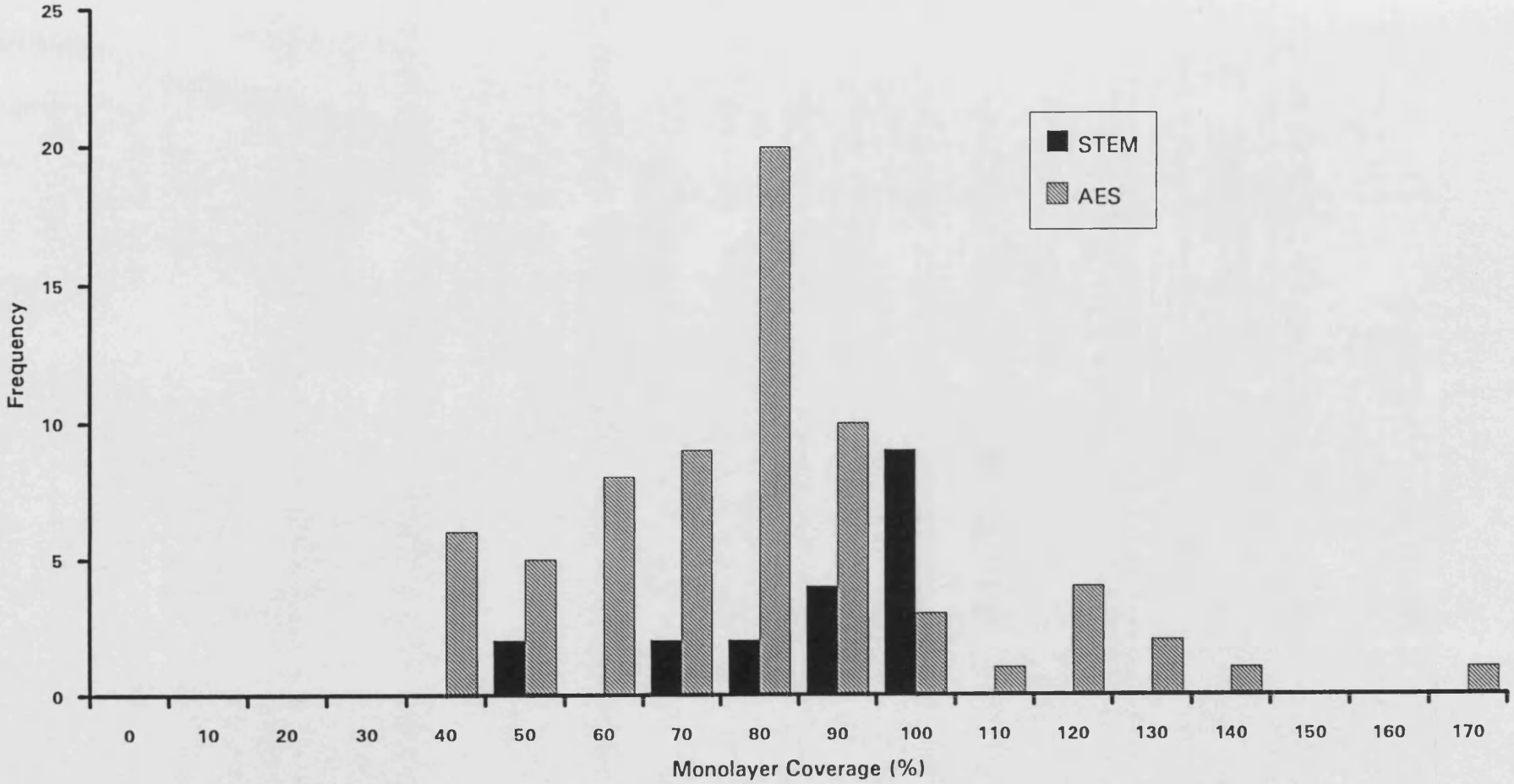

Figure 6.14 Histogram of chromium monolayer coverage in alloy S560, AES and STEM data

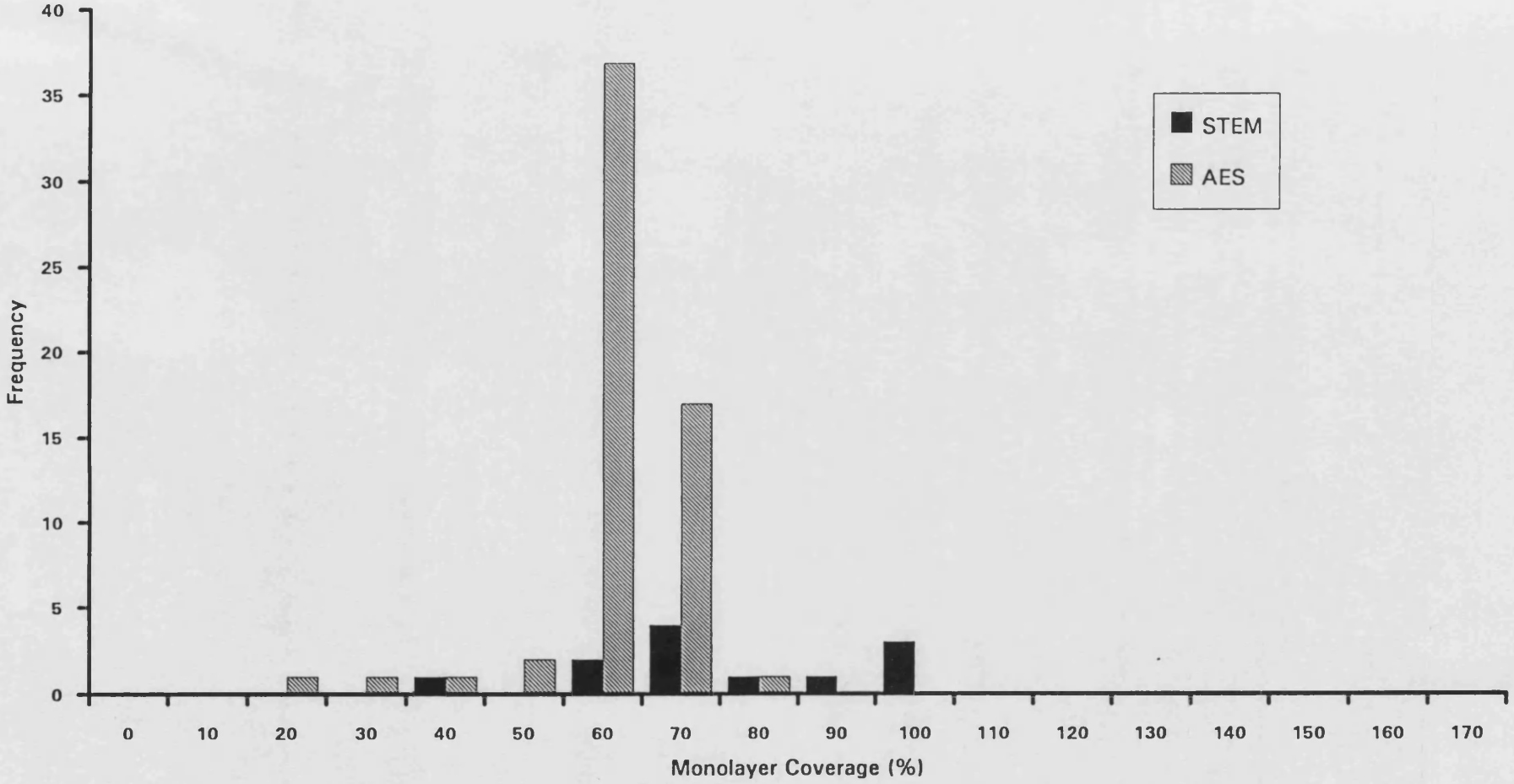

Figure 6.15 Histogram of phosphorus monolayer coverage in alloy S300, AES and STEM data

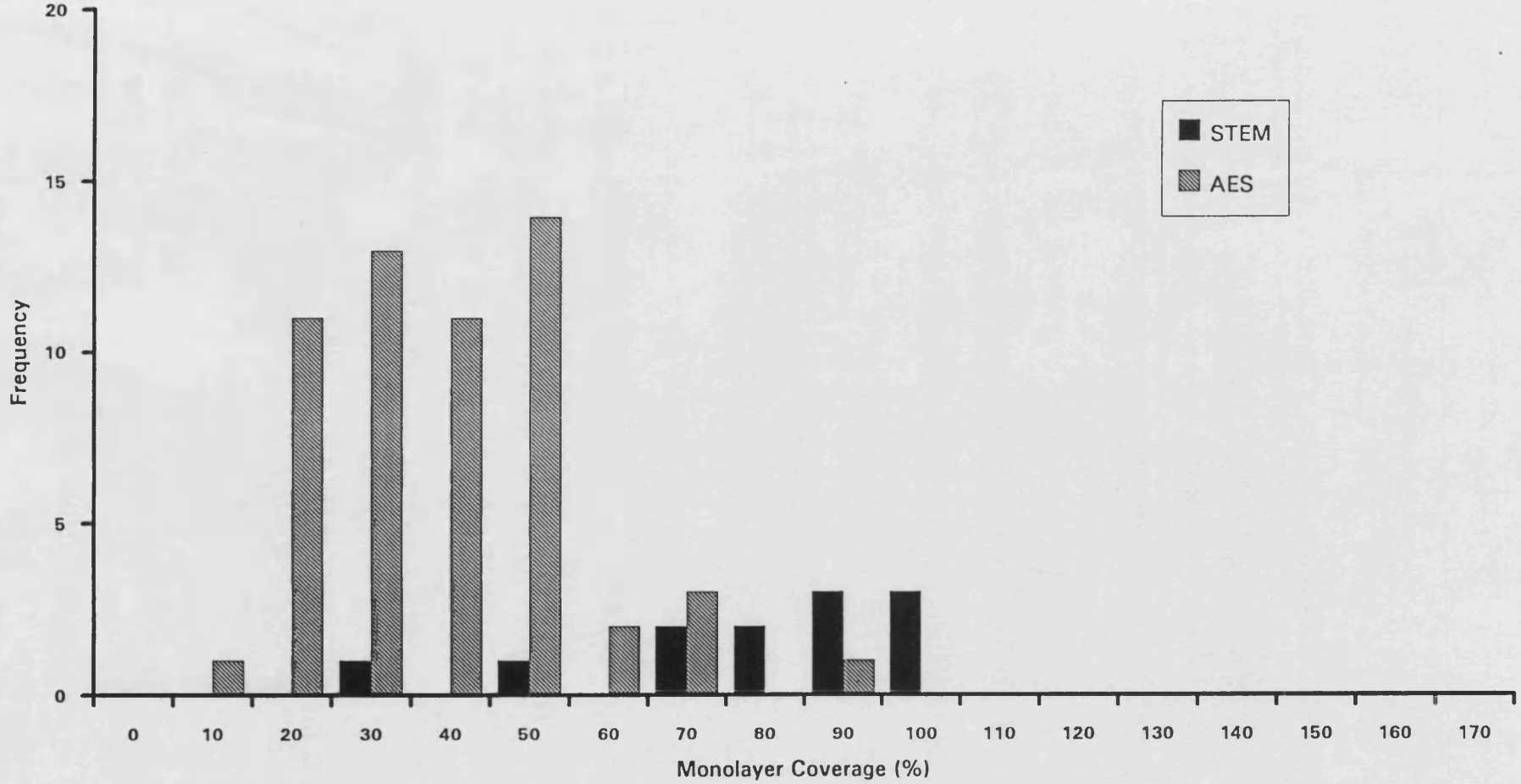

Figure 6.16 Histogram of chromium monolayer coverage in alloy S300, AES and STEM data

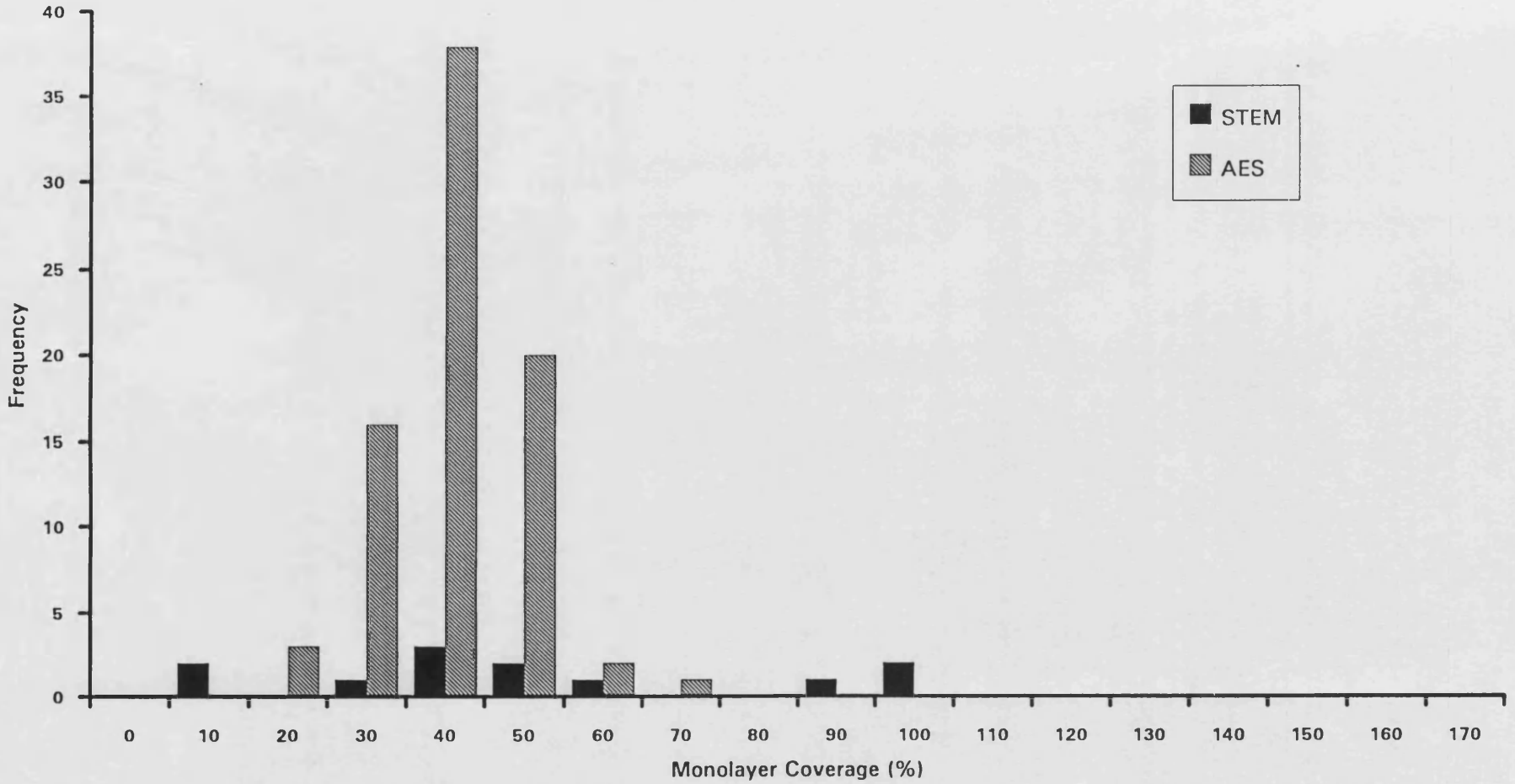

Figure 6.17 Histogram of phosphorus monolayer coverage in alloy S120, AES and STEM data

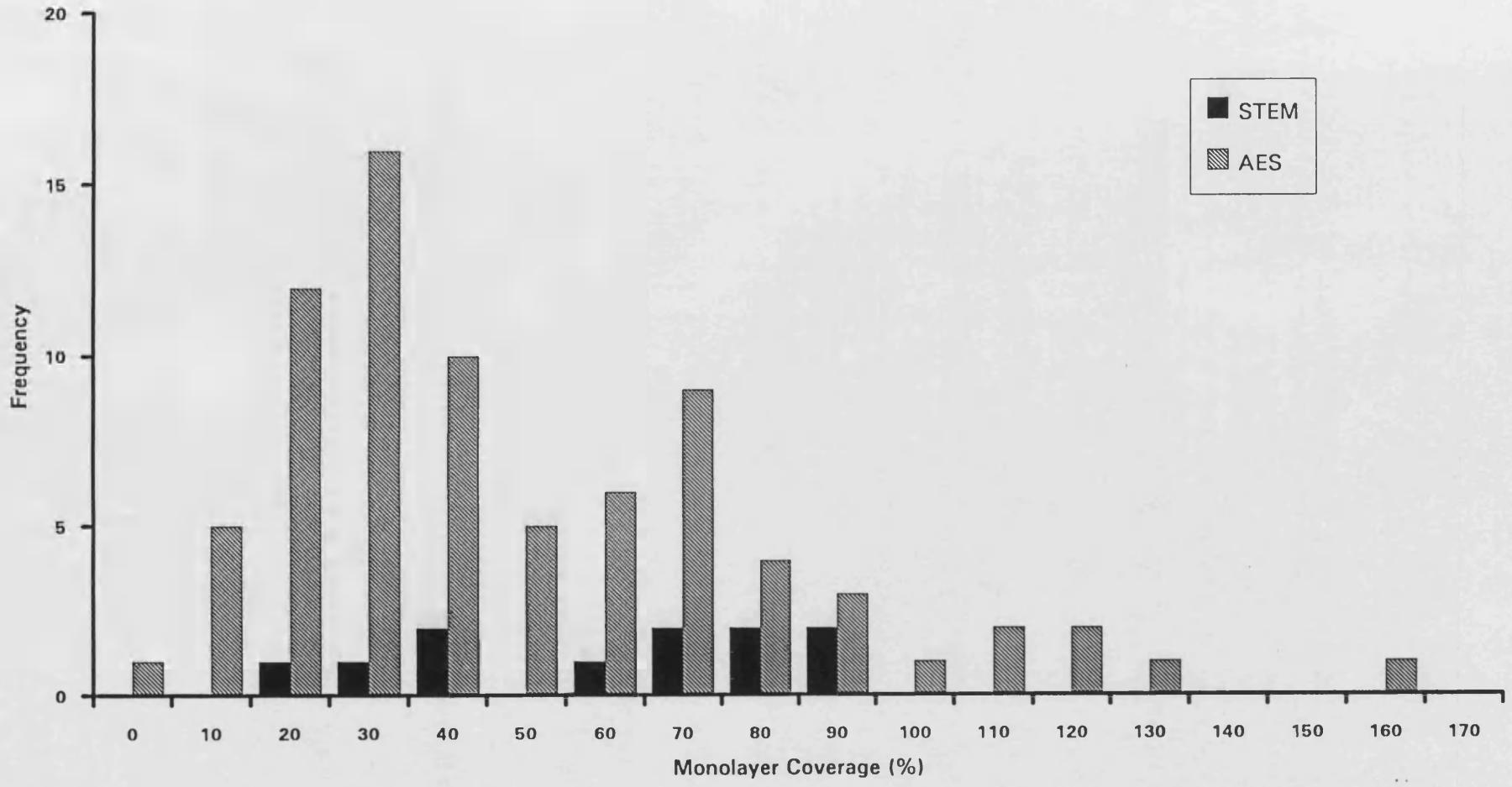

Figure 6.18 Histogram of chromium monolayer coverage in alloy S120, AES and STEM data

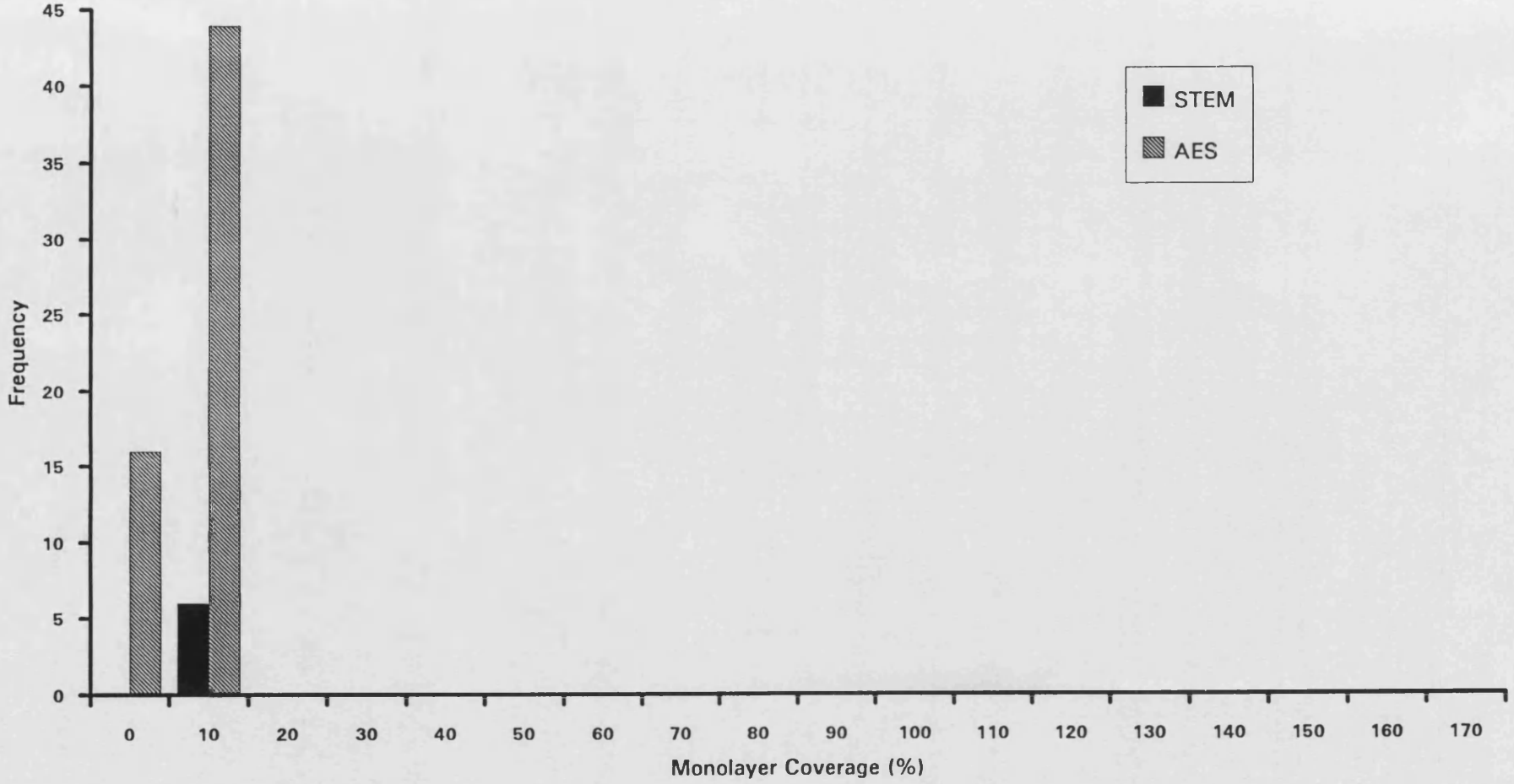

Figure 6.19 Histogram of phosphorus monolayer coverage in alloy S25, AES and STEM data

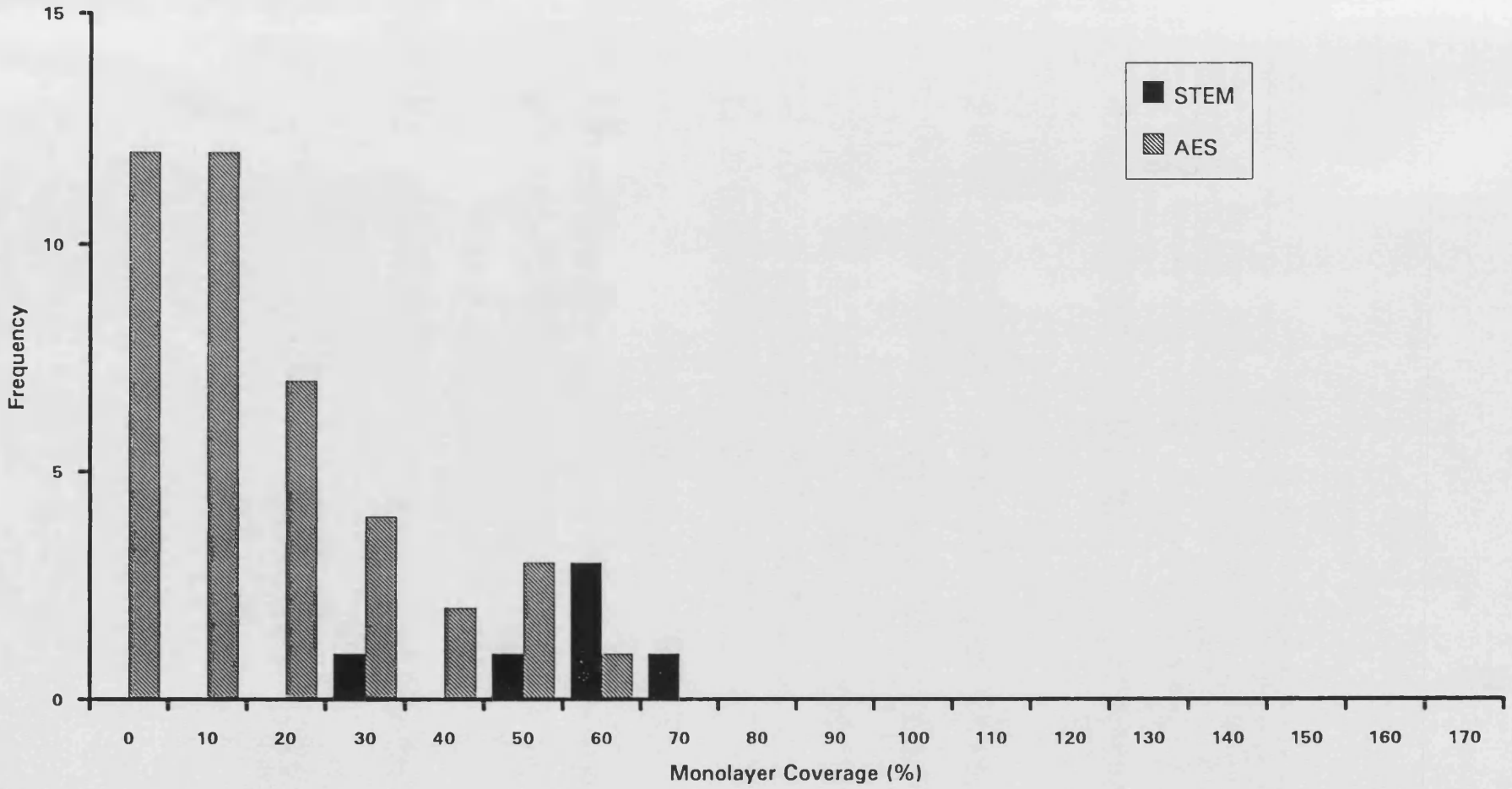

Figure 6.20 Histogram of chromium monolayer coverage in alloy S25, AES and STEM data

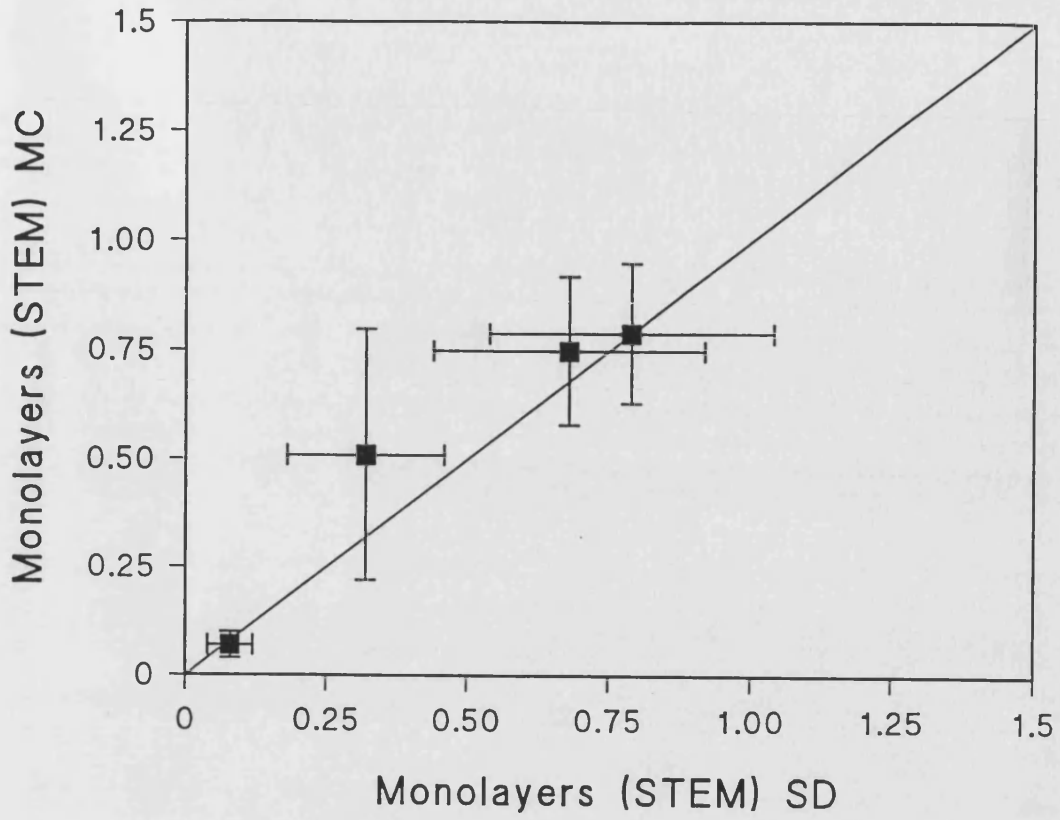

Figure 6.21 Youden plot comparing phosphorus monolayer coverage calculated from STEM data by simple deconvolution and Monte Carlo methods

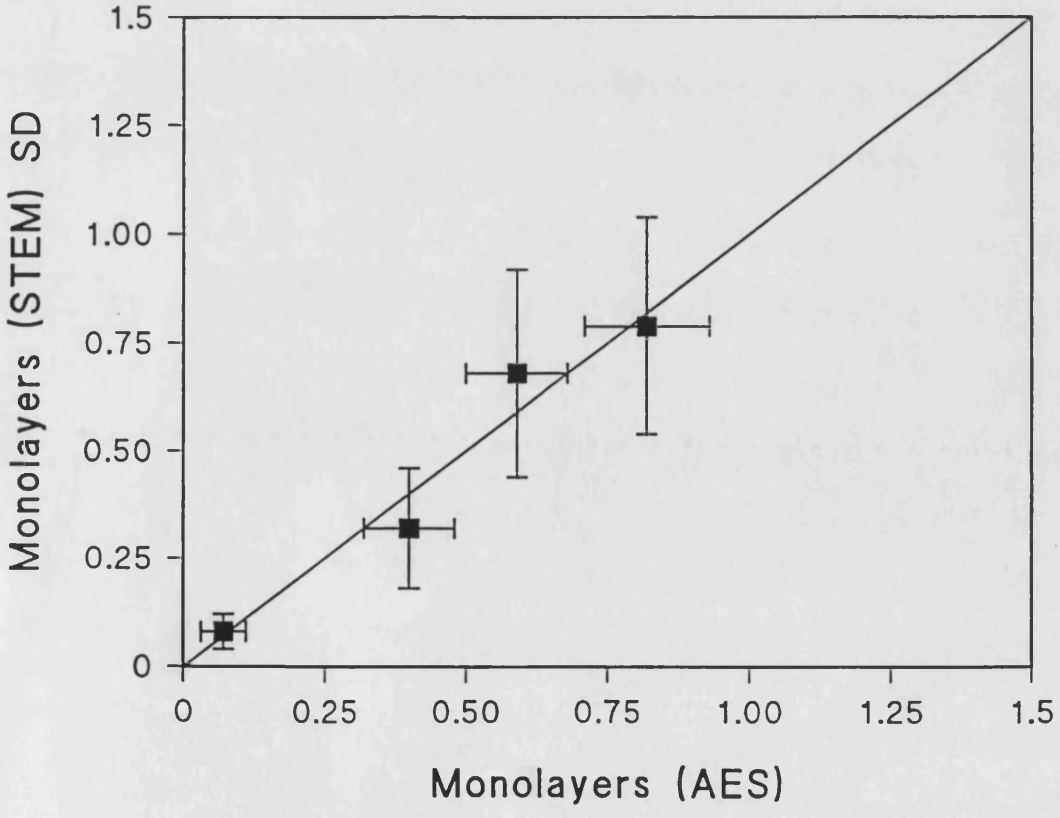

Figure 6.22 Youden plot comparing phosphorus monolayer coverage calculated from STEM data by simple deconvolution method and AES data

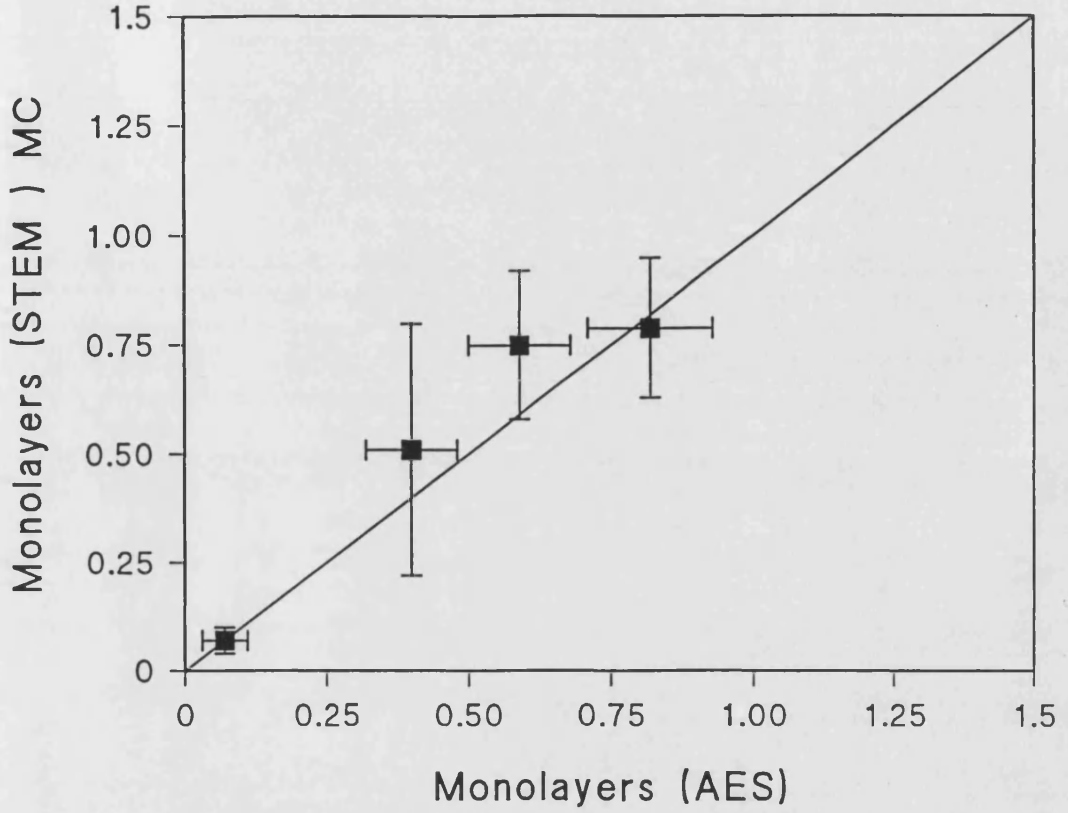

Figure 6.23 Youden plot comparing phosphorus monolayer coverage calculated from STEM data by Monte Carlo method and AES data

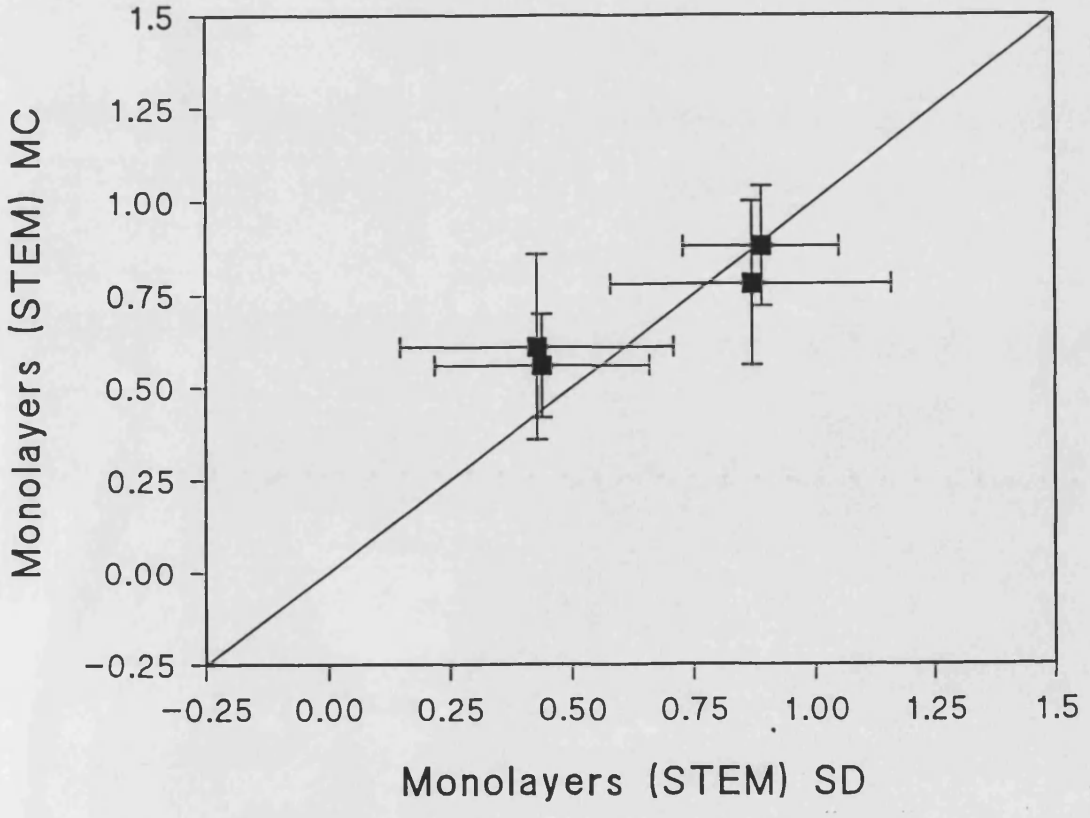

Figure 6.24 Youden plot comparing chromium monolayer coverage calculated from STEM data by simple deconvolution and Monte Carlo methods

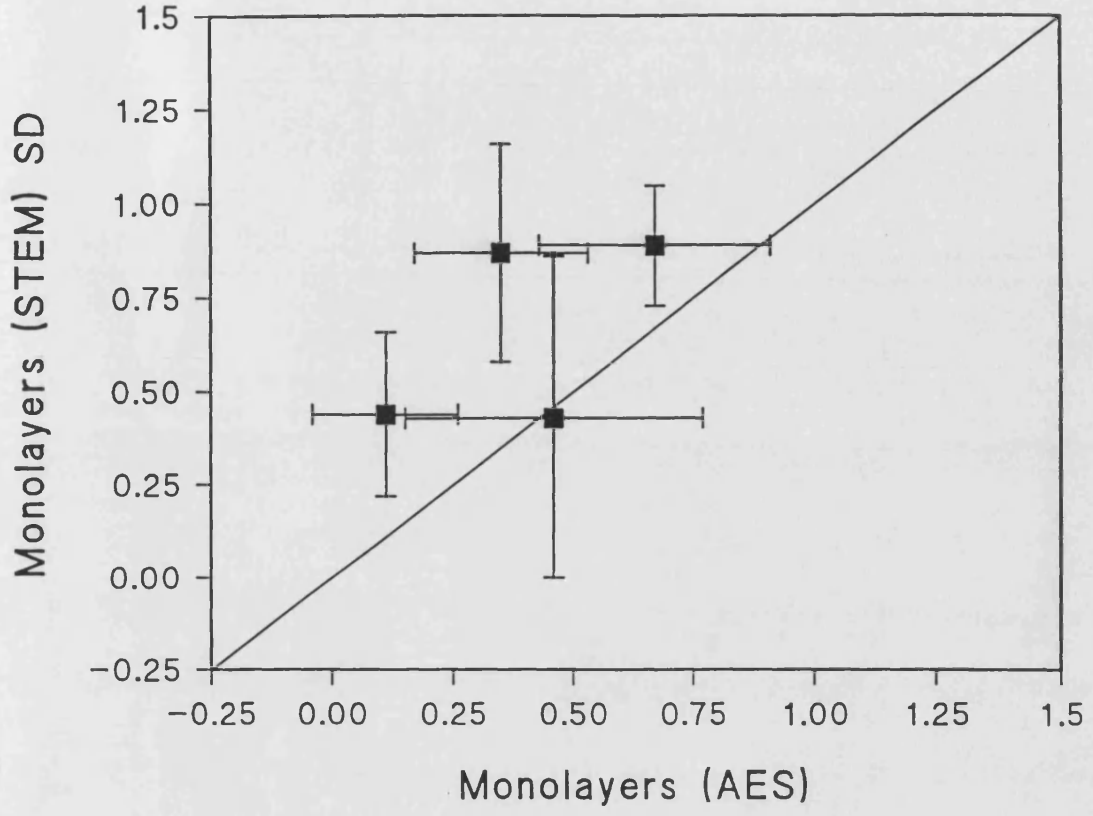

Figure 6.25 Youden plot comparing chromium monolayer coverage calculated from STEM data by simple deconvolution method and AES data

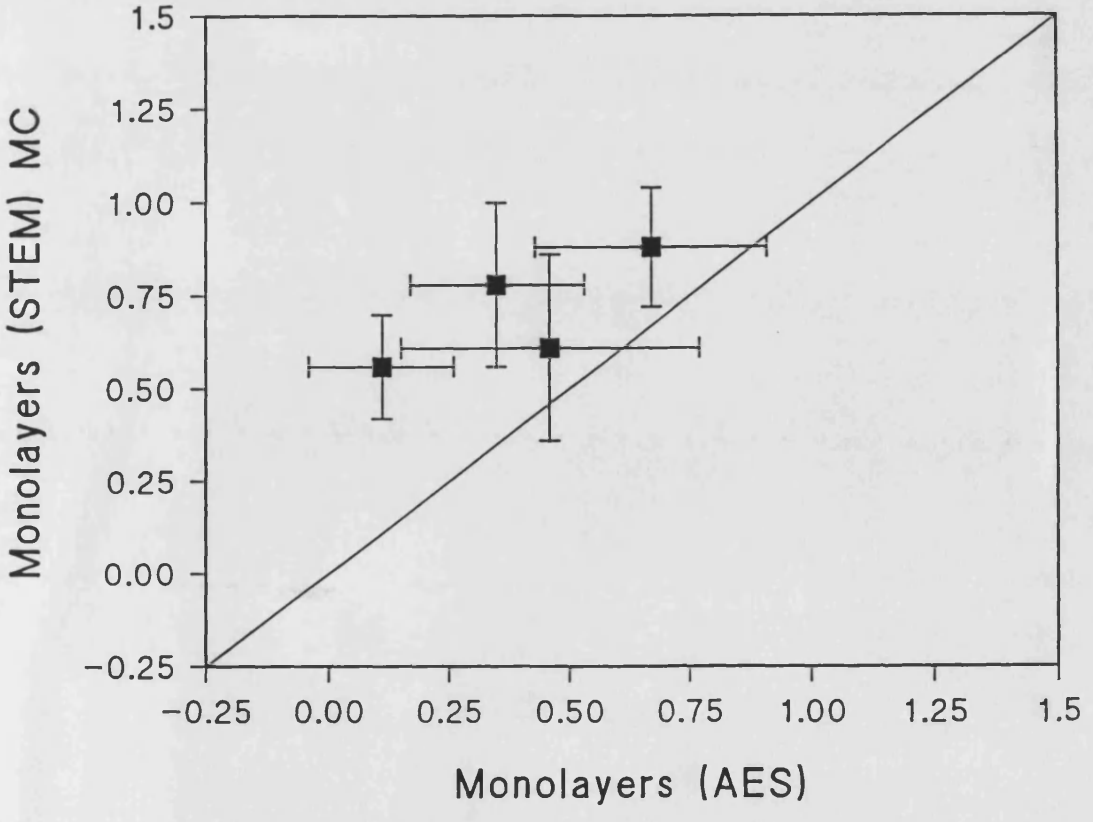

Figure 6.26 Youden plot comparing chromium monolayer coverage calculated from STEM data by Monte Carlo method and AES data

Chapter 7 Conclusions and Future Work

7.1 Conclusions

The objectives of this thesis were:

(i) to assess the applicability of Auger electron spectroscopy (AES) and scanning transmission electron microscopy with energy dispersive x-ray analysis (STEM/EDX) as techniques for the measurement of interfacial segregation in casts of 9% chromium ferritic steel containing varying levels of phosphorus.

(ii) to develop experimental techniques to optimise the detection capabilities of each technique.

(iii) to develop quantification routines to enable the percentage monolayer coverage of phosphorus and chromium to be determined from the raw data produced by each technique.

(iv) to determine the minimum detectable levels of segregation achievable by both techniques under the experimental conditions used.

(v) to compare the levels of segregation calculated by each of the techniques to allow direct comparison of the data.

(vi) to suggest conditions under which each technique is favourable

Both AES and STEM/EDX techniques have been amply demonstrated as capable of detecting interfacial segregation of phosphorus and chromium in the alloy system studied. The segregation of chromium was detectable even with the presence on the grain boundaries of precipitates identified as $M_{23}C_6$ by convergent beam electron diffraction in the TEM.

Using AES, the enrichment of both phosphorus and chromium was found to reduce rapidly to matrix values when the surface of a grain boundary facet was eroded by ion bombardment. This confirms that the segregation is equilibrium in nature and restricted to a very narrow region adjacent to the grain boundary (~3 atom planes). The variation in chemical composition measured perpendicular to a grain boundary in the STEM exhibited a full width at half maximum of 3-5nm. This width was affected by changes in the size of the electron probe. It can therefore be concluded that the chemical composition profile measured by the STEM reflects the electron distribution within the probe formed by the field emission gun rather than the true elemental distribution at the grain boundary.

Scanning electron microscopy showed that the low temperature fracture mode of the alloys was a mixture of intergranular fracture along the prior austenite grain boundaries and transgranular cleavage. The proportion of intergranular fracture decreased with a decrease in bulk phosphorus content. STEM analysis showed that the segregation of phosphorus and chromium was restricted to the prior austenite grain boundaries in all except the most heavily doped alloy (S560), where segregation was also detected at lath boundaries at a similar level to that at the prior austenite boundaries. The AES technique was not able to confirm this finding due to the lath boundaries not being exposed during fracture.

The phosphorus on the intergranular facets exposed by fracture in the AES was found to be mobile under the influence of high beam current density, probably by a surface diffusion mechanism. The phosphorus was stable under the influence of the 5nA beam used to collect data in this study. However, the phosphorus segregated to grain boundaries examined in the STEM was found to be stable under the influence of the electron probe, despite the high current density produced by the field emission gun.

Altering the size of the electron probe in the STEM affected the magnitude of the signal detected from the segregant relative to the matrix signal. Anything which resulted in a larger probe size, such as increasing the size of the beam defining aperture, examining thick foils, defocusing the beam or increased levels of drift, decreased the detected signal. Factors which decreased the size of the beam increased the magnitude of the signal detected from the segregant relative to the matrix signal. The signal detected from the segregant at a grain boundary using the STEM technique was also very sensitive to the alignment of the boundary with the incoming electron beam.

Quantitative AES data were obtained using the formulations proposed by Seah (1983) for the segregation of a single element over a pure matrix of a second element. The model was extended to allow the quantification of the extent of a two component segregant over a multi-component matrix containing precipitates rich in one of the segregating species. This is the first use of such routines and, when included with the determination of matrix and precipitate contributions to the grain boundary signals resulted in the most complete analysis of this type of material using AES. The quantification routines determined percentage monolayer coverage of both phosphorus and chromium.

Two methods of converting the EDX data to obtain percentage monolayer coverage of phosphorus and chromium were investigated. The first was a simple convolution of the electron current distribution with the segregant, assumed to be present as a thin layer at the grain boundary. The second method was to model the interaction between individual electrons with the segregant and matrix atoms using Monte Carlo calculations. The major difference between these two methods is that the Monte Carlo method models the effect of beam broadening, which is neglected in the simple convolution method. Comparison of the results of these two methods of analysing the EDX data showed that both gave similar results. Only in the thickest samples examined ($t > 150$nm) were significant differences noted between

the two methods of data analysis. This indicates that the use of a simple beam broadening estimates, such as that of Goldstein (1977), to define analytical resolution in EDX is inaccurate.

Comparison of the results obtained by the AES and EDX techniques showed that, despite the limitations of the quantification routines, the techniques yielded similar levels of phosphorus segregation. Agreement in levels of chromium segregation determined from the two experimental techniques was, however, not so good due to the added problems incurred in isolating the signal arising from segregated chromium from the contributions of matrix and precipitates.

The minimum detectable segregation level of phosphorus was determined to be ~6% of a monolayer for both AES and STEM. However, the minimum detectable mass of phosphorus in the STEM is significantly lower than in the AES due to the smaller probe sizes used in the STEM.

The AES technique is well suited to the examination of simple systems, containing little or no precipitation, in which a single species segregates. If failure of the AES specimen occurs predominantly by intergranular fracture a large number of grain boundaries can be examined thus providing good statistics. More complex systems containing precipitation and several segregating species are easier to analyse using the STEM technique. However, fewer boundaries are available for analysis in a STEM sample and the statistics therefore tend to be poorer. Samples which do not fail by intergranular fracture at all can only be analysed by STEM.

The study which has been undertaken is the most systematic comparison so far conducted of the techniques of AES and STEM/EDX as methods for quantifying grain boundary segregation. The work has confirmed the credibility of the techniques. It has been shown that both techniques give good results, provided careful analysis procedures are followed and contributions to grain boundary signals from sources such as precipitates and matrix are calculated. The study of the

STEM/EDX technique has also established the effects of variations in experimental parameters such as size of beam defining aperture, drift and focus instabilities. Although this work has been conducted on a ferritic steel, to facilitate the direct comparison of the techniques, the analysis routines which have been developed are equally applicable to other systems both metallic and non-metallic.

The work presented in this thesis gives a better understanding of the potential and limitations of the AES and STEM/EDX techniques for use in quantitative measurement of interfacial segregation. As such it fills the gap which was present in the use of these two powerful techniques.

7.2 Suggestions for Future Work

To improve the data obtained in the STEM it is difficult to increase the number of boundaries which can be examined in a session, therefore the most likely improvements will come from efforts to decrease the uncertainty in each experimental point.

The magnitude of the signal detected from a segregant is inversely related to the diameter of the probe. However, reducing the size of the probe reduces the current it contains which in turn decreases the x-ray production rate and requires longer counting times to obtain statistical accuracy. Consequently one way forward would be to use a brighter electron source. This would require an advance in electron source technology as the field emission gun utilised on the HB501 is the brightest type of source currently available. A reduction in electron probe diameter at the sample could also be achieved by the incorporation of an objective lens with a lower coefficient of spherical aberration, however such lenses generally have a smaller gap between the pole-pieces and therefore restrict sample tilting. The statistical accuracy associated with an x-ray peak is related to the square root of the

number of characteristic counts it contains. Therefore increasing the x-ray count rate will improve the accuracy obtainable in a given time. One possibility is to increase the solid angle over which the x-rays are collected by the detector. This can be achieved by increasing the physical size of the detector crystal and/or moving it closer to the specimen or even interfacing more than one EDX detector to the microscope. The detector used throughout this study subtends a solid angle of 0.08 steradians at the sample. It is now possible to increase this to approximately 0.2. The use of two such EDX detectors would give a factor of 5-6 increase in x-ray count rate over the detector configuration currently on the STEM. Each of these approaches to increasing the x-ray count rate may be detrimental to the process of high spatial resolution analysis. The use of larger Si(Li) crystals increases the likelihood of imperfections which can lead to problems of incomplete charge collection. Closer proximity of the detector to the sample increases the probability of the detector picking up x-ray signals from sources other than the area of the sample illuminated by the primary beam, thus requiring more accurate collimation of the x-rays onto the detector. Increasing the count rate using these methods will also require an improvement in the throughput capability of pulse-processors if the detector dead-time is not to increase dramatically. Due to the limited space around a sample in modern AEM the interfacing of two EDX detectors close to a sample may restrict the range of tilt angles which the sample can be moved through, also for optimum performance the sample would have to be angled favourably towards both detectors which are mounted at right angles to each other. The move to a higher accelerating voltage in a dedicated STEM will give a better peak to background ratio for x-ray spectra but also increases the possibility of specimen damage due to the increased electron energy.

Another development in STEM is the use of parallel electron energy loss detection. In this technique it is possible to collect an EELS spectrum simultaneously over approximately 1000 channels. Because of this a spectrum can

be collected in a very short timespan, e.g. 1-2 seconds. This rapid acquisition time eliminates the problems often encountered collecting x-ray spectra from small microstructural features such as drift, focus fluctuations and contamination build-up under the beam. The quantification of EELS data is also improving through the use of software routines developed to deconvolute the effect of multiple scattering of the electrons in the foil. An additional advantage of the EELS technique is that only those electrons which have been scattered through small angles enter the spectrometer and electrons which are scattered through large angles, i.e. those which contribute to beam broadening, do not contribute to the measured spectrum. Consequently an EELS profile will have a smaller value of FWHM than a EDX chemical composition profile collected with a similar sized electron beam.

In the AES field instrumental improvements to give better image and analytical resolution are being made. Included in this is the use of field emission electron sources. However, care must be exercised with these high brightness sources not to increase the beam current density too much and risk moving the segregant species. In a similar manner to parallel detection of the EELS spectrum multi-channel analysers are becoming available on the Auger electron spectrometers. In this case only three to five channels are collected simultaneously rather than 1000, so the reduction in acquisition time is not so dramatic. In addition spectrum acquisition time is not often a limiting factor in AES studies.

Improvements in the commercial software available to quantify AES data are also being made to allow more automated analysis.

References

Allen S M, Phil Mag, 43A, 1981, p325

Archarov B I and Skornyakov N N, Trudy Inst Fiz Metal Akad Nauk SSSR, 16, 1955, p75.

Auger P, Comp Rendus, 180, 1925, p65.

Baumann S F and Williams D B, J of Microscopy, 123(3), 1981, p299.

Berning G L P and Coleman W J, Surface Science, 173, 1986, p411.

Binnig G and Rohrer H, IBM Journal Research and Development, 30, 1986, p355; Review of Modern Physics, 57, 1987, p615

Bishop H E, Private communication.

Boersch H, Zeit. Tech. Phys., 20, 1939, p346

Bouchet D and Priester L, Journal of Materials Science, 14, 1979, p2205.

Bragg W H and Bragg W L, Proc. Roy. Soc., A88, 1913, p428.

Breummer S M, Charlot L A, Thomas M T and Jones R I J, EPRI-RD-3859, 1985, Vol I.

Briant C L, Acta Metall, 33(7), 1985, p1241.

Briant C L and Andresen P L, Met Trans A, 19A, 1988, p495.

Bullough R, Wood M H and Little E A, Tenth Conf on Effects of radiation on materials , ASTM STP 725, Eds Kramer D, Brager H R and Perrin J S, American Society for Testing of Materials, 1981, p593.

Busch H, Ann. Phys., 4, Series 81, 1926, p 974.

Busch H, Ann. Phys., 4, Series 83, 1927, p 849.

Castaing R, Ph.D. Thesis, University of Paris 1951.

Cauchois Y, J. de Phys., 3, 1932, p320.

Clarke D R, Scanning Electron Microscopy, 1, 1978, p77.

Cliff G and Lorimer G W, J of Microscopy, 103, 1975, p203.

Colliex C and Mory C, "Quantitative Electron Microscopy", 25th Scottish Universities Summer School in Physics, Eds Chapman J N and Craven A J, 1984, p305.

Cooke C J and Duncumb P, X-ray Optics and Microanalysis, eds. Mollenstedt G and Gaukler, (Berlin: Springer), 1969, p245.

Cooke C J and Openshaw I K, Electron Microscopy 1970 Vol 1, Paris: Societe Francaise de Microscopie Electronique, p175.

Craven A J, Adam P F and Howe R, Proc Inst of Phys Electron Microscopy and Analysis Group (EMAG) Conf, Newcastle-upon-Tyne, Ed Tatlock G, Sept 1985, p189.

de Broglie M, J. Phys. et Radium, 4, 1914, p265.

Doig P and Flewitt P E J, J Microsc Spectrosc Electron, 8, 1983, p193.

Doig P and Flewitt P E J, J of Microscopy, 112(3), 1978, p257.

Doig P, Lonsdale D and Flewitt P E J, Metal Science, 16, 1982a, p335.

Doig P, Lonsdale D and Flewitt P E J, Met Trans A, 12A, 1982b, p1277.

Duncumb P and Cosslett V E, Proc. Symp. X-ray Microsc. and Microradiog., Camb., 1956,p374.

Dupouy J M, Carteret Y, Aubert A and Boutard J L, Ferritic alloys for use in nuclear techniques, Snowbird, Utah, USA, June 19-23, 1983

Egerton R F and Cheng S C, Ultramicroscopy, 21, 1987, p231.

Egerton R F, "Electron Energy Loss Spectroscopy in the Electron Microscope", Plenum Press, New York, USA, 1986.

El Gomati M M and Prutton M, Surf Sci, 72, 1978, p485.

Ellis M B D, Lewandowski J J and Knott J F, Proc 7th Int Conf on "Strength of metals and alloys", Montreal, Canada, 12-16 Aug 1985, Eds McQueen H J, Bailon J P, DicksonJ I, Jonas J J and Akben M G, Pergamon Press, Oxford.

Erhart H, Grabke H J and Önel K, Proc Conf, "Advances In The Physical Metallurgy And Applications Of Steels", Metals Society, University of Liverpool, 21-24 Sept 1981, p282.

Eyre B L, Edwards B C and Titchmarsh J M, Advances in the physical metallurgy and application of steels, University of Liverpool, 21-24 Sept, 1981.

Farrow R C, Joy D C and Maher D M, Microbeam Analysis, 1979, p41

Fujita T, Metal Progress 33, August 1986

Fukuya K, Nakahigashi S and Terasawa, Scripta Met, 19(8), 1985, p959.

Garrett-Reed A J, Mottishaw T D, Worrall G M and Smith G D W, IOP Conf Series No 68, Pub Adam Hilger, 1983, p311.

Gettes D S and Thomas L E, Ferritic alloys for use in nuclear techniques, Snowbird, Utah, USA, June 19-23, 1983.

Goldstein J I, Costley J L, Lorimar G W and Reed S J B, SEM/1977, 1, Ed Johari O, IITRI, Chicago Ill., p315.

Gouy M, Ann. Physique., 5, 1916, p241.

Greaves R H and Wrighton, "Pratical Microscopical Metallography", Chapman and Hall, 1967, p126.

Gryzinski M, Phys Rev, 138A, 1965, p336.

Guttmann M, Surface Science, 53, 1975, p213.

Guttmann M, Phil Trans Roy Soc, A295, 1980, p169.

Harris L A, J Appl Phys, 39, 1968, p1419.

Herzog R F K, Poschenrieder W P and Satkiewicz F G, NASA, Contract No NAS5-9254, final report GCA-TR-67-3N, 1967.

Herzog R F K and Viehblòck F, Phys. Rev, 76, 1949, p855.

Horton J A and Miller M K, Acta Metall, 35 (1), 1987, p133.

Hosoi, Private Communication to Titchmarsh J M, 1989.

Hosoi J, Oikawa T, Inoue M, Kokubo Y and Hama K, Ultramicroscopy, 7, 1981, p147

Ichimura S, Shimizu R and Langeron J P, Surface Science, 124, 1983, pL49.

Inman M C and Tipler H R, Acta Met, 6, 1958, p73.

Jablonski A, Surf Interface Anal, 2, 1980, p39.

Johann H H, Zeit. Phys., 69, 1931, p185.

Johansson T, Naturwiss, 20, 1932, p758.

Johansson T, Zeit Phys., 82, 1933, p507.

Joshi A and Stein D F, J Inst Met, 99, 1971, p178.

Joy D C, Egerton R F and Maher D M, Scanning Electron Microscopy II, 1979, p817.

Kameda J, Mao X and Bevolo A J, J Nuc Mat, 179-181, 1991, p1034.

Karlsson L and Norden H, J Phys, C9, 1984, p391.

Kayano H, Narui M, Ohta S and Morozumi S, J Nucl Mat, 133 & 134, 1985, p644

Kaye G W C, Phil. Trans. Roy. Soc., A209, 1909, p123.

Kelly P M, Jostens A, Blake R Gand Napier J G, Phys Stat Sol (3), 31, 1975, p771.

Kenik , Mat Res Soc Symp Proc, Vol 62, 1986, p209.

Klueh R L, Nuclear Engineering and Design, 72, 1982, p329.

Knoll M, Zeit. Tech. Phys., 16, 1935, p467.

Knoll M and Ruska E, Ann. Phys., 12, 1932a, p607.

Knoll M and Ruska E, Ann. Phys., 12, 1932b, p641.

Kouh Simpson Y, Carter C B, Morrissey K J, Angelini P and Bentley J, J of Materials Science, 21, 1986, p2689.

Lander J J, Phys Rev, 91, 1953, p1382.

Leapman R, Fiori C E and Swyt C R, J Microsc, 133, 1984a, p239.

Leapman R, Fiori C E and Swyt C R, Analytical electron microscopy - 1984b, Ed Williams D B and Joy D C, San Francisco Press, San Francisco, p83.

Lechtenberg T, J Nucl Mat, 133 & 134, 1985, p149.

Leipold M H, "Ceramic Microstructures", Proc 3rd Berkeley Int Conf , Eds Fulrath R M and Pask J A, Wiley Inter Science, 1968, p289.

le Poole J B, Proc 3rd Europ Conf Elec Microsc, (Prague: Czech Acad Sci) 1964, p439.

Liebel H J and Herzog R F K, J. Appl. Phys., 34, 1963, p2893.

Lorimer G W, Al-Salman S A and Cliff G, Developments in Electron Microscopy and Analysis, Ed Misell D C, Institute of Physics, London, 1977, p369

McLean D, "Grain Boundaries in Metals". Clarendon Press, Oxford, 1957.

McMahon C J, Proc 4th Bolton Landing Conf, Publishing Division, Baton Rouge, 1974, p525.

Malis T F, Cheng S C and Egerton R F, J Electron Microscopy Techniques, 8, 1988, p193.

Michael J R and Williams D B, Met Tran A, 15A, 1984, p99.

Michaelson H B, J Appl Phys, 48, 1977, p4729.

Miller M K, Beaven P A and Smith G D W, Surface and Interface Analysis, 1, 1979, p149.

Molinari C and Joud J C, "Physical chemistry of the solid state: applications to metals and their compounds", Ed Lancombe, Elsevier Science Publishers, Amsterdam, 1984, p151.

Müller E W, Ann. Meeting of El. Mic. Soc. of America, Pennsylvania State Univ, 1955

Müller E W, Proc. 4th Int. Conf. Electron Microscopy, Berlin, (Springer, Berlin), 1, 1958, p820

Muroga T, Yoshida N, Miyamoto Y and Murakami H, Materials Science Forum, Vols 15-18, 1987, p1415.

Nakamura T, Shinoda T and Watanabe H, Trans Iron Steel Inst, 19(6), 1979, p365.

Newbury D E and Myklebust R L, "AEM 1981", Ed R H Geiss, San Francisco Press Inc., 1981, p91.

Norris D I R, Baker C and Titchmarsh J M, Radiation of Stainless Steels, Proc of Symposium, Berkeley Nuclear Laboratories, Ed Norris D I R, 1986, p86.

Ogura T, Makino A and Masumoto, Met Trans A, 15A, 1984, p1563

Okumura M, Yurioka N, Imai K and Nakamura H, Trans Jap Welding Soc, 16(1), 1985, p57.

Pande C S, Suenaga M, Vyas B, Isaacs H S and Harling J, Scripta Met, 11, 1977, p681.

Partridge A and Tatlock G J, Surface and Interface Analysis, 18, 1992, p713.

Paulus M in "The role of grain boundaries and surfaces in ceramics", Eds,. Kriegel W W and Palmer H, Vol 3 "Materials Science Research", Plenum Press, New York, 1966, p31.

Penn D R, J Electron Spectrosc, 9, 1976,p29.

Phythian W J, Foreman A J E, English C A, Buswell J T, Hetherington M, Roberts K and Pizzini S, Effects of Irradiation on Materials: 15th International Symposium, ASTM STP 1125, Eds Stoller R E, Kumar A S and Gelles D S, American Society for Testing and Materials, Philadelphia, 1992, p131.

Powell C J, Use of monte carlo calculations in electron probe microanalysis and scanning electron microscopy, Ed Newbury D E and Yakowitz, National Bureau of Standards special publication 460, US Dept of Commerce, Sanfrancisco, 1976, p97.

Powell B D and Mykura H, Acta Met, 21, 1973, p1151.

Powell B D and Woodruff D P, Phil Mag, 34, 1976, p169.

Reuter W, Proc Sixth International Conf on X-ray Optics and Microanalysis , Eds Shinoda G, Kohra K, Ichinokawa, Univ of Tokyo Press, 1972, p121.

Riviere J C, Solid State Surface Sci, 1, 1969, p79.

Russ J C, Fundamentals of energy dispersive x-ray analysis, Butterworths, London, 1984, p118.

Seah M P, "Practical Surface Analysis", Eds Briggs D and Seah M P, Wiley, New York, USA, 1983, Chap 5 p181.

Seah M P and Dench W A, Scanning Electron Microscopy II, Chicago, 1983a, p521.

Seah M P and Dench W A, Surface and Interface Analysis, 1(1), 1979, p2.

Sekine T, Mogami A, Kudoh M and Hirata K, Vacuum, 34(6), 1984, p631.

Shastry C R and Judd G, Met Trans, 3, 1972, p779.

Shimizu R and Ichimura S, Surf Sci, 112, 1981, p386.

Shin K S and Meshii M, Proc 7th Int Conf on "Strength of metals and alloys", Montreal, Canada, 12-16 Aug 1985, Eds McQueen H J, Bailon J P, DicksonJ I, Jonas J J and Akben M G, Pergamon Press, Oxford.

Sickafus K and Sass S L, J Vac Sci Technol, A3(3), 1985, p1525.

Smith D A and Smith G D W, Proc Conf on "The microstructure and design of alloys", Cambridge, UK, August 1973,1 (29), p144.

Spence J C H, Reese G, Yamamoto N and Kurizki G, Phil Mag B, 1983, L39.

Starke H, Ann. Phys., 66, 1898, p49.

Statham P J, X-ray Spectrometry, Vol 5, 1976a, p16.

Statham P J, J Phys E: Sci Instrum, vol 9, 1976b, p1203.

Titchmarsh J M, 11th Int Congress on X-ray Opticics and Microanalysis (IXCOM), London, Canada, Eds Brown J D and Packwood R H, 1986, p337.

Titchmarsh J M and Vatter I A, Radiation of Stainless Steels, Proc of Symposium, Berkeley Nuclear Laboratories, Ed Norris D I R, 1986,

Titchmarsh J M and Vatter I A, Proc NATO advanced workshop on "The evaluation of advanced semiconductor materials by electron microscopy", Ed Cherns D, Bristol University, Sept 1989, p111.

Turner P J and Papazian J M, Metal Sci Journal, 7, 1973, p81.

Vander-Sande J B, Garrett-Reed A J, Chiang Y and Thorvaldsson T, Ultramicroscopy, 14, 1984, p65.

Vatter I A and Hippsley C A, AEA-RS-2092, 1991a

Vatter I A and Hippsley C A, Proc of the International Atomic Energy Agency Specialists' Meeting on "Thermal and Mechanical Degradation in Reactor Materials", Abingdon, England 19-21 Nov 1991b, p181.

Vatter I A and Titchmarsh J M, Ultramicroscopy, 28, 1989, p236

Wall M, PhD Thesis, Imperial College, London, 1987.

Westbrook J H and Aust K T, Acta Met, 11, 1963, p1151.

Westbrook J H, Metallurgical Reviews, 9, 1964, p415.

Westbrook J H and Wood D L, J Inst Met, 91, 1962, p174.

White C L, Padgett R A, Liu C T and Yalisove S M, Scripta Met, 18, 1984, p1417.

Yamanaka K and Ohmori Y, Trans Iron Steel Inst Japan, 19(6), 1979, p339.

Youngbin I M and Danyluk S, Met Trans A, 18A, 1987, p19.

Zaluzec N J, Introduction to analytical electron microscopy, Ed Hren J J, Goldstein J I and Joy D C, New York, Plenum Press,1979, p143.

Key to Acronyms used in Text

ADC	Analog-to-digital converter
AEM	Analytical electron microscope
AES	Auger electron spectroscopy
APFIM	Atom probe/field ion microscopy
BSE	Backscattered electrons
CB	Coherent Bremsstrahlung
CBED	Convergent beam electron diffraction
CHA	Concentric hemispherical analyser
CMA	Cylindrical mirror analyser
CRR	Constant retard ratio
CRT	Cathode ray tube
DBTT	Ductile to brittle transition temperature
DPA	Differential pumping apertures
EDX	Energy dispersive x-ray
EELS	Electron energy loss spectroscopy
EPMA	Electron probe microanalysis
eV	Electron volts
FEG	Field emission gun
FET	Field effect transistor
FIM	Field ion microscope
FLS	Filtered least squares
FWHM	Full width at half maximum
IGP	Ion getter pump
MCA	Multi-channel analyser
NA	Numerical aperture
OA	Objective aperture
PPHR	Peak-to-peak height ratio

ppm	Parts per million
RTS	Ratio thin section
SADA	Selected area diffraction aperture
SADP	Selected area diffraction pattern
SE	Secondary electrons
SEM	Scanning electron microscope
SIMS	Secondary ion mass spectroscopy
SNR	Signal-to-noise ratio
STEM	Scanning transmission electron microscopy
STM	Scanning tunnelling microscope
TEM	Transmission electron microscope
TOFMS	Time of flight mass spectroscopy
UHV	Ultra-high vacuum
UPS	Ultra-violet photo-electron spectroscopy
VFC	Voltage-to-frequency converter
VOA	Virtual objective aperture
WDX	Wavelength dispersive x-ray detector
XPS	X-ray photo-electron spectroscopy

Figure Captions

Acknowledgements

The author is grateful to acknowledge the financial support of the Underlying Research Programme of AEA Technology for the funding of this work.

I am indebted to my supervisors Dr J M Titchmarsh (AEA Technology) and Professor V D Scott (Bath University) for their guidance, encouragement and discussions throughout this period of study.

I would like to acknowlege the assistance of Drs H E Bishop and C A Hippsley for helpful discussions on AES analysis and Mr A W James and Mr R Cooke for their undertaking some of the sample preparation.

Finally I would like to express my appreciation of my wife, Nicky, for her patience, understanding and tolerance during the lengthy course of this work.